2015

Microalloying, processing optimisation and friction stir welding of ferretic stainless steel thick plate

Jian Han
University of Wollongong

UNIVERSITY OF WOLLONGONG

MICROALLOYING, PROCESSING OPTIMISATION AND FRICTION STIR WELDING OF FERRETIC STAINLESS STEEL THICK PLATE

A thesis submitted in fulfilment of

the requirements for the award of the degree

DOCTOR OF PHILOSOPHY

from

UNIVERSITY OF WOLLONGONG

by

Jian Han
B. Eng., M. Eng.

School of Mechanical, Materials and Mechatronic Engineering
Faculty of Engineering and Information Sciences

February, 2015

ACKNOWLEDGEMENTS

I wish to express my sincere appreciation and gratitude to my supervisor, Prof. Huijun Li, and co-supervisor, Prof. Frank Barbaro, for their valuable guidance, support, comments, inspiration and close supervision during my PhD candidature. It was a great pleasure working with them and I hope I can continue to work with them in the future.

I am deeply grateful to Dr. Zhixiong Zhu, Yan Ma and Chen Shen for their valuable discussion, encouragement and friendship.

I wish to thank the members from Baosteel for their expertise and extensive use of facilities. A special thanks to Mr. Bin Guo and Dr. Laizhu Jiang for their support, Dr. Haifeng Yu, Li Ma, Haigang Xu, Zhiyu Wang, Dr. Wei Du for their input into my research.

I am also grateful to all the members of the Faculty of Engineering and Information Sciences at the University of Wollongong especially to Prof. Zhengyi Jiang, A/Prof. Cheng Lu, Dr. David Wexler, Bob de Jong, Dr. Chingtun Peng, Liang Chen, Mitchell Nancarrow, Azdiar Adil Gazder and Greg Tillman for their technical assistance. I would also like to thank Engineering Enquiry Centre staff for assisting in administration work.

I would like to acknowledge family support especially by my father, my late mother, my father and mother in-law, my aunt and sister.

Last but not least, my warm appreciation and respect are due to my beloved wife, Weiyi Li for allowing me to stay away from home, taking care of our daughter, her understanding, continuous encouragement and patience throughout my PhD candidature and to my daughter, Ruiyi Han, for putting up with me during the good and the bad times that are part of doing a PhD.

ABSTRACT

With the breakthroughs in metallurgical technology and their excellent performance in hostile environment, ferritic stainless steel (FSS) grades are developed and extensively applied to replace pricy austenitic groups. Among ferritic groups, the frequently-used grades are 18Cr-2Mo and 17Cr ultra purified FSS stabilised by the elements of Nb, Ti and V. However, the bottleneck of ferritic groups with thick scales (above 4 mm) is their relatively high ductile-brittle transition temperature (DBTT). Thus, it is imperative to develop FSS with lower DBTT. On the other hand, to extend the use of FSS, welding is an indispensable process to produce steel structures in main industry. The development of novel welding methods attracts much attention.

In this research, the effects of microalloying and processing optimisation on the designed FSS thick plates were investigated to develop high-quality products. Then, friction stir welding (FSW) is selected as a suitable procedure to fabricate the joints with excellent mechanical properties. To satisfy the ultimate requirements of properties, the microstructure and mechanical properties of both produced steels and their FSW joints were modified and examined.

The microalloying investigation focused on the relationships of the microstructure and mechanical properties of the microalloyed 18Cr-2Mo FSS thick plates. The different combinations of Nb, V and Ti are designed to explore the optimum use of stabilised elements in 18Cr-2Mo grades. In order to study the influences of stabilisation on the

microstructure and mechanical properties of the four designed steels, Thermo-Calc calculation was performed to predict the equilibrium phase diagrams. Afterwards, the microstructure, i.e. grain size and precipitation, of as-annealed specimens was analysed by means of optical microscopy (OM), scanning electron microscopy (SEM) and transmission electron microscopy (TEM), X-ray diffraction (XRD) and energy dispersive spectroscopy (EDS). Also, electron backscatter diffraction (EBSD) mapping was constructed to characterise grain boundary (GB). The mechanical properties, including tensile strength and impact toughness, were tested to correlate with the microstructure. It was found that the addition of Nb/(Nb + V) is beneficial to the grain refinement and precipitation distribution. When Ti is added, TiN forms above the liquidus, and large TiN particles evidently impair impact toughness. The mechanical testing indicates that optimal transformation of grain size, precipitation in Nb and Nb-V stabilised 18Cr-2Mo thick plates contributes to improvement of mechanical properties, such as strength and impact toughness.

In the processing optimisation research, the correlations of microstructural characterisation, i.e. grain size, texture and grain boundary, and mechanical properties, including tensile strength and impact toughness of Nb, Ti and V microalloyed 17Cr FSS thick plates with and without warm rolling are studied. The mechanism of the warm rolling is explained. To demonstrate the influences of warm rolling on the designed steels, the microstructure of as-annealed specimens was observed using OM. The results of texture and GB from XRD and EBSD show that the addition of warm rolling procedure leads to refinement of grain size, modification of texture, and then optimisation of GB, including grain boundary character distribution (GBCD) and GB

connectivity. Meanwhile, the mechanical testing indicates that the optimal transformation resulted from warm rolling procedure is beneficial to the mechanical properties of 17Cr FSS thick plates.

During the fabrication of purified FSS grades, the grain refinement is essential to maintain the final mechanical properties of thick scale plates. The microstructure and mechanical properties of a friction stir welded 18Cr-2Mo FSS thick plate were investigated. The plates with excellent properties were welded at a constant rotational speed and a selected welding speed using a W-Re/cBN (cubic boron nitride) composite tool. With optimised welding parameters, the high-quality welds were successfully produced and the microstructure and mechanical properties were studied by means of OM, SEM, EBSD and hardness and impact toughness testing. The improvement in mechanical properties of the joints is mainly related to the remarkably fine-grained microstructure of equiaxed ferrites in the friction stir welded joint. Additionally, the ratios of low-angle grain boundary in the stir zones significantly increase, and the texture becomes strong. Compared with the base material, the mechanical properties of the joints are maintained at a comparatively high level.

ABBREVIATIONS AND SYMBOLS

Abbreviations

FCC	face-centered cubic
BCC	body-centered cubic
AISI	American Iron and Steel Institute
ASS	austenitic stainless steel
FSS	ferritic stainless steel
SCC	stress corrosion cracking
DSS	duplex stainless steel
MSS	martensitic stainless steel
PHSS	precipitation hardening stainless steel
BM	base material, base metal
HAZ	heat affected zone
ISSF	International Stainless Steel Forum
WSA	World Steel Association
NSSC	Nippon Steel & Sumikin Stainless Steel
JFE	JFE Steel Corporation
POSCO	Pohang Steelworks
TISCO	Taiyuan Iron & Steel Group
Baosteel	Baoshan Iron & Steel Group
LCC	life cycle cost
YS	yield strength
UTS	ultimate tensile strength
P.I	pitting index
PRE	pitting resistance equivalent
DBTT	ductile-brittle transition temperature
CVN	Charpy-V notch

FTP	fracture transition plastic
NDT	nil ductility temperature
FATT	fracture appearance transition temperature
CVN	Charpy-V notch
MDOT	minimum design operating temperature
LEFM	linear elastic fracture mechanics
HSLA	high strength low alloy
GB	grain boundary
GBC	grain boundary character
GBE	grain boundary engineering
GBCD	grain boundary character distribution
LAB	low-angle boundary
HAB	high-angle boundary
CSL	coincidence site lattice
CSLB	coincidence site lattice boundary
FSW	friction stir welding
TWI	The Welding Institute
EBSD	electron backscatter diffraction
SFE	stacking fault energy
TIG	tungsten inert gas
MMA	manual metal arc
MIG	metal inert gas
DSEN	direct current electrode negative
DCEP	direct current electrode positive
WM	weldment
FL	fusion line
OM	optical microscopy
SEM	scanning electron microscopy
TEM	transmission electron microscopy
EDS	energy dispersive spectroscopy
XRD	X-ray diffraction

$FeCl_3$	ferric chloride
HCl	hydrochloric acid
FEG-SEM	field emission gun scanning electron microscope
ODF	orientation distribution function
RD	rolling direction
ND	normal direction
TD	transverse direction
TMP	thermomechanical processing
SZ	stir zone
TMAZ	thermomechanically affected zone
AS	advancing side
RS	retreating side
SD	shear direction
WD	welding direction

Symbols

γ	austenite
α	ferrite
L	liquid
σ	Sigma phase
χ	Chi phase
M_s	martensite start temperature
K_I	fracture toughness
σ	applied stress
α	crack length
β	crack length and component geometry factor
K_{IC}	plane-strain fracture toughness
σ_y	flow or fracture stress, or both
k_y	Hall-Petch slope

σ_0	lattice friction stress
C	constant related to stress state and average ratio of normal to shear stress on the slip plane
μ	shear modulus
γ	effective surface energy of implied crack
E_y	Charpy impact energy
E_{OF}	lower shelf energy
E_{SF}	lower shelf energy
λ_F	transition width parameter
T_{OF}	temperature above which transition occurs
T_C	DBTT
d	grain size or mean linear intercept
K_Q	fracture toughness
θ	angle of boundary
Σ	reciprocal density of coinciding site
$f_{2\text{-}CSL}$	fraction of triple junctions that have two special boundaries
$f_{(1\text{-}3\text{-}CSL)}$	fraction of triple junctions that are active unit entities

TABLE OF CONTENTS

LIST OF FIGURES

LIST OF TABLES

PART A

INTRODUCTION

&

LITERATURE REVIEW

1. INTRODUCTION

1.1. BACKGROUND

Without the fluctuation of nickel price, ferritic stainless steel (FSS) is a suitable alternative material for many supposedly “austenitic-only” applications. Recent breakthroughs in metallurgical technology have made it possible for extensive utilisation of FSS due to the improvement of the properties, including corrosion resistance, weldability, formability, etc.

18Cr-2Mo and 17Cr ultra purified ferritic stainless steels that contains chromium (molybdenum) and stabilising elements are the appropriate candidates to replace AISI 316 and AISI 304 austenitic grades applied in industrial fields, such as chemical complete equipment, water treatment tank, brewing equipment, etc. 18Cr-2Mo and 17Cr FSS thick plates (above 4 mm) are the groups that newly developed to replace more costly austenitic stainless steel (ASS) grades in special corrosive environments as excellent contenders. However, the limitation of the FSS group for thick scale is its high ductile-brittle transition temperature (DBTT). This is an urgent issue to be addressed if the development of this group is driven due to a strong economic force by the customers.

Although FSS grades are recognised as the materials with comparatively low toughness because of body-centered cubic (BCC) crystal structure, there are still a number of methods

that can be used to modify the mechanical properties of 18Cr-2Mo and 17Cr FSS besides the control of interstitial elements. The choices of microalloying and processing optimisation are applied to the design of materials, and friction stir welding (FSW) is used to obtain the applicable welds.

1.2. OBJECTIVE OF CURRENT RESEARCH

The main objective of this research work is to design the qualified FSS thick plates through microalloying and processing optimisation. Also, to minimum or eliminate the loss of mechanical properties during welding, suitable welding method is also a focus for the designed plates. The relationships between microstructure, orientation, texture, grain boundary, etc., and mechanical properties were investigated in order to explain the mechanisms of the base materials and their welds with high performance.

2. LITERATURE REVIEW

2.1. INTRODUCTION OF STAINLESS STEEL

2.1.1. Introduction

Stainless steel is a generic term for a large family of corrosion resistant alloys containing at least 10.5 wt.% chromium and other alloying elements [1, 2]. The minimum chromium content (10.5 wt.%) is necessary to form a "passive film" [3], which increases corrosion and wear resistances of stainless steels. Alloyed with sufficient chromium, steel absorbs oxygen from the air (or from aerated aqueous solutions) to form and maintain a thin, transparent oxide layer. This passive layer can dramatically decrease corrosion resistance [4, 5], shown in **Figure 2-1** [6]. The film is rapidly self-repairing in the presence of oxygen and if damaged by abrasion, cutting or machining [7]. However, to prevent pitting and rusting in more hostile environments, such as moist atmospheres and polluted environments, or in the presence of elements like carbon, higher chromium contents should be added [8].

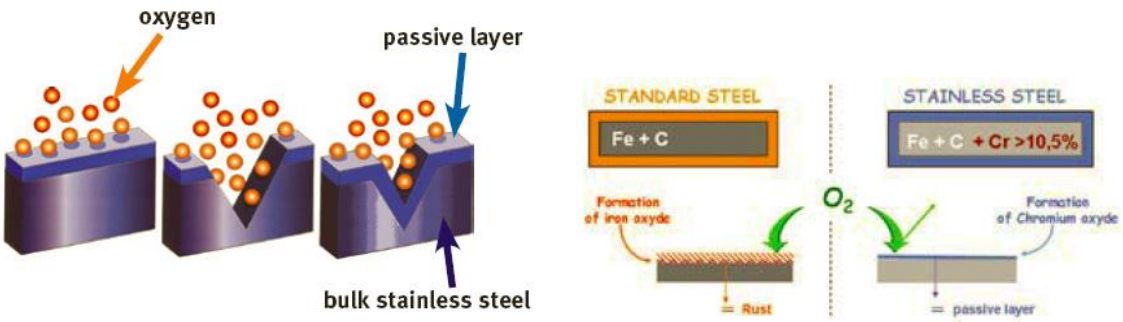

(a) (b)

Figure 2-1 Schematic diagrams of being stainless.

2.1.2. Stainless steel grades

Stainless steels are usually divided into five categories: austenitic (face-centered cubic structure, FCC), ferritic (body-centered cubic structure, BCC), austenitic-ferritic so-called duplex, martensitic, and precipitation hardening groups. For stainless steel producers, they are usually classified into below grades: manganese austenitic, standard austenitic chromium-nickel, standard chromium-nickel-molybdenum, high performance austenitic, ferritic, martensitic, duplex, high temperature in details [9]. **Table 2-1** lists the abbreviations of the involved composition elements.

Table 2-1 Abbreviations of composition elements involved.

Element	Abbr.	Element	Abbr.	Element	Abbr.
iron	Fe	chromium	Cr	sulfur	S

carbon	C	nickel	Ni	phosphorus	P
nitrogen	N	molybdenum	Mo	aluminium	Al
oxygen	O	niobium	Nb	plumbum	Pb
manganese	Mn	titanium	Ti	selenium	Se
silicon	Si	vanadium	V	cobalt	Co
copper	Cu	zirconium	Zr	tungsten	W

2.1.2.1. Austenitic stainless steel (ASS): Fe-Cr-Ni-(Mo) and Fe-Cr-Mn-N alloys

For austenitic grades, the elements, such as Cr, Ni, Mo, allow them to maintain an austenitic microstructure from cryogenic temperature up to the melting point of the alloy. The key properties of ASS group are highly durable corrosion resistance, high ductility, low yield stress, relatively high tensile strength and good weldability. Common usages include equipments for chemical industry, domestic appliances, and architectural applications. A typical composition is 18 wt.% Cr and 8 wt.% Ni, as found in popular AISI 304 [10] (Short for 304, and unless otherwise indicated, a grade designation is originally assigned by the American Iron and Steel Institute).

2.1.2.2. Ferritic stainless steel (FSS): Fe-Cr-(Mo) alloys

In ferritic grades, C is kept to a low level and the Cr content can range from 10.5 to 30 wt.%. Although some ferritic grades contain Mo, only Cr is present as the main metallic

alloying element. These grades cannot be hardened through heat treatment. Ferritic grades are magnetic and selected when corrosion resistance is a primary need, particularly chloride stress corrosion cracking (SCC). Common applications of this type steel are automotive exhaust systems, automotive trims and hot water tanks, etc.

2.1.2.3. Duplex stainless steel (DSS): Fe-Cr-Ni-(Mo)-N alloys

For duplex grades, C is kept to a low level, Cr and Ni contents range from 21 to 26 wt.% and from 3.5 to 8 wt.% respectively, and sometimes Mo is contained (up to 4.5 wt.%). These grades have a mixed structure of ferrite and austenite, and offer physical properties reflecting this structure. These alloys are magnetic, and provide higher tensile and yield strengths than ASS grades. Common uses are marine applications, petrochemical plants, desalination plants and papermaking industry, etc.

2.1.2.4. Martensitic stainless steel (MSS): Fe-Cr-C-(Ni-Mo) alloys

These alloys have a Cr content ranged from 11.5 to 18 wt.%. They have relatively high C content (0.15 ~ 1.2 wt.%) compared to other stainless steels and Mo can also be added. The modified grades add N when reducing C in order to increase the corrosion resistance of martensitic grades. These grades can be hardened through heat treatment, i.e. quenching and tempering like plain carbon steels, to offer high strength and hardness. The common uses are knife blades, surgical instruments, shafts, etc.

2.1.2.5. Precipitation hardening stainless steel (PHSS): Fe-Cr-Ni-(Mo-Al-Cu-Nb) alloys

High strength, middling corrosion resistance and ease of fabrication are the primary benefits offered by this family. These grades exhibit high strength after a low temperature (500 ~ 800 ℃) heat treatment. Since lower temperature can be used, concerns on part distortion are minimised, allowing them to be used for high precision parts. PHSS groups have an initial microstructure of austenite or martensite. Austenitic phases are converted to martensitic ones through heat treatment before precipitation hardening can be done. Precipitation hardening occurs when the heat aging treatment causes hard intermetallic compounds to precipitate out from the crystal lattice as the martensite is tempered. Common uses are in the aerospace and some other high-technology industries.

2.1.3. Equilibrium phase diagram

Equilibrium phase diagrams can be used to describe phase transformation and phase stability in stainless steels [11]. The Fe-Cr binary system, the Fe-Cr-C and Fe-Cr-Ni ternary systems are usually described to predict microstructure evolution as they apply to the various grades of stainless steels.

2.1.3.1. Fe-Cr system

The Fe-Cr phase diagram shown in **Figure 2-2** is the starting point for describing stainless steel phase stability, since Cr is the primary alloying element [12]. At low Cr concentrations, a "loop" of γ (austenite) exists in the temperature range of 912 ~ 1394 ℃. Alloys with greater than 12.7 wt.% Cr are fully α (ferrite) at elevated temperature, while those with less than this amount of Cr form at least some austenite at temperatures within the γ loop. Alloys with less than about 12.7 wt.% Cr are completely austenitic microstructure at temperatures within the γ loop. Upon rapid cooling, this austenite can be transformed to martensite.

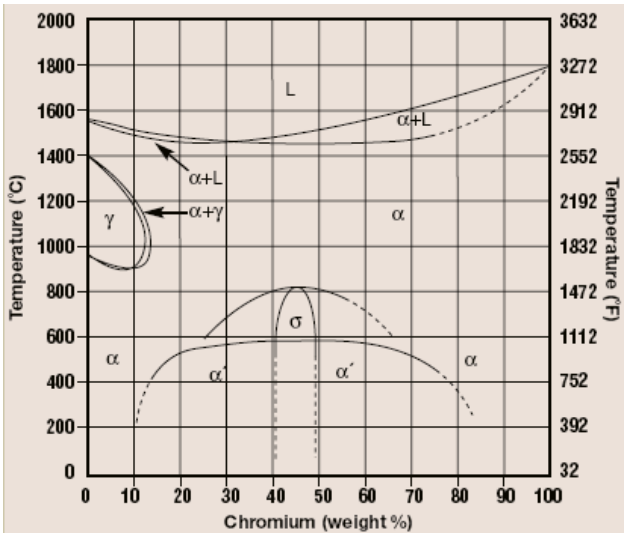

Figure 2-2 Fr-Cr equilibrium phase diagram.

2.1.3.2. Fe-Cr-C system

The addition of C to the Fe-Cr system significantly alters and complicates phase equilibrium. Since C is an austenite promoter, it expands the γ loop, allowing austenite to be stable at elevated temperatures with much higher Cr contents. The effect of C on the expansion of the austenite phase field is shown in **Figure 2-3**. Even small addition of C results in a dramatic expansion of the γ loop. This is important for the development of MSS. These steels must be austenite phase at elevated temperatures since for martensite to form during cooling.

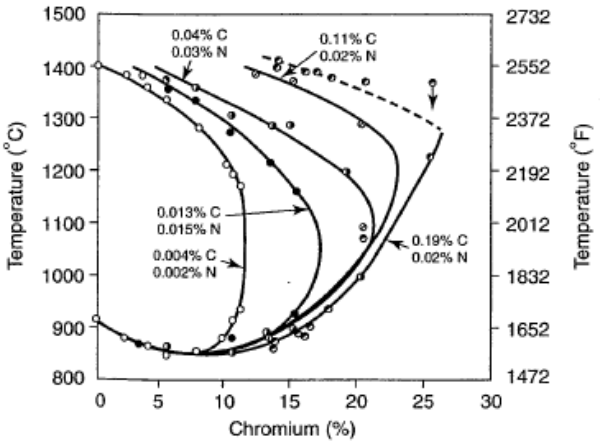

Figure 2-3 Effect of C on expansion of austenite phase field.

The pseudobinary diagrams based on the 17Cr system with variable C is shown in **Figure 2-4**. At higher constant Cr levels in the Fe-Cr-C system, the ferrite phase field expands and the austenite phase field shrinks, which is due to the ferrite-promoting effect of Cr. Thus, the ferrite that forms at elevated temperature is more stable, and higher C contents are

required to form elevated-temperature austenite. This diagram is the basis for medium Cr FSS and medium Cr, high C MSS, such as 430 and 440.

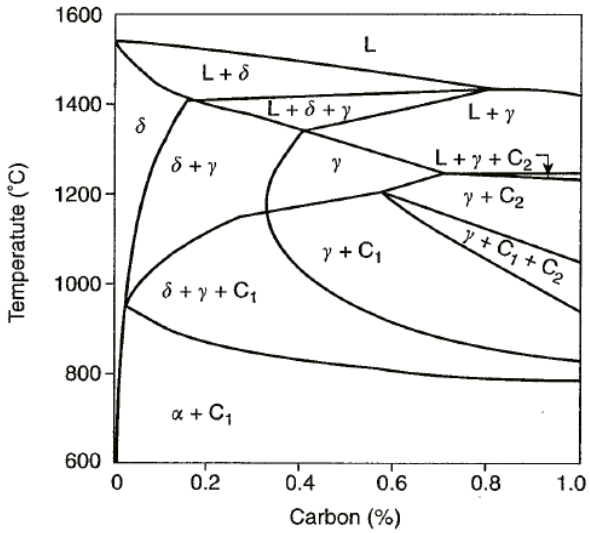

Figure 2-4 Fe-Cr-C pseudobinary diagram at 17 wt.% Cr: C_1 is a $(Fe,Cr)_{23}C_6$ carbide; C_2 is a $(Fe, Cr)_7C_3$ carbide; L is liquid.

2.1.3.3. Fe-Cr-Ni system

Addition of Ni to the Fe-Cr system also expands the austenite phase field and allows austenite to be a stable phase at room temperature. Liquidus and solidus projections of the Fe-Cr-Ni system are available in **Figure 2-5**. The liquidus surface exhibits a single, dark line that runs from near the Fe-rich apex of the triangle to the Cr-Ni side. This line separates the composition that solidifies as primary ferrite and that solidifies as primary austenite.

The solidus surface exhibits two dark lines that run from near the Fe-rich apex to the Cr-Ni-rich side of the diagram. Between these two lines the austenite and ferrite phases coexist with liquid just above the solidus, but only with one another just below the solidus. This region separates the ferrite and austenite single-phase fields below the solidus. It should be explained that these lines terminate at the ternary eutectic point. Arrows on these lines represent the decreasing temperature.

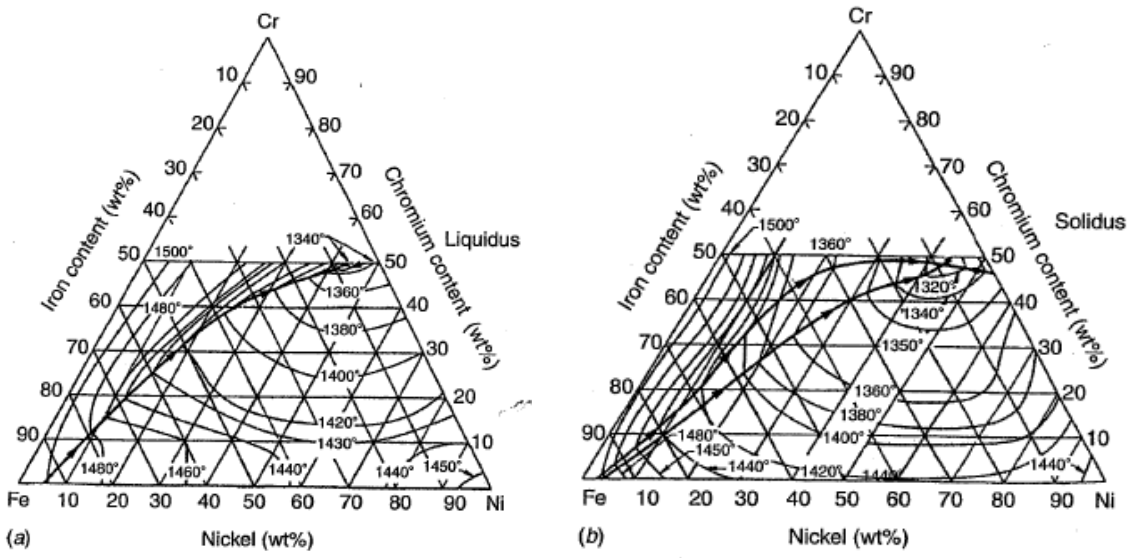

Figure 2-5 Liquidus and solidus projections of Fr-Cr-Ni ternary system.

By taking a constant-Fe section through the ternary phase diagram from liquidus to room temperature, a pseudobinary Fe-Cr-Ni phase diagram can be generated. Such diagram has been constructed at 70 wt.% Fe based on isothermal ternary sections and is shown in **Figure 2-6**. Due to a ternary system, the phase fields exist in three dimensions, resulting in three-phase fields that cannot occur on a standard binary phase diagram.

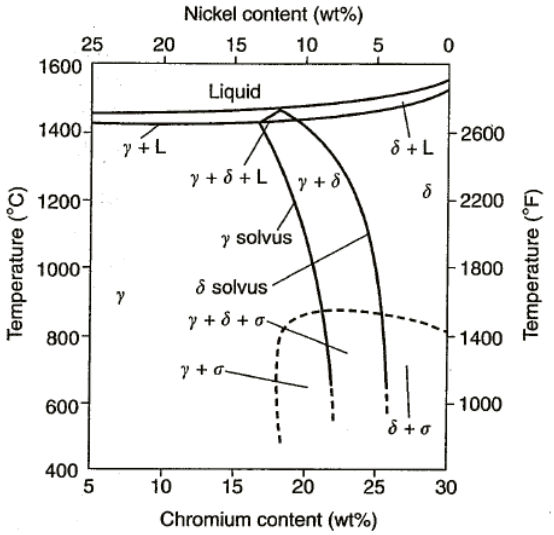

Figure 2-6 Pseudobinary sections of Fe-Cr-Ni ternary system at 70 wt.% Fe.

The small triangular region between the solidus and liquidus lines is the three-phase (γ + α + L) region, which separates alloys that solidify as austenite (to the left) from those that solidify as ferrite. Alloys that solidify as austenite (to the left of the three-phase triangle) remain as austenite upon cooling to room temperature. Alloys that solidify as ferrite at composition just to the right of the three-phase triangle, cool through the two-phase (γ + α) region. This results in the transformation of some ferrite to austenite. At composition farther to the right of the triangle (higher Cr/Ni ratios), ferrite becomes increasingly stable, until ultimately a fully ferritic structure exists toward the far right side of each diagram.

Anton Schaeffler [13] created a constitution diagram for weld metal microstructure based on chemical composition, and his diagram contained Cr- and Ni-equivalent formulas for the axes. Outokumpu Oyj modified the Schaeffler diagram (**Figure 2-7**) [14], and uses it to

characterise stainless steel microstructure comparing with the structural balance in similar grades or casts with the same processing history. The diagrams, such as Delong, Schoefer, Potak and Sagalevich, are also used to predict the microstructure of steels and their weld metals [11].

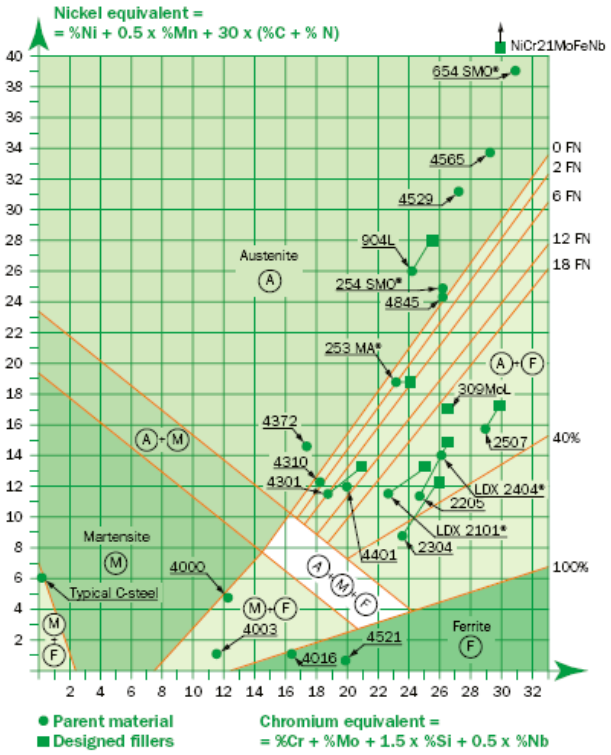

Figure 2-7 Modified Schaeffler diagram (steel grades with European standard [15]).

So far, some limitations of classical phase diagrams have been overcome by powerful computer programs that use thermodynamic information to construct phase diagrams for common alloy systems. “Thermo-Calc software” has gained world-wide reputation as a

powerful software package for thermodynamic calculations [16], which is useful for predicting microstructure evolution in stainless steel.

2.1.4. Effect of alloying elements in stainless steel

Microstructure of stainless steel mainly depends on chemical composition and manufacturing procedure [17]. Alloying elements affect the equilibrium phase relationships related to the stability of the austenite, ferrite and martensite phases. ASS contains high levels of Cr, Ni and other elements which promote the formation of the austenite phase. FSS contains a balance of elements, such as high Cr contents, which causes that ferrite is the predominant metallurgical phase present. MSS is austenitic at elevated temperature, but this austenite is unstable and transforms upon cooling. By balancing austenite- and ferrite-promoting elements, the microstructure of stainless steel can be controlled. This balance has important implications with respect to mechanical properties, corrosion resistance and weldability.

Elements added to stainless steels can be divided into those that promote, or stabilise, either the ferrite or the austenite phase (martensite is a transformed phase that forms from austenite upon cooling from elevated temperature). **Table 2-2** lists austenite- and ferrite-promoting elements for stainless steel.

Table 2-2 Austenite- and ferrite-promoting elements.

Classify	Element
Austenite-promoting elements	Cr, Mo, Si, Nb, Ti, Al, V, W
Ferrite-promoting elements	Ni, Mn, C, N, Cu, Co

2.1.4.1. Interstitial elements

C and N are the most potent austenite-promoting elements, and thus the levels of these elements must be carefully controlled for the purpose of precise microstructure balance.

Carbon

Little C can dissolve in the ferrite as an interstitial element, and the second phase of carbide with high hardness can form during the cooling process after being heated at the high temperature. Hence, to fix the second phases distributed along and inside the grains, some stabilised elements should be added. In general, high C content needs high Cr content, so it can decrease the dissolved Cr in the base material (BM), which induces the inclination of intergranular corrosion. Meanwhile, the capability of passivating is influenced. It is well known that C does harm to corrosion, and C expands the austenite region in ferrochromium alloys, which makes it possible for FSS with high content of C to generate dual-phase microstructure [18].

Nitrogen

N is usually present as an impurity in many stainless steels but is an intentional addition to some of the austenitic grades and almost all the duplex grades. Similar to C, N is a powerful solid solution strengthening agent, and the additions of as little as 0.15 wt.% can dramatically increase the strength of austenitic alloys. The strengthening effect of N in austenite is especially pronounced at cryogenic temperature. For the DSS, N is added to improve strength, but more important, to increase resistance to pitting and crevice corrosion. Some duplex grades contain up to 0.3 wt.% N. Although the solubility of N in stainless steels is relatively low, particularly in the ferrite phase, the addition of Mn to the ASS grades increases the solubility of N.

Oxygen

The element of O in BCC metals promotes the occurrence of intergranular failure, and extensive fractography reveals no such phenomenon in the alloys. Above the critical C content, no amount of O addition can cause the fracture mode to revert back to intergranular failure [19, 20].

2.1.4.2. Corrosion resistance elements

Chromium

Cr is one of the most important elements, which determines the corrosion resistance of stainless steel with a compact and stabilised film on the surface that forms under the environment of oxide media. In ferrochromium alloy, when the Cr content is beyond 12.7 wt.%, alloys do not generate any phase transformation when heated and cooled, and keep BCC microstructure during any heat treatment temperature.

Nickel

For stainless steel, Ni is apparently helpful to the mechanical properties, especially toughness. Although Ni has no direct influence on the passive layer, it exerts a beneficial effect, particularly in sulphuric acid environments. Furthermore, Ni containing ASS grades exhibit a wide range of mechanical properties. For instance, in low Cr FSS grades, such as 12Cr steel, Ni is usually added to deliver higher toughness.

Molybdenum

In stainless steel, Mo exists in the phases of solid solution and precipitates. Mo can increase the hardness and strength through solid solution strengthening at the expense of ductility. Mo can also promote the enrichment of Cr in passivation film, which can increase stabilisation of the passivation film. That accounts for the beneficial effect of Mo with

respect to corrosion resistance of stainless steel. In addition, Mo can stimulate the precipitation of σ (sigma), χ (chi) phases, which undoubtedly influences the ductility, toughness, corrosion resistance of steels [21, 22].

2.1.4.3. Stabilising elements

Niobium

Nb is utilised in stainless steels as a stabilising element to improve creep resistance. As far as corrosion resistance is concerned, it is well known that stabilising the grade by Nb additions prevents the risk of intergranular corrosion in heat affected zones (HAZ). Therefore, Nb is added in sufficient amounts, depending on C and N levels (ferritic types). Moreover, the addition of Nb is one of the most effective methods to improve thermal fatigue resistance and toughness [23].

Titanium

Ti is also commonly utilised in stainless steels as a stabilising element to improve resistance to pitting corrosion since stable Ti_2S has been found to preferably form in to MnS that acts as pit initiation sites. In low alloy steels, Ti has a strong affinity with C, N and O. When dissolved in steel, Ti can increase hardenability.

As stabilising elements, Nb and Ti can form carbide and nitride easily. The formation of carbide and nitride, to some extent, can avoid the combination of Cr with C and N, which is beneficial to the corrosion properties of steel. For the mechanical properties, Nb and Ti are used to increase the strength of stainless steels at the room or high temperature [24, 25].

Vanadium

The element V is another possible stabilising element as it is a fairly effective carbide and nitride former. It is not commercially used as a stabilising element since it is ineffective in significantly reducing sensitisation [26]. However, there are still numbers of advantages in adding V to the alloy: Firstly, the precipitation of V rich carbonitrides reduces the amount of these interstitials in the matrix, even though V is not effective as a stabilising element on its own. Then the element V has been reported to increase the ductility of the alloy in both welded and unwelded conditions.

2.1.4.4. Other elements

There are a number of other intentional alloying elements added to stainless steels for specific applications. S, Se, and Pb are used to machining grades to improve machinability by allowing higher machining speeds and improved tool life. W is added to some DSS grades to improve pitting corrosion resistance. Al is used in some of the lower Cr FSS grades to improve general corrosion resistance. Co is an effective solid-solution

strengthener, and in MSS grades it can be added to increase martensite start temperature (M_s).

2.2. MEDIUM-CHROMIUM FERRITIC STAINLESS STEEL

FSS is classified as such because the predominant metallurgical phase present is ferrite. These alloys possess good resistance to SCC, pitting corrosion and crevice corrosion (particularly in chloride environments). They are usually applied in a variety of applications where corrosion resistance, rather than mechanical properties (strength, ductility and toughness), is the primary service requirement.

2.2.1. Ferritic stainless steel groups

FSS grades can be divided into four categories: low-Cr grade (Cr: 10.5 ~ 12.5 wt.%), medium-Cr grade (Cr: 15 ~ 20 wt.%), high-Cr grade (Cr: >25 wt.%), and superferritic alloys. Low-Cr grades are used for applications such as automotive exhaust systems, where resistance to general corrosion is superior to carbon steels. Medium- and high-Cr grades are applied in more aggressive corrosion environments, such as chemical plants, pulp and paper mills, and refineries. Superferritic alloys are provided to chemical processing industries, where resistance to corrosion in severe oxidising media is necessary. International Stainless Steel Forum (ISSF [27]), a branch of World Steel Association (WSA), suggests FSS grades

fall into five groups [28] – three families of standard grades (groups 1 ~ 3) and two of "special" grades (groups 4 & 5), shown in **Figure 2-8**.

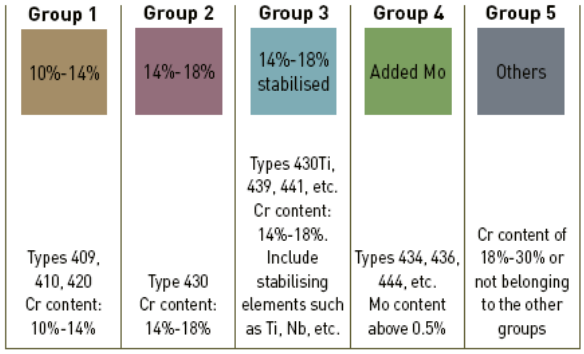

Figure 2-8 Five groups of FSS grades classified by ISSF.

A number of medium-Cr grades have been developed over recent years for use in demanding environments, nevertheless, they are relatively difficult to fabricate. There are a number of well-known leading manufacturers of FSS, such as Nippon Steel & Sumikin Stainless Steel (NSSC), JFE Steel Corporation (JFE), Pohang Steelworks (POSCO), Taiyuan Iron & Steel Group (TISCO), Baoshan Iron & Steel Group (Baosteel). Among them, JFE only focuses on the production of FSS grades (except austenitic thick plates). **Figure 2-9** gives the series of JFE medium-Cr FSS products [29], it is well known that the elements, such as Nb, Ti, Mo and Cu, are frequently added in designing FSS for different applications.

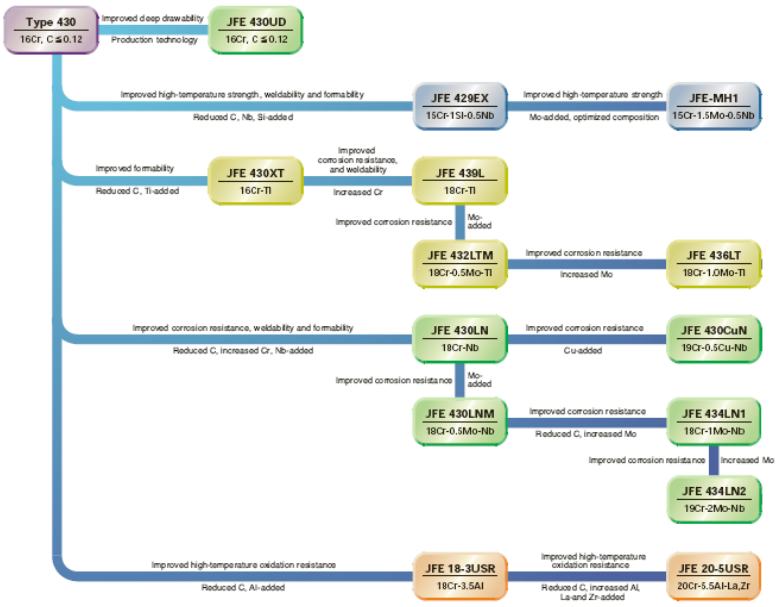

Figure 2-9 JFE FSS product tree and design thoughts [29].

2.2.2. Advantages of medium-chromium grades

Stainless steel is a durable, low-maintenance material with considerable life cycle cost (LCC) advantages over carbon steel. It is also recyclable because over 60% of new stainless steel is made from scrap. Top quality FSS grades have existed for amounts of years so far, and much intensive research and development have gone into defining the remarkable grades currently available. The economic advantages and technical merits of FSS grades have been appreciated by certain market sectors for years, and these benefits are becoming more widely understood with extensive acceptance of both existing and evolving markets [28].

2.2.2.1. Stable cost and price

Stainless steel producers and users, notably, are greatly puzzled by the high and volatile price of Ni (**Figure 2-10**), which is an essential element used in austenitic and duplex stainless steel grades.

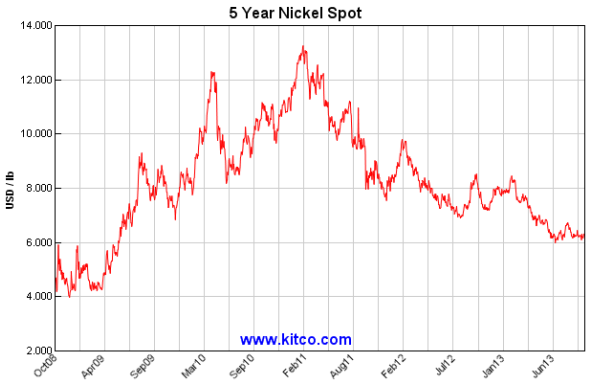

Figure 2-10 Ni prices during year range between 2008 and 2013 [30].

FSS grades, with comparatively low and stable price yet impressive technical characteristics, are now providing alternative materials for many supposedly "austenitic-only" applications. Containing no Ni, ferritic groups basically consist of Cr, whose price is historically very stable.

2.2.2.2. Special technical advantages

The main technical virtues of stainless steel can be summarised as follows: corrosion resistance, aesthetic appearance, heat resistance, recyclability, and biological neutrality. And FSS grades boast all the advantages that most ASS ones have over carbon steels in terms of corrosion resistance, i.e. longevity. FSS actually outperforms ASS in several characteristics.

Mechanical properties

The stress-strain curves, shown in **Figure 2-11**, demonstrate that FSS grades have the stress-strain curves quite similar to those of plain carbon steels and are characterised by good ductility with moderately high yield strength (YS, 0.2% proof stress), high ultimate tensile strength (UTS) and good total elongation performance.

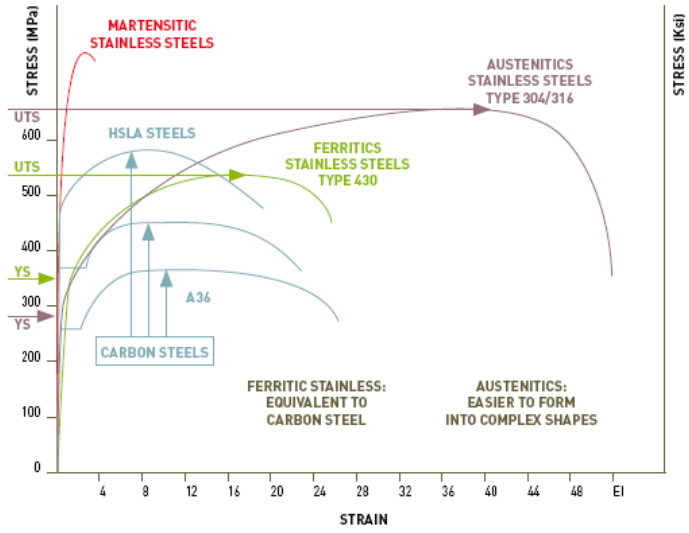

Figure 2-11 Stress-strain curves of several steel groups [28].

Physical properties

Besides being magnetic, FSS grades also have some other useful advantages over ASS grades. Thermal conductivity, for instance, is notably higher which means that they can spread heat efficiently and thus be suitable for applications such as heat exchangers while a low thermal expansion coefficient reduces distortion during thermal processing.

Corrosion resistance

(a) Pitting corrosion resistance

The pitting corrosion resistance of FSS is fundamentally determined by chemical composition rather than by crystal structure and the well known pitting index (P.I) [29] or pitting resistance equivalent (PRE) formula for both FSS and ASS grades are indicated in **Equation 2-1** and **Equation 2-2** [1, 29], respectively.

For FSS:

$$P.I = \%Cr + 3.3 \times \%Mo \qquad \textbf{Equation 2-1}$$

For ASS:

$$P.I = \%Cr + 3.3 \times \%Mo + 16 \times \%N \qquad \textbf{Equation 2-2}$$

A comparison of pitting corrosion resistance properties of ferritic groups with those of austenitic SUS 304 and SUS 316 (SUS is a grade designation of Japanese Industry Standard [31, 32]) clearly highlights the key role of Cr and shows that the corrosion resistance of Ni-containing grades can be matched by majority of the family of FSS grades, as shown in **Figure 2-12** ("JFE" is the designation of product grade by JFE Steel Corporation).

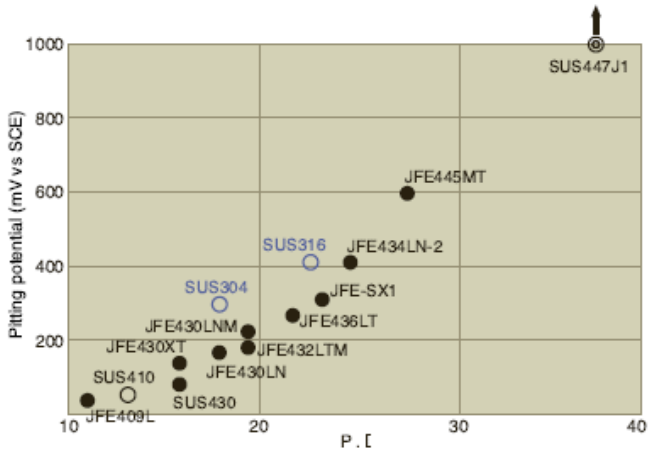

Figure 2-12 Pitting corrosion resistance comparison of FSS and ASS grades [29].

(b) Atmospheric corrosion resistance

Atmospheric corrosion occurs on steel surface, in the thin, wet film created by humidity in the air, and is usually initiated by the presence of impurities such as chlorides or sulfur

compounds in the industrial environment. The effect of different environments and thus levels of impurities on corrosion is displayed in **Figure 2-13**. For example, chloride deposits in a humid, marine atmosphere clearly enhance corrosion.

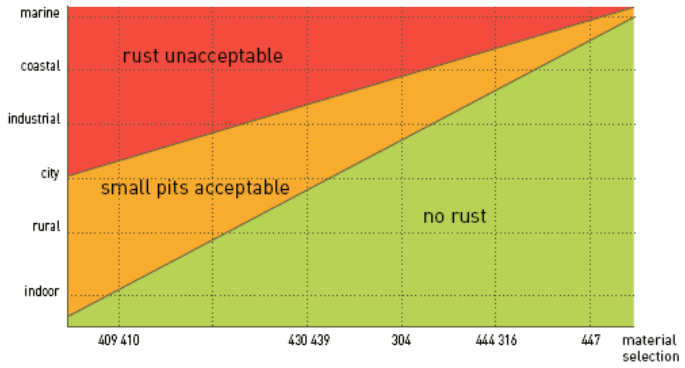

Figure 2-13 Atmospheric corrosion resistance comparison of ferritic and austenitic grades [28].

(c) Oxidation resistance

High-temperature oxidation is known as "dry corrosion" which typically occurs at temperatures greater than 500 ℃ and in an oxidising atmosphere with or without thermal cycle.

When stainless steel is heated, the increased level of Cr forms a protective Cr oxide surface "scale" or layer that protects the steel substrate and thus delays further oxidation. The scale and the metal substrate have different thermal expansion behaviours, which can affect the

scale's stability, especially in service conditions of frequent thermal cycling. If the difference in expansion coefficient of the scale and the metal substrate is too high, spalling will occur, especially during thermal cycling, and leads to excessive metal loss through continual scale formation.

Due to their lower thermal expansion coefficient, ferritic grades are less prone than austenitic alloys to high-temperature cyclic oxidation scaling. This is a particular advantage in applications such as heating systems, burners or exhaust systems.

Besides the advantages in mechanical, physical and corrosion resistance properties, FSS group also owns certain characteristics in weldability and formability.

In brief, FSS grades have possess significant advantages in comparison with ASS grades and carbon steels. Increased resistance to corrosion, oxidation and SCC offer a host of other technical, aesthetic and practical advantages.

The combination of low cost and good properties makes FSS grades highly desirable in various applications [33-36], such as: automotive, building and construction, food equipment, home and office, industry, transportation.

For thick plate applications, the most important property is toughness, without which, thick plates would have limited applicability. And the design and manufacturing of thick plate are focused on in the following chapters.

2.3. TOUGHNESS OF MEDIUM-CHROMIUM FERRITIC STAINLESS STEELS

Recent breakthroughs in metallurgical technology, which include ultra purification ((C + N) ≤ 250 ppm) and addition of stabilising elements [37, 38], have improved the various properties of FSS grades. Thus, the newly developed purified and stabilised FSS grades are now excellent contenders to replace some more costly ASS grades in special corrosive environments. The current limitation of FSS grades, compared with ASS grades, is the higher ductile-brittle transition temperature (DBTT), which is typically above room temperature especially when thickness exceeds 5 mm [39].

At present, there is a strong economic driving force for the development and improvement of thick FSS grades for the stainless steel industry [40], but for its successful application, the toughness limitation must be improved to gain universal acceptance. Therefore, the current technical challenge is the development of FSS grades with enhanced alloy designs that not only optimise economics but also improve the toughness of this steel group.

2.3.1. Introduction of steel toughness

The ability of a material to deform plastically and to absorb energy in the process before fracture, i.e. fracture resistance, is termed “toughness” [41]. The key to improve toughness is a good combination of strength and ductility. “Material toughness” equates to a slow absorption of energy by the material. Several variables have a pronounced influence on the toughness of a material, which include strain rate, temperature and also stress intensity or notch effect.As a rule, the toughness decreases as: the rate of loading increases; temperature is lowered; notch effect is related to the distribution of stress.

There are several standard types of toughness testing that generate data for specific loading conditions and/or component design approaches. Three of them, including notch toughness, impact toughness and fracture toughness, will be discussed, especially impact toughness.

2.3.2. Notch toughness

Notch toughness is the ability of a material to absorb energy under the action of an applied load or stress and in the presence of a known flaw.

Notch toughness is measured with a variety of specimens such as the Charpy-V notch (CVN) type or the dynamic tear test type. With the specimens and by varying the loading speed/temperature, it is possible to generate curves shown in **Figure 2-14**. Typically only

static and impact loading testing is conducted but it should be recognised that many components in service see intermediate loading rates in the range of the dashed red line.

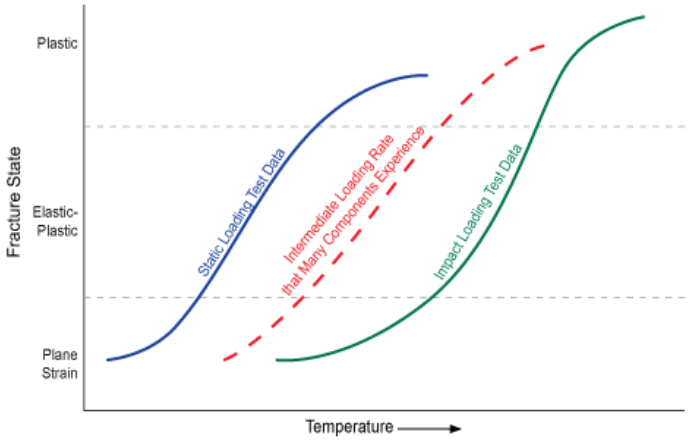

Figure 2-14 Notch toughness curves [41].

2.3.3. Impact toughness

The impact toughness of a material can be determined with a Charpy or Izod test. Impact properties are not directly used in fracture mechanics calculations, but the impact tests continue to be used as a quality control method to assess notch sensitivity and for comparing the relative toughness of materials.

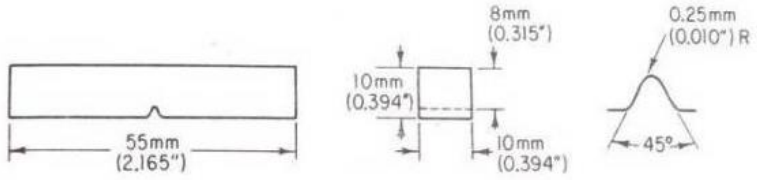

(a)

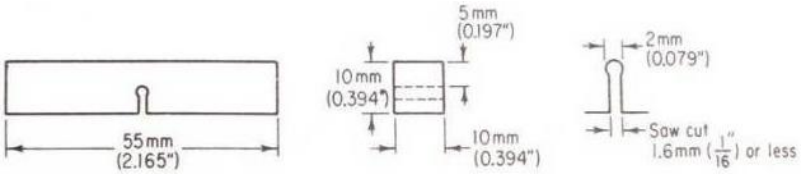

(b)

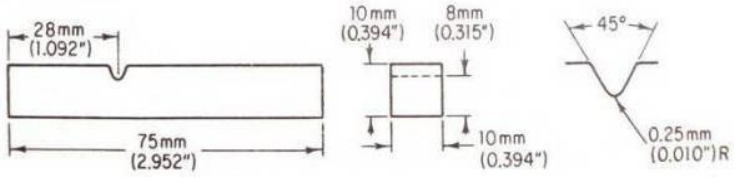

(c)

Figure 2-15 Types of notches for specimens: (a) V notched Charpy type; (b) keyhole notched Charpy type; (c) V notched Izod type.

The Charpy and Izod tests use different specimens and methods of holding the specimens, generally the V notch and the keyhole notch are used (**Figure 2-15**), but both tests utilise a pendulum-testing machine (**Figure 2-16**). The impact toughness of a material is determined by measuring the energy absorbed in the fracture of the specimen. This is simply obtained by recording the height at which the pendulum is released and the height to which the pendulum swings after it has struck the specimen.

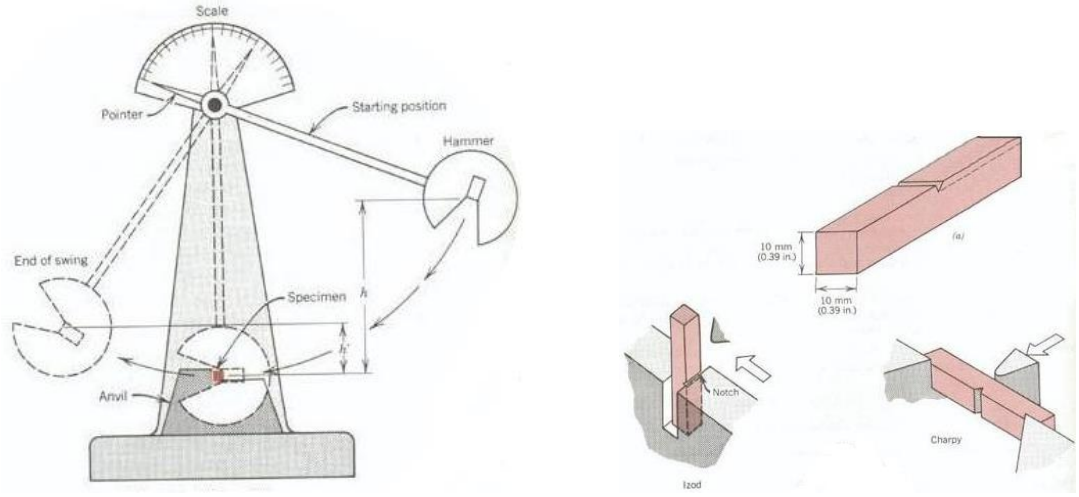

Figure 2-16 Charpy or Izod impact test [42].

Since toughness is greatly influenced by temperature, a Charpy or Izod test is often repeated numerous times with each specimen tested at different temperatures. This produces a graph of impact toughness for the material as a function of DBTT.

Ductile-brittle transition temperature (DBTT)

The impact toughness versus temperature graph for a material is shown in **Figure 2-17** (fracture transition plastic (FTP) is the temperature above which the fracture is 100% fibrous shear. This is the most conservative estimate; nil ductility temperature (NDT) is the temperature below which the fracture is 100% cleavage shear; fracture appearance transition temperature (FATT) is the temperature at which the fracture surface is 50-50% cleavage and fibrous. This can alternatively be based on the mean of the upper and lower shelf energies). It can be seen that at low temperatures, material is more brittle and impact

toughness is low, and at high temperatures material is more ductile and impact toughness is higher. The DBTT is the boundary between brittle and ductile behaviour and this temperature is an important consideration in the selection of a material. DBTT, most often measured in CVN impact tests, has been frequently used to make judgments concerning the adequacy of fitness for purpose at the expected minimum design operating temperature (MDOT) [43]. And furthermore, the DBTT is influenced by a large number of extrinsic factors that can result in differences in nominal values of up to 100 ~ 200 ℃.

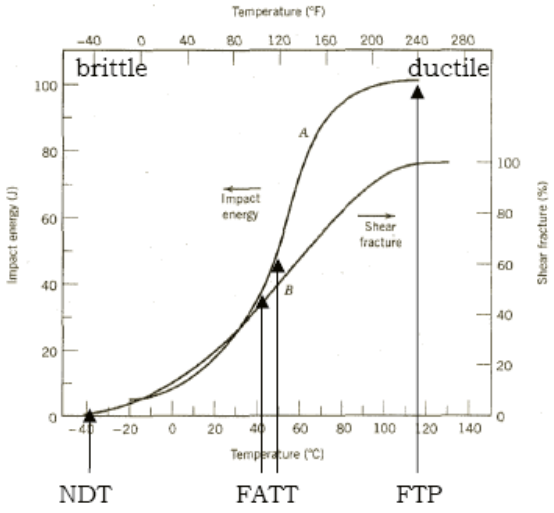

Figure 2-17 DBTT curves of steels [41].

Rosenfield and Majumdar illustrated an understanding of the fracture mechanisms of steel in DBTT region [44], analyses should be related not only with crack initiation, but also with crack propagation.

2.3.4. Fracture toughness

Fracture mechanics is the science of understanding the relationship between stress, material properties and the size of a preexisting flaw. Fracture toughness is usually regarded as a measure of material resistance to extension of a crack [45]. It is an important material property since the occurrence of flaws is not completely avoidable in the processing, fabrication, or service of a material.

The stress intensity factor *K* is used in fracture mechanics to predict the stress state near the tip of a crack caused by a remote load or residual stresses [46]. Three linearly independent cracking modes are used in fracture mechanics, seen in **Figure 2-18**. Mode Ⅰ fracture is the condition of largest tensile loading, which is the most commonly encountered.

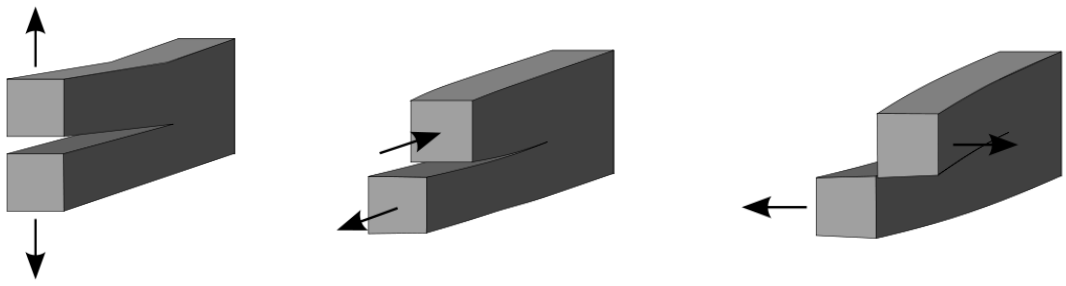

(a) (b) (c)

Figure 2-18 Three modes of crack loading [41]: (a) Model Ⅰ: opening; (b) Model Ⅱ: in-plane shear; (c) Model Ⅲ: out-of-plane shear.

The stress intensity factor is a function of loading, crack size and structural geometry, which can be represented by **Equation 2-3**.

$$K_I = \sigma\sqrt{\pi\alpha\beta} \qquad \textbf{Equation 2-3}$$

Where: K_I is the fracture toughness in MPa$\sqrt{\text{m}}$; σ is the applied stress in MPa; α is the crack length in m; β is a crack length and component geometry factor that is different for each specimen and is dimensionless.

Once the thickness exceeds the critical dimension, the value of K_I becomes relatively constant and this value, K_{IC}, is a true material property which is called the plane-strain fracture toughness.

In this thesis, impact toughness will be used to describe the ability of material to absorb the energy.

2.3.5. Toughness characteristic of medium-chromium ferritic stainless steels

Figure 2-19 presents the considerable variation of toughness for different types of stainless steels, ranging from excellent toughness at all temperatures for austenitic steels to the relatively brittle behaviour of martensitic steels.

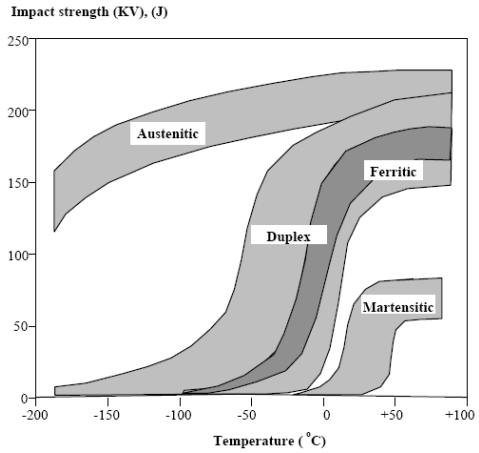

Figure 2-19 Impact toughness for different stainless steel groups [47].

FSS grades are structurally simple. At room temperature, the microstructure consists of ferrite with a BCC crystal structure [48]. The fact that the crystal structure is BCC accounts for much of the brittleness observed in these alloys. As the temperature is decreased, BCC materials display a substantial increase in lattice friction stress. This increase manifests itself in an increase in the DBTT, in accordance with the Cottrell model (**Equation 2-4**) [49], which states that the DBTT occurs when:

$$\sigma_y k_y d^{1/2} = k_y^2 + \sigma_0 k_y d^{1/2} \geq C\mu\gamma \qquad \textbf{Equation 2-4}$$

Where σ_y is flow or fracture stress, or both; k_y is Hall-Petch slope; σ_0 is lattice friction stress; d is grain size; C is a constant related to stress state and average ratio of normal to shear stress on the slip plane; μ is shear modulus; γ is effective surface energy of an implied crack.

Manufacturing conditions and compositional variations influence the mechanical property parameters of σ_y, k_y, σ_0, d and γ. Generally, the impact toughness of FSS grades is evaluated in terms of DBTT. Compliance with **Equation 2-4** is generally associated with the tendency for flow stress to increase with decreasing temperature. High strain rates and constraints to plastic flow have the effect of raising the flow stress and lowering the value of C and, thus, promoting compliance to **Equation 2-4**. In FSS grades, it may be observed that metallurgical conditions with higher overall DBTT values display greater sensitivity to strain rate and constraint.

2.4. FACTORS INFLUENCING TOUGHNESS OF FERRITIC STAINLESS STEELS

Although FSS grades are recognised as the materials with comparatively poor toughness due to the BCC crystal structure, there are still a number of factors that influence this important mechanical property.

2.4.1. Introduction

The factors influencing the toughness of FSS grades have been extensively investigated over the past several years [50]. It has been presented that the detrimental effects of interstitial elements are related with second phases and grain size. Second phases, including precipitation, predominantly initiate at grain boundaries but can also occur on dislocations [51, 52], and can be in the form of carbides, nitrides and oxides, as well as Cr-rich ferrite, Laves phase [53] and σ phase [54]. Moreover it is well known that oxide and nitride inclusions, such as TiO_x, MgO, Al_2O_3, TiN [55], may affect the toughness greatly. Thermomechanical processes, such as hot working, cold working and heat treatment, and welding procedures can significantly affect toughness properties as a direct result of their effects on grain size and precipitation [48].

The factors mentioned above will be explained in the following chapters.

2.4.2. Interstitial elements

The basic cause of BCC brittleness is the sensitivity of these materials to interstitials. While high purified metals may be ductile at very low temperature, slightly less pure alloys have relatively high DBTT values. Brittleness in these BCC materials can be attributed to interstitial elements locking dislocations during working process, which causes the flow stress to increase, due to its solubility level. However, the solubility level of interstitials in

BCC metals is extremely low, shown in **Figure 2-20** [48], that it is rarely possible to distinguish between the effects of solute embrittling and second phase precipitates. The precipitates, in fact, become more important than the solute level when the amount of interstitial elements significantly exceeds the solubility limitation.

The presences of C or N, in excess of the solubility limit, serve to increase the DBTT. This embrittling effect is closely related with the number and size of carbides, nitrides and oxides formed at the grain boundaries and/or on the dislocations [56]. Yoo *et al*. [57] demonstrated that in Nb-containing stainless steel, with the increase of C and N, the coarse Nb(C,N) particles in the matrix serve as void formation sites, which lead to a low fracture property. With respect to **Equation 2-4**, thick precipitate films act as strong barriers to slip propagation across the grain boundaries and raise k_y. Grain boundary (GB) carbides and nitrides are suppressed by quenching from above the solution temperatures when the interstitial content is low. However, the resulting fine intragranular precipitation may increase the DBTT by increasing σ_0.

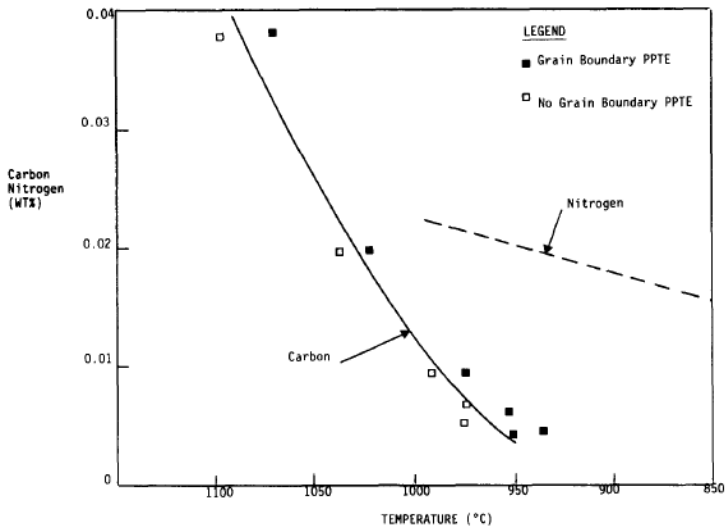

Figure 2-20 Solubility of C and N in a 26 wt.% Cr steel with temperature [48].

Binder and Spendelow [58] proposed that it was not the presence of Cr but rather the level of interstitial elements such as C and N that result in the formation of precipitation distributions accounting for the lack of toughness in these alloys. The combined influence of (C + N) levels on toughness is presented in **Figure 2-21**.

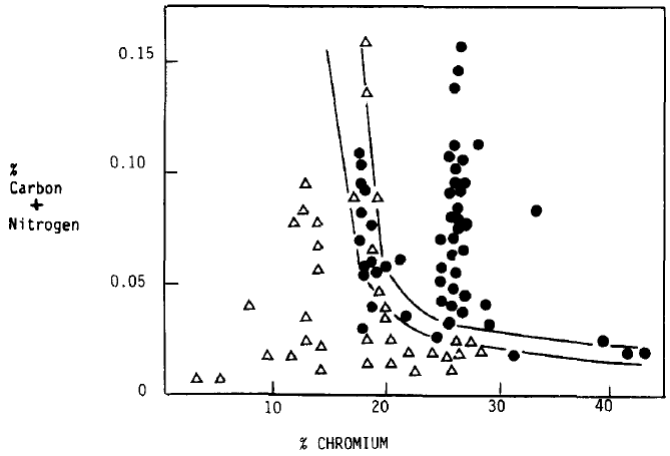

Figure 2-21 Influence of C and N on toughness of Fe-Cr alloys: △ high impact toughness alloys; ● low impact toughness alloys [48].

Mueller [50] studied the effects of varying C and N contents in alloys with several different constitutions. **Figure 2-22** shows the variation of C and N contents on the impact energy of 17Cr alloys. Annealed at 815 ℃, the influences of C content on the DBTT and upper shelf energy are significant. However, similar phenomena do not happen in the steels containing N. The lower temperature of annealing results in coarser precipitates, which are not as effective in raising the lattice friction or locking dislocations as the fine precipitates. This phenomenon is not unique for FSS grades but can be applied to most BCC ferritic steels [59].

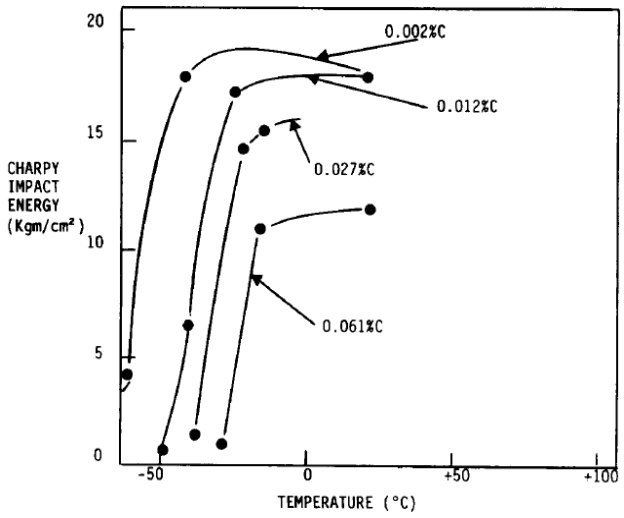

(a)

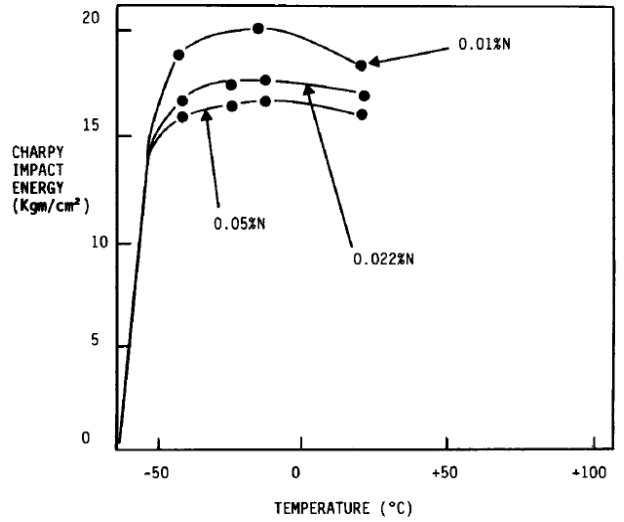

(b)

Figure 2-22 Transition curves for Charpy specimens of 17Cr FSS grades heated at 815 ℃: (a) steel with 0.002 to 0.061 wt.% C; (b) steel with 0.01 to 0.057 wt.% N [48].

Semchyshen *et al*. [60] investigated the high temperature embrittlement of high interstitial FSS grades. **Figure 2-23** demonstrates the effects of C and N on alloys annealed at 1150 ℃.

The increase in DBTT of the alloys is considerable compared with the heat treatment temperature 815 ℃.

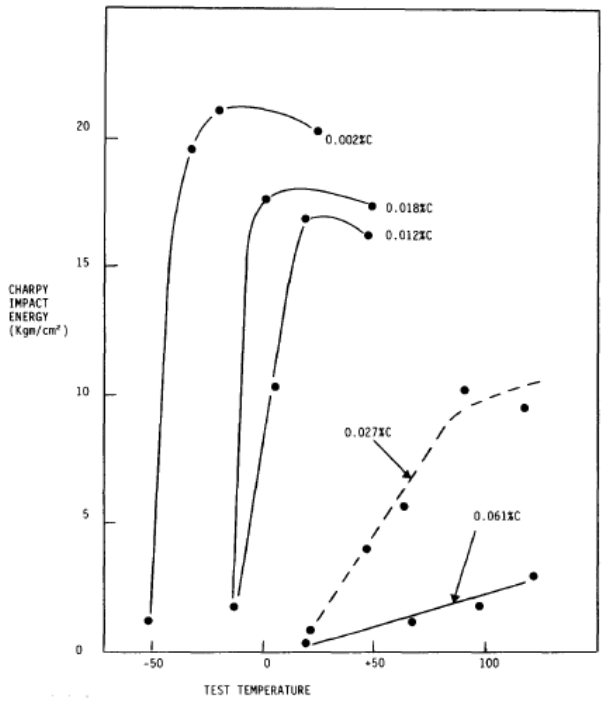

(a)

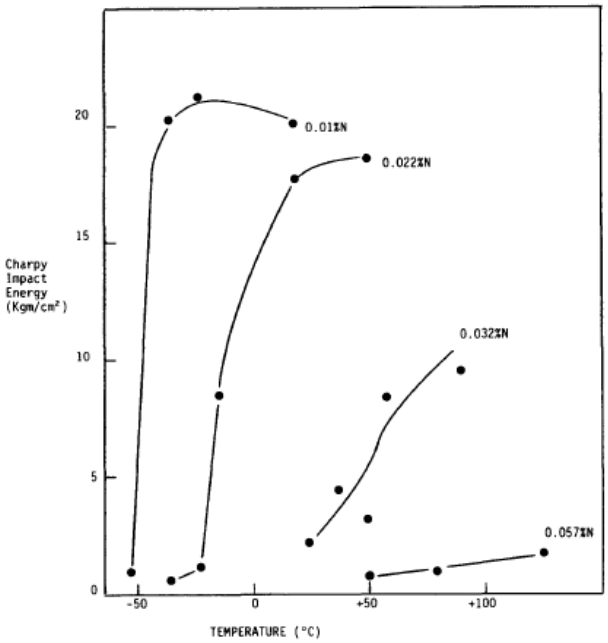

(b)

Figure 2-23 DBTT curves for Charpy specimens of 17Cr FSS grades heated at 1150 ℃: (a) steel with 0.002 to 0.061 wt.% C; (b) steel with 0.01 to 0.057 wt.% N [48].

Rinebolt and Harris [61] also presented the CVN DBTT curves for several normalised pearlitic steels with different C contents (similar with FSS), and the result is similar with the alloys heat treated at 1150 ℃, shown in **Figure 2-24**. Johnson and Storey [62] calculated the contribution of the ferrite to the impact energy as a function of temperature, which was accomplished by subtracting the pearlite contributions. In **Figure 2-25**, the full lines show the resulting curves for 0.20, 0.31 and 0.41 wt.% C. It was then concluded that the DBTT can be better represented by **Equation 2-5**.

$$E_y = E_{OF} + E_{SF} exp\left(-\frac{\lambda_F}{T - T_{OF}}\right) \qquad \textbf{Equation 2-5}$$

Where E_y is the Charpy impact energy; E_{OF} and E_{SF} are the lower and upper shelf energies for ferrite; λ_F is transition width parameter for ferrite; T is temperature; T_{OF} is the temperature above which the transition occurs in ferrite. The curves derived in this manner are shown as dashed lines in **Figure 2-25**.

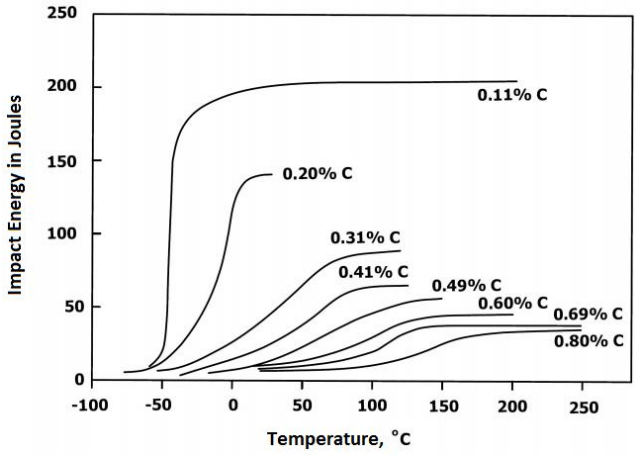

Figure 2-24 CVN DBTT curves for several normalised steels [61].

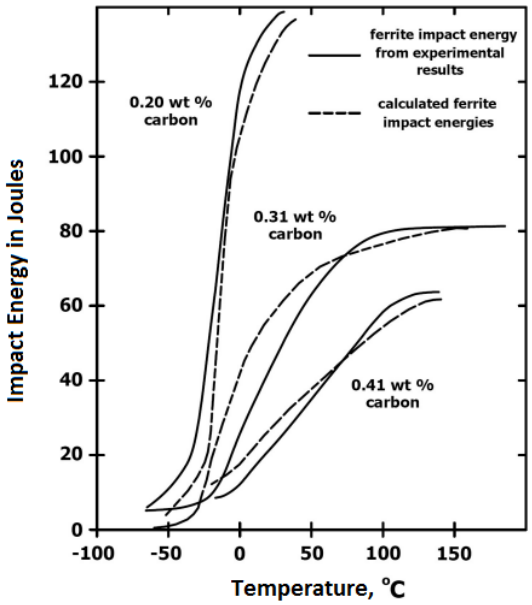

Figure 2-25 Ferrite impact energies derived from experimental results (full line) and from **Equation 2-5** (dashed line) [62].

Van Zwieten and Bulloch [19] stated that for 40Cr FSS, the toughness is independent if the interstitial contents are above a certain level, which is ascribed to the oversaturation of dislocation precipitation sites.

It is generally claimed [56] that C and N can reduce the impact toughness properties due to the formation of carbides and nitrides at the grain boundaries and/or on the dislocations, while O has only a small detrimental effect. Honda and Taga [63] found that the critical O content depends on the C content. Although O in BCC metals promotes the occurrence of intergranular fracture, when the C content reached a certain level, the brittle fracture of cleavage type instead of intergranular fracture happens, even at high O levels.

The precipitation of carbides, nitrides or carbonitrides is ultimately dependent on the composition of the steels. Based on the points from Grubb and Wright [64], in high interstitial alloys, both (C + N) in solution and (C + N) precipitates contributed to embrittlement, while in low interstitial alloys only (C + N) precipitation caused severe embrittlement. However, relatively little literatures are available regarding the effects of O and oxides on toughness properties of FSS grades.

2.4.3. Grain size

Although the effect of grain size on the toughness properties of FSS grades is well researched, but real operating mechanism is not well understood.

The Cottrell model (**Equation 2-4**) illustrates clearly that fine grain size is beneficial to toughness increment, because the GBs of fine grains provide barriers to a propagating crack, which can absorb energy through deflection of the crack direction. DBTT happens easily when *d* is large. The **Equation 2-6** illustrates that the growth of grain size can increase the value of DBTT. Meanwhile, the **Equation 2-6** [65] relating grain size to transition temperature has been verified for several metals. The relationship can be stated as:

$$T_C = A + B\, d^{1/2} \qquad \textbf{Equation 2-6}$$

Where T_C is DBTT; A and B are constants; and d is the mean linear intercept in mm. Paton [39] gave an example of **Equation 2-6** for the FSS grades studied: $T_c = 80 - 11.5d^{-1/2}$.

It has been presented by Plumtree and Gullberg [66] that the DBTT tends to increase concomitantly with grain size, shown in **Figure 2-26**. For 25Cr steels with different grain sizes after the selectable heat treatment procedures, the DBTT increases with grain size linearly.

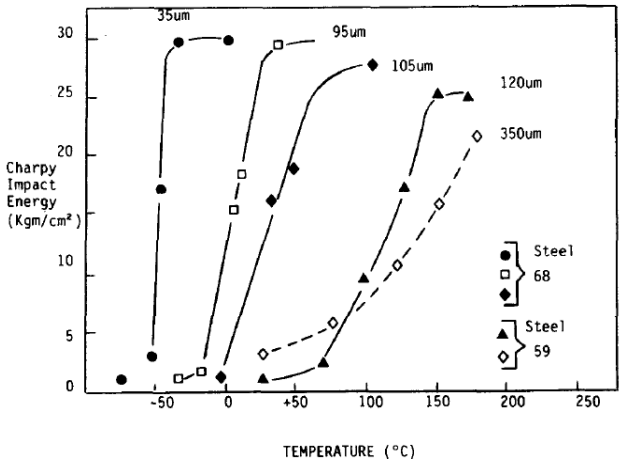

Figure 2-26 Charpy impact energy transition curves for steels at various grain sizes: Steel 68: 25Cr steel with 0.003 wt.% C + 0.012 wt.% N; Steel 59: 25Cr steel with 0.009 wt.% C + 0.015 wt.% N [66].

Ohashi *et al*. [67] pointed out that the DBTT is raised with increasing grain size, while the shelf energy is primarily independent of grain size. However, for the specimens having brittle welded cracks, the grain size dependency of shelf energy and DBTT is small. This

indicates that the effect of grain size contributes mainly to the resistance of brittle fracture initiation and only slightly to the propagation of brittle fracture. In addition, Wasén [68] found that the influence of coarse grain size on the near-threshold fatigue crack growth in ferritic steels is related to the roughness of fracture surface.

On the other hand, the differences between grain sizes normally developed have been pointed by several researchers to have no significant effect on the DBTT [69, 70]. Mintz *et al*. [71] proposed that the difficulty in quantifying the effect of grain size on toughness was due to the uncertain contribution of other variable, such as carbide thickness. Although fast cooling may result in a finer grain size, it can be accompanied by an increase in hardness in the ferrite matrix, which may offset part improvement in toughness from grain refinement. A coarse grain size from slow cooling resulted in coarse carbides which can also decrease toughness. Therefore, it is possible that the apparent absence of the grain size effect on impact behaviour is due to the obscuring effect of other variables.

2.4.4. Microalloying elements

The principle problem of FSS grades is their susceptibility to sensitisation [72]. Since ferrite has a low solubility for C and N, carbides and nitrides, generally the type $M_{23}C_6$ and M_2N, can precipitate out, forming Cr depleted zones around these precipitates [26]. The precipitation usually occurs at grain boundaries, which are then surrounded by Cr depleted

zones in the sensitised state, resulting in intergranular attack when exposed to a corrosive environment [73].

Sensitisation occurs whenever FSS grades are heated to a sensitising temperature, such as during themomechanical processing and welding. Annealing of these alloys is usually performed to allow Cr to rediffuse into the Cr depleted zones. Thus, it is necessary to develop FSS grades that are inherently resistant to sensitisation. Undoubtedly, the second phases, including carbides, nitrides, oxides, σ and χ phases etc., are of primary importance to the DBTT besides the corrosion resistance [48].

If the C and N contents are lowered to below the solubility limit in ferrite, Cr rich precipitates and their associated Cr depleted zones will not readily form [74]. It is possible to reduce sensitisation by making use of stabilising, which refers to the addition of any alloying elements that form carbides and nitrides more stable than those formed by Cr. If enough C and N are tied up forming the stabiliser precipitates, the formation of Cr rich precipitates, and thus sensitisation, is greatly reduced. The stabiliser carbonitrides may form at higher temperatures than Cr carbides or nitrides, thereby raising the sensitisation temperature. The stabilisation ratio of FSS is calculated by interstitial elements divided by stabilising elements, shown in **Equation 2-7**. Usually, the stabilisation ratio should be in the range of 13 ~ 25 [75], which can satisfy the requirements of intergranular corrosion resistance.

$$Stabilisation\ ratio = \frac{(Nb + Ti + V)}{(C + N)} \qquad \textbf{Equation 2-7}$$

Therefore, in order to grasp the principles of microalloying, the knowledge of the solubilities of the microalloy carbides and nitrides regarding the stabilisation elements, such as Nb, Ti, V, together with their precipitation behaviours, is required. An understanding of the role of different microalloying elements can be gained from the solubility data summarised in **Figure 2-27** [76]. It is well seen that TiN is extremely stable and can withstand dissolution at high temperature during reheating prior to rolling. Nb nitride and carbide have relatively low solubilities, and may precipitate out in the later stages of rolling. V, on the other hand, has a high solubility even at temperatures as low as 1000 ℃.

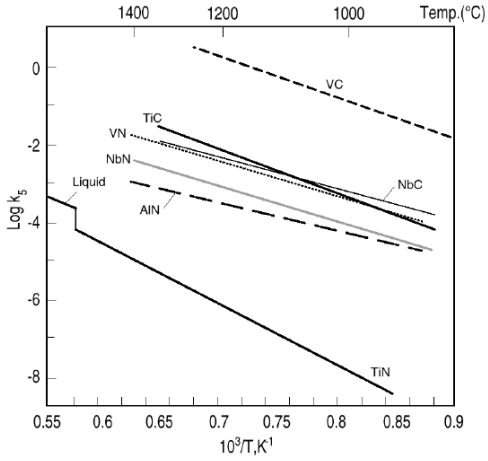

Figure 2-27 Solubilities of microalloy carbides and nitrides.

The diagram of **Figure 2-28** gives the solvus temperature for carbides and nitrides of alloying elements, which shows that the potential stabilising elements are Nb, Ti, V, Zr and Ta [77].

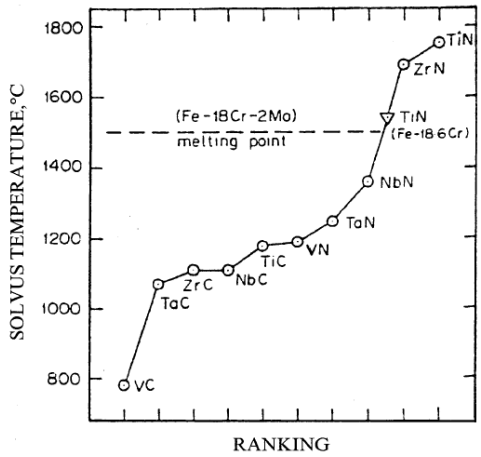

Figure 2-28 Calculated solvus temperature in Fe for MX (M-metal, X-C or N) stabiliser compounds.

Some important and conventional stabilising elements are summarised regarding the impact toughness effects of FSS products.

2.4.4.1. Niobium

Less reactive than Ti, Nb forms less stable carbides and nitrides [77], while still exhibiting sufficient carbide and nitride stability to be useful in preventing sensitisation effects. Nb

carbonitrides form in preference to Cr rich carbides and nitrides, thus keeping the alloy against sensitisation.

Kuzucu and Aksoy *et al*. [23, 78] studied the effects of Nb on the toughness of FSS. For 17-18Cr FSS containing 0.5 ~ 3.0 wt.% Nb, unhomogenised specimens consist of ferrite, $M_{23}C_6$, NbC and σ phase (additional Nb_2C forms in the specimen containing 3.0 wt.% Nb). And after homogenisation treatment between 1100 ~ 1150 ℃, the microstructure of all specimens consists of two phases, ferrite and NbC. The toughness of all experimental steels increases after homogenisation, especially those containing 1.5 ~ 3.0 wt.% Nb. However, the toughness of the steels containing 0.5 ~ 1.0 wt.% Nb is nearly same with that without Nb (no precise size of specimens, which were cut from bars 20 mm in diameter), shown in **Figure 2-29**. The reason for the increase in toughness was explained by the decrease in the amount of $M_{23}C_6$ formed at the grain boundaries. This can be testified in **Figure 2-30**, which displays that Nb does not have a significant effect on toughness of the unhomogenised specimens [78].

However, usually the content of Nb can be controlled based on the stabilisation ratio, since the amount of stabiliser added is critical, and above a certain level they may cause the toughness to decrease [79, 80], which means that the situation is seldom when Nb addition is over 1.0 wt.%. Abo *et al*. [79] suggested that Nb additions around 8 ~ 10 times the amount of (C + N) produce the optimum toughness in 18-21Cr FSS grades.

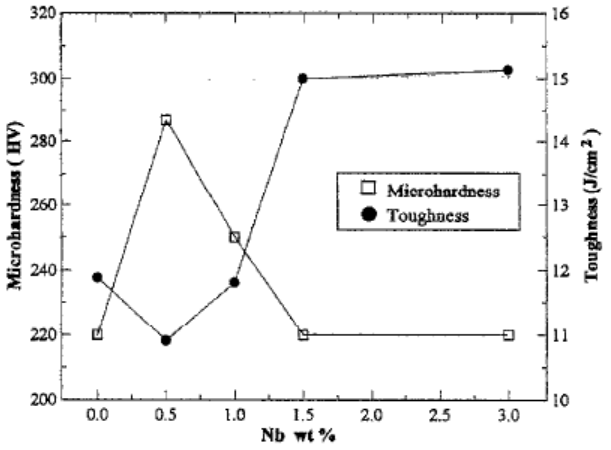

Figure 2-29 Toughness versus Nb ratio for homogenised 17-18Cr FSS grades.

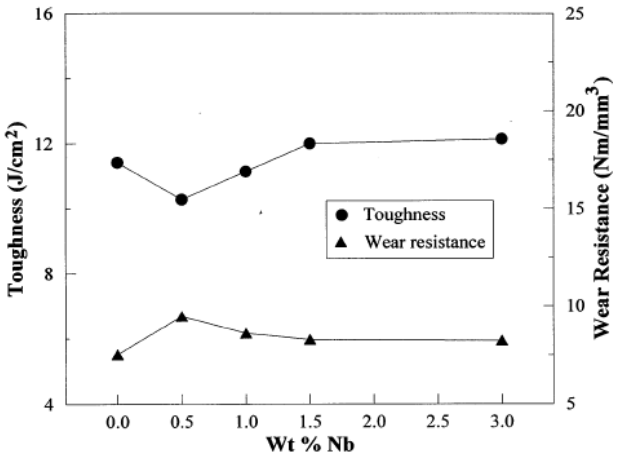

Figure 2-30 Toughness versus Nb ratio for unhomogenised 17-18Cr FSS grades.

Anttila *et al*. [81] pointed that for 21Cr FSS cold rolled plates with 3 mm thickness, Nb-rich steels have improved toughness compared to that of Ti-rich ones when they are all annealed from 925 to 1030 ℃, aiming at achieving full recrystallisation with around 30 μm grain size (CVN specimens with the sub-size of 3 mm × 10 mm × 55 mm), shown in **Figure 2-31**. The cooling methods (air-cooling and water-quenching) alter the

microstructure in the Nb stabilised steel, i.e. smaller precipitates, presumably NbC, appear for air-cooled material, although both cooling routes form large laths of NbC aligned parallel to the rolling direction. Supposedly, the hard and cuboidal TiN may act as crack initiation sites, and a comparatively high DBTT is observed in the Ti containing steels. Although it is concluded that increasing Nb content as a stabiliser decreases the DBTT, there was no further explaination.

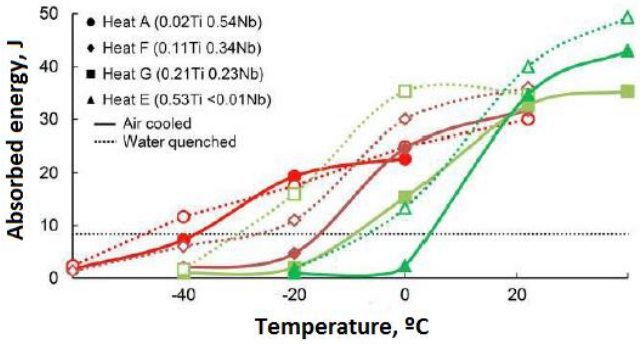

(a)

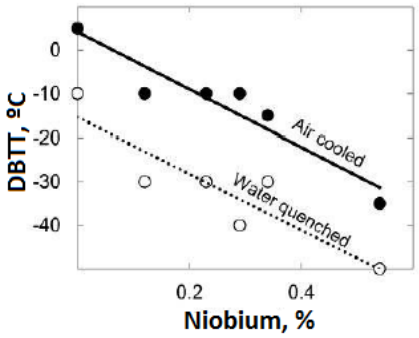

(b)

Figure 2-31 Impact toughness of 21Cr FSS grades: (a) impact toughness curves of different composition; (b) effect of Nb and cooling methods on the DBTT.

Van Zwieten and Bulloch pointed that Nb is effective in retarding the increase in transition temperature [48], displayed in **Figure 2-32**. However, there are no other detailed experiment data.

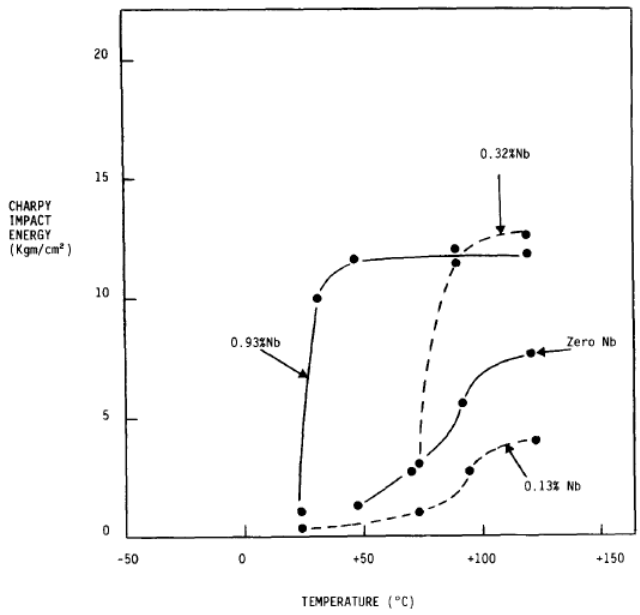

Figure 2-32 Charpy impact transition curves for 18Cr-2Mo FSS grades with various Nb additions.

For Nb stabilised steels, the small and spherical precipitates form during producing process may be beneficial to toughness, which is caused by the refinement of grain size. Meanwhile, the effects of overstabilising with Nb are gradual, and not as pronounced as those for overstabilising with Ti [82]. Furthermore, Nb is not active, which can avoid the formation of oxides or sulphides to a great extent, and has a comparatively low solubility in ferrite, which will not be taken into solid solution in significant amounts [26]. Nb addition below

1.0 wt.% is positive to the critical pitting potential and induction time of high Cr FSS [83]. In addition, high temperature strength of Nb-added steel has been confirmed by the mechanisms of solid solution and dynamic precipitation strengthening [24].

Malfiet *et al*. [84] mentioned that in 15Cr-0.45Nb-0.010C-0.015N steel, three types of precipitates can be observed, i.e. Fe_2Nb, $Nb_x(C,N)_y$ and $Fe_3Nb_3X_x$ (X: C or N). Fe_2Nb is observed at 800 ℃. $Fe_3Nb_3X_x$ precipitates form at the grain boundaries between 700 ~ 1000 ℃. At 1000 ℃, they lose stability with respect to $Nb_x(C,N)_y$. And at 970 ℃, the precipitation of $Fe_3Nb_3X_x$ is observed in the neighbourhood of a dissolving $Nb_2(C,N)$ precipitate, which is concluded that $Fe_3Nb_3X_x$ is directly related to the dissolution of $Nb_2(C,N)$ through the redistribution of C and N. Sim *et al*. [85] observed that for 15Cr-0.38Nb-0.010C-0.016N steel, Nb(C,N), Fe_2Nb and Fe_3Nb_3C precipitated out during aging process. And the coarsening rate of Fe_2Nb was much faster than that of NbC due to the incoherent interface between Fe_2Nb and the Fe matrix.

There are still some shortages with Nb stabilisation. Besides Nb-stabilised welds may show hot or solidification cracking, which is suspected of forming low melting eutectics with Nb [86], the grains in Nb-stabilised weld metal are elongated, columnar grains growing epitaxially from the centreline of the weld, which is weak to some properties [87].

2.4.4.2. Titanium

Ti is the highly reactive element that forms comparatively stable TiN and TiC precipitates in the presence of N and C. TiN forms above the liquidus, which is extremely stable and only dissolve at very high temperature. Since the formation of TiN happens in the molten steel, it brings the effect of refining the solidification structure [88]. However, Du *et al*. pointed that the coarse TiN particles are acting as cleavage initiation sites by fractographic analyses [89], which is testified by many researchers [51, 81, 90, 91]. This decrease in toughness may even occur at the situation that Ti contents below the level required to fully prevent sensitisation.

When stabilised with Ti, Wood [92] found that excess Ti influences the mechanical properties of annealed 18Cr FSS grades as a potent element for solid solution strengthening to a less degree than that of corresponding weld.

Grubb *et al*. [93] illustrated that for 1.6 mm cold rolled 26Cr FSS sheet with total (C + N) levels of about 82 ppm, Ti lowers the DBTT of material which has undergone lengthy heat treatment at low temperature, but raises the DBTT in all other cases. However, the toughness of high-interstitial FSS grades is improved by stabilisation. That means the effects of Ti should be related with interstitial elements.

Van Zwieten and Bulloch found that Ti is a little complex in changing transition temperature [48], seen in **Figure 2-33**, but there are still no other detailed experiment data.

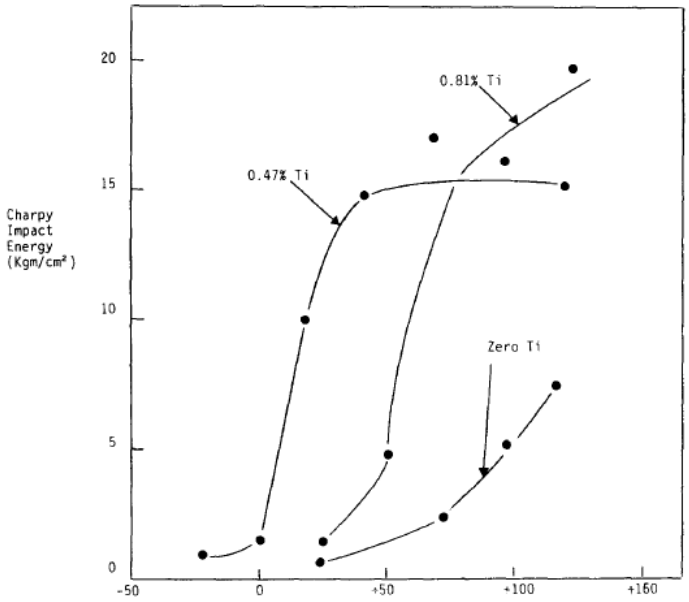

Figure 2-33 Charpy transition curves for 18Cr-2Mo FSS grades with various Ti additions.

Regarding the advantages of Ti, Ti sulphides are shown to form in preference to Mn sulphides, which are known to act as pitting initiation sites. Since TiN forms in molten steel, where it acts as nucleation sites for heterogeneous solidification, resulting in a fine grained equiaxed structure. In addition, Ti carbonitride precipitates are helpful to pin the grain boundaries in the HAZ of welds, thus retarding grain growth.

Besides the large and cubic Ti(C,N) particles that form owing to the mutual solubility of TiN and/or TiC [94] particles, which decreases the impact toughness significantly by acting as crack initiators, there are still several other disadvantages of Ti stabilisation. Firstly, excess Ti additions above the levels required to be stabilised can cause a decrease in ductility and an increase in DBTT. Secondly, sensitisation of the Ti stabilised FSS may

occur when exposed to high temperatures and followed by rapid cooling due to dissolving out of TiC from the Ti(C,N) precipitates, which results in the non-equilibrium carbonitride precipitates growing around the remaining TiN particle, or releasing of C atoms from the Ti(C,N) precipitate, which combine with Cr to form $Cr_{23}C_6$ [95].

It may be possible to overcome some of the detrimental effects of Ti stabilisation in the properties of base materials by combining the Ti addition with other stabilising elements, such as Nb, V and Zr. Most situations that Ti is used to stabilise FSS with other elements, are always related to the increasing of formability and weldability [96], since it is well accepted that TiN is able to promote an equiaxed region since this particle forms in the molten steel at a high temperature.

2.4.4.3. Vanadium

The element V is another stabilising element as it is a fairly effective carbide and nitride former. As a strong carbide-forming element, V is ranked the head of the other alloying elements, in preventing the formation of $M_{23}C_6$ carbides [97]. It is not frequently used as a stabilising element since it is regarded ineffectively in reducing sensitisation. In fact, V stabilisation requirements should, like Nb stabilisation, be close to theoretical requirements, owing to the fact that V does not form stable oxides or sulphides in stainless steels [26].

Premachandra and Paton [98] showed that V has a beneficial effect on impact toughness (DBTT), but not on fracture toughness (K_Q) after annealed at 815 ℃ (**Figure 2-34**). The mechanism of the impact toughness improvement is probably related with the removal of coarse Cr carbonitrides from the GBs. Meanwhile, the Charpy impact transition curve for 18Cr-4V FSS is provided in **Figure 2-35**, which displays that annealing the alloy at 815 ℃ gives impact energy absorption values more than 100 J when tested at 0 ℃ (5 mm gauge).

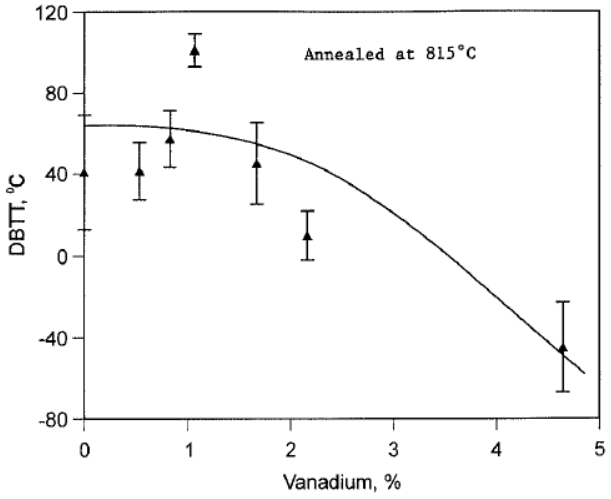

(a)

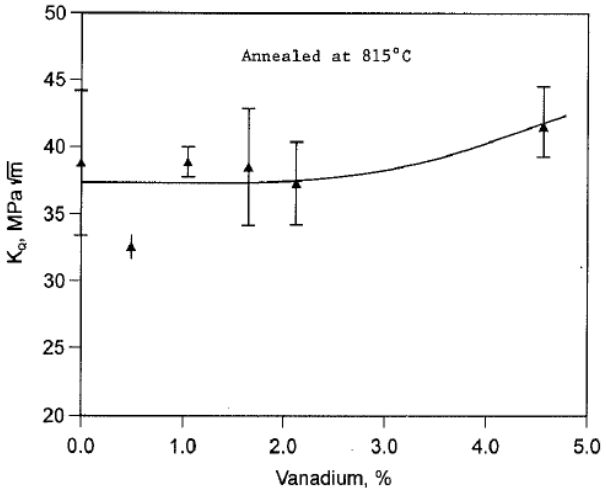

(b)

Figure 2-34 Variation in DBTT and K_Q with increasing V content in 18Cr FSS grades: (a) DBTT (5 mm gauge longitudinal); (b) K_Q (10 mm gauge longitudinal).

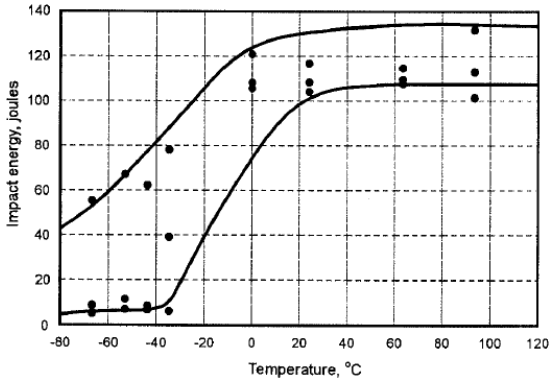

Figure 2-35 Charpy impact transition curve for 18Cr-4V FSS.

Paton [39] found that V, alone, is not a potent stabiliser, and a small addition of Nb is necessary to improve toughness. The carbides of Nb and Ti are more stable than those of V and can thus form at a higher temperature, where the mobility of Nb and Ti in the ferrite

matrix will be sufficient to allow rapid diffusion into a depleted zone. The lower dissolution temperature of V carbides could also be responsible for the poor stabilisation properties observed in the weld metal. On the other hand, Kuzucu *et al*. [97] observed that the element V delays the grain coarsening because of the existence of VC carbides at the grain boundaries. However, the relationship between the grain size and precipitation was not mentioned.

Grubb [86], however, pointed that the actual stabilisation requirements of 29Cr-4Mo FSS were 9 times greater than theoretical predictions. Meanwhile, the carbides of Nb and Ti were more stable than that of V. The mobility of Nb and Ti in the ferrite matrix allowed rapid diffusion into a depleted zone, which is aroused due to the formation of some precipitates, such as $Cr_{23}C_6$ and Cr_2N.

Compared with Nb and Ti, the effectiveness of V element is not very clear. So far, it is reported that the precipitation of V-rich carbonitrides reduces the amount of the interstitials in the matrix, even though it is not effective as a stabilising element on its own. The effects of using V to partially replace Nb/Ti as a stabilising addition are currently being researched by some manufactures.

2.4.4.4. Dual stabilisation

In the typical standards, such as ASTM A240 [99], EN 10088 [15] JIS 4304 and JIS 4305 [31, 32], considerable FSS grades prefer the method of dual stabilisation, and (Nb + Ti) stabilisation is mostly used. From the separate analysis of Nb and Ti, it is not difficult to understand the pros and cons of (Nb + Ti) dual stabilisation. The problem is that large cuboidal Ti carbonitrides have the deleterious effect on toughness. On the other hand, the element Ti mitigates weld cracking problems promoted by Nb due to TiN particles, which form in the melt, act as heterogeneous nucleation sites for crystal growth, and result in a fine grained equiaxed structure. The effects of TiN on the weld are beneficial to the mechanical properties [87]. The fine grained structure reduces the concentration of tramp elements at the grain boundaries. Furthermore, less Nb can decrease the amount of low melting phases that will form at the grain boundaries. That is why the addition of Ti should be considered in 12Cr FSS thick plate because of its weld properties [18, 100]. Above points make the allocation of Nb and Ti crucial in dual-stabilised FSS grades.

Shan *et al*. [33] compared the grain structures and the precipitates of pure 17Cr FSS with different Nb and Ti microalloying cast ingots, and concluded that the combined addition of Nb and Ti leads to the minimum grain size and maximum equiaxed grain proportion. However, the annealing microstructures are not mentioned in this paper, which may influence the properties of the final products.

Craven *et al*. [101] studied the complex heterogeneous precipitation in Nb-Ti high strength low alloy (HSLA) steels, and explained that the least soluble phase is based on TiN and it

forms the cores of the (Nb,Ti)(C,N) complexes. Its precipitation occurs at high temperature, i.e. early in the process. The Nb/Ti ratio in the core is markedly affected by the cooling rate during solidification and thermomechanical processing.

As mentioned before, V is not a potent single stabiliser, and a small addition of Nb is necessary to prevent intergranular corrosion. Paton [39] demonstrated that after annealing at 1100 ℃ the particles containing substitutional elements were strongly bonded to interstitials, e.g. Nb(C,N) and V(C,N), in 18Cr-4V-0.1Nb FSS. Tokuno *et al.* [102] observed the distribution and morphology of the precipitates in 9 wt.% Cr ferritic steel containing Nb and V, which are thought to be complex to act as obstacles for the dislocation glide. Plate-like V nitrides are formed adhering to spherical Nb(C,N) during tempering. Onizawa *et al*. [103] controlled the contents of Nb and V to analyse their effects on 9 wt.% Cr steel, and found that four types of precipitation, i.e. Nb(C,N), V(C,N), $M_{23}C_6$ and $Cr_2(C,N)$, form after aging at 600 ℃ for 6000 hours. Nb(C,N) can be observed in the steels which contain Nb. In contrast, V(C,N) can be observed only in the steels containing V of more than 0.12 wt.%. The combination of Nb and V is designed in some microalloying cast steels to effectively prevent undesirable grain growth and can also contribute to precipitation strengthening [104].

Cavazos [72] studied characterisation of precipitates formed in a 409 FSS stabilised with Ti and Zr, and found that Zr oxide particles form during solidification act as nuclei to the epitaxial nucleation of Ti carbides and nitrides. Since all the precipitates generate inside the

ferritic grain, and there is no formation of Cr carbides or nitrides, which guarantees a good corrosion resistance of the studied steel.

(Ti + V) composition system is seldom considered since Ti and N rich inclusion are likely to have depleted the matrix of V thereby resulting in a significant reduction in the number of fine strengthening precipitates dispersed in the matrix [105]. And the effects of V are considered not to be as apparent as Nb due to the stability of precipitate and solid solubility [106].

Dual stabilisation method is a preferable choice if the advantages of stabilised elements are considered, removing or avoiding the disadvantages of them.

2.4.5. Producing processes

What producing processes influence the ultimate properties of FSS grades are related with the microstructure evolutions that they bring, such as grain size, precipitation [67]. In addition, some other factors unconfirmed still have connections with the modification of properties. For instance, Šmida & Bošanský [107, 108] pointed out that the occurrence of deformation twinning could possibly play an important role in the DBTT of some polycrystalline ferritic steels. Usually, producing processes involve hot working, cold working and heat treatment (including cooling).

2.4.5.1. Hot working

Grain refinement of pure medium- and high-Cr FSS during hot working processes does not occur readily because there is no phase transformation, and meanwhile, recrystallisation behaviour is not easy to happen during this process. Thus, it has been found that even after heat treatment, 40Cr FSS has a coarse grain size of Number 2-3 (ASTM E112) [109]. Controlled working involves the refinement of the grains by recrystallisation process during rolling, and decreasing the finishing temperature and increasing reduction of per pass are always used. In stabilised stainless steels, microalloying elements always retard recrystallisation, but the precipitation may sometimes inhibit grain growth after recrystallisation [110].

Gao *et al*. [40] carried out a rolling procedure at a low temperature for 17Cr FSS to obtain a significant refinement of the recrystallised microstructure, and succeeded in decreasing the DBTT of the studied steel. Meanwhile, the DBTT could be closely related to the occurrence of deformation twinning. Taguchi *et al*. [111] developed the ultrafine grained 12Cr-1Zr steels by implementing mechanical alloying method and hot extrusion, which improves Charpy impact toughness twice.

Besides refining grain size, hot working may also accelerate some detrimental phases, such as σ phase. Therefore, precipitation behaviours of these detrimental phases should be paid

attention to when controlled working is used. This is also the reason why heat treatment has to be utilised to dissolve these phases after hot working.

2.4.5.2. Cold working

The effect of cold working on toughness of FSS grades is still unclear. In any case, cold working increases the flow stress σ_y, and thick cold rolling even doubles the value of σ_y [112, 113]. According to **Equation 2-4**, cold working should pronouncedly promote satisfaction, which induces the occurrence of the DBTT. It is reported that the general effect of cold working is: DBTT increase of 1 ~ 2 ℃ per percent rolling reduction [49]. Although the embrittlement effect increases with DBTT during cold working related with the rate of work hardening, the reduction of plate thickness slows down the increase of DBTT.

Cold working may complicate other forms of embrittlement, such as second phases, which may be separated or cracked from the matrix during cold rolling.

2.4.5.3. Heat treatment

For a number of FSS groups, if annealing temperature is high, i.e. more than 1000 ℃, rapid grain growth happens. But if annealing temperature is decreased to 500 ~ 900 ℃ range,

second phases, such as σ and χ phases, will appear. Even if the annealing process is performed at a high temperature, rapid cooling could lead to embrittlement sometimes.

It has been reported [114] that the temperature of annealing had a significant effect on toughness, especially when annealed above 900 ℃. It was found that the higher the annealing temperature, the lower the room temperature toughness. This phenomenon was ascribed to the increasingly precipitates which locked the dislocations.

As displayed in **Figure 2-36**, rapid cooling rates enhance the toughness of alloys with total (C + N) in solution, which at low levels can have a favourable effect on toughness. However, as the (C + N) level increases, the effect is reduced and at high (C + N) levels, rapid quenching from temperatures above 1000 ℃ raised the DBTT [115].

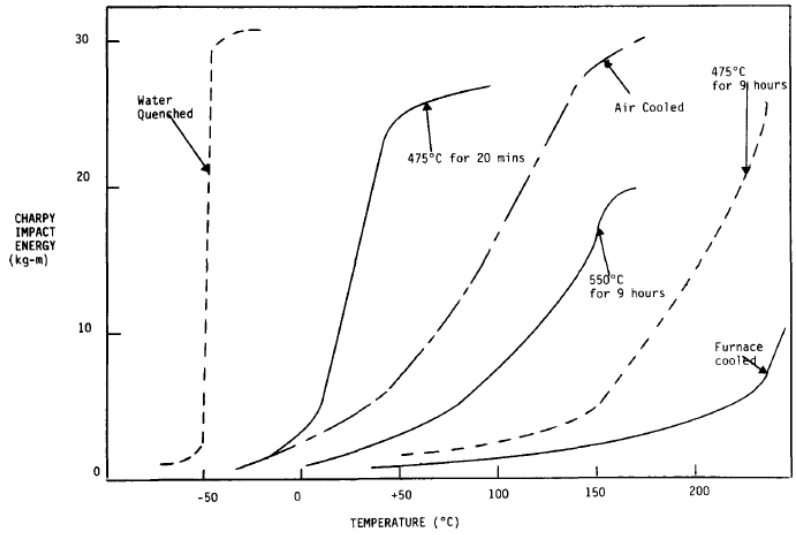

Figure 2-36 Impact energy data for a 25Cr alloy with (C + N) in solution after various isothermal treatment and cooling rates from 850 ℃.

The modern alloys with pretty low (C + N) levels have avoided some severe problems, even quenching will produce optimum toughness. But for different FSS groups, the parameters of heat treatment should be designed separately.

2.4.6. Grain boundary character

It is well understood that the toughness of steels is controlled by different microstructural constituents that can be considered as material flaws to some degree [116]. Some of them, like inclusions, are intrinsic while some others depend on processing conditions, such as grain boundaries (GBs), GB carbides, hard second phases. Fracture is controlled by several

steps [117]: the nucleation of a microcrack at a microstructual flaw when a critical stress is exceeded, followed by the propagation of a crack through the microstructure.

An important structural parameter, which is related with processing conditions and affects the properties of metallic materials, is grain boundary character (GBC) [118], and the grain boundary engineering (GBE) focuses on the development of optimal GBC in metallic material. It has been reported that GBE plays an important role in governing mechanical properties of materials, such as strength, ductility and creep properties [119]. In the field of GBE, GBCD and GB connectivity have shown a close connection with these properties [120, 121].

The grain boundaries are divided into three categories: low angle ($\theta < 2°$), medium angle ($2° \leq \theta < 15°$) and high angle ($\theta \geq 15°$) and it is considered that low angle boundaries (LABs) contribute to the dislocation strengthening, while the other two boundaries constitute the Hall-Petch contribution. Therefore, when toughness is concerned, LABs are not the main factors, while the density and distribution of high angle boundaries (HABs) define the cleavage unit size controlling the propagation of brittle fracture. That means ($\theta \geq 15°$) was determined as the threshold angle that defines the cleavage unit size [122]. GBE involves a series of treatments designed to convert a fraction of the high-energy grain boundaries (random boundaries) to low-energy grain boundaries [123].

How to control the fraction of so-called “special” boundaries, i.e. those having dense

coincident site lattice (CSL), is characterised by the reciprocal density of coinciding sites, Σ. A number of authors have suggested that an increased proportion of CSL-related boundaries should improve material's resistance to intergranular cracking [124]. The CSL boundaries (CSLBs), together with LABs, belong to low-energy boundaries. And the CSL model is employed to describe GBCD by classifying grain boundaries as low-Σ CSLBs ($\Sigma \leq 29$ and $\Delta\theta \leq 15°\Sigma^{-1/2}$) [125] and high-Σ CSLBs ($\Sigma > 29$, random boundaries) [123]. For example, in FCC metals with low stacking fault energy (SFE), most of the special boundaries developed by GBE are Σ3 or $\Sigma3^n$ CSLBs related with twin boundaries. As the "special" boundaries, low-Σ CSLB involves lower boundary energies, less impurity or solute segregation, smaller diffusivity, higher resistance to GB sliding and crack nucleation and propagation compared to general boundaries (random boundaries).

Figure 2-37 displays a schematic representation of grain boundary structure-dependent fracture processes occurring in a polycrystal, in which fracture mode and fracture characteristics are controlled by GBCD and by other GBCD-related microstructural factors [126]. In a polycrystal the connection of random boundaries leads to crack propagation so that the local distribution and the configuration of high-energy boundaries (reversely low-energy boundaries) become important in addition to the averaged GBCD.

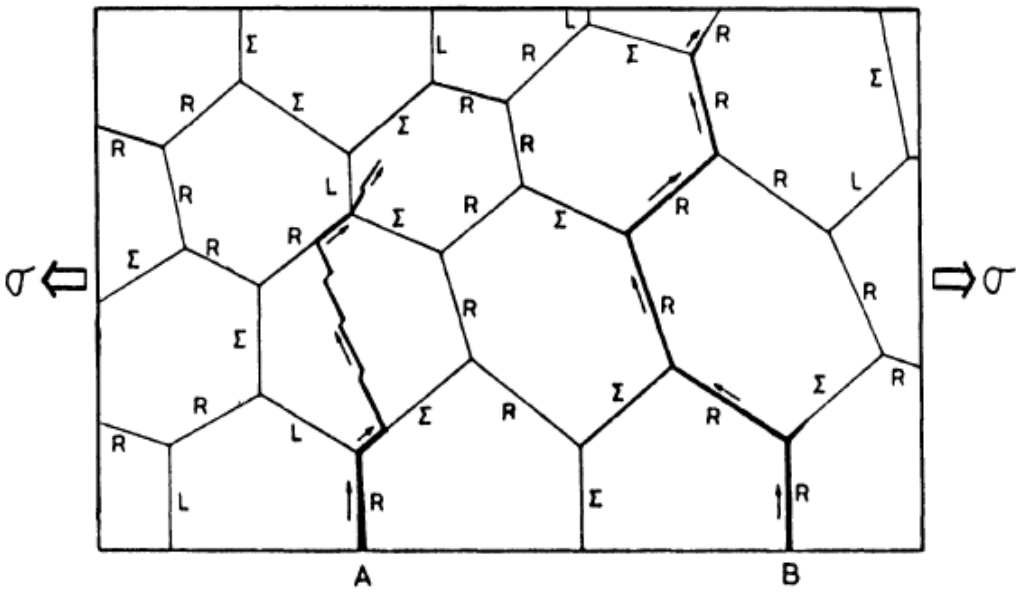

Figure 2-37 Schematic representation of grain boundary structure-dependent fracture processes in a polycrystal. Path A: combined process of intergranular and transgranular fracture. Path B: typical intergranular fracture.

The relatively recent electron backscatter diffraction (EBSD) techniques allow determining the mesotexture of the steels and distinguish the grain boundaries in terms of their misorientation. Consequently, even for simple ferrite microstructures, optically measured grain sizes can be significantly different from those obtained by EBSD [127].

2.4.7. Thickness of material

As mentioned above, the reduction of material thickness slows down the increase of DBTT during cold working in spite of flow stress σ_y, work hardening rate and second phases. In

fact, it is acceptable that material thickness is another significant factor affecting the DBTT level of FSS grades.

Theoretically, Wright and Lula [49] judged that with thin gauge, the metal at the notch tip is not substantially constrained in the direction perpendicular to the strip plane. As gauge increases, constraint occurs in this perpendicular direction and the stress state becomes triaxial at the crack tip. The increased constraint of thicker gauge has the effect of lowering *C* in **Equation 2-4** and results in higher DBTT values. They compared the effect of gauge on the DBTT for several FSS grades, shown in **Figure 2-38**, and displayed the relationship between the thickness of FSS grades and DBTT values. Generally, thinner material displays decreased DBTT to a point where very light gauges may have no practical toughness limitation. In addition, part effects of thickness come from grain size refinement after processing, such as rolling and forging.

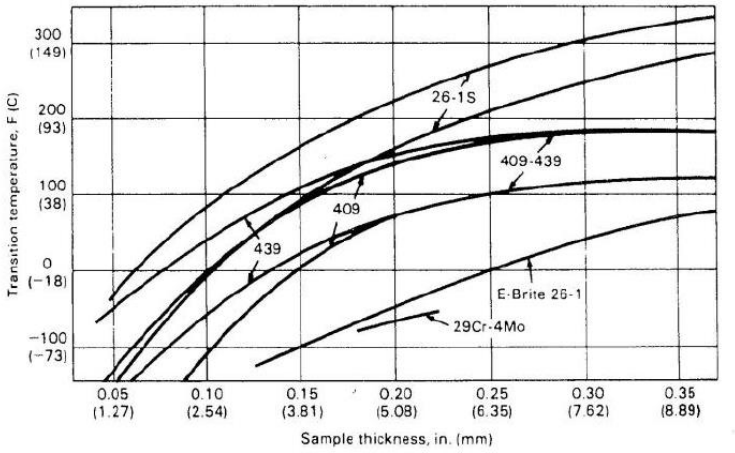

Figure 2-38 DBTT values for several FSS grades as a function of section thickness.

2.5. FRICTION STIR WELDING OF MEDIUM-CHROMIUM FERRITIC STAINLESS STEEL

It is not easy to acquire the FSS grades with satisfactory properties. And furthermore, since a large amount of FSS grades are used in the field of construction at the moment, the machining properties of these grades are essential in consideration the practical situation, for instance welding, forming, riveting. Among them, welding is the most popular one, which is almost utilised in each field. Therefore, besides the properties of the BM, how to maintain the machining properties of FSS, such as welding, is a non-ignorable issue to be faced by a number of researchers. The two main concerns during welding the ferritic grades are grain coarsening and high hardness in the HAZ. The latter is associated with both loss of ductility and notch toughness [5]. Since the pure FSS grades do not experience any phase transformation during the solidifying process, the traditional arc welding methods are not beneficial to the properties of the welds for the ferritic steel group. And this is the reason why friction stir welding is selected in this study. These years, more and more research has focused on the friction stir welding of pure FSS, aiming at acquire the joints with high-quality. And this can avoid the problems that happen during the other joining method, for instance, arc welding.

2.5.1. Introduction of friction stir welding

Friction stir welding (FSW) is a solid state joining process invented at The Welding Institute (TWI) of UK [128], which holds promise as an effective method of suppressing development of sensitisation in welds due to some sort of welding process with low heat input [129] and eliminates the melting and solidification associated problems, such as liquation and solidification cracking [130]. It is well acceptable that FSW process produces high-quality joints with a finer homogeneous microstructure and better mechanical properties than conventional welding processes [131]. FSW has evolved as a technique of choice in the routine joining of aluminium components [132], however, FSW of ferrous alloys including FSS has been recognised to be a little difficult for several reasons including high temperatures and severe wear resistance conditions encountered by the welding tool during the process [133].

2.5.2. Application of friction stir welding in ferritic stainless steel

Amounts of literatures have been published in the FSW field of low FSS, especially 11 ~ 12 wt.% Cr group [134-138], however, limited papers were reported with respect to FSW of medium and high chromium FSS group. Park *et al.* [139] examined the microstructural evolution and mechanical properties of friction stir welded 430 stainless steel. The joint was made using a rotational and welding speed of 550 rpm and 80 mm/min respectively, and the coarser elongated BM was modified to pretty fine duplex microstructure of ferrite and martensite resulted in significant improvement in mechanical properties. Bilgin *et al.* [140] observed that for the 430 steel he studied, the best mechanical resistance values, i.e.

tensile strength and impact energy, were obtained at tool rotational speed of 1120 rpm and traverse speed of 125 mm/min with the constant tool pressure force of 3.5 kN and tool angle of 0 º.

2.6. DEVELOPMENT OF FERRITIC STAINLESS STEEL THICK PRODUCTS WITH HIGH TOUGHNESS

It is extensively accepted that FSS grades have various advantages in comparison with ASS grades. From the traditional knowledge regarding FSS grades, there are some inevitable limitations for the usage of FSS products with thick gauge. However, the fact is that more and more FSS products have been applied in the various fields, especially industry. The key issue is how to solve the existing problems in this product group. In this thesis, two types of main FSS grades, 18Cr-2Mo and 17Cr ferritic steels, are put emphasis on and studied by means of microalloying and modifying producing processes.

18Cr-2Mo FSS is a ferritic type stainless steel containing 18 wt.% Cr, 2 wt.% Mo and some stabilising elements. Due to the Cr and Mo contents, the steel presents higher pitting corrosion resistance than other ferritic grades [141]. The general corrosion resistance of 18Cr-2Mo steel is comparable to that of austenitic 316 [142]. 17Cr FSS is a most popular ferritic type stainless steel containing 17 wt.% Cr, in order to improve its properties, the decrease of (C + N) contents and the addition of stabilising elements are implemented. 17Cr FSS is extensively applied instead of 304 due to its comparatively low cost and

mature producing process.

At present, 18Cr-2Mo and 17Cr FSS thick plates have been partly utilised in industrial fields, such as chemical complete equipment, water treatment tank, brewing equipment, etc. However, for FSS thick plate, the limitation of the toughness is the primary problem that should be resolved in these application occasions. Therefore, how to improve the toughness of this steel group is vital to its application.

From the manuals of global stainless steel manufacturers, seldom product lists involve ferritic type thick plates. However, there are still several top stainless steel manufacturers, which popularise FSS thick plates worldwide aiming at increasing its stainless steel market share. JFE [143] produces 410L and 430 FSS thick plate from 6.0 to 50.0 mm, however, there is a limitation of the width (1.0 ~ 4.0 m) and length (4.0 ~ 13.5 m) for plate products. Another Japanese stainless steel manufacturer, NSSC also has various grades of FSS thick plates [144], such as 405, 410L and 430, and its producing thickness of Cr FSS thick plate is from 4.0 to 60.0 mm (for 405 and 430, the thickness cannot be more than 40.0 mm). The width (1.4 ~ 3.2 m) and length (up to 12.5 m) are also set for sale. 18Cr-2Mo series steel, which belongs to a special group of medium-Cr FSS, is named “SUS 444” in JIS standard [31], and “NSSC 190L” in NSSC product manual. The thickness and width ranges of the products that NSSC can provide are 4.0 ~ 12.0 mm and 1.4 ~ 2.6 m, respectively.

According to the detailed introductions provided by the manufacturers, it is known that there are a few FSS products in the global market that are designed for the occasions of high toughness applications. Two types of FSS thick plates are selected for reference, and their design thoughts are compared with the detailed studies in this thesis. Although their toughness properties are not indicated, it is well realised by the manufacturers that for thick products and their weldment, toughness properties are always the key factors for manufacturers to consider.

2.6.1. NSSC 190L

Medium-Cr FSS named NSSC 190L is one of high corrosion resistant and toughness FSS grades recommended by NSSC [145]. Its composition system is 19Cr-2Mo-Nb-V with low C and N, which is exclusively developed for the usage as thick plate due to its high performance of toughness and weldability. The detailed chemical composition of NSSC 190L is listed in **Table 2-3**, from which, the design thought of NSSC 190L should focus on the low contents of C and N with additions of stabilising elements, Nb and V. There is some limitation for V, which supposedly means more content of V may be possibly useless or even detrimental to the toughness. Meanwhile, the contents of Si and Mn are relatively low, which is in accordance with the concept of "Clean Steel". The mechanical properties are listed in **Table 2-4**, the YS value of NSSC 190L with two kinds of thickness is higher compared with traditional SUS 444, which is probably related with the addition of Nb and V.

Table 2-3 Chemical composition of NSSC 190L.

Element	C	N	P	S	Si
Specification JIS G 4304	≤ 0.025	≤ 0.025	≤ 0.040	≤ 0.030	≤ 1.00
Typical type	0.004	0.008	0.025	0.003	0.07
Element	Mn	Cr	Mo	Nb (together with other stabilisers: Ti, Zr)	V
Specification JIS G 4304	≤ 1.00	17.00 ~ 20.00	1.75 ~ 2.50	8 × (C + N) ~ 0.80	-
Typical type	0.07	18.75	1.82	0.156	0.06

Table 2-4 Mechanical properties of NSSC 190L.

	SUS 444 in Specification JIS G 4304	Typical type (t: thickness)	
		t = 6 mm	t = 12 mm
YS, MPa	≥ 245	412	392
UTS, MPa	≥ 410	500	500
Elongation, %	≥ 20	35	35
Hardness, HBW	≤ 217	166	170

Besides significant mechanical performance for both BMs and their welds, NSSC 190L keeps a high level of pitting corrosion resistance, almost similar with SUS 316L, shown in **Figure 2-39**, and it is understandable that NSSC 190L displays lower corrosion rates when

tested at the experimental temperatures of 30, 40 and 60 ℃ for 48 hours than that of SUS 304L and SUS 316L in the solution of 50g/l ($FeCl_3$ + HCl), but when at 50 ℃, the result is reverse. For SCC resistance in high-temperature (300 ℃) chloride solution (Cl^-: 600 ppm), besides the reliable SCC resistance of the BM, there is also no occurrence of SCC for the tungsten inert gas (TIG) and manual metal arc (MMA) welds of NSSC 190L using various heat inputs after U-bending testing, shown in **Table 2-5**.

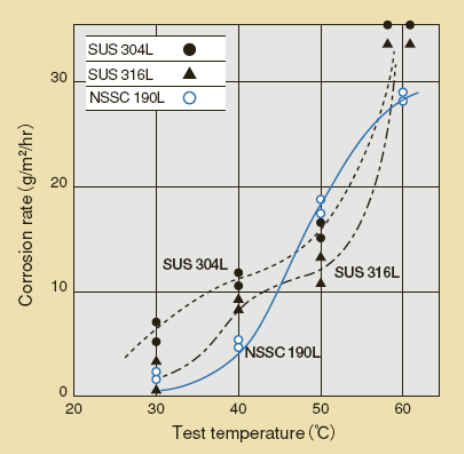

Figure 2-39 Comparison of pitting corrosion resistance among three stainless steels.

Table 2-5 Results of SCC resistance for NSSC 190L.

Base metal	Welding material	Welding method	Heat input, kJ/mm	Result of microscopic observation
NSSC 190L	D 316UL	TIG	1.08 1.44 1.93	No occurrence of SCC

		2.40
	MMA	1.34

Meanwhile, NSSC 190L is superior to SUS 304L in the aspect of oxidation resistance, and to SUS 316L in organic acid resistance. In consideration of the properties mentioned above, NSSC 190L is suitable to be extensively applied in the fields of petroleum refining, petro-chemical and desalinisation equipment, industrial heat exchanger, gas manufacturing facility, Cl^- containing device, hot water tank, etc., according to the recommendation of NSSC.

2.6.2. JFE SUS 430

SUS 430 is the most popular medium-Cr FSS, which is chosen by quite a few customers due to its good performance and reasonable price. In the JFE stainless steel thick plate manual, SUS 430 can be provided in the form of thick plate ranged from 6.0 ~ 50.0 mm. And the mechanical properties of JFE SUS 430 in the specification are listed in **Table 2-6**, and meanwhile, the toughness property can be guaranteed by the producer if JFE SUS 430 thick plate is applied in the industrial fields. However, JFE does not provide the real instance of SUS 430 thick plate.

Table 2-6 Mechanical properties in specification for JFE SUS 430.

YS, MPa	UTS, MPa	Elongation, %	Hardness, HV
205	450	22	200

It is imaginable that impact toughness is vital for both BM and WM of thick plate if welding process is necessary, and attention should be paid to if FSS thick plates are supplied to the customers from the regions with low application temperature. In spite of BCC structure, there is still some space for property modification of FSS grades, such as the addition of stabilising elements, processing optimisation, which is beneficial to the popularisation and application of FSS thick group.

2.7. SUMMARY AND SCOPE OF THIS WORK

In this chapter, a brief introduction of the stainless steel groups and the effects of different elements on these groups were given at first. Meanwhile, the equilibrium phase diagrams of various composition systems were provided to explain the mechanisms of phase evolutions. Then, the characteristics of medium-Cr FSS were demonstrated to emphasise the necessity of developing this product group. After that, the contents regarding toughness were illustrated, which is beneficial to study in-depth the improvement of impact toughness.

Factors that influence the toughness of FSS group have been summaried, such as interstitial elements, grain size, microalloying elements, processing parameters, grain boundary

character and thickness of material, and these factors play vital roles in affecting the impact toughness of the studied steels in accordance with the relative references. Furthermore, the friction stir welding of this steel group was proposed as a preferable jointing method for this special steel grade.

Finally, the FSS thick grades produced by NSSC and JFE, i.e. NSSC 190L and JFE SUS 430, were analysed to explain the meaningful development of FSS thick plates worldwide.

PART B

EXPERIMENTAL INVESTIGATION

3. EXPERIMENTAL INSTRUMENTS AND METHODOLOGIES

3.1. INTRODUCTION

In this chapter, the experimental instruments and methodologies used in the studies of the thesis will be briefly illustrated, and the details, such as experimental parameters, will be displayed in the following chapters.

The experimental investigation was carried out using the series of medium-Cr ferritic stainless steels (FSS) listed below.

- ✧ For microalloying study:

– Nb and (Nb + Ti) stabilised 18Cr-2Mo FSS (**Chapter 4**);

– (Nb + V) and (Nb + Ti + V) stabilised 18Cr-2Mo FSS (**Chapter 5**).

- ✧ For processing optimisation study:

– (Nb + Ti + V) stabilised 17Cr FSS (**Chapter 6**).

- ✧ For friction stir welding (FSW) study:

– (Nb + V) stabilised 18Cr-2Mo FSS (**Chapter 7**).

3.2. MATERIALS

The materials used in this thesis were manufactured in Stainless Steel R & D Center of Baoshan Iron & Steel Co., Ltd. located in Shanghai, P. R. China. 18Cr-2Mo FSS, whose relative standards and grades are listed in **Table 3-1**, is a ferritic type stainless steel containing 18 wt.% Cr, 2 wt.% Mo and some stabilising elements, such as Nb, Ti, V and Zr. Because of Cr and Mo contents, the steel presents higher corrosion resistance than other ferritic grades [139]. The general corrosion resistance of 18Cr-2Mo steel is comparable to that of austenitic AISI 316 [142]. 17Cr FSS (**Table 3-1**) is a ferritic type stainless steel containing 17 wt.% Cr and some stabilising elements, whose design thought is similar with other FSS grades. This steel is extensively utilised in civil application instead of austenitic AISI 304.

Table 3-1 Relative grades and standards regarding 18Cr-2Mo and 17Cr FSS.

Standard	Grade name	Note
ASTM A240/A240M [146]	S44400/444 430	Unless otherwise indicated, a grade designation originally assigned by the American Iron and Steel Institute (AISI).
JIS G 4304 [31]/G 4305 [147]	SUS 444 SUS 430	

BS EN 10088 [15]	X2CrMoTi18-2 (1.4521) X6Cr17 (1.4016)	Steel designation name (number)
GB/T 4237 [148]	019Cr19Mo2NbTi 022Cr17Ti	

At present, 18Cr-2Mo and 17Cr FSS thick plates (above 4 mm) have been applied in several limited industrial fields due to the characteristics of their mechanical properties, such as water treatment, brewing, etc.

3.2.1. Materials for microalloying

In order to control the amounts of C and N contents, the experimental materials used for microalloying study were melted in a 50 kg vacuum induction furnace. The casting cylinder-shaped ingots with the diameter of 120 mm were hot forged into the intermediate size (thickness × width × length), hot rolled into plates with the designed thickness, annealed at a certain temperature for some selected durations aiming at sufficient recrystallisation and fine annealing microstructure, and then cooled. The steel composition systems and codes are listed in **Table 3-2**. It is noted that all steels have been coded for ease of reference. The Nb, (Nb + Ti), (Nb + V) and (Nb + V + Ti) stabilised steels are coded to N#, NT#, NV# and NVT#.

Table 3-2 Illustration of composition systems and steel codes of 18Cr-2Mo FSS grades used in the investigation.

Classification	Steel	Composition system	Steel code
Microalloying	Nb and (Nb + Ti) stabilised 18Cr-2Mo steels	Nb stabilised	N#
		(Nb + Ti) stabilised	NT#
	(Nb + V) and (Nb + Ti + V) stabilised 18Cr-2Mo steels	(Nb + V) stabilised	NV#
		(Nb + V + Ti) stabilised	NVT#

3.2.2. Materials for processing optimisation

The experimental materials used for processing optimisation study were also melted in a 50 kg vacuum induction furnace, and the casting ingots with the diameter of 120 mm were hot forged into the intermediate size, hot rolled into plates with fixed thickness, annealed at a certain temperature for some time. The steel composition system and codes are listed in **Table 3-3**. The (Nb + V + Ti) stabilised 17Cr FSS grades used for processing optimisation are named as 17CrT#, 17CrP1# and 17CrP2#, respectively.

Table 3-3 Illustration of composition systems and steel numbers of 17Cr FSS grades used in the investigation.

Classification	Steel	Composition system	Steel code
Processing optimisation	(Nb + Ti + V) stabilised 17Cr steels	(Nb + Ti + V) stabilised	17CrT#
			17CrP1#
			17CrP2#

3.2.3. Material for friction stir welding

The experimental material used for FSW processes is similar with that of NV# in the microalloying investigation. And the steel composition system and code are listed in **Table 3-4**.

Table 3-4 Illustration of composition system and steel number of 18Cr-2Mo FSS used in the investigation of FSW.

Classification	Steel	Composition system	Steel code
FSW	(Nb + V) stabilised 18Cr-2Mo steels	(Nb + V) stabilised	18CrFSW#

3.3. PHASE CALCULATION

As the best and most powerful software package, Thermo-Calc software was used in this thesis for calculating the stable heterogeneous phase equilibria. For Thermo-Calc prediction in this thesis, all calculations are based on thermodynamic database TCFE6. There exists a wide selection of high-quality databases for various purposes that include amounts of different materials. The databases are produced through critical assessment and systematic evaluation of experimental and theoretical data [16]. In this thesis, the below calculations were applied.

– Phases and their composition;

– Transformation temperatures, such as liquidus and solidus;

– Phase diagrams.

Although the equilibrium phase that described by Thermo-Calc prediction is only a balanced one, they can still provide the reference to analysis of precipitation. In fact, the real phases will be modified based on the various parameters in the manufacturing procedure since the manufacturing process is still unbalanced even after heat treatment.

3.4. METALLOGRAPHY

After sample preparation, microstructural characterisation of the specimens was carried out using optical microscopy (OM), scanning electron microscopy (SEM) and transmission electron microscopy (TEM). OM was used to observe general microstructural features, such as grain size, whilst SEM was used principally to observe the fracture surfaces and comparatively large precipitates (> 0.5 μm) of the specimens. Usually, the result of electron backscatter diffraction (EBSD) collected from SEM was applied to check crystallographic orientation. TEM was carries out to analyse the morphology of fine particles (< 0.5 μm) appearing during producing process. Chemical composition of precipitates was analysed by energy dispersive spectroscopy (EDS) detectors, which are attached to both SEM and TEM instruments. Further detailed analyses of precipitates in steels were achieved by complete extraction of non-metallic particles in a solution, and finally validated by X-ray diffraction (XRD).

3.4.1. Sample preparation for metallography

The specimens for microstructural observation (OM and SEM) were cut using a blade of Struers 50A13, mounted in bakelite (Polyfast powder) for easy handling, polished in a standard metallographic way by Struers automatic polisher Tegrapol 21. The specimens were ground by 220# SiC paper, roughly polished with a DP-Plan cloth and 9 μm diamond spray, finely polished with a MD-Mol cloth and 3 μm diamond spray, a MD-Dur cloth and 1 μm diamond spray in turn. Subsequently, the specimens were etched or electrolytic etched in special solutions listed in **Table 3-5**.

Table 3-5 Solutions used during microstructure observation in this study.

Steel code	Solution	Method	Parameter
N#, NT#, NV#, NVT#	5 vol.% ferric chloride ($FeCl_3$) and 5 vol.% hydrochloric acid (HCl)	Etching	–
17CrT#, 17CrP1#, 17CrP2#	5g Cu_2SO_4, 20 ml hydrochloric acid (HCl) and 20 ml H_2O	Etching	–
18CrFSW#	10 wt.% oxalic acid	Electrolytic etching	Voltage: 4 V Time: 6 min

3.4.2. Optical microscopy (OM)

Based on visible light and a series of lenses, OM is used to magnify images of specimens. The microstructures of specimens were observed using OM of Leica DMR and Zeiss Axioplan 2 in this thesis. The longitudinal section is for microstructure observation, including grain size, precipitation. The grain size was measured by the software of Image 2 using planimetric method.

3.4.3. Scanning electron microscopy (SEM)

SEM is a type of electron microscopy by means of scanning the surface of a specimen with a focused beam of electrons. JEOL 6490 and FEI Quanta 600FEG operating SEM were used to investigate the microstructure in the studies, precipitation (> 0.5 μm) of the specimens and the fracture surfaces of the broken Charpy impact specimens. If the composition of phase needs to be confirmed, atomic concentrations of precipitates were analysed by EDS. The method of preparation for specimen is same with OM observation.

3.4.4. Electron backscatter diffraction (EBSD)

EBSD is a microstructural crystallographic technique used to examine grain orientation, misorientation-angle distribution and grain boundary in materials. In this study, JEOL 7001F field emission gun scanning electron microscope (FEG-SEM) was used to acquire the information about the orientation of the sub-grains and to construct the EBSD maps of various base materials. Specimens for EBSD were electropolished in A3 solution (40 ml perchloric acid, 410 ml methanol and 250 ml butoxythanol) at 50 V for 90 s.

The EBSD maps were collected from the FEG-SEM, and the software of HKL Channel 5 was used to analyse the acquired maps in offline mode.

3.4.5. Transmission electron microscopy (TEM)

The selected region of the specimen was machined into a 3 mm cylinder. Disks, 3 mm in diameter and thickness of 200 μm were prepared by first cutting with a Struers Accutom-50 cutting machine with a slow speed SiC bladed saw. The disks were then ground to a final thickness of less than 80 μm using successively finer grades of SiC paper to remove equal amounts of material from both sides of the disk. This ensured that any gross deformation from sawing and previous grinding was removed. Disks were electrolytically polished using a twin jet electropolisher Struers Tenupol 3 with a 4 vol.% perchloric acid and methanol solution cooled to -40 °C, operating at a total current of 160 ~ 180 mA. The disks after electropolishing were further ion milled using Leica EM RES101 for higher quality.

Thin foils were prepared for the observation of fine precipitates (< 0.5 μm) with TEM instruments of JEOL JEM 2100F and JEOL JEM 2010. Atomic concentrations in precipitates were distinguished by EDS.

3.4.6. Extraction

To identify the detailed precipitates of the studied steels through the other method, complete extraction of non-metallic particles in the solution of 90 vol.% formaldehyde and 10 vol.% HCl was processed. Then, the precipitation powders were obtained after the base materials were dissolved.

3.4.7. X-ray diffraction (XRD)

Since high percentages of precipitation powders remain undissolved, the XRD testing was used to determine the varieties of the particles. The instrument of X-ray diffractometer of Philips X'Pert PRO MPD was used in this thesis.

Furthermore, the textures formed during manufacturing processes were measured by using XRD on a Bruker D8 discover diffractometer with Co-K_α radiation, and orientation distribution functions (ODFs) $f(g)$ were calculated by the series expansion method according to Bunge (the maximum expansion degree, $l_{max} = 22$) from three incomplete pole figures {1 1 0}, {2 0 0} and {1 1 2}.

3.5. MECHANICAL PROPERTIES

Mechanical properties of the specimens were measured, focusing on tensile strength, impact toughness and hardness testing and aiming at evaluating the strength, hardness, ductility and impact toughness properties under different microalloying and processing control thoughts. ASTM A370 [149] is the whole standard cover procedures and definitions for the mechanical testing of stainless steel.

3.5.1. Tensile testing

Measurements of tensile tests were conducted in the machine of INSTRON-5985. The yield strength (YS), ultimate tensile strength (UTS) and elongation were measured during tensile testing. ASTM A370 [149] and ASTM E8/E8M [150] was selected during tensile tests. And the machined specimens for tensile testing are shown in **Figure 3-1**, and its dimension data are listed in **Table 3-6**.

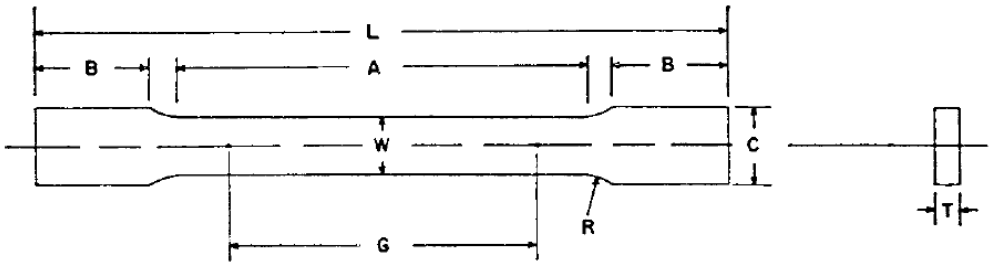

Figure 3-1 Machined tensile specimen.

Table 3-6 Dimension data for tensile specimen.

	Standard specimens, Sheet-type
G-Gage length	50.0 ±0.10 mm
W-Width	12.5 ±0.25 mm
T-Thickness	Thickness of material
R-Radius of fillet, min	13 mm
L-Over-all length, min	200 mm
A-Length of reduced section, min	60 mm
B-Length of grip section, min	50 mm

C-Width of grip section, approximate	20 mm

3.5.2. Impact toughness testing

The Charpy-V impact toughness of the studied steels was investigated by the machine of INSTRON-9250. Since the thickness of specimen is limited to the thickness between 5.4 ~ 8 mm, sub-size Charpy-V notch (CVN) specimens 5 mm (or 3.3 mm) × 10 mm × 55 mm cross-section were machined with the transverse direction perpendicular to the rolling direction of the plate. A 2 mm deep CVN was cut through the thickness direction parallel to the rolling plane. All Charpy specimens were prepared transverse to the rolling direction of the plate. Measurements were conducted according to ASTM A370 [149] and ASTM E23 [151]. And the machined specimens for impact toughness testing are shown in **Figure 3-2** and **Figure 3-3**, and their dimension data are listed in

Table 3-7.

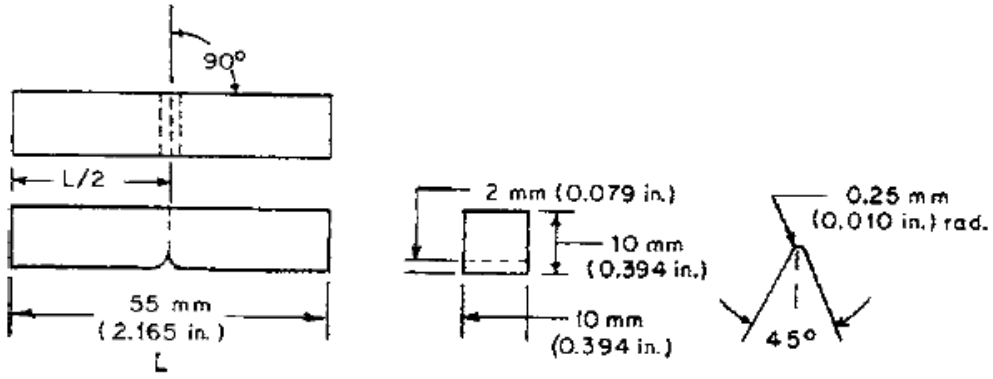

Figure 3-2 Machined Charpy specimen with full size.

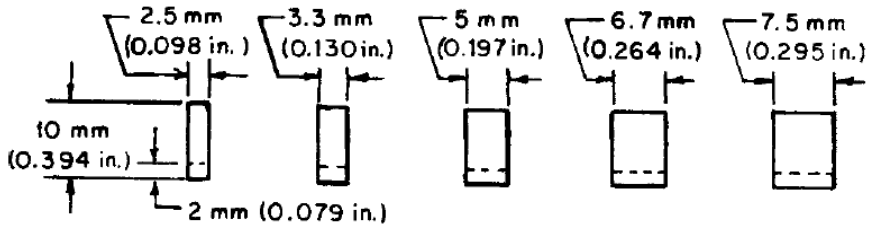

Figure 3-3 Dimension of standard sub-size Charpy specimens.

Table 3-7 Dimension data for Charpy specimen.

	Standard full size specimen and permissible variations
Notch length to edge	90 ± 2 º
Adjacent sides shall be at	90 ± 10 min
Cross-section dimensions	±0.075 mm
Length of specimen (L)	+0, -2.5 mm
Centring of north (L/2)	±1 mm
Angle of notch	±1 º
Radius of notch	±0.025 mm
Notch depth	±0.025 mm
Finish requirements	2 μm on notched surface and opposite face; 4 μm on other two surfaces

3.5.3. Hardness testing

The Vickers hardness testing was performed using a load of 0.1 kg and a dwell time of 15 s according to ASTM A370 [149] and ASTM E384 [152], and the corresponding instrument is DuraScan 70 automatic hardness tester. Specimen preparation should be performed in accordance with standard guide for preparation of metallographic specimens [153].

3.6. SUMMARY

The commonly used experimental instruments and methodologies in the studies were introduced in this chapter. The particular and detailed experimental procedures as well as experimental results will be presented and discussed in the relative chapters.

4. MICROALLOYING WITH NB/(NB + TI)

4.1. INTRODUCTION

In this chapter, the elements of Nb and Ti were added to 18Cr-2Mo ferritic stainless steel (FSS) thick plates to investigate the effects of microalloying, i.e. single (Nb) and dual (Nb + Ti) stabilisation, on microstructure and mechanical properties. It is well known that the detrimental influence of interstitial elements, C and N, can be militated by stabilisation with either Nb, V, Ti or Zr, which form strong carbides and nitrides [19, 48]. The stabilising elements Nb and/or Ti are commonly employed because of their effectiveness during processing and also on mechanical properties. As consequence, these two elements have been extensively investigated by numerous researchers, seen in **Chapter 2.4.4**.

Although Ti & Zr are the stronger nitride formers, Nb exhibits a unique combination of both carbide and nitride stability [77], and most importantly more stable than Cr carbide and nitride, which guarantees corrosion resistance of FSS grades. Ti, which is probably the most commonly employed stabiliser, however has significant disadvantages. The formation of TiN, which is depending on concentration levels, can form in the liquid and so produce an inappropriate size distribution of precipitate.

The current commercially favoured approach is the use of a combined addition of both Nb and Ti, which provides effective stabilisation and also cost benefits. Although Ti is cheaper compared with Nb, the technical and quality benefits that it brings provide the basis for increased production yields and production throughputs. This chapter compares the use of Nb and (Nb + Ti) in terms of stabilisation and the mechanical properties for 18Cr-2Mo FSS thick plate processing.

Besides the precipitation reactions through the different microalloying elements, the roles of grain boundaries (GBs) are evaluated to investigate whether or not it is applicable to explain the change of impact toughness properties. It is recognised that grain boundary engineering (GBE) plays a very important role in governing mechanical properties of materials [120], such as strength and ductility. But usually, the theory of GBE focuses on the modification of thermomechanical treatment, which is studied in details in **Chapter 6** and aims at transforming a fraction of the high-energy grain boundaries (random boundaries) to low-energy grain boundaries. And meanwhile, low-energy boundaries are identified as low-Σ coincidence site lattice boundaries (CSLBs, or "special" boundaries [154]), including low-angle boundaries (LABs) [123]. The coincident site lattice (CSL) model was developed [120] to describe grain boundary character distribution (GBCD) by classifying grain boundaries as low-Σ CSLBs ($\Sigma \leq 29$ and $\Delta\theta \leq 15°\Sigma^{-1/2}$) [125] and high-Σ CSLBs ($\Sigma > 29$, random boundaries) [123]. Here, the Σ is the reciprocal density of coincident sites at the grain boundaries between two adjoining grains. Among the low-Σ CSLBs, Σ1 (i.e. LABs) and Σ3 are usually the dominant boundaries.

As described in **Chapter 2**, the effects of Nb and Ti on the mechanical properties of FSS are a subject of debate in the public domain. The work in this chapter aims to clarify the influence of Nb and Ti on the strength and toughness of 18Cr-2Mo thick plates, using two different composition systems: single Nb and dual (Nb + Ti).

4.2. EXPERIMENTS

4.2.1. Materials

The manufacturing procedures of the materials used in this study were presented in **Chapter 3.2.1**, the designed size of the hot rolled plates was 30 mm × 250 mm × 200 mm (thickness × width × length), and after being heated at 1150 ℃ for 240 min, the 30 mm forged plates were hot rolled into 8 mm plate (the rolling reduction was around 73.3%) during the temperature range of 900 ~ 1120 ℃. Finally, the hot rolled plates were annealed at 1080 ℃ for 8 min, followed by cooling in water. These hot rolling parameters and short time annealing heat treatment at high temperature were employed because it closely simulates the practical manufacturing conditions in the stainless steel branch of Baosteel Group.

The chemical composition of the studied steels is listed in **Table 4-1**. The stabilisation ratios of N# and NT# steels are 23.2 and 18.3, respectively, which are calculated using **Equation 2-7**. The results mean both steels can satisfy the requirements of intergranular

corrosion resistance [26, 155, 156]. For N#, due to high Nb content, the stabilisation ratio is a little higher, which will also provide bring high strength during the design process of FSS.

Table 4-1 Chemical composition (in wt.%) of studied steels.

Steel no.	C	Si	Mn	Cr	Mo	Nb	Ti	N	Fe
N#	0.0087	0.32	0.19	18.75	1.88	0.41	-	0.0090	Bal.
NT#	0.0075	0.32	0.17	18.50	1.81	0.21	0.11	0.0100	Bal.

The levels of C and N contents are similar for two studied steels, which is the precondition to research the effects of stabilised elements since C and N, especially C [48, 50, 56, 57], can influence the final properties of steels greatly. As demonstrated in **Chapter 2**, it is extensively acceptable that low ratios of interstitial elements are beneficial to the toughness of steels.

4.2.2. Phase calculation

For the equilibrium phase diagrams of these two studied steels provided by Thermo-Calc, the recommended temperature range is from 500 to 1600 ℃. Phase calculation, including precipitation reactions, were illustrated by modifying the temperature scale, i.e. *X* axis, from 500 ~ 1600 ℃ to 500 ~ 1000 ℃, and the mole scale, i.e. *Y* axis, from 0 ~ 1 mole to 0 ~ 0.20 mole. The equilibrium phases calculated are balanced, which can provide the reference to analyse the predicted phases during the practical manufacturing processes.

4.2.3. Microstructure analyses

As-annealed specimens were prepared for microstructure analyses. The longitudinal sections (rolling direction, RD) of specimens were observed using optical microscopy (OM) Zeiss Axioplan 2. The grain sizes were measured using the software of Image 2. The coarse precipitates and fracture surfaces of the specimens were observed with scanning electron microscopy (SEM) FEI Quanta 600FEG and JEOL 6490, respectively. And transmission electron microscopy (TEM) JEOL JEM 2100F was used to analyse fine precipitates. Qualitative microanalysis of precipitates was determined by energy dispersive spectroscopy (EDS) on both SEM and TEM.

4.2.4. Electron backscatter diffraction (EBSD) mapping

Prior to EBSD mapping, the unmounted specimens were polished down by 1200# SiC paper, followed by electropolishing on the Struers LectroPol-5. EBSD mapping was operated at the excitation voltage of 15 kV. The step size was 2 μm based on the grain size reference, and the entire mapped area was 2.4 mm × 1.8 mm at a magnification of 50×. The collected data were post-processed by HKL Channel 5 software.

4.2.5. Tensile strength and impact toughness testing

Tensile testing was performed at room temperature with strain rate of 5×10^{-3} s^{-1}. The yield strength (YS), ultimate tensile strength (UTS) and elongation were measured using standard techniques. The Charpy impact toughness of 18Cr-2Mo FSS was investigated in the temperature range between -40 and 40 ℃, using sub-size (5 mm × 10 mm × 55 mm) specimens. All Charpy specimens were prepared transverse to the RD of the plate. The testing standards include ASTM A370 [149], ASTM E8/E8M [150] and ASTM E23 [157].

4.3. RESULTS

4.3.1. Equilibrium diagram

Figure 4-1 and **Figure 4-2** show the equilibrium phases of the studied 18Cr-2Mo steels, i.e. N# and NT#, by Thermo-Calc software. **Figure 4-1** displays that, for N#, FCC_A1#2, accepted as the precipitate regarding Nb, forms at 1220 ℃, and then Z phase, regarded as CrNbN [158], precipitates out at the temperature of 950 ℃. And for NT#, due to the fact that TiN appears in the liquid. After TiN, the other precipitates, such as TiC, NbN and NbC, are inclined to generate in some order. From the results of Thermo-Calc prediction, the corresponding temperature for FCC_A1#2, known as Nb/Ti precipitation, is 1490 ℃, which is illustrated in **Figure 4-2**.

Between the temperature range of 600 ~ 900 ℃, it can be seen that Laves phase, Chi phase and Sigma#1 phase precipitate out for both steels, and below 600 ℃, another Sigma phase,

i.e. Sigma#2 phase, forms. For N# and NT#, the composition of all precipitates that may appear during manufacturing is listed in **Table 4-2**.

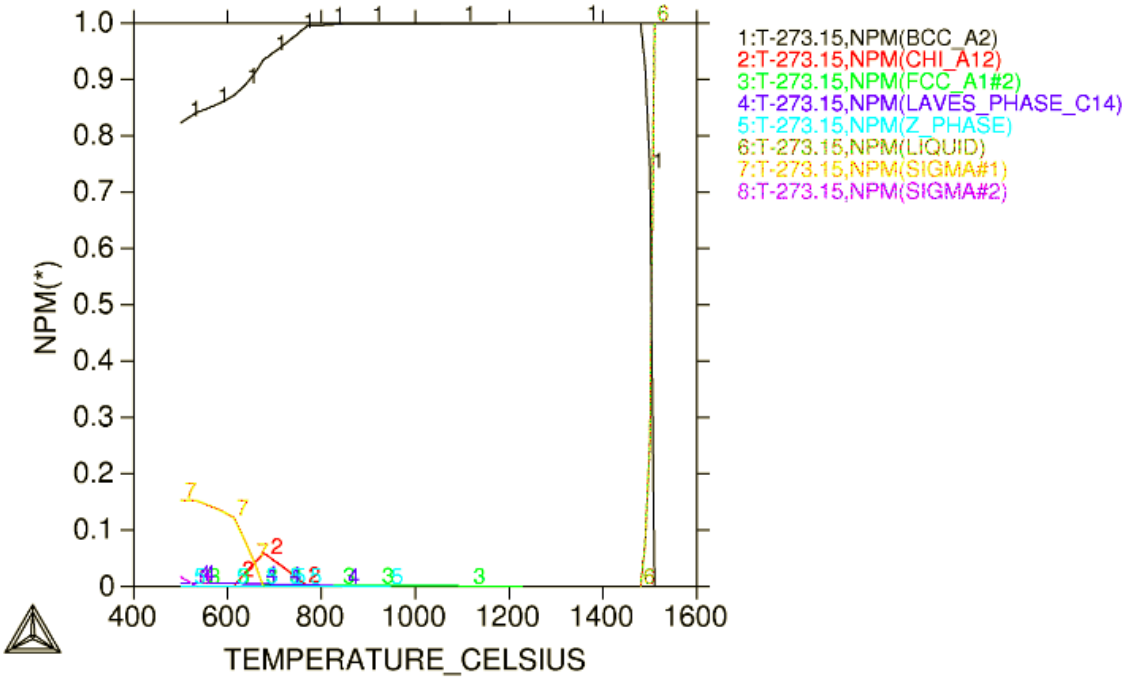

(a)

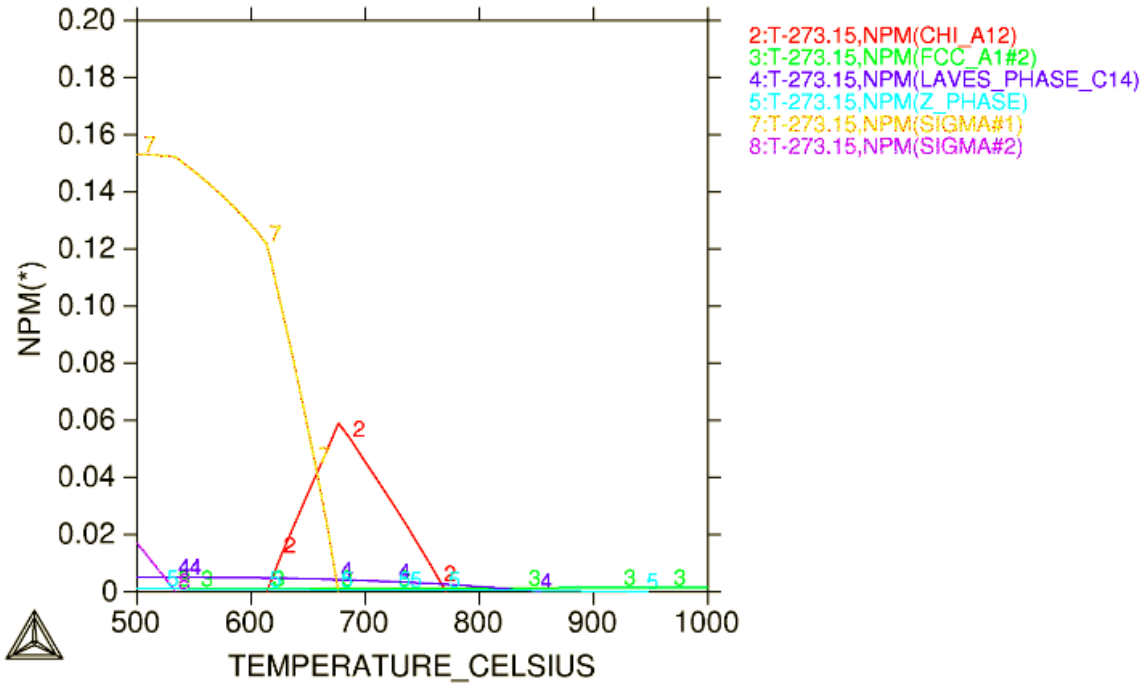

(b)

Figure 4-1 Calculated equilibrium molar fractions of phases of Nb-stabilised steel: (a) *Y* axis from 0 ~ 1 mole; (b) *Y* axis from 0 ~ 0.20 mole.

N#: 1 Ferrite (BCC_A2); 2 Chi phase (CHI_A12); 3 Nb precipitate (FCC_A1#2); 4 Laves phase (LAVES_PHASE_C14); 5 Z phase (Z_PHASE); 6 Liquid (LIQUID); 7 Sigma#1 phase (SIGMA#1); 8 Sigma#2 phase (SIGMA#2).

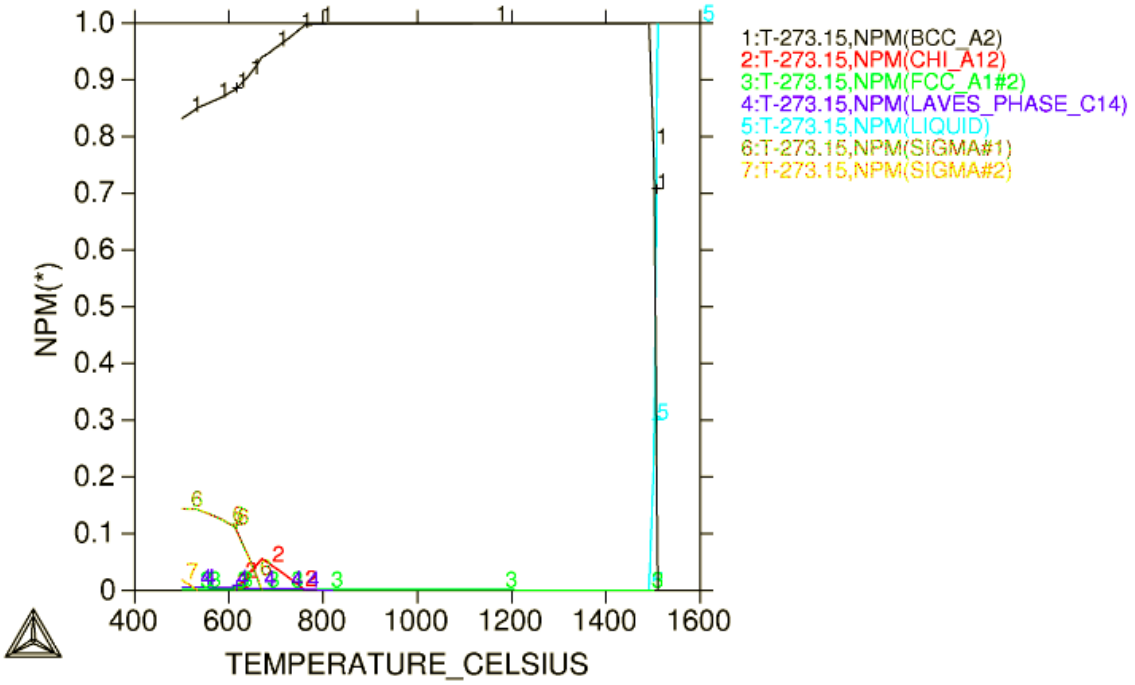
1:T-273.15,NPM(BCC_A2)
2:T-273.15,NPM(CHI_A12)
3:T-273.15,NPM(FCC_A1#2)
4:T-273.15,NPM(LAVES_PHASE_C14)
5:T-273.15,NPM(LIQUID)
6:T-273.15,NPM(SIGMA#1)
7:T-273.15,NPM(SIGMA#2)
NPM(*)
1.0
0.9
0.8
0.7
0.6
0.5
0.4
0.3
0.2
0.1
0
400
600
800
1000
1200
1400
1600
TEMPERATURE_CELSIUS

(a)

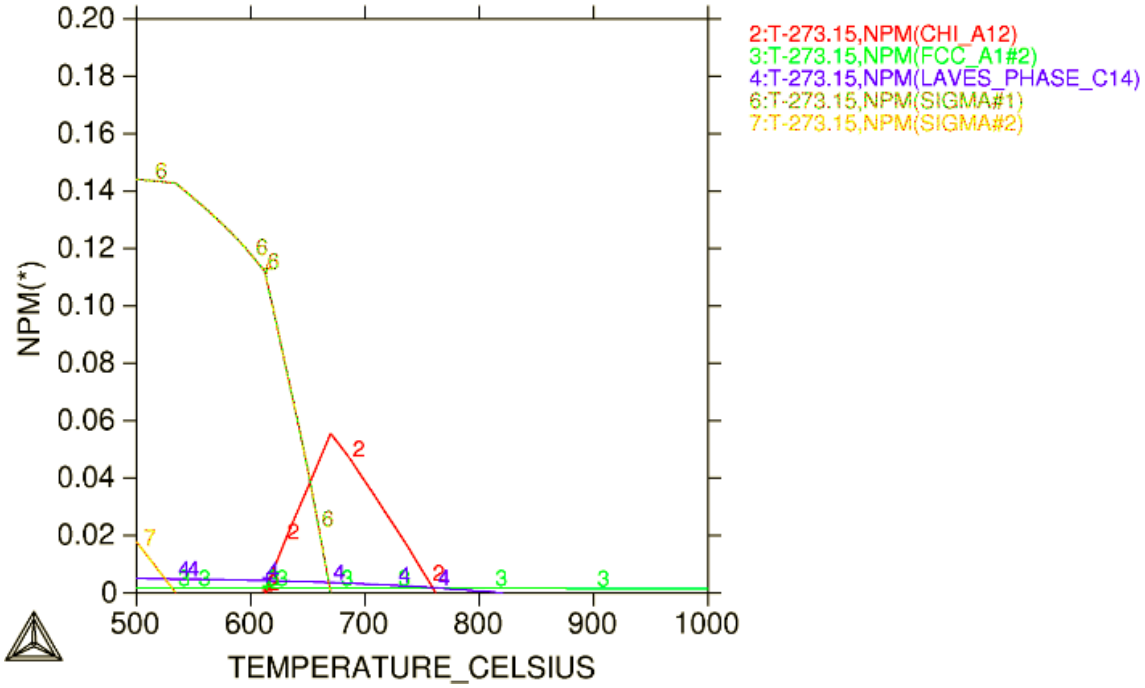

(b)

Figure 4-2 Calculated equilibrium molar fractions of phases of (Nb + Ti)-stabilised steel: (a) *Y* axis from 0 ~ 1 mole; (b) *Y* axis from 0 ~ 0.20 mole.

NT#: 1 Ferrite (BCC_A2); 2 Chi phase (CHI_A12); 3 Nb/Ti precipitate (FCC_A1#2); 4 Laves phase (LAVES_PHASE_C14); 5 Liquid (LIQUID); 6 Sigma#1 phase (SIGMA#1); 7 Sigma#2 phase (SIGMA#2).

Table 4-2 Composition of precipitates formed for studied steels.

Precipitate	Composition
FCC_A1#2	Nb(C,N)
Z phase	CrNbN [158]
Chi phase	Varied from $Fe_{36}Cr_{12}Mo_{10}$ to $Fe_{36}Cr_{12}Mo_3Ti_7$ [159, 160]

Laves phase	Fe_2Nb [53, 161, 162]
Sigma phase	Fe(Cr,Mo), rich in Cr, Mo [159]

4.3.2. Microstructure

4.3.2.1. Grain size

It is evident that the microstructure of pure 18Cr-2Mo FSS grade is single ferrite phase from Thermo-Calc prediction, and the results of OM are displayed in **Figure 4-3**. Furthermore, the distributions of grain sizes are given in **Figure 4-4**. Through planmetric measurement and statistics, the average grain sizes of N# and NT# are approximately 212.1 and 262.6 μm, respectively. For the grains ranged from below 60 to 240 μm, N# contains 67.3%, which is more than that of NT#, 52.4%. And for the grain that from 240 to 480 μm, N# contains 25.5% grains of this size range, less than NT#, 33.3%. For both steels, even 7.1% and 14.3% grains are larger than 480 μm for N# and NT#. Considering the average grain sizes and relative distributions of N# and NT# steels, Nb stabilised steel acquired smaller grain sizes than that stabilised with (Nb + Ti). Furthermore, the grain sizes of both steels are not homogenised since their grain distributions are scattered. For the grain distributions of two studied steels, N# has the grains that concentrate in the range of less than 60 to 240 μm. Comparatively, NT# has those sizes in the range of 90 to 300 μm.

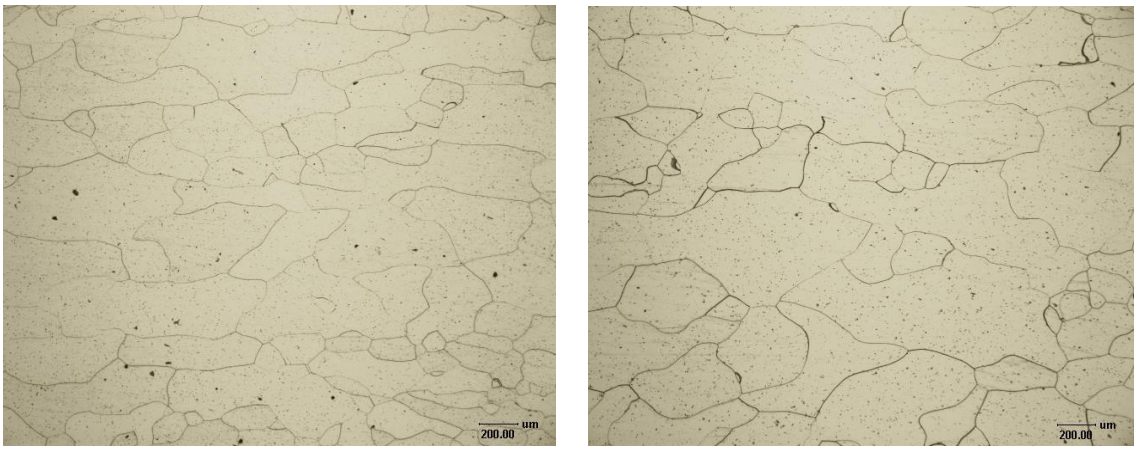

(a) (b)

Figure 4-3 OM images of studied steels: (a) Nb-stabilsed; (b) (Nb + Ti)-stabilised.

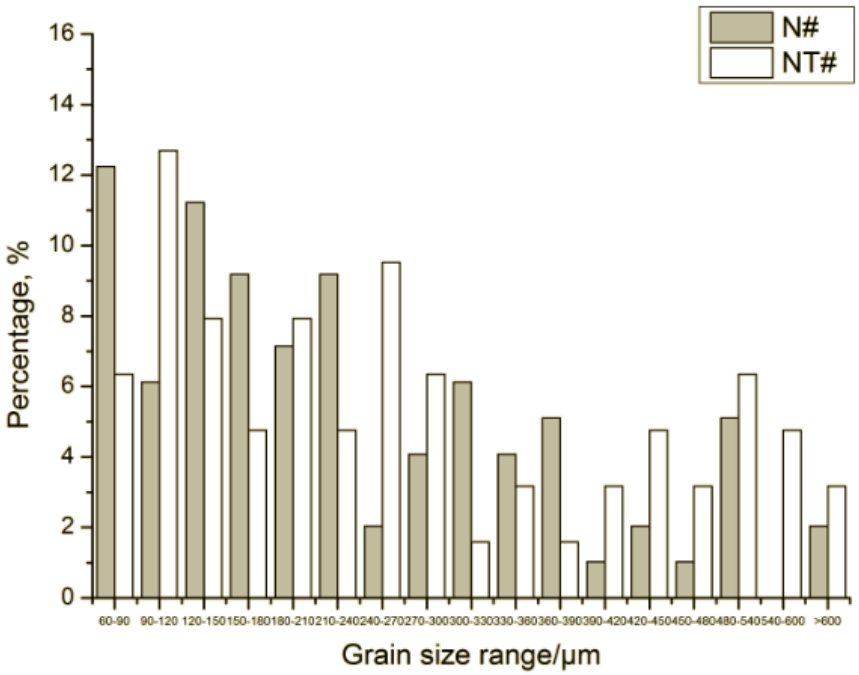

Figure 4-4 Distributions of grain sizes for two studied steels.

4.3.2.2. Precipitation

Figure 4-5 shows the distribution results of precipitation under SEM for N# and NT#. Roughly, the precipitates are higher in quantity for N#, and bigger in size for NT#. In principle, it is possible for Nb carbonitrides to form in the FSS grade stabilised by the single element Nb, and for Nb, Ti carbonitrides to generate in FSS grades stabilised by the dual Nb and Ti elements. Furthermore, besides the distributions of precipitation close to the grain boundaries, there are some particles appearing at the boundaries for N#, however, the same phenomenon does not occur for NT#. The particles at the boundaries may resist the growth of grains to some degree.

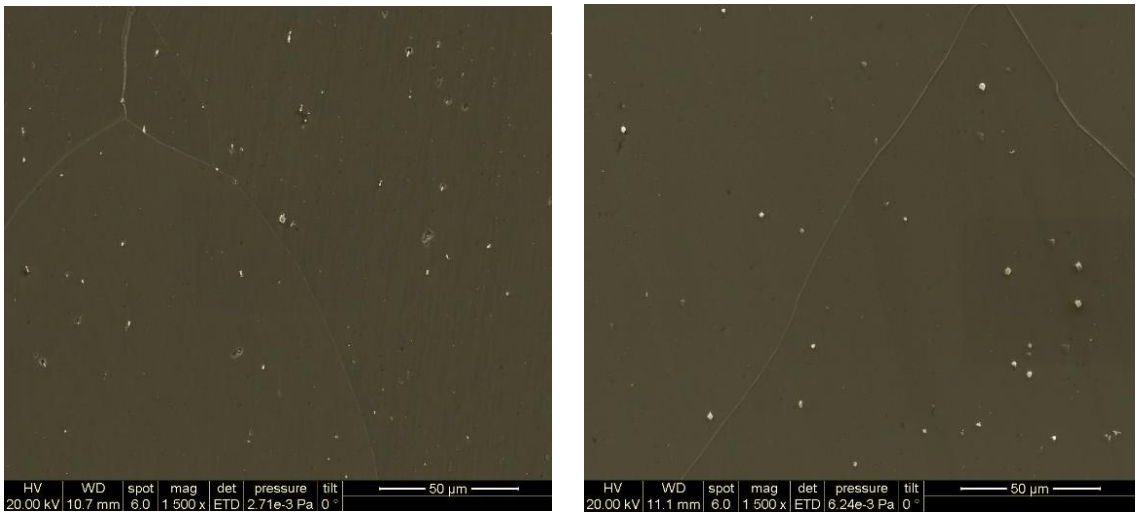

(a) (b)

Figure 4-5 SEM images of precipitation for studied steels: (a) Nb-stabilsed; (b) (Nb + Ti)-stabilised.

Figure 4-6 and **Figure 4-7** display the SEM images and EDS analyses of the precipitates of N# and NT#. For N#, the precipitate of FCC_A1#2, which is considered to be Nb(C,N) particle, forms at the high temperature. Z phase generates after Nb(C,N), which is hard to become stable in such a short time [158], i.e. 8 min. From **Figure 4-6**(a), the fine precipitates distributing at and along the grain boundaries are confirmed by EDS to be NbC (**Figure 4-6**(b)). From **Figure 4-8**(a) and (b)-(e), it is observed the shapes and sizes of NbC particles differ from each other. At the same time, **Figure 4-8**(f) and (g) show the small precipitate of Nb(C,N). It is reported the average diameters of the spherical Nb(C,N) are around 500 nm in 9 wt.% Cr ferritic steels [102]. But here, the size of Nb(C,N) is only around 100 nm, which is possible to be related to the composition of Nb, C and N.

For NT#, since the element of Ti is a strong nitride forming element, a couple of cuboidal TiN precipitates of the size of around 2.5 μm are found distributing in the matrix (**Figure 4-7**(a) and (b)). Meanwhile, NbN is found attached to the particle of TiN. As the contents of Ti and Nb in the studied steel are more than critical Stoichiometric values as-certained by the ideal chemical matching of (Ti,Nb)N, and thus, the interstitial N should be fully stabilised by Ti and Nb theoretically. The (Ti,Nb)N particles with different sizes (0.8 μm and 230 nm) and shapes can be observed under TEM (**Figure 4-9**(a)-(d)).

Then, NbC and TiC have the similar solid solubilities. In low carbon steels with Nb and Ti additions, NbC is more stable than TiC at higher temperatures in ferrite throughout the ferrite stability range [163]. From **Figure 4-9**(e)-(g), it is evident that a 30 nm NbC particle

together with Fe/Cr precipitate, appears together with the single precipitate of Fe/Cr carbide, which is also around 30 nm. These pretty small particles can be ignored since they have no influence to the properties of N#. In the steel of NT#, most N is occupied by Ti, and the nitrides of Nb are found attached to TiN. The formation of Fe/Cr carbide is related to the annealing process, which is not able to dissolve all Fe/Cr carbides during such a short annealing time. However, such a small particle will not influence the final properties of the studied NT#.

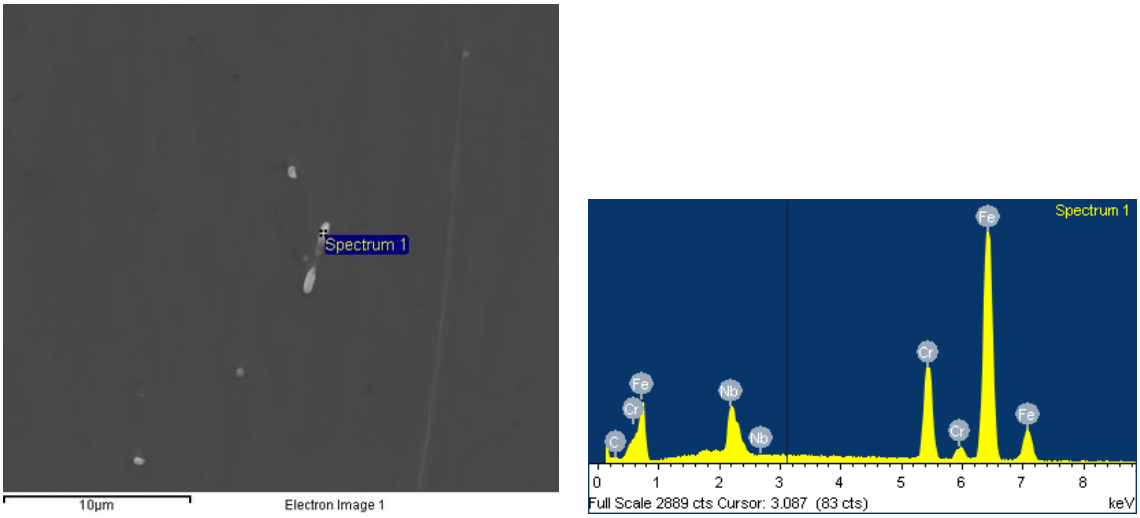

(a) (b)

Figure 4-6 SEM images and EDS analyses of precipitates for Nb-stabilised steel: (a) SEM image and (b) EDS analysis of precipitate.

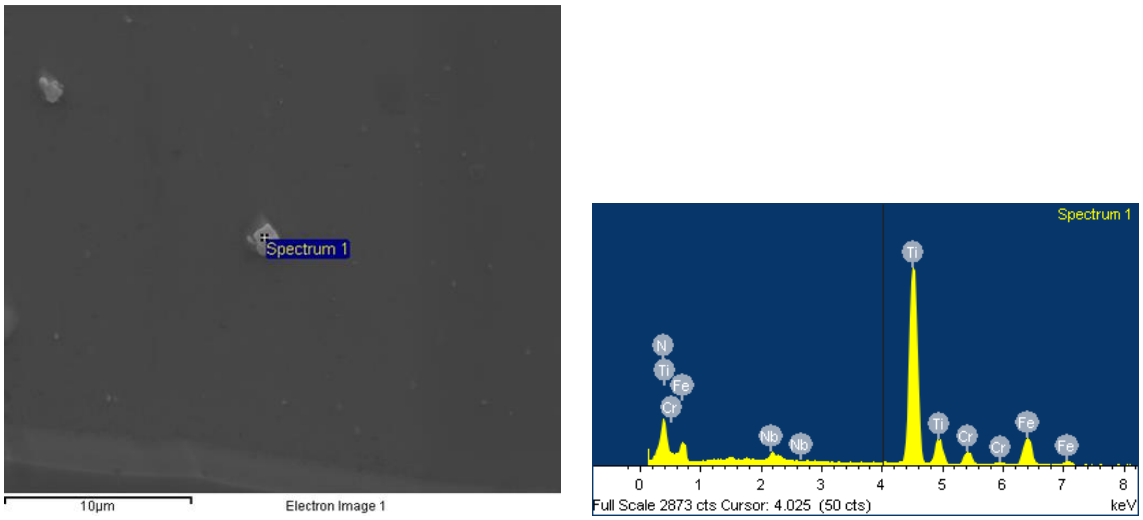

(a) (b)

Figure 4-7 SEM images and EDS analyses of precipitates for (Nb + Ti)-stabilised steel: (a) SEM image and (b) EDS analysis of precipitate.

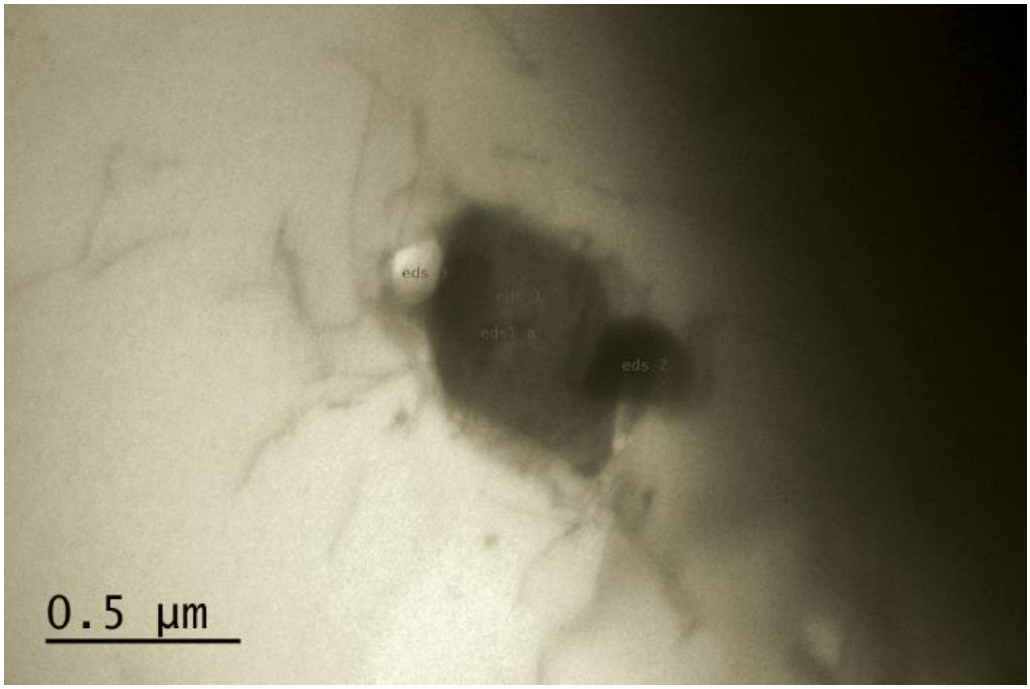

(a)

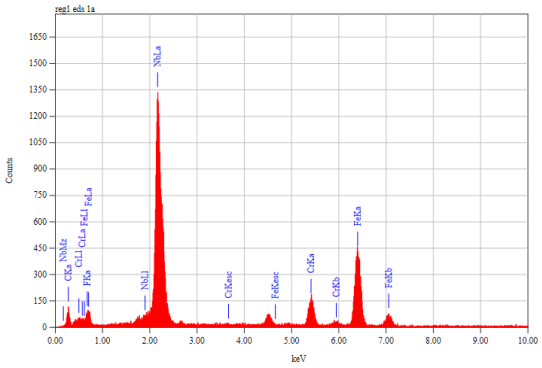
reg1 eds 1a
Counts
keV
NbLa
CrKa
CrLl
FeLl
FeLa
NbMz
FKa
NbLl
CrKesc
FeKesc
CrKa
CrKb
FeKa
FeKb

(b)

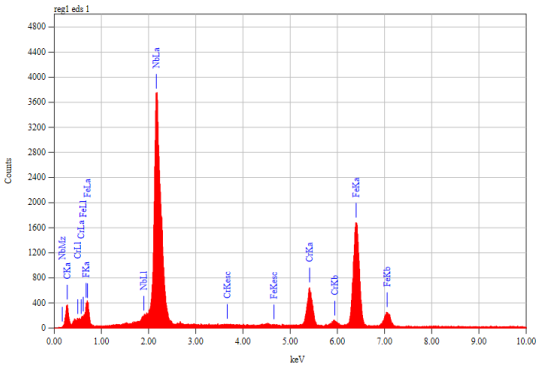
reg1 eds 1
Counts
keV
NbLa
CKa
NbMz
CrLl
CrLa
FeLl
FeLa
FKa
NbLl
CrKesc
FeKesc
CrKa
CrKb
FeKa
FeKb

(c)

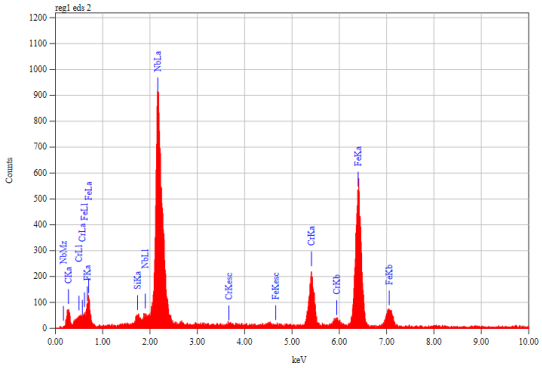
reg1 eds 2
Counts
keV
NbLa
CKa
NbMz
CrLl
CrLa
FeLl
FeLa
FKa
SiKa
NbLl
CrKesc
FeKesc
CrKa
CrKb
FeKa
FeKb

(d)

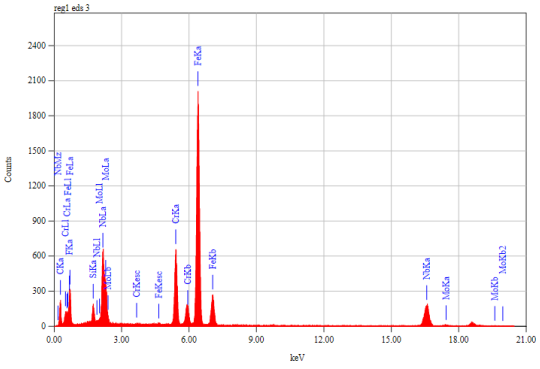
reg1 eds 3
Counts
keV
FeKa
NbMz
FeLl
FeLa
CrLl
CrLa
FKa
MoLl
MoLa
NbLa
NbLl
CKa
SiKa
NbKesc
OKesc
FeKesc
CrKa
CrKb
FeKb
NbKa
MoKa
MoKb
MoKb2

(e)

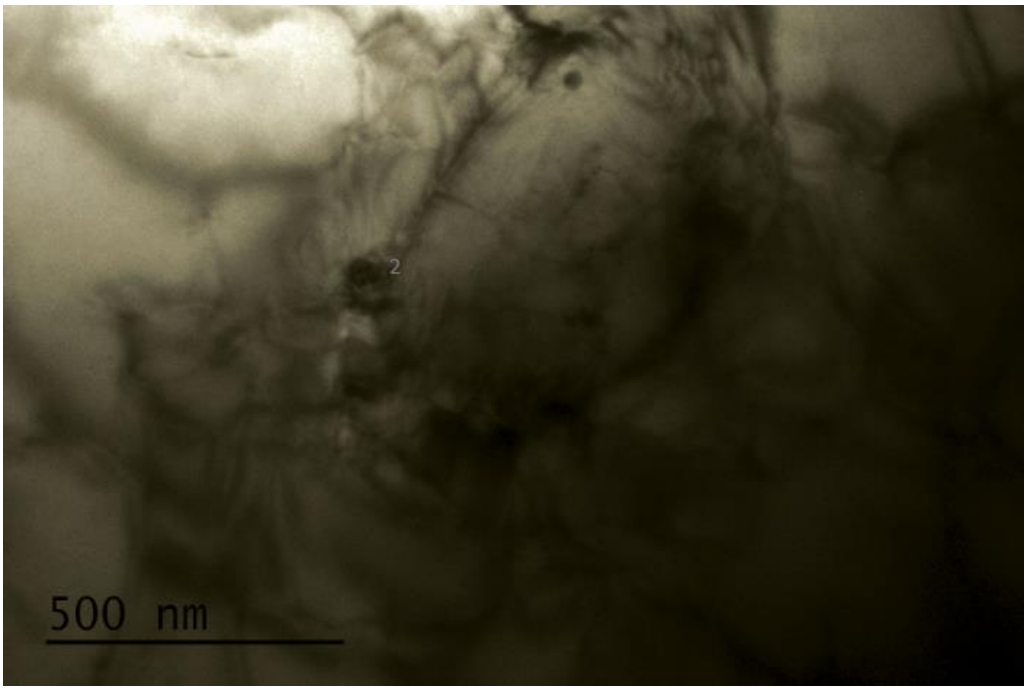

(f)

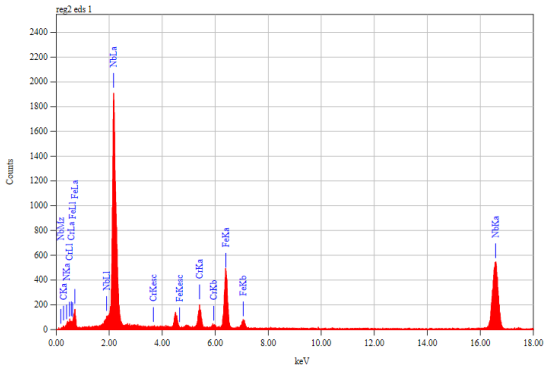

(g)

Figure 4-8 TEM images and EDS analyses of precipitates for Nb-stabilised steel: (a) TEM images of precipitates 1-1a, 1-1, 1-2, 1-3 and (b)(c)(d)(e) EDS analyses of precipitates 1-1a, 1-1, 1-2, 1-3; (f) TEM image of precipitate 2-1 and (g) EDS analysis of precipitate 2-1.

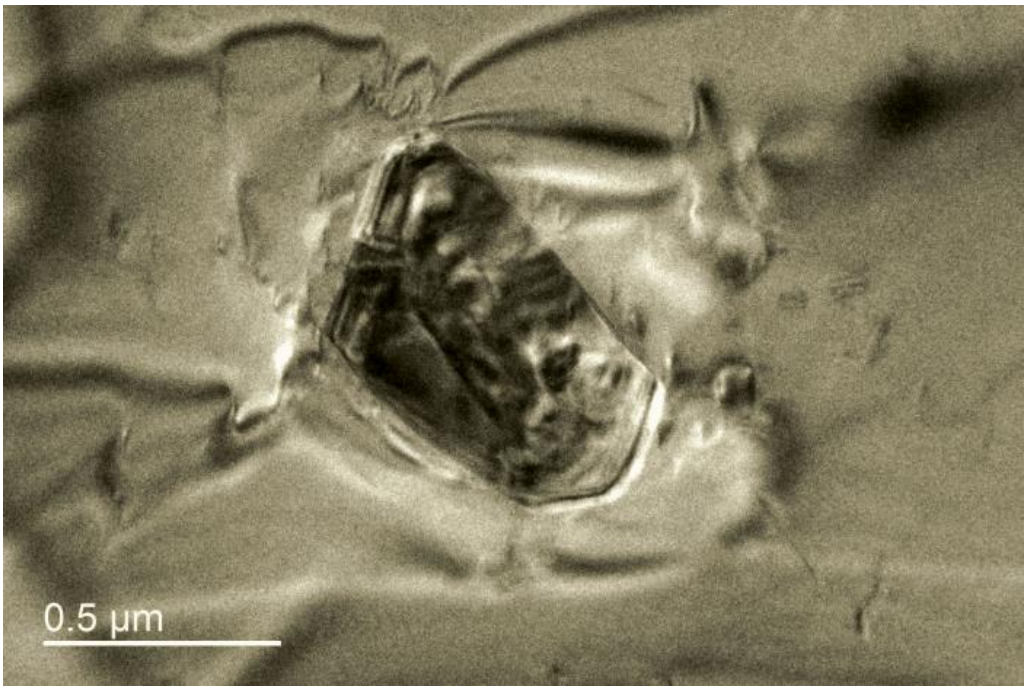
0.5 µm

(a)

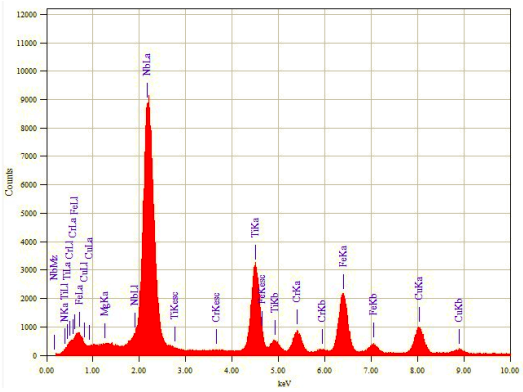
Counts
keV
NbLa
TiKa
FeKa
CuKa
NbMz
NKa
TiLl
TiLa
CrLl
CrLa
FeLl
FeLa
CuLl
CuLa
MgKa
NbLl
TiKesc
CrKesc
FeKesc
TiKb
CrKa
CrKb
FeKb
CuKb

(b)

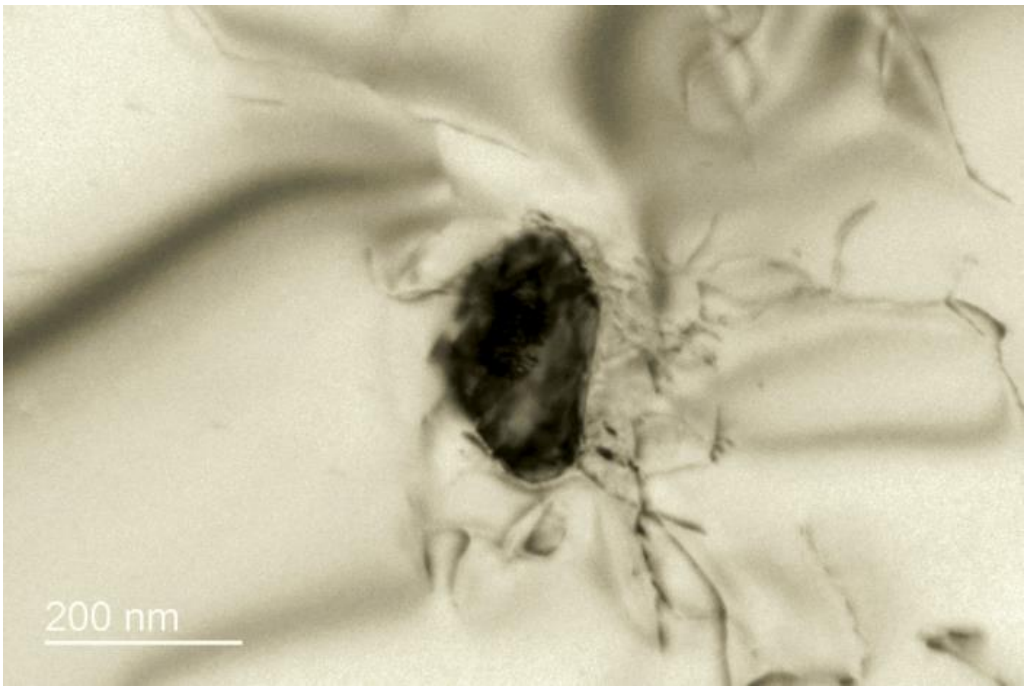
200 nm

(c)

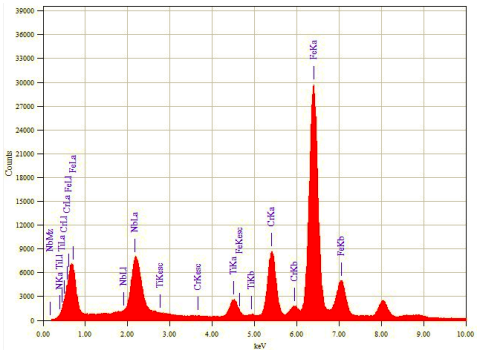
Counts
keV
NbMz
NKa
TiLl
TiLa
CrLl
CrLa
FeLl
FeLa
NbLl
NbLa
TiKesc
CrKesc
TiKa
FeKesc
TiKb
CrKa
CrKb
FeKa
FeKb

(d)

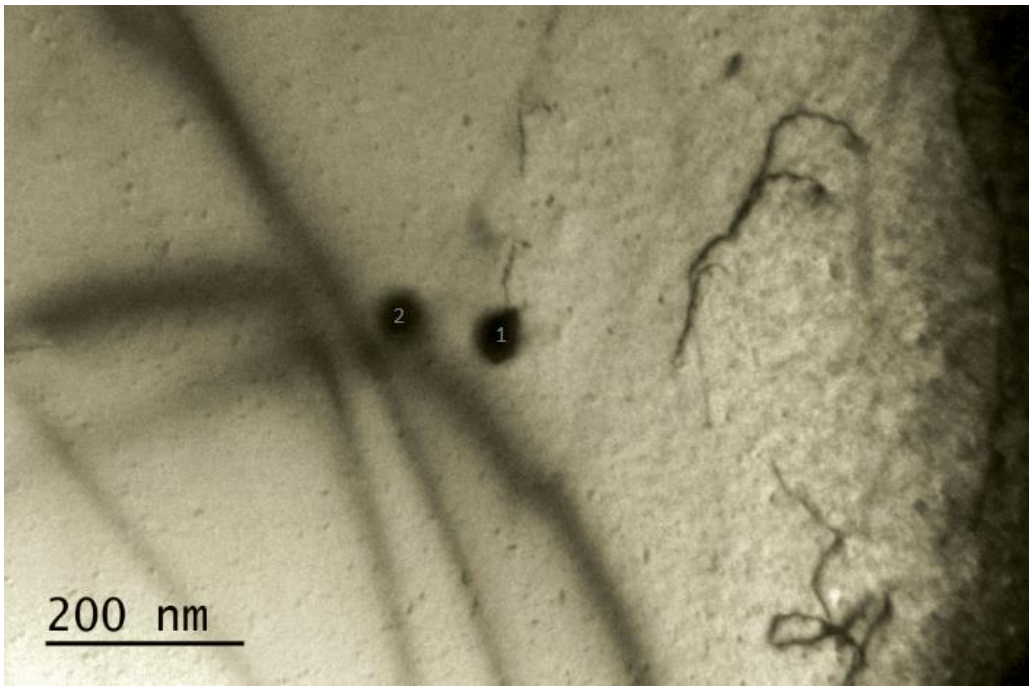

(e)

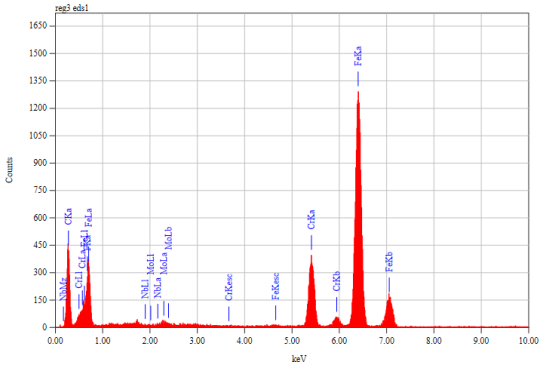

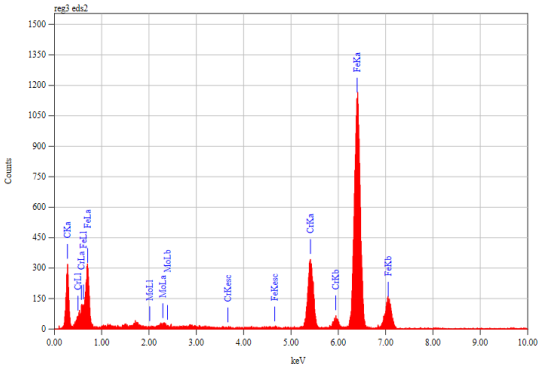

(f) (g)

Figure 4-9 TEM images and EDS analyses of precipitates for (Nb + Ti)-stabilised steel: (a)(c) TEM images of precipitates (Ti,Nb)N and (b)(d) EDS analyses of precipitates (Ti,Nb)N; (e) TEM images of precipitates 3-1, 3-2 and (f)(g) EDS analyses of precipitates 3-1, 3-2.

4.3.3. Orientation map and misorientation distribution

In the orientation maps of N# and NT# (**Figure 4-10**(a) and (d)), it can be seen that the volume fractions of grains with three orientations are random, no matter what type of microalloying is applied. That means there is no dominant orientation in either steel alloy design. The low-angle boundaries (LABs) ($2° < LAB < 15°$) [164] and the high-angle boundaries (HABs) ($HAB > 15°$) are depicted as black and red lines respectively in **Figure 4-10**(b) and (e). It is well acceptable that the grain boundaries of both N# and NT# are composed predominantly of HABs with very few LABs. And the misorienation-angle distributions for N# and NT# demonstrate that the misorientation angles between uncorrelated grains are similar, which are close to a random status (**Figure 4-10**(c) and (f)).

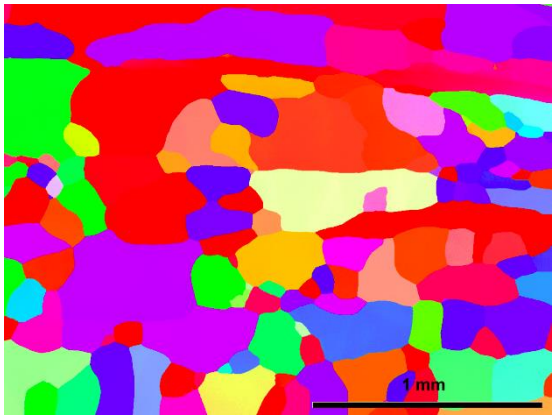

(a)

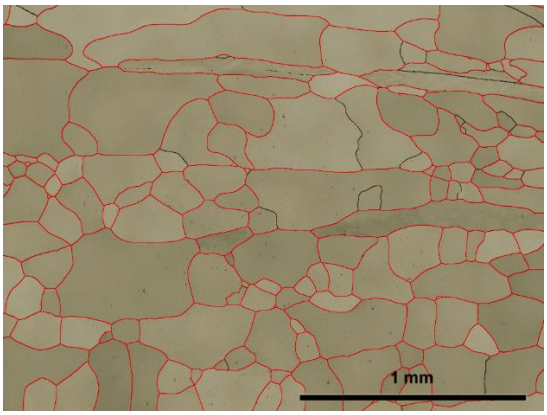
1 mm

(b)

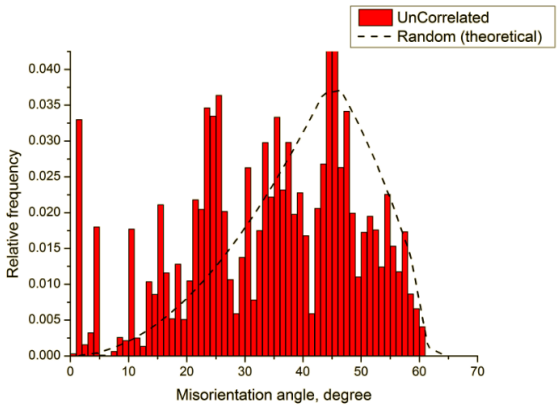
UnCorrelated
Random (theoretical)
Relative frequency
0.040
0.035
0.030
0.025
0.020
0.015
0.010
0.005
0.000
0
10
20
30
40
50
60
70
Misorientation angle, degree

(c)

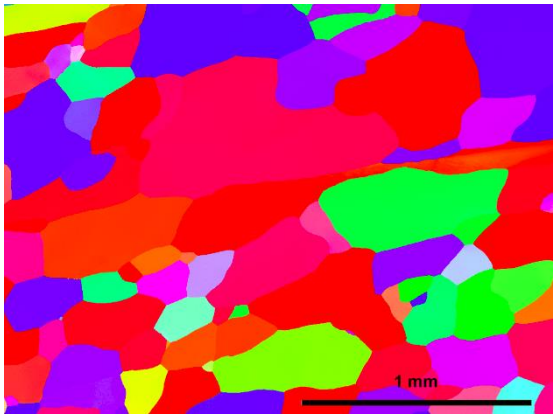
1 mm

(d)

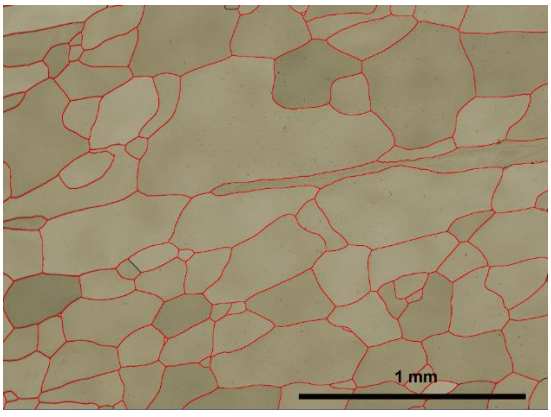
1 mm

(e)

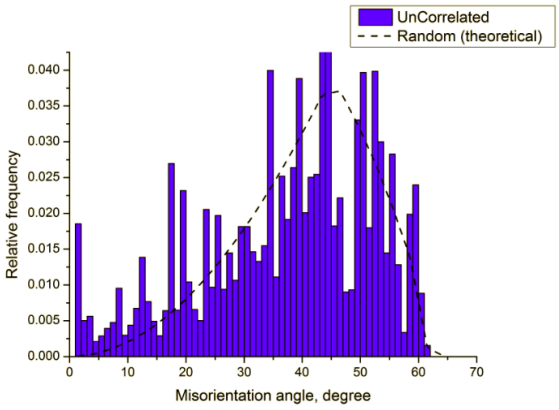
UnCorrelated
Random (theoretical)
Relative frequency
0.040
0.035
0.030
0.025
0.020
0.015
0.010
0.005
0.000
0
10
20
30
40
50
60
70
Misorientation angle, degree

(f)

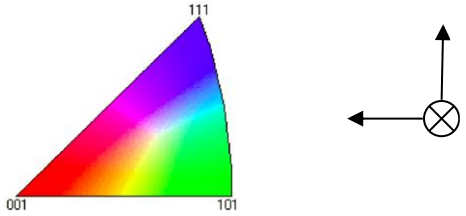

(g)

Figure 4-10 Orientation maps and misorienation-angle distributions of studied steels (RD: rolling direction; ND: normal direction; TD: transverse direction): (a)(b)(c) Nb-stabilised steel; (d)(e)(f) (Nb + Ti)-stabilised steel; (g) appendix.

4.3.4. Grain boundary character distribution (GBCD)

The results of GBCD for two studied steels are displayed in **Figure 4-11**. Three groups of grain boundaries, involving LABs, Σ3 ~ Σ29 and random boundaries, are similar for two studied steels. LABs and Σ3 ~ Σ29 for two steels are 3.93% (N#), 2.95% (NT#) and 4.37% (N#), 4.03% (NT#), respectively. For low-Σ CSLBs (**Figure 4-12**), the LABs (Σ1) and some special grain boundaries (Σ3 and Σ5) appear in high frequency, comparatively. For Σ3, two studied steels acquire 0.86% and 1.29%, and for Σ5, 0.36% and 1.20%, respectively.

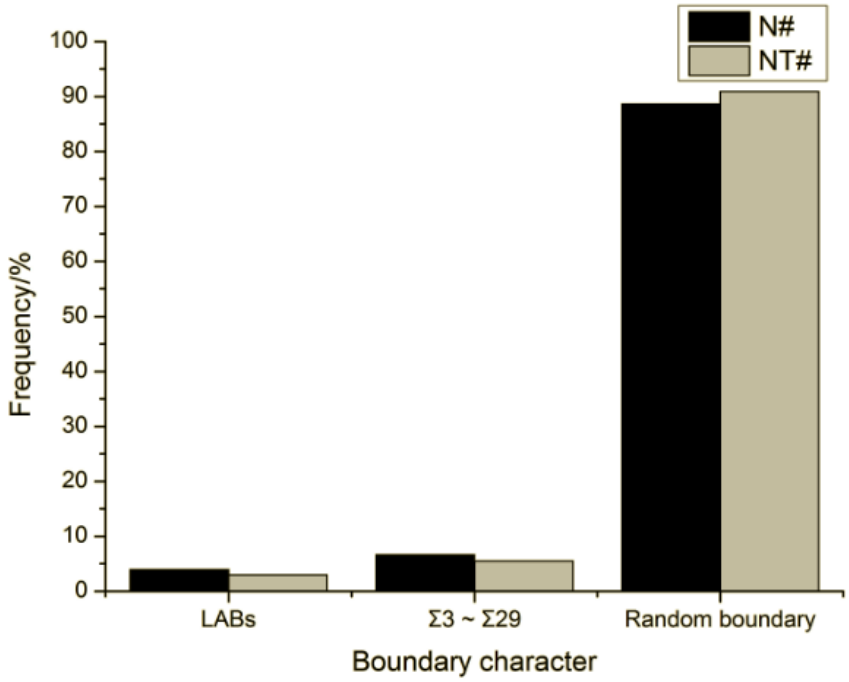

Figure 4-11 GBSD results of Nb-stabilised and (Nb + TI)-stabilised steels.

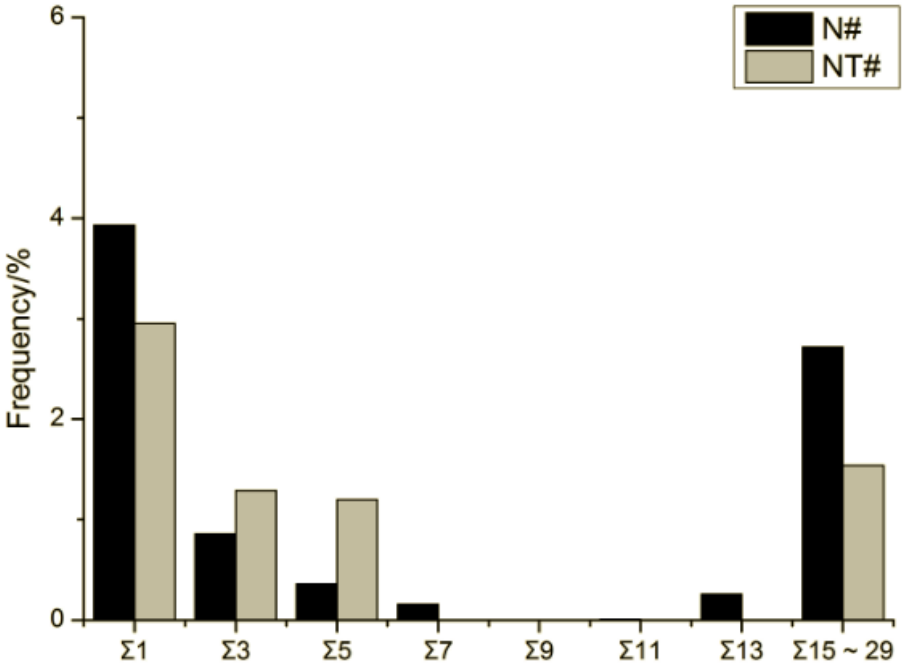

Figure 4-12 Low-Σ CSLB distributions of Nb-stabilised and (Nb + Ti)-stabilised steels.

4.3.5. Tensile strength

Table 4-3 displays the tensile strength properties of N# and NT# specimens measured at room temperature. It is clear that their YS values are similar. Meanwhile, the values of UTS for N# are a little higher, i.e. by 4.3 MPa, in comparison with NT#. And by contrast, the elongations are a little lower, i.e. by 5.4%. The tensile strength properties are comparatively stable from **Table 4-3**, and the values of UTS and elongation are very close to the average results except YS of N#.

Table 4-3 Tensile properties of studied 18Cr-2Mo steels.

Steel no.	YS (MPa)	Average YS (MPa)	UTS (MPa)	Average UTS (MPa)	Elongation (%)	Average Elongation (%)
N#	336.45 346.88	341.7	485.20 487.06	486.1	26.37 24.80	25.6
NT#	342.55 339.90	341.2	483.39 480.29	481.8	32.45 29.62	31.0

4.3.6. Impact toughness

Figure 4-13 shows the impact toughness values of N# and NT# tested from -40 to 40 ℃. For each FSS grade, the drop of impact values occurs predominantly when the testing temperature is reduced to a low degree. Comparatively, N# possesses superior toughness

since almost its toughness at each testing temperature in the range of -40 ~ 40 ℃ is higher than that of NT#. However, N# still has not reached its DBTT value due to its unstability in toughness even at the highest 40 ℃.

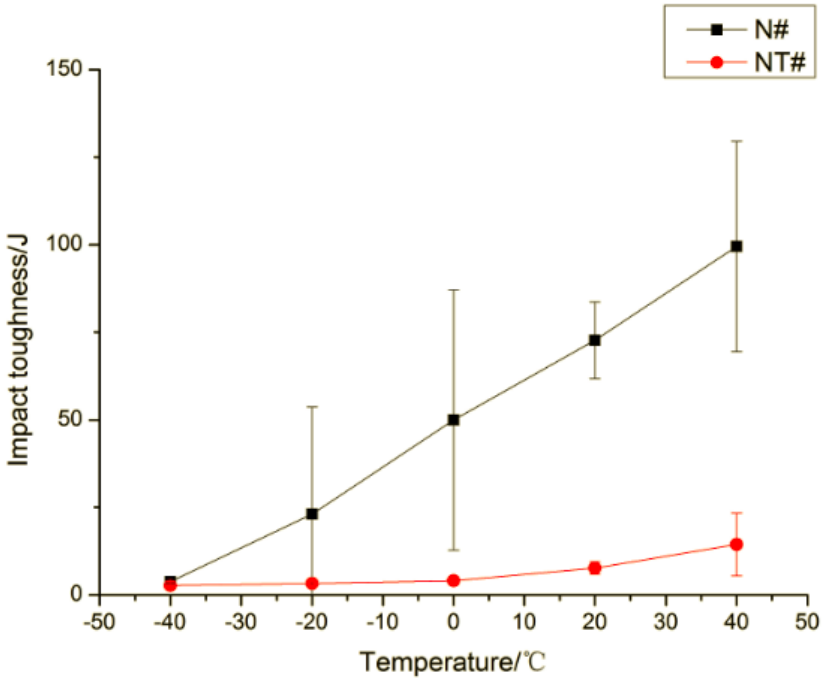

Figure 4-13 Charpy impact values of Nb-stabilised and (Nb + Ti)-stabilised steels from -40 to 40 ℃.

The fracture surfaces of N# and NT# were analysed using the instrument of SEM, exhibited in **Figure 4-14** and **Figure 4-15**. The specimens impacted between -40 and 40 ℃ were cleaned and observed. When impacted at 40 ℃, the fractographs of N# (**Figure 4-14**(b) and (c)) present a mixed ductile/brittle fracture mode, which comprises both flat facets and plastic deformed dimples. Due to the mixed structure, the impact energy of N# at 40 ℃

expressed unstability. Especially in the fracture surface of **Figure 4-14**(c), both shear cracks and holes can be observed, which illustrates the transition situation of the impacted specimen. When the impacting temperature is decreased to 0 ℃, the mixed structures (**Figure 4-14**(e) and (f)) still exist, the difference is that the flat facets turn smoother, and the holes of the deformed dimples are larger and shallower, which expresses the lower impact energy compared to 40 ℃. When tested at -40 ℃, the facture surface turns pure river-like (**Figure 4-14**(h)), which consists of smooth flat facets and shear cracks, and implies lower impact toughness of specimen. For NT#, the surface fractures from being impacted at different temperatures are alike (**Figure 4-15**(b), (d) and (f)), i.e. flat facets, which indicate the brittleness of all the specimens. The results of surface fractures are coincident with the impact values, shown in **Figure 4-13**.

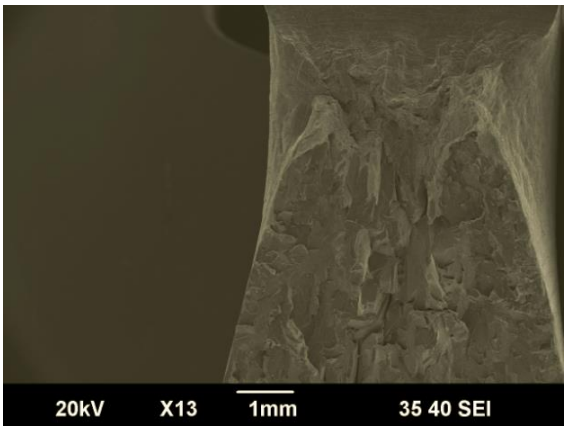

(a)

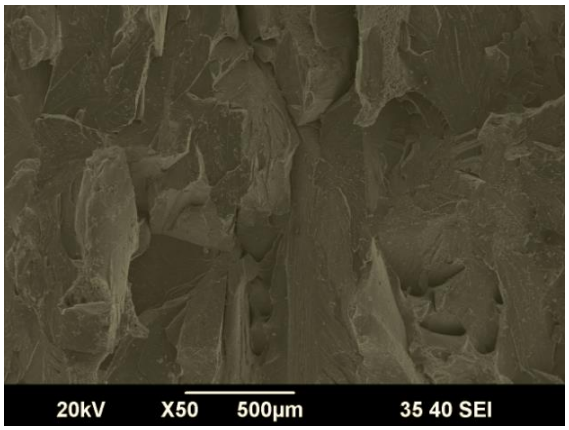
20kV X50 500µm 35 40 SEI

(b)

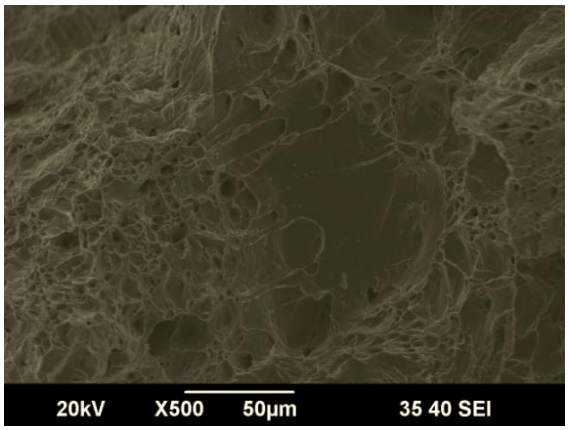
20kV X500 50µm 35 40 SEI

(c)

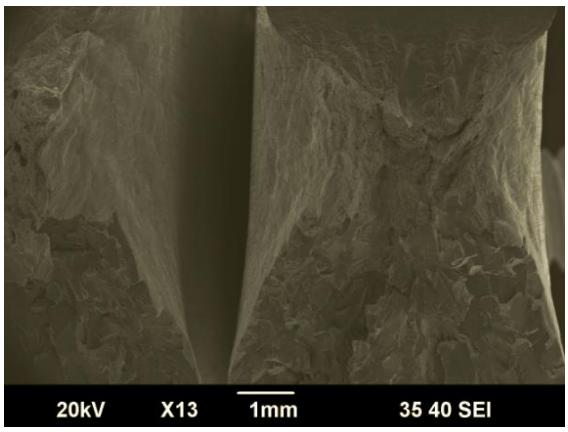
20kV X13 1mm 35 40 SEI

(d)

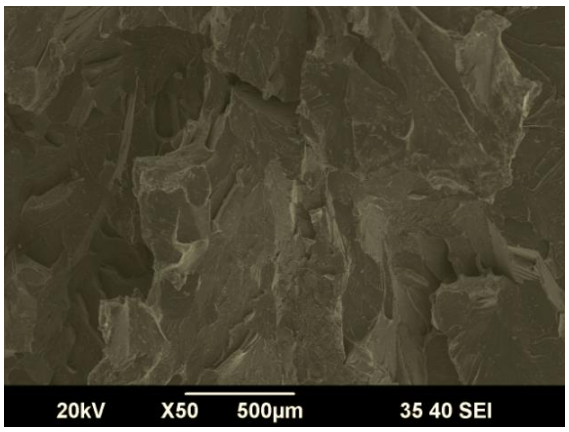
20kV X50 500µm 35 40 SEI

(e)

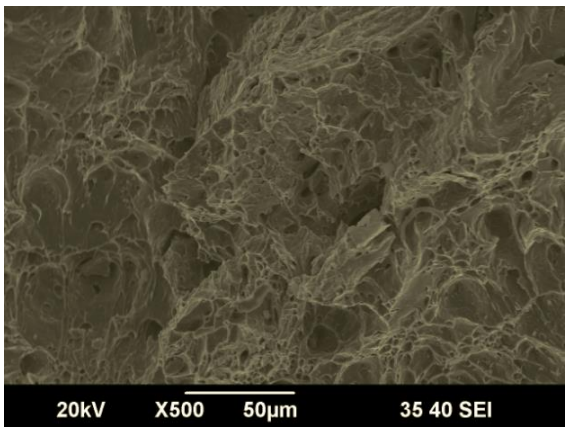
20kV X500 50µm 35 40 SEI

(f)

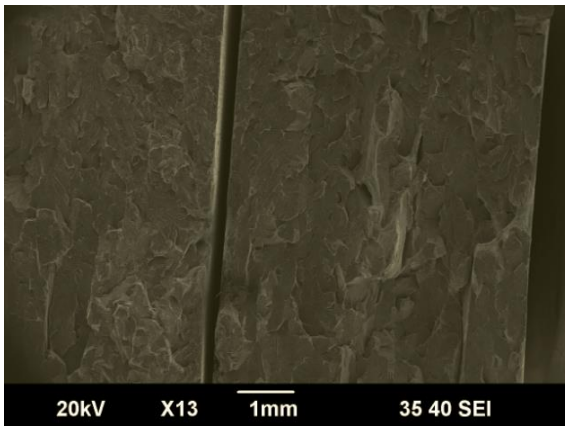

(g)

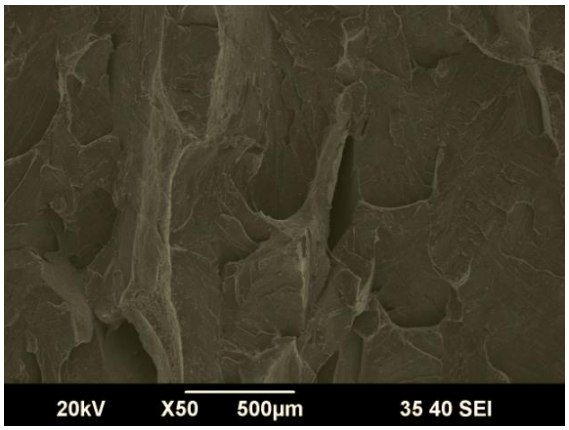

(h)

Figure 4-14 Overall fracture appearances of Nb-stabilised specimens impacted at: (a) 40 ℃; (d) 0 ℃; (g) -40 ℃ and SEM fractographs of Nb-stabilised specimens impacted at: (b)(c) 40 ℃; (e)(f) 0 ℃; (h) -40 ℃.

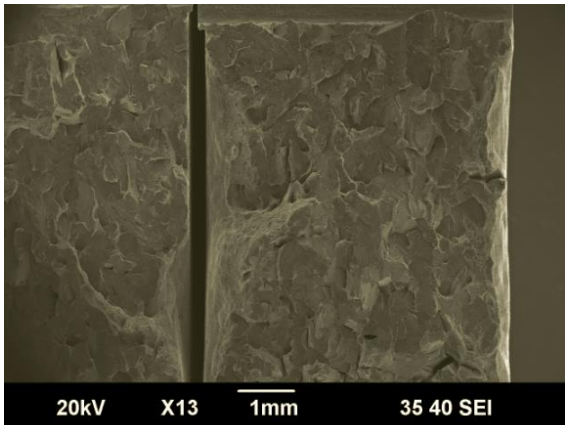

(a)

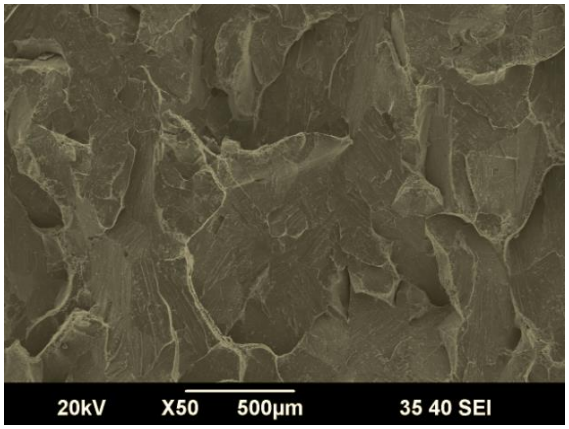

(b)

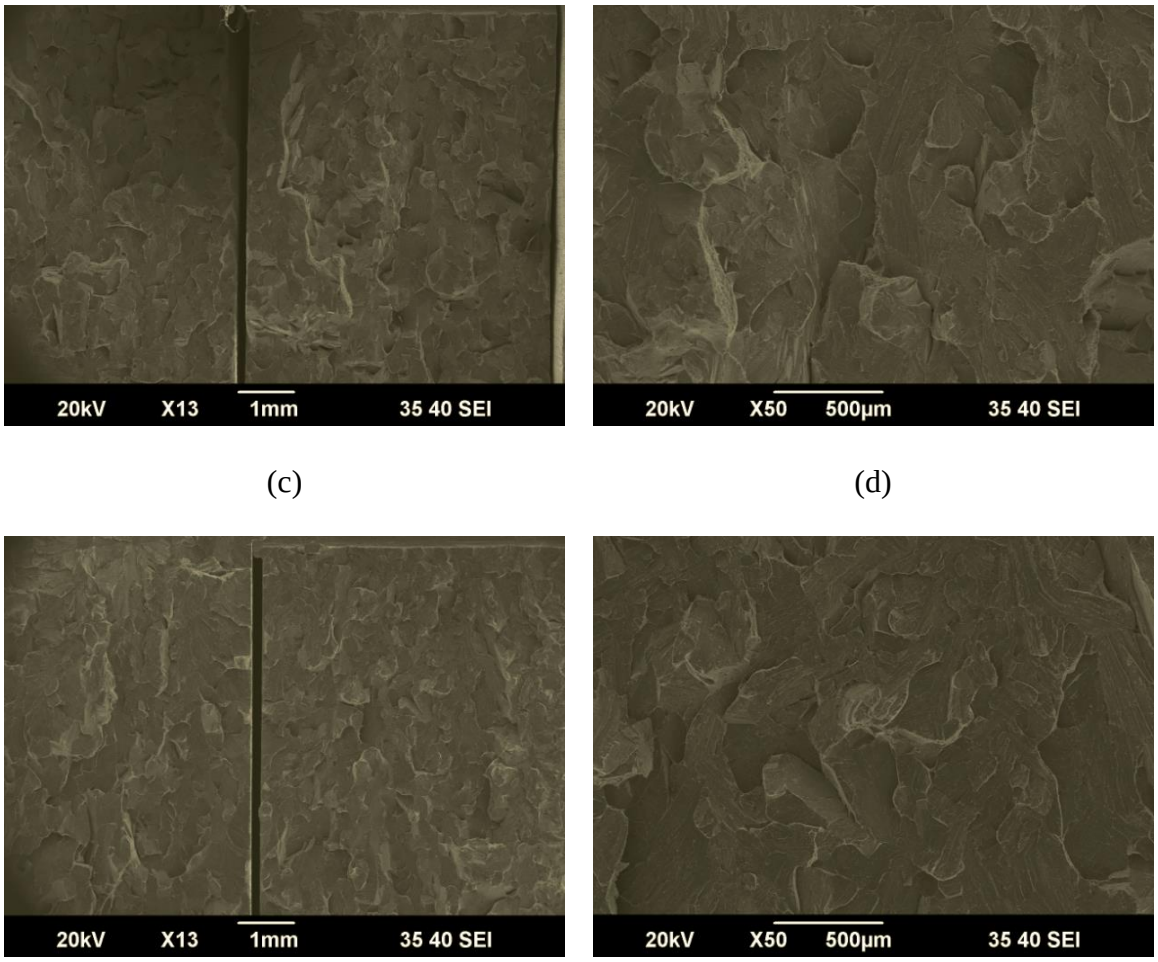

Figure 4-15 Overall fracture appearances of (Nb + Ti)-stabilised specimens impacted at: (a) 40 ℃; (c) 0 ℃; (e) -40 ℃ and SEM fractographs of NT# specimens impacted at: (b) 40 ℃; (d) 0 ℃; (f) -40 ℃.

4.4. DISCUSSION

4.4.1. Microstructure

For the studied steels N# and NT# that acquire a single ferrite microstructure, the grain size is the key point related with the properties besides the precipitation situations. Several factors determine the final ferrite grain size. Firstly, the homogenisation progress of two steels is not sufficient due to their low reduction and short annealing time; secondly, microalloying is the vital factor that decides the grain size since it is able to be used to control the precipitates, which distribute at and along the grain boundary. However, the control of grain size possibly occurs under the following conditions: the precipitation should generate at high temperature, the duration in the process of high temperature should be long enough for resisting the grain sizes. Certainly, there are still some effective methods to modify grain size besides microalloying, for example, thermomechanical processing, viz. controlled rolling, heat treatment, etc. [48], which will be investigated in **Chapter 6**. Based on **Figure 4-4**, the average grain size for N# is smaller than that of NT#. Based on **Equation 2-6** and Paton's instance [39], the grain refinement is beneficial to the toughness properties of the studied steel. This conclusion can be related to the extension path of the crack generated during impact testing. The fine gain is beneficial to resist the spread of the crack effectively in this case.

It is well understood that Nb and Ti are both strong forming elements of carbide and nitride, however, the precipitation behaviours of second phases are complicated and mainly dependent on the liquid/solid condition, the solid solubility, the effect of other elements

[106]. It is already made clear that: (1) TiN forms above the liquidus, which is extremely stable and only dissolve at very high temperature (shown in Figure 2-28). Thus, for NT#, TiN is confirmed to form at first; (2) below the liquidus, the reported precipitation order according to temperature is NbN, TiC, NbC [26], but for different composition systems and manufacturing processes, the precipitation situation will be changed.

4.4.2. Grain boundary (GB)

As the interactional results of the polycrystal grains, the structures of GBs are determined by grain character and orientation. Meanwhile, the types and distributions of GBs are influenced by the misorientation of the grains. It has been well established that GB plays an important role as the preferential site for metallurgical phenomena [121, 126]. Theoretically, the large fraction of low-energy boundaries (low-Σ CSLBs) is positive to its properties due to less purity or solute segregation, lower diffusivity, higher resistance to grain boundary sliding and crack nucleation and propagation compared to general boundaries (random boundaries). Among the low-Σ CSLBs, the contribution of Σ1 and Σ3 boundaries to property improvement was found to be prominent [164]. A higher frequency of random boundaries can bring about a dominant intergranular fracture. In other words, intergranular brittleness occurs when random boundaries occupy a large fraction [165]. For the two studied steels, the frequencies of low-energy boundaries for N# and NT# are 11.4% and 9.1%, respectively. The whole fractions of Σ1 and Σ3 are similar, i.e. 4.79% and 4.24%. Separately, the ratio of Σ1 for N# is 0.98% higher than that of NT#, and meanwhile Σ3 is

0.84% lower. Furthermore, the percentage of random boundaries for N# (88.6%) is lower than that for NT# (90.9%). Regarding GB, for N#, the improvement of impact toughness may be benefited by the allocation of low-energy boundaries and random boundaries to some degree.

4.4.3. Tensile strength and impact toughness

Besides the increase of impact property that fine grain size brings about to the metal, it also leads to the increase of strength. However, N# does not express the apparent advantage in strength. That should be two reasons to explain this phenomenon. Firstly, the homogenisation of grains for N# and NT# is not good, which can cause different strengthening effects in the steel itself. Then, besides grain refinement, there are other factors that determine the final strength of the studied steels, such as dispersion strengthening of precipitation, solution strengthening of the elements of Nb and Ti. However, the strengthening mechanisms for N# and NT# are supposed to be interactive ones of several factors. Although with more Nb and fine grain size, N# only obtains 5 MPa higher in UTS and even 5% loss in elongation.

The influences of GBs on the mechanical properties of the studied steels are confirmed, however, the effectiveness should be not very evident based on the character results of both steels' GBs.

At present, it is accepted that the coarse precipitates, such as TiN, result in a loss of toughness [166]. Big TiN particle forms in the liquid, and sometimes precipitation of NbN attaches itself on the surface of TiN (C can be ignored since the count of C is very low in EDS). (Ti,Nb)N or TiN particles with the sizes of 1.5 ~ 3 μm have been found in the annealing steels impacted at the temperature ranged from -40 to 40 ℃. These big particles are associated with the initiation of brittle fracture [51, 89, 90], which leads to the loss of impact toughness for NT#. **Figure 4-16** reveals the found precipitate (Ti,Nb)N/TiN locating at the initiation of cleavage fractures, which testifies the negative influence of large particle and can be regarded as inclusions in the steels. Three critical steps are involved in a big particle, i.e. (Ti,Nb)N/TiN initiated cleavage fracture process, i.e. the microcrack nucleates at the big particle; the microcrack penetrates the matrix across the particle-matrix interface and grows into a grain-sized crack; the grain-sized crack continues to propagate across the grain boundaries and becomes unstable, resulting in cleavage fracture [91]. This point can be taken into account regarding the toughness comparisons of the studied steels.

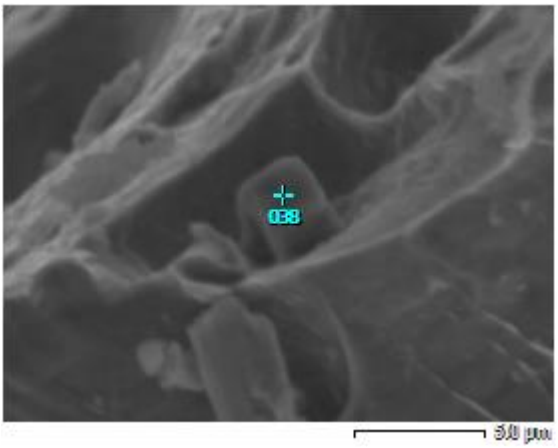
038
50 µm

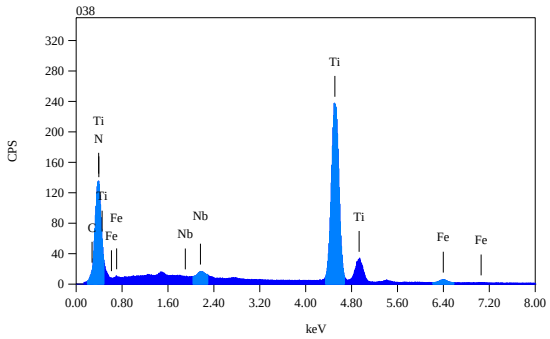
038
CPS
keV
Ti
N
Fe
Nb
0.00
0.80
1.60
2.40
3.20
4.00
4.80
5.60
6.40
7.20
8.00

(a) (b)

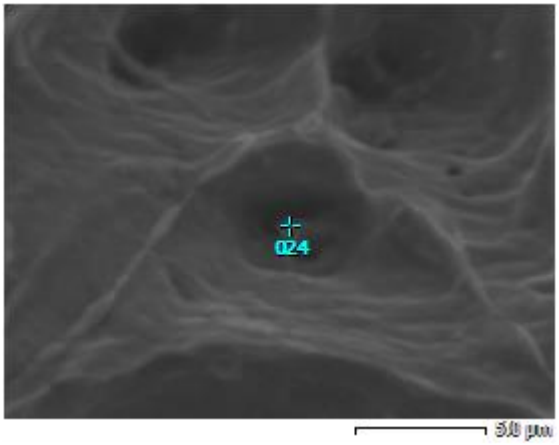
024
50 µm

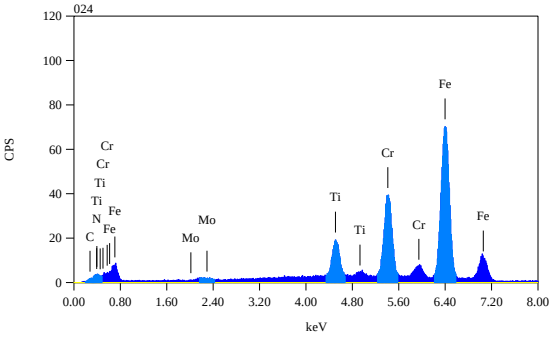
024
CPS
keV
Cr
Ti
N
C
Fe
Mo
0.00
0.80
1.60
2.40
3.20
4.00
4.80
5.60
6.40
7.20
8.00

(c) (d)

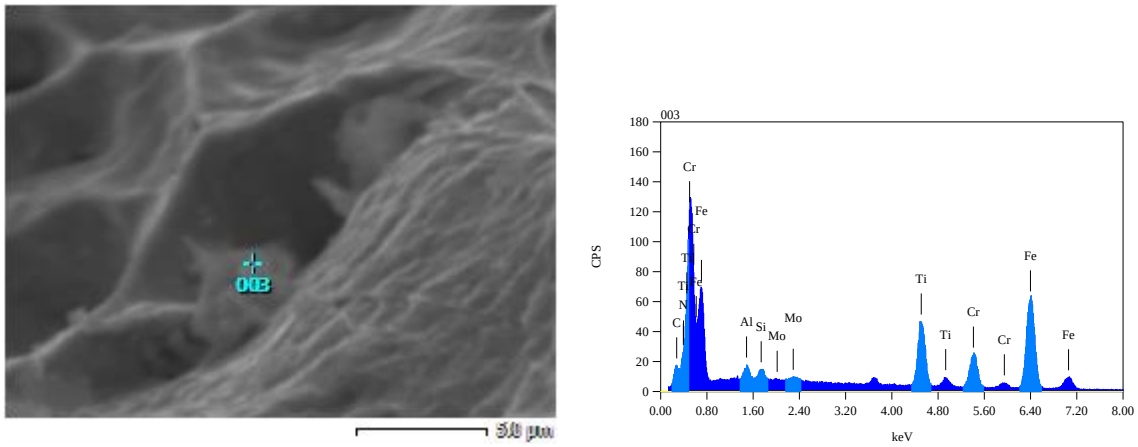

(e) (f)

Figure 4-16 (Ti,Nb)N/TiN particles appearing at initiation of cleavage fractures and corresponding EDS analyses for (Nb + Ti)-stabilised specimens impacted at: (a)(b) 40 ℃; (c)(d) 0 ℃; (e)(f) -40 ℃.

With respect to the phenomenon that the toughness values for N# at 40 ℃ are not stable, several possibilities aroused by the nonuniform of the steel may be considered: (1) The irregular distributions of inclusions and precipitates may influence the scattered generation of microcracks, which grow into grain-sized cracks during penetrating. (2) The inhomogeneous grain sizes may influence a variety of propagation paths of grain-sized crack. For instance, for the regions that grains are smaller, cracks meet with the larger resistance from GBs.

In respect of the nucleation and growth of the (Ti, Nb)N/TiN particles, it is indeed that the existing coarse particles are detrimental to the toughness of the studied 18Cr-2Mo stainless

steel. As it is mentioned, TiN forms above the liquidus, which is extremely stable and only dissolve at very high temperature. The formation of TiN in the liquid phase can increase the density of nucleation sites [167]. Some researchers have investigated the precipitation in (Nb + Ti)-stabilised steel, depending on the Ti lever, as much as 90% of the total Nb may remain in solid solution [168]. Then, Nb is prone to attaching on the surface of TiN particle, which is described in **Figure 4-17** [36]. From **Figure 4-16**, it is evident that the sizes of TiN particles are in some range. Although the fine (Ti, Nb)N/TiN particles have not been found under microscope, they are supposed to exist, which do not influence the toughness of the studied steels.

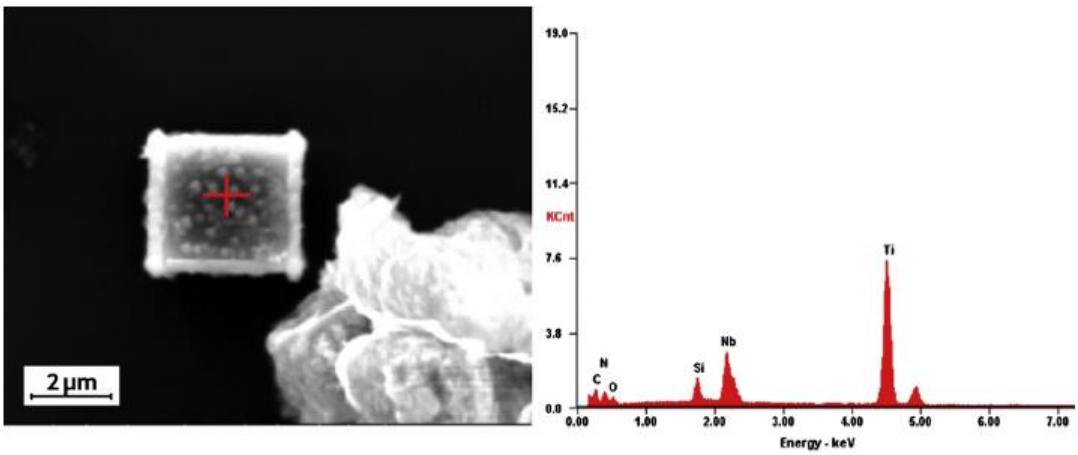

Figure 4-17 SEM and EDS of (Ti, Nb)N particle: (a) micrographs of precipitates; (b) EDS of precipitates.

4.5. CONCLUSIONS

The effects of microalloying on the microstructure and grain boundary of 18Cr-2Mo FSS grades stabilised by Nb and (Nb + Ti) were investigated. The connection between Ti addition and mechanical properties was discussed. The following conclusions can be drawn:

(1) For Nb and (Nb + Ti) stabilised 18Cr-2Mo FSS grades, the grain sizes exist the difference of around 50 μm, which does affect the mechanical properties of the studied steels, especially impact toughness. The strength result of N# that influenced by inhomogeneous grain sizes is only 5 MPa higher in UTS.

(2) For N#, NbC and Nb(C,N) are the main precipitates, however for NT#, primary precipitates are (Ti,Nb)N/TiN, NbC. The addition of Ti can modify the precipitation behaviour of Nb composition system, especially the formation of TiN particle.

(3) Ti addition degrades its toughness properties due to the large (Ti,Nb)N/TiN particles, which usually initiate the cleavage fracture process. Therefore, Ti is not an adaptable element for stabilising 18Cr-2Mo FSS thick plate, to which high impact toughness is needed.

(4) The microalloying of Nb and (Nb + Ti) has not brought about the modification of grain boundary a lot. For these two studied steels, the grain boundaries are almost same, which

means that GBCD is not the main factor related to ultimate mechanical properties of 18Cr-2Mo FSS grades.

Based on the above results, the element of Nb for stabilising FSS appears to be more suitable to the mechanical properties, i.e. strength and impact toughness, in this study. Meanwhile, the effects of manufacturing parameters, such as hot rolling reduction and processing optimisation, are also essential to microstructure and mechanical properties of 18Cr-2Mo FSS thick plates, which are discussed in the following chapters.

5. MICROALLOYING WITH (NB+V)/(NB+V+TI)

5.1. INTRODUCTION

In this chapter, Ti was added to (Nb + V) stabilised 18Cr-2Mo ferritic stainless steel (FSS) thick plates to further investigate the role of microalloy additions on microstructure and mechanical properties of purified FSS thick plate. It is already mentioned previously that the detrimental effect of interstitials may be controlled by the addition of stabilising Nb, Ti and V, which are able to form strong carbides and nitrides. V is added to the studied steels instead of part Nb since V has a strong tendency to form carbide and nitride, which can disperse V precipitates at the specific temperatures [106]. These advantages of V are beneficial for the development of FSS thick plate.

For these frequently used stabilising elements, Nb is usually a good stabiliser since it is beneficial to most mechanical properties. Whereas, the addition of Ti can degrade toughness due to the formation of large TiN particles that initiate the cleavage fracture process [169] based on the results in **Chapter 4**. V is helpful to strength due to its effect of solution strengthening, which can compensate the strength loss arising from low C and N contents. Meanwhile, it has also been reported that the benefit is obtained in impact toughness by the addition of V, which is probably associated with the removal of coarse Cr carbonitrides from the grain boundary [106]. Therefore, the alloy design of V addition aims

at increasing mechanical properties, especially toughness, which is beneficial to extensive application of this grade in industry. However, for (Nb + V) and (Nb + V + Ti) composition systems, the relationship between precipitation and toughness needs further systematic investigation.

For (Nb + V) stabilised FSS, Nb and V are both strong forming elements of carbide and nitride, whereas, the precipitation evolution is dependent on various factors, such as liquid/solid condition, solid solubility, influences of other elements [106]. For (Nb + V + Ti) stabilised FSS, the related literatures are seldom found, which also increases the meaning to study in this chapter.

5.2. EXPERIMENTS

5.2.1. Materials

The manufacturing procedures of the materials used in this study were displayed in **Chapter 3.2.1**, and the designed size of the hot rolled plate is 40 mm × 250 mm × 200 mm (thickness × width × length). After being heated at 1130 ℃ for 240 min, the 40 mm forged plate was hot rolled into 6 mm plate (the rolling reduction is around 85.0%) during the temperature range of 850 ~ 1100 ℃. After that, this plate was annealed at 950 ℃ for 30 min, followed by cooling in air. The manufacturing procedures in this research are a little different compared to that in **Chapter 4**, aiming at a best condition of the studied steels.

The chemical composition of the 18Cr-2Mo steels measured is listed in **Table 5-1**. The stabilisation ratios of NV# and NVT# are 19.1 and 21.2, respectively, which are calculated by interstitial elements divided by stabilising elements, shown in **Equation 2-7**. The results mean both steels have good properties of intergranular corrosion resistance.

Table 5-1 Chemical composition (in wt.%) of studied steels.

Steel no.	C	Si	Mn	Cr	Mo	Nb	V	Ti	N	Fe
NV#	0.0047	0.093	0.090	17.83	1.81	0.15	0.14	-	0.0105	Bal.
NTV#	0.0046	0.080	0.081	17.95	1.78	0.15	0.11	0.05	0.0101	Bal.

Comparisons of N# and NT# have been introduced in **Chapter 4**, the contents of (C + N) of NV# and NVT# are even lower, especially C, which means these two steels are comparatively more purified than the steels studied in **Chapter 4**. For FSS grade, this may be beneficial to properties, especially impact toughness. Of course, the decrease of C content may lead to the reduction of the strength. However, one of the effects for V element is to contribute to strength relying on its solution and dispersion strengthening.

5.2.2. Phase calculation

For the equilibrium phase prediction of these two studied steels by Thermo-Calc software, the used temperature range is from 500 to 1600 ℃. The details of phase, including precipitation, were illustrated by changing the scale of *Y* axis from the range of 0 ~ 1 mole

to 0 ~ 2 $\times 10^{-3}$/6 $\times 10^{-3}$ mole. As mentioned before, the situation that described by the equilibrium phase diagram is balanced, which only provides the reference to analysis of precipitation. The practical phases will be modified based on the various parameters in the manufacturing process.

5.2.3. Microstructure analyses

As-annealed specimens for microstructural analyses were cut, and prepared according to the standard metallographic procedures. The longitudinal section of specimen was observed using optical microscopy (OM) Zeiss Axioplan 2. The grain sizes were measured by computer program using planimetric method. The precipitates of the specimens were observed with scanning electron microscopy (SEM) FEI Quanta 600FEG and transmission electron microscopy (TEM) JEOL JEM 2010. Qualitative microanalysis of precipitates was determined by energy dispersive spectroscopy (EDS), which are attached to both instruments of SEM and TEM. Further detailed analyses of precipitates in steel NV# were achieved by complete extraction of non-metallic particles examined by X-ray diffractometer (XRD).

5.2.4. Tensile strength and impact toughness testing

Tensile tests were performed at room temperature with strain rate of 5 $\times 10^{-3}$ s^{-1}. The yield strength (YS), ultimate tensile strength (UTS) and elongation were measured. The

Charpy-V impact toughness of 18Cr-2Mo FSSs was investigated in the temperature range between -40 and 60 ℃, using sub-size (5 mm × 10 mm × 55 mm) specimens. All Charpy specimens were prepared transverse to the rolling direction of the testing plate. The corresponding standards include ASTM A370 [149], ASTM E8/E8M [150] and ASTM E23 [157].

5.3. RESULTS

5.3.1. Equilibrium diagram

Figure 5-1 and **Figure 5-2** show the equilibrium phases of the studied 18Cr-2Mo steels by Thermo-Calc calculation. **Figure 5-1**(a) and (b) display that for the composition system of NV#, Z-phase, accepted as Cr(V,Nb)N [158], precipitates at 1130 ℃, and then the temperatures for the precipitates of Nb/V to appear are 1100 ℃ and 1070 ℃, respectively. And for NVT#, due to the fact that TiN appears in the liquid, the other precipitates are inclined to forming around TiN. Then, the corresponding temperature for Nb/V/Ti precipitation is 1440 ℃, which is influenced by TiN and illustrated in **Figure 5-2**(a) and (b).

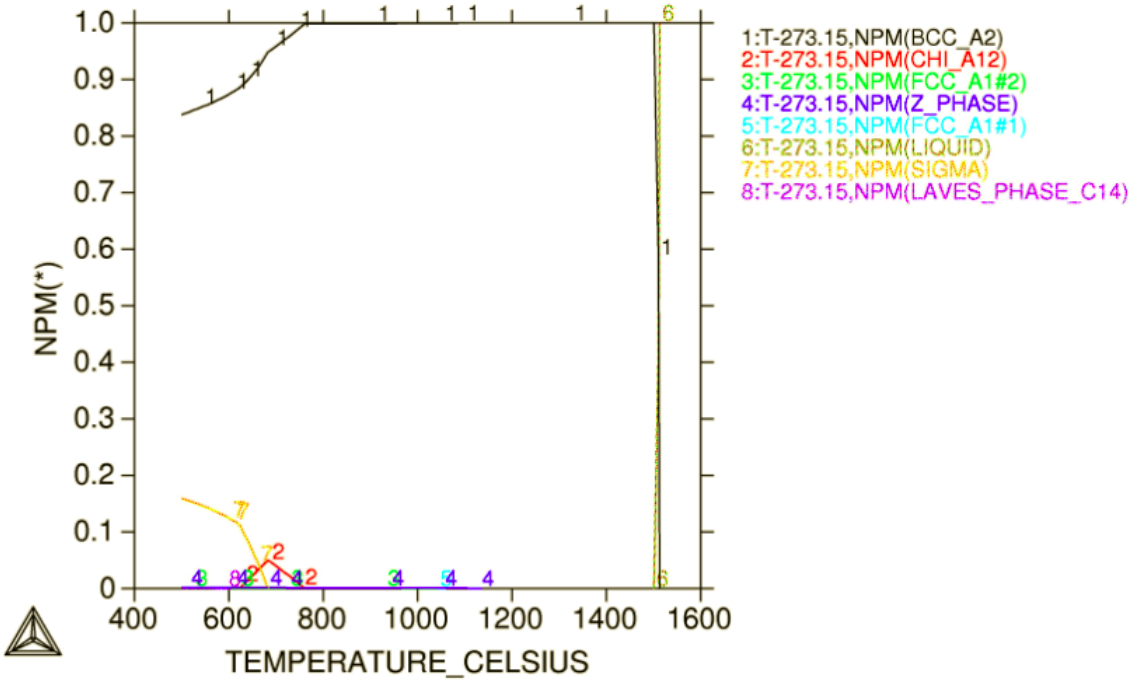
1:T-273.15,NPM(BCC_A2)
2:T-273.15,NPM(CHI_A12)
3:T-273.15,NPM(FCC_A1#2)
4:T-273.15,NPM(Z_PHASE)
5:T-273.15,NPM(FCC_A1#1)
6:T-273.15,NPM(LIQUID)
7:T-273.15,NPM(SIGMA)
8:T-273.15,NPM(LAVES_PHASE_C14)
NPM(*)
TEMPERATURE_CELSIUS
1.0
0.9
0.8
0.7
0.6
0.5
0.4
0.3
0.2
0.1
0
400
600
800
1000
1200
1400
1600

(a)

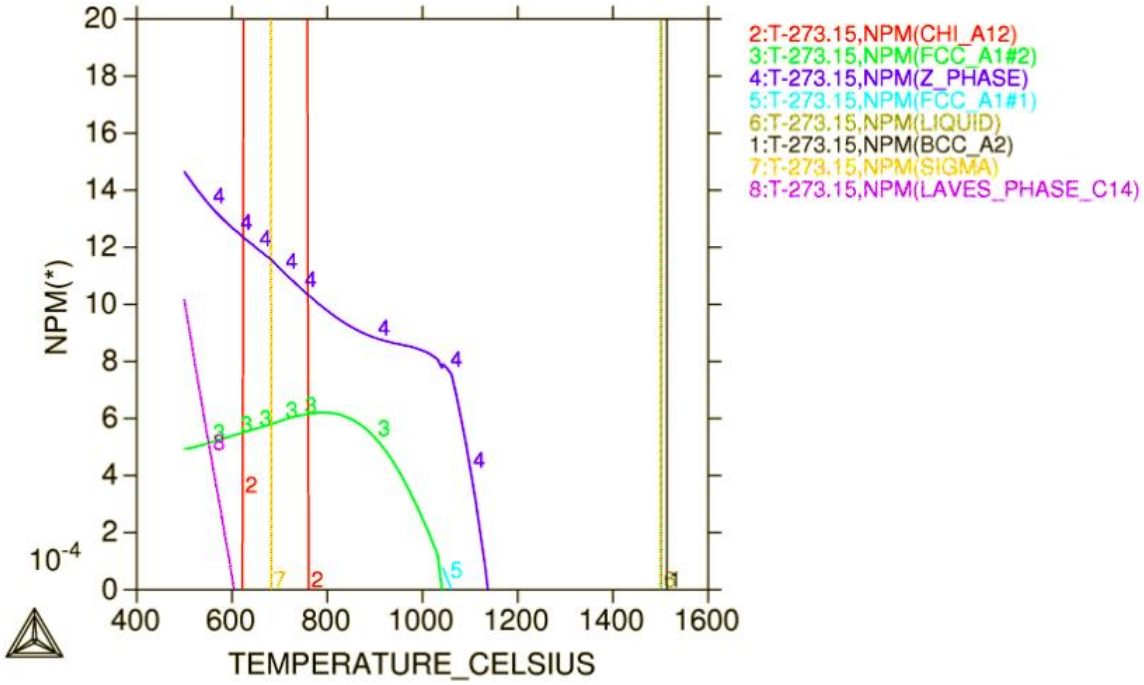

(b)

Figure 5-1 Calculated equilibrium molar fractions of phases for (Nb + V)-stabilised steel: (a) *Y* axis from 0 ~ 1 mole; (b) *Y* axis from 0 ~ 2 $\times 10^{-3}$ mole.

NV#: 1 Ferrite (BCC_A2); 2 Chi phase (CHI_A12); 3 Nb/V#1 precipitate (FCC_A1#2); 4 Z phase (Z_PHASE) ; 5 Nb/V#2 precipitate (FCC_A1#1); 6 Liquid (LIQUID); 7 Sigma phase (SIGMA); 8 Laves phase (LAVES_PHASE_C14).

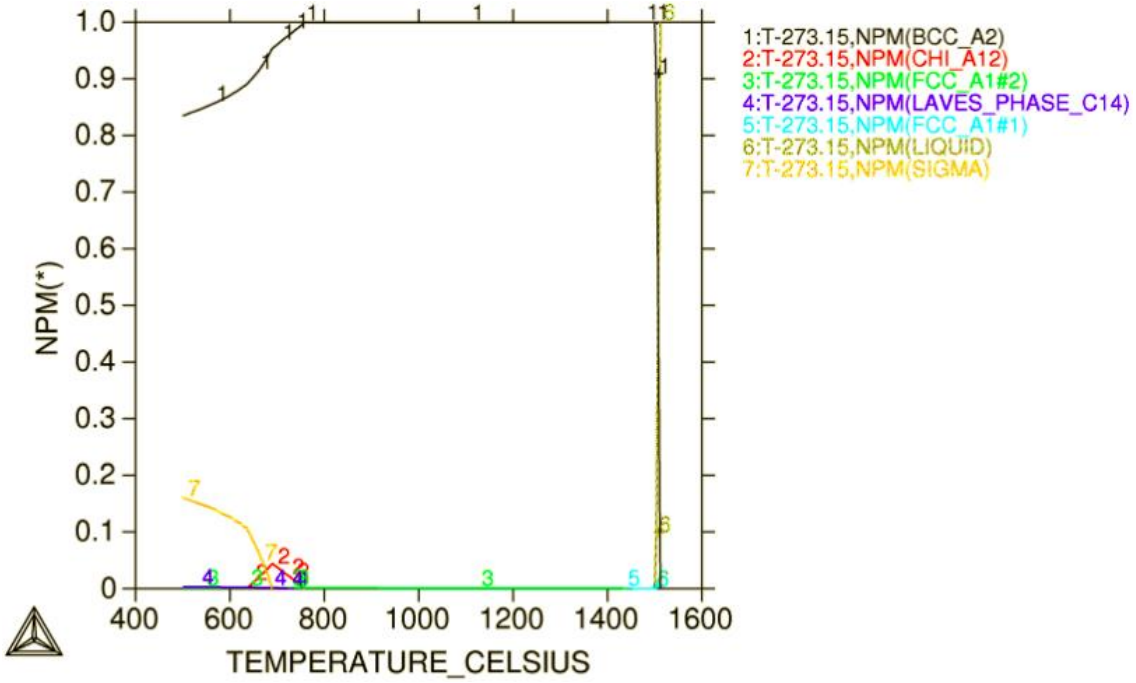
1:T-273.15,NPM(BCC_A2)
2:T-273.15,NPM(CHI_A12)
3:T-273.15,NPM(FCC_A1#2)
4:T-273.15,NPM(LAVES_PHASE_C14)
5:T-273.15,NPM(FCC_A1#1)
6:T-273.15,NPM(LIQUID)
7:T-273.15,NPM(SIGMA)
NPM(*)
1.0
0.9
0.8
0.7
0.6
0.5
0.4
0.3
0.2
0.1
0
400
600
800
1000
1200
1400
1600
TEMPERATURE_CELSIUS

(a)

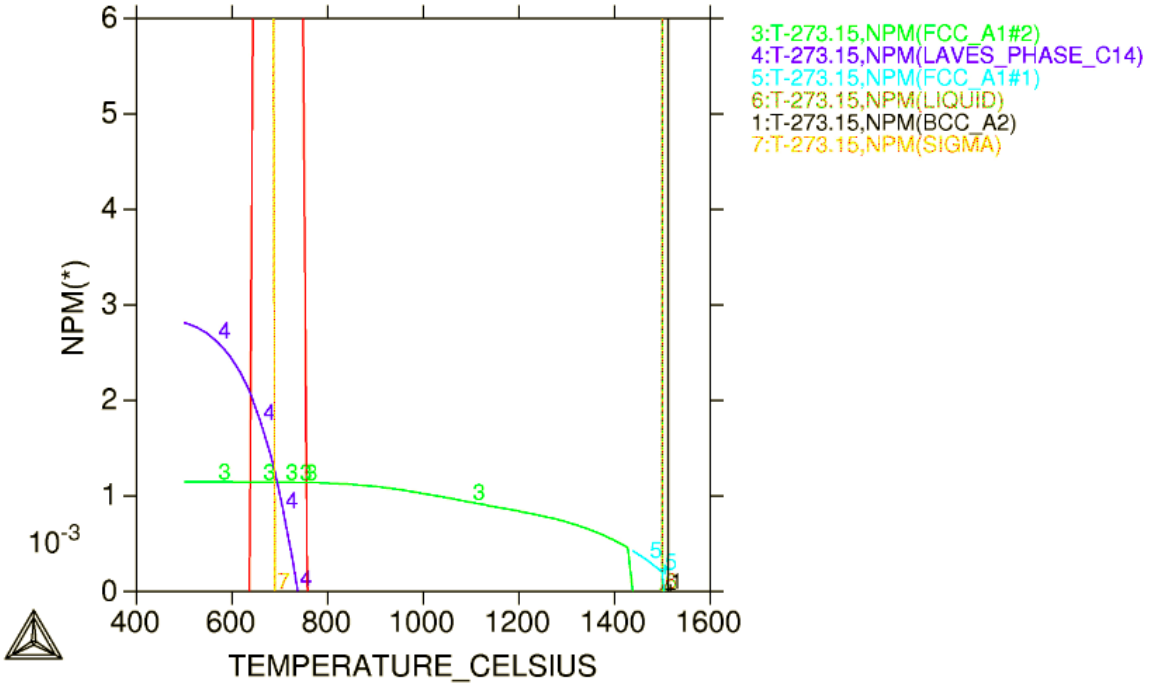

(b)

Figure 5-2 Calculated equilibrium molar fractions of phases for (Nb + V + Ti)-stabilised steel: (a) *Y* axis from 0 ~ 1 mole; (b) *Y* axis from 0 ~ 6 $\times 10^{-3}$ mole.

NVT#: 1 Ferrite (BCC_A2); 2 Chi phase (CHI_A12); 3 Nb/V/Ti precipitate (FCC_A1#2); 4 Laves phase (LAVES_PHASE_C14); 5 TiN (FCC_A1#1); 6 Liquid (LIQUID); 7 Sigma phase (SIGMA).

5.3.2. Microstructure

5.3.2.1. Grain size

It is well known from **Figure 5-3** that the microstructure of 18Cr-2Mo FSS grades is single ferrite phase. The average grain sizes of NV# and NVT# are approximating to 154.6 and 185.8 μm, respectively. The distributions of grain sizes are given in **Figure 5-4**. For the grain that from 40 to 180 μm, NV# acquires 5.8% more than that of NVT#, reaching 66.1%. And for the grains from 180 to 300 μm, NVT# has 30.0%. Even more than 13.3% grains are bigger than 300 μm in NVT#. By comparison, (Nb + V) stabilised steel obtained finer grains than that of (Nb + V + Ti) stabilised one, which means the addition of Nb and V exerts the grain refining effect. But if Ti is added to (Nb + V) steel, the refining effect degrades.

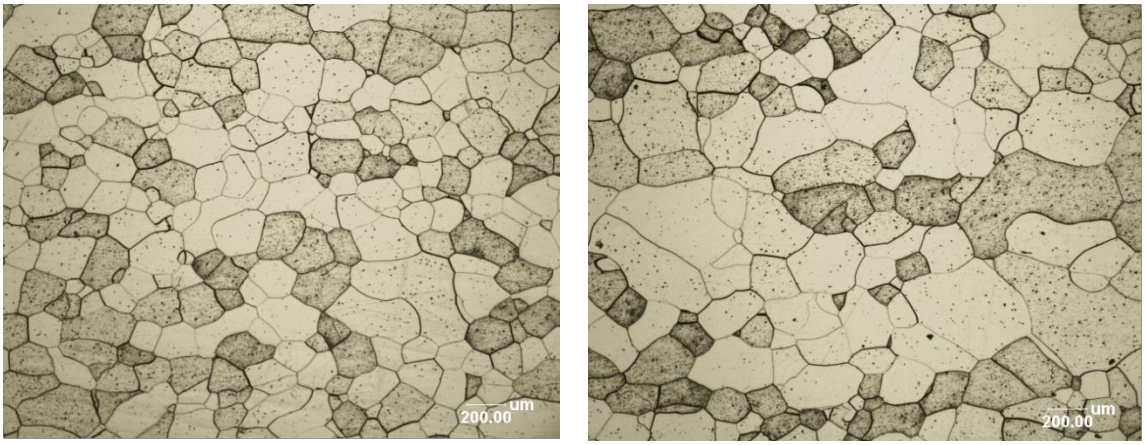

(a) (b)

Figure 5-3 OM images of studied steels: (a) (Nb + V)-stabilised; (b) (Nb + Ti + V)-stabilised.

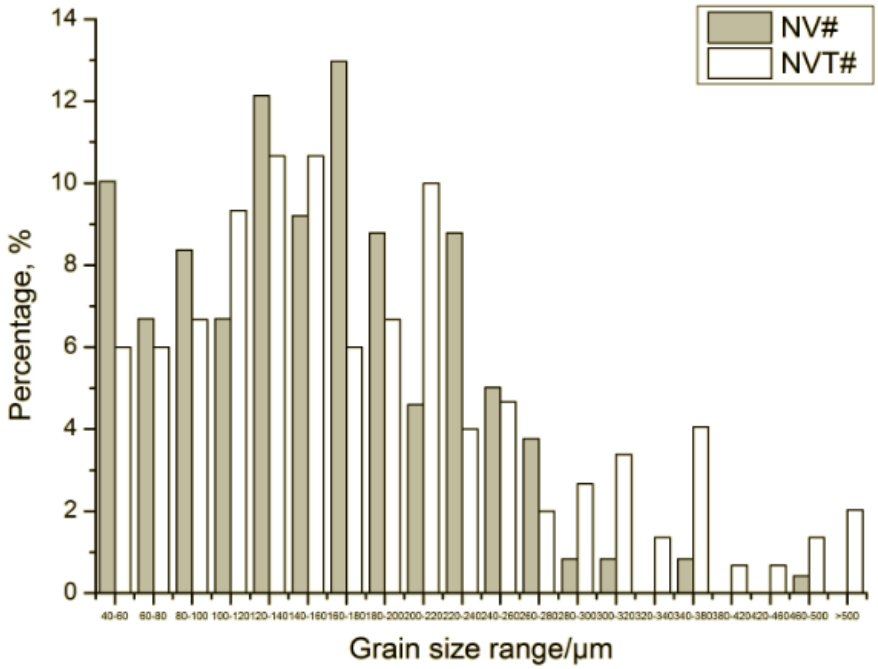

Figure 5-4 Distributions of grain sizes for (Nb + V)-stabilised and (Nb + Ti + V)-stabilised steels.

5.3.2.2. Precipitation

Figure 5-5 and **Figure 5-6** display the SEM images and EDS analyses of the precipitates of NV# and NVT#. For NV#, the formation of Z phase, Cr(V,Nb)N, is unstable in short annealing time, hence, the typical MX precipitates appearing are Nb/V carbonitride according to Thermo-Calc calculation. Usually, in the high Cr steels with Nb and V, MX precipitates can be divided into two groups, Nb(C,N) and VN [158]. Amounts of fine precipitates distributing in the grain are probably Nb(C,N) and VN particles, which are shown in **Figure 5-5**(a). Nb(C,N) is confirmed by EDS (**Figure 5-5**(b)), however, VN

precipitate (in the upper left circle of **Figure 5-5**(a)) is hard to distinguish by means of SEM since the VN particle is the smallest particle found in high Cr steel [158]. From **Figure 5-7**(a) and (c), it is observed that some fine particles of MX adhering to Nb(C,N) in NV# are VN, and the size of this complex precipitate is less than 200 nm. In the meantime, **Figure 5-7**(a) and (b) show the precipitate of NbC. It is reported the average diameters of the spherical Nb(C,N) and the plate-like V-nitride adhering to Nb(C,N) are around 500 nm and 180 nm in 9 wt.% Cr ferritic steels [102], and meanwhile, the size of Nb and V precipitates together with C and N will be changed with the concentration ratio of Nb/V [170].

For NVT#, in the presence of Ti, which is the strong nitride forming element, some cuboidal TiN precipitate of the average size of about 3 μm is found distributing in the matrix (**Figure 5-8**(a) and (b)). At the same time, Nb is found in the particle of TiN, and it is possible that NbN generates on the surface of TiN. NbN precipitates out after TiN and just below the liquidus. As the amount of Ti in steel is more than critical value as-certained by the ideal chemical matching of (Ti,Nb)N, and thus, the interstitial atom nitrogen has fully been stabilised by Ti and Nb theoretically. Then, NbC and TiC have the similar solid solubility. In low carbon steels with Nb and Ti additions, NbC is more stable than TiC at higher temperatures in ferrite throughout the ferrite stability range [163]. From **Figure 5-8**(a)-(c), it is observed that some fine particles of MX besides the coarse particle (Ti,Nb)N in NVT# are rich in Nb, which are (Nb,Ti)C and NbC. VN is seldom found since N is almost occupied by Ti.

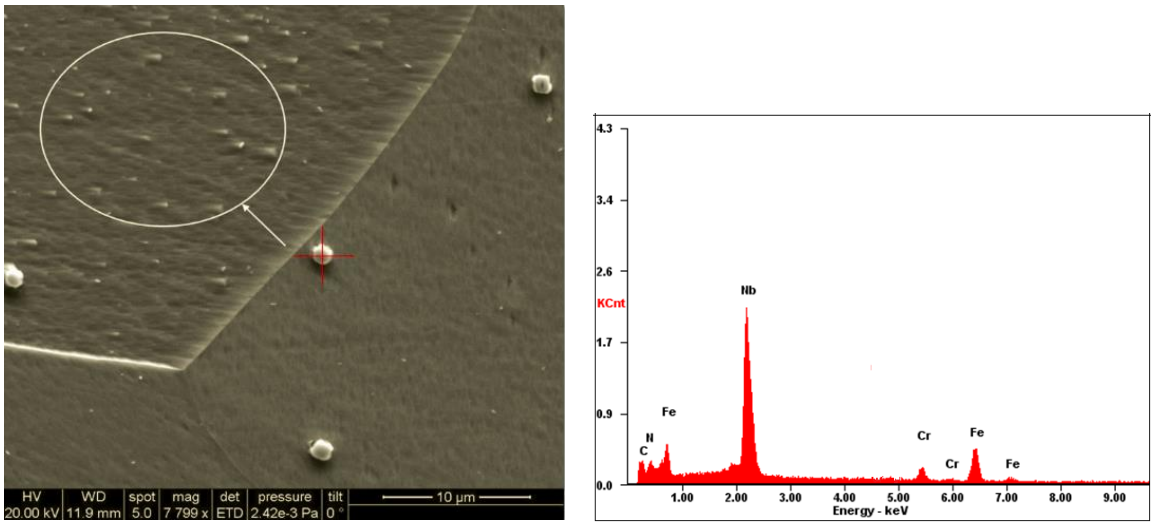

(a) (b)

Figure 5-5 SEM images and EDS analyses of precipitates for (Nb + V)-stabilised steel: (a) SEM image and (b) EDS analysis of precipitate.

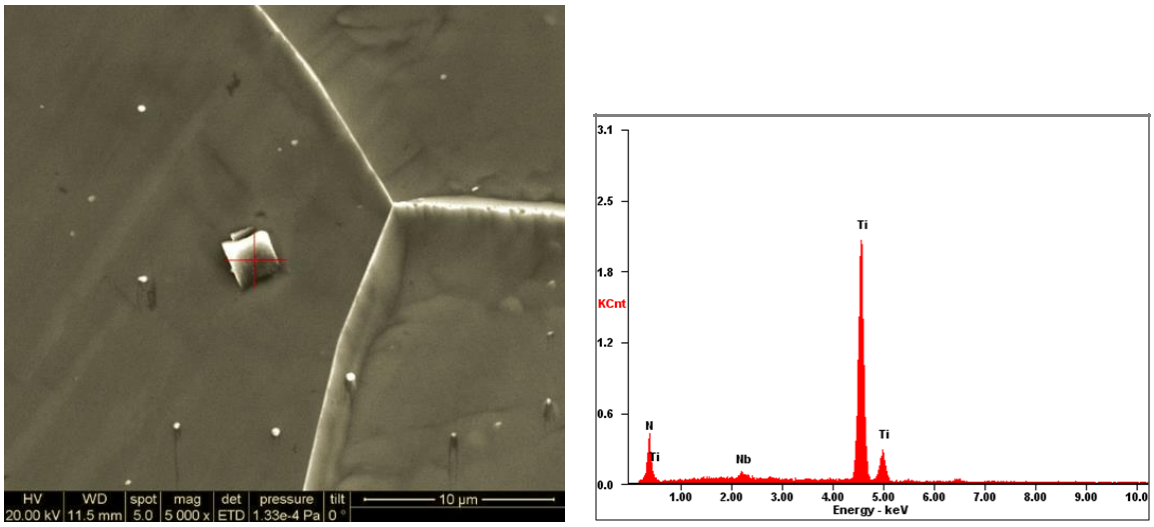

(a) (b)

Figure 5-6 SEM images and EDS analyses of precipitates for (Nb + V + Ti)-stabilised steel: (a) SEM image and (b) EDS analysis of precipitate.

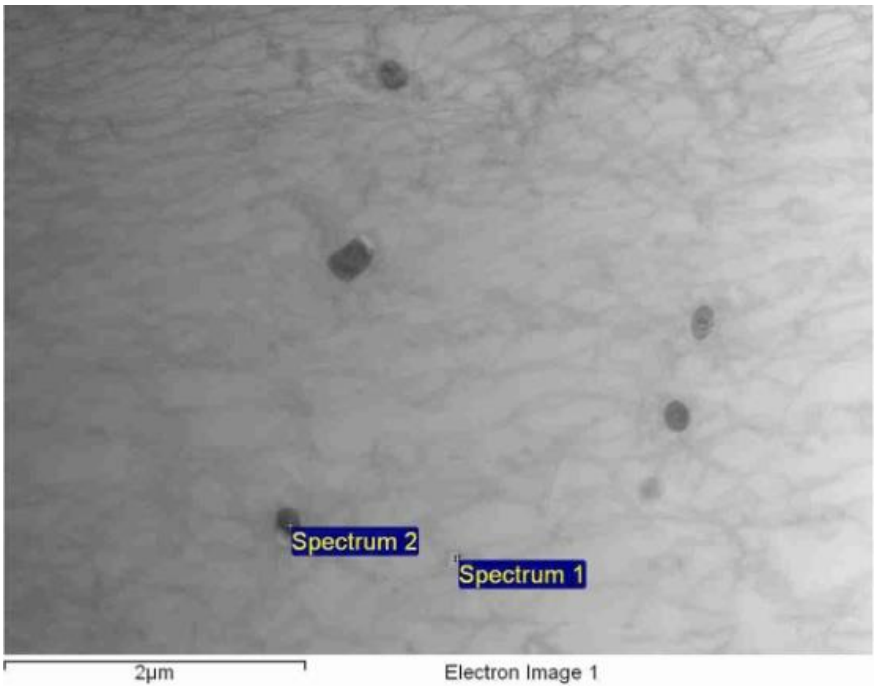

(a)

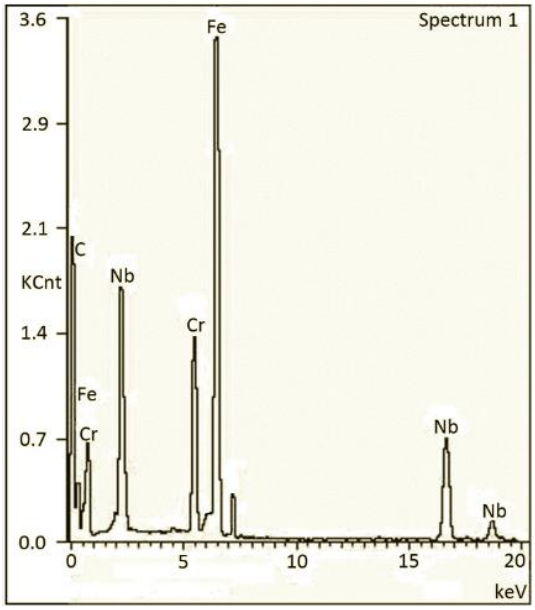

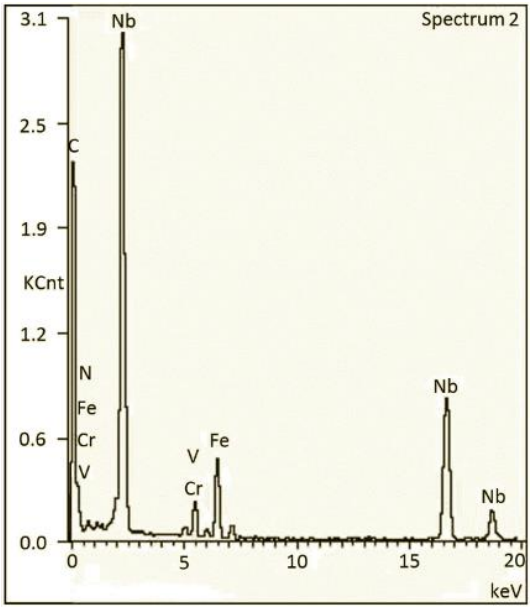

(b) (c)

Figure 5-7 SEM images and EDS analyses of precipitates for NV#: (a) TEM image of NV# and (b)(c) EDS analyses of precipitates.

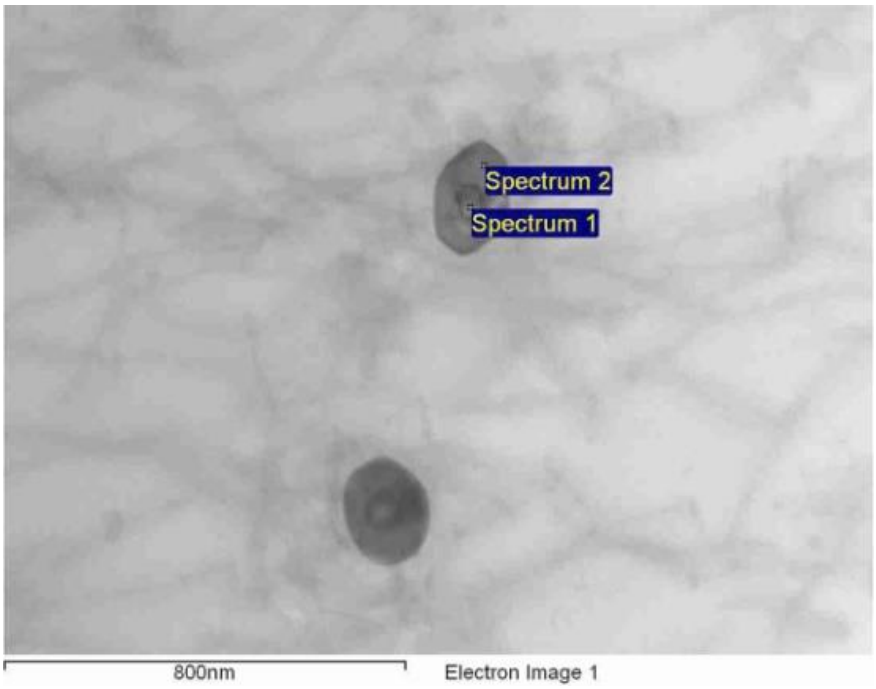

(a)

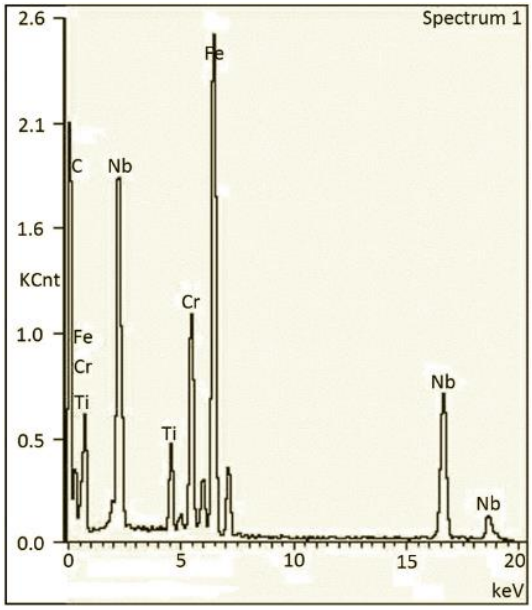

(b)

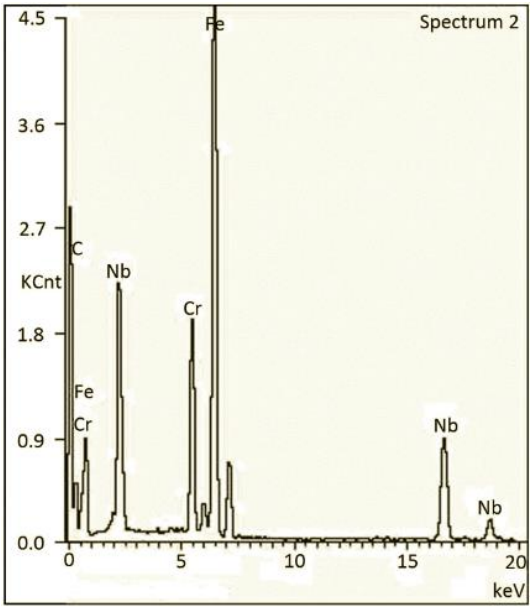

(c)

Figure 5-8 SEM images and EDS analyses of precipitates for (Nb + V + Ti)-stabilised steel: (a) TEM image and (b)(c) EDS analyses of precipitates.

5.3.3. Tensile strength

Table 5-2 lists the tensile strength properties of NV# and NTV# specimens at room temperature. It is demonstrated that the tensile value of Nb-V stabilised steel is around 30 MPa higher, no matter YS or UTS, and meanwhile, the elongations of two steel are similar.

Table 5-2 Tensile properties of studied 18Cr-2Mo steels.

Steel no.	YS (MPa)	Average YS (MPa)	UTS (MPa)	Average UTS (MPa)	Elongation (%)	Average Elongation (%)
NV#	341.23 333.78	337.5	473.45 466.58	470.0	33.03 31.06	32.0
NTV#	303.68 301.39	302.5	445.22 439.83	442.5	32.45 33.58	33.0

5.3.4. Impact toughness

Figure 5-9 shows the impact toughness values of NV# and NVT# from -40 to 60 ℃. For each FSS, the drop of impact values occurs predominantly when temperature is reduced to a low degree. Comparatively, NV# owns better toughness since its critical temperature is 0 ℃, but for NVT#, 20 ℃, at which their toughness has been decreased to an unstable or a low level.

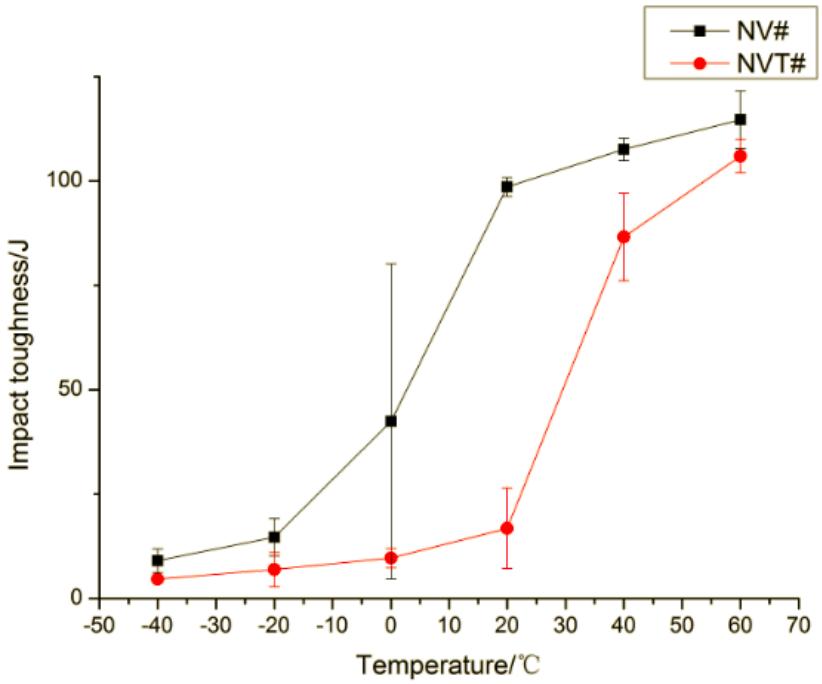

Figure 5-9 Charpy impact values of NV# and NVT# from -40 to 60 ℃.

The fracture surfaces of NV# and NVT# were analysed by means of SEM, shown in **Figure 5-10** and **Figure 5-11**. The specimens impacted between -40 and 60 ℃ were observed. When impacted at 60 ℃, the fractograph of NV# (**Figure 5-10**(b)) presents a fracture with plastic deformed dimples, which shows a characteristic of ductile fracture [171]. Some holes can be seen, which are larger and deeper in contrast to that of NVT# (**Figure 5-11**(b)), and indicate more severe deformation [172]. If the impacting temperature is turned to -40 ℃, the fracture morphology of NV# is river-like, which consists of many flat facets and shear cracks (**Figure 5-10**(f)). But for NVT# tested at -40 ℃, the fracture surfaces become smoother (**Figure 5-11**(d)), which implies lower impact toughness of sample compared with that of NV#. For NV#, when measured at 0 ℃, the fracture morphology is mixed one,

which consists of many small flat facets surrounded by ductile dimples, and indicates that its impact energy may be changeable. But for NVT# tested at the critical temperature, the mixed fracture does not appear at 20 or 40 ℃.

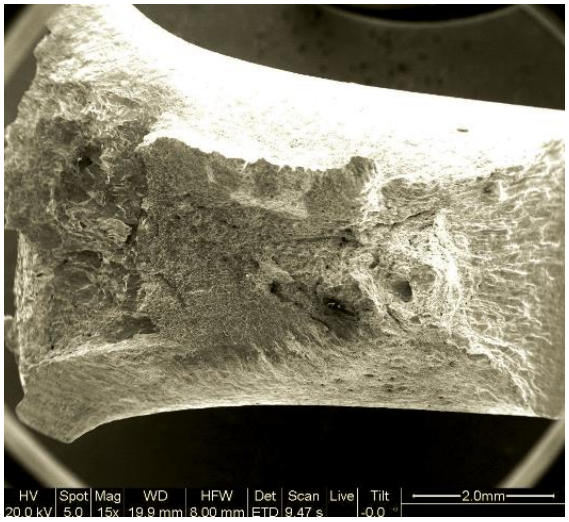

(a)

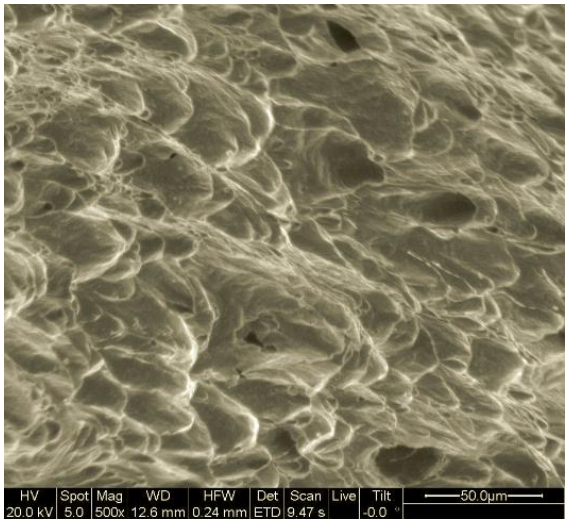

(b)

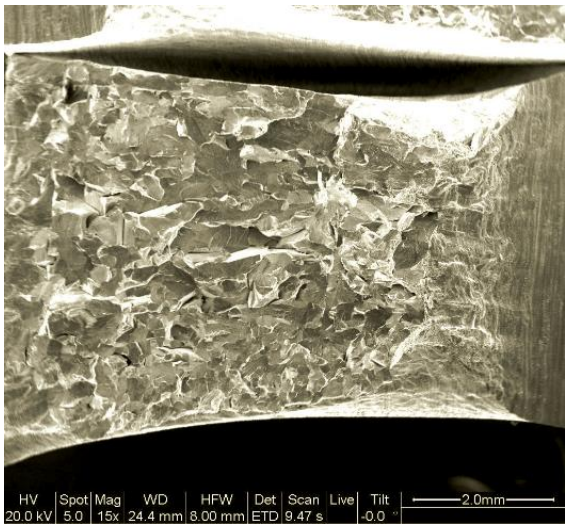

(c)

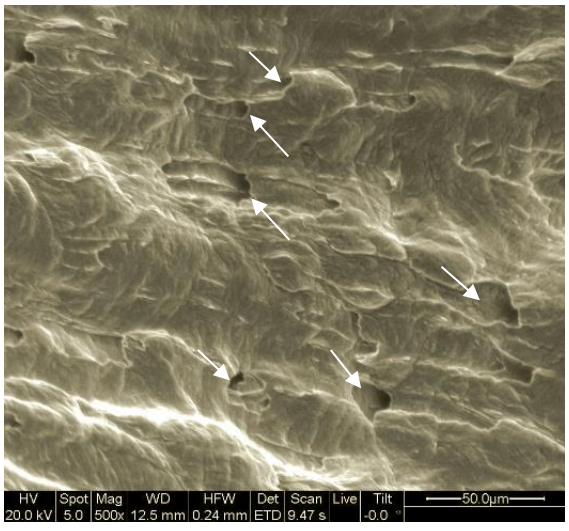

(d)

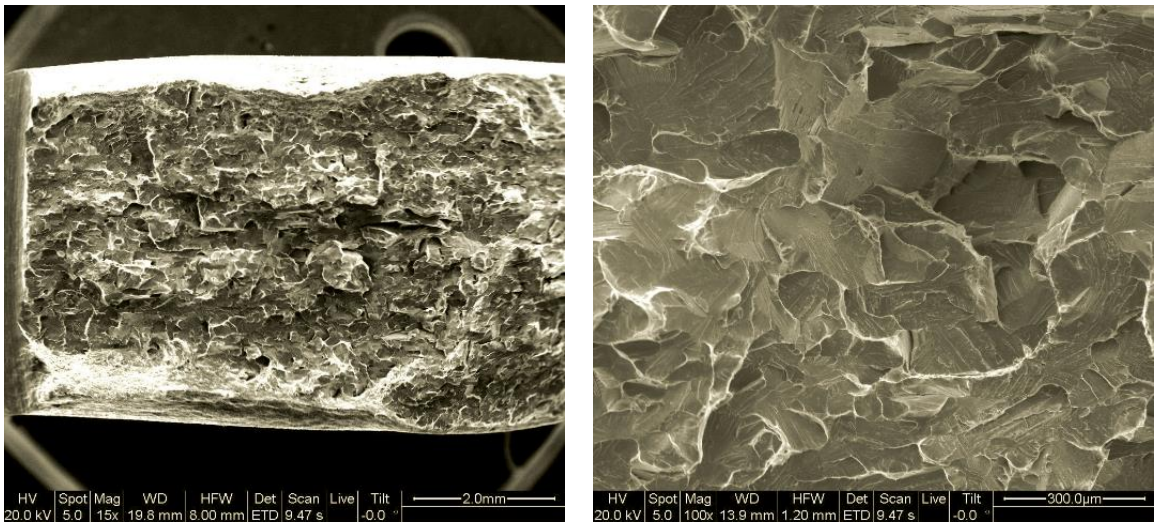

(e) (f)

Figure 5-10 Overall fracture appearance of (Nb + V)-stabilised specimens impacted at: (a) 60 ℃; (c) 0 ℃; (e) -40 ℃ and SEM fractographs impacted at: (b) 60 ℃; (d) 0 ℃; (f) -40 ℃.

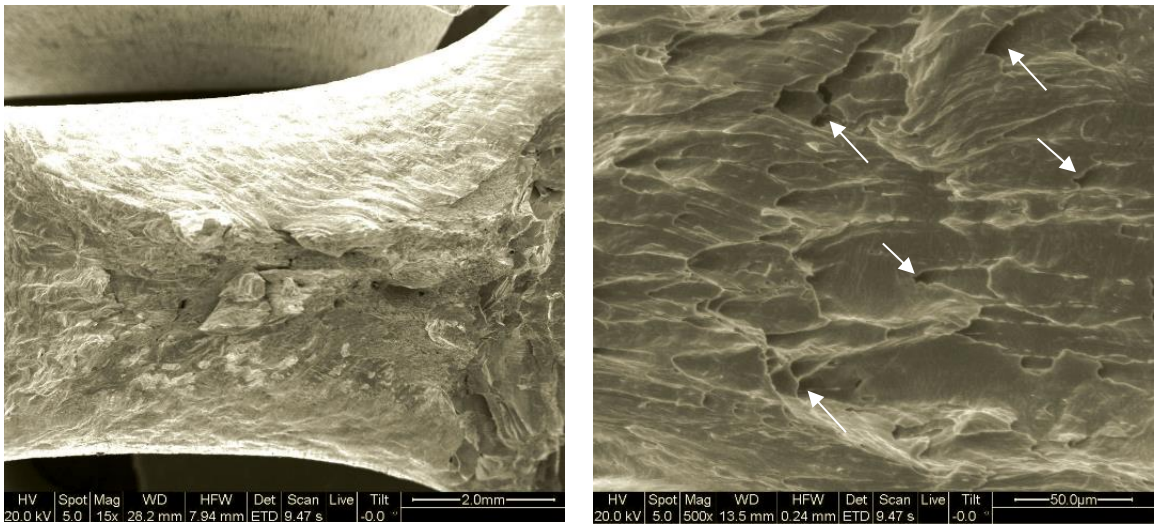

(a) (b)

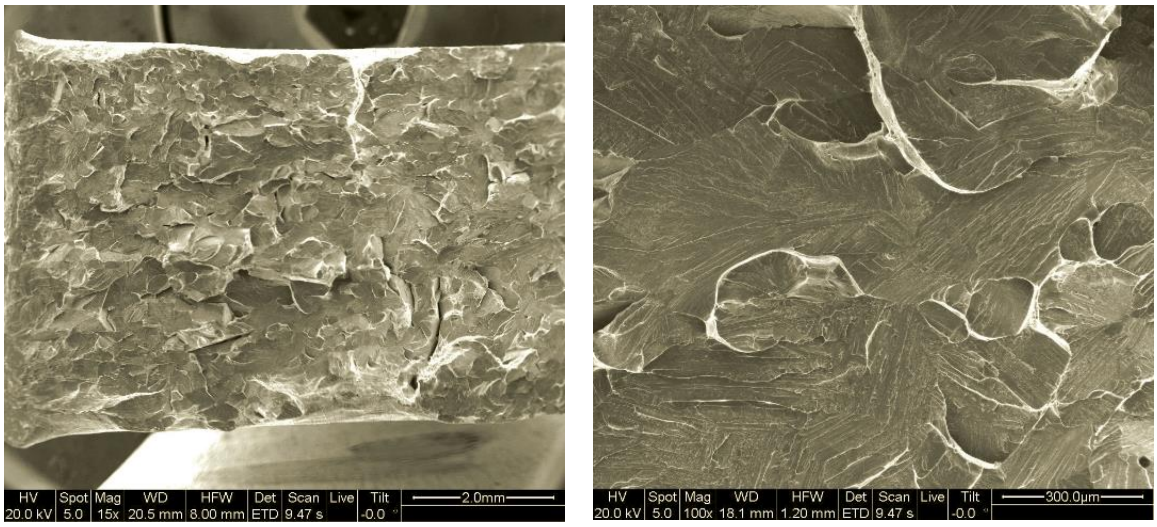

(c) (d)

Figure 5-11 Overall fracture appearance of (Nb + V + Ti)-stabilised specimens impacted at: (a) 60 ℃; (c) -40 ℃ and SEM fractographs impacted at: (b) 60 ℃; (d) -40 ℃.

5.4. DISCUSSION

5.4.1. Microstructure

For the microstructure results of NV# and NVT#, firstly, their homogenisation is better than that of the steels studied in **Chapter 4**, which is related with larger reduction and longer annealing duration; secondly, microalloying is another key factor that determines the grain size since it is able to be used to control the precipitates, which can affect the modification of grains. At the same time, solution strengthening of Nb and V is also a considerable reason. Nb and V addition may improve the strength of the studied steels,

which are supposed to be caused by solution and dispersion strengthening of Nb and V, together with refinement of grain size, etc. However, compared with the results of tensile strength for N# and NT#, NV# and NTV# obtain a little lower strength, which is related to the content of C and the manufacturing procedures (rolling reduction, heating treatment, etc).

Due to the increase of rolling reduction (from 40 mm to 6 mm, 85.0 %) compared to N# and NT#, the grain sizes of NV# and NVT# are refined to some degree in this study. Certainly, there are still some other effective methods during fabrication regarding adjustment of grain size, for example microalloying and thermomechanical processing. Precipitation of Nb and V can influence the grain size [173], and the grain refinement of Nb-V steel is possibly related with the amount of fine precipitates, such as Nb and V carbonitrides, which form at the grain boundaries, shown in **Figure 5-12**, and contributes not only to toughness of NV#, but also to strength due to dispersion strengthening [101]. From the results of Thermo-Calc calculation (**Figure 5-1**(c) and (d)), the formation of TiN happens in the molten steel, and brings the effect of refining the solidification structure [174]. However, Du *et al.* [89] did not find the relationship between TiN particle size and grain size by statistical analyses, which means that the large TiN is not effective in preventing the growth of ferrite grain size. For other fine precipitates, Andersen and Grong [175, 176] set up the analytical modeling of grain growth in metals in the presence of precipitation, which determined the grain boundary pinning effect together with particle coarsening.

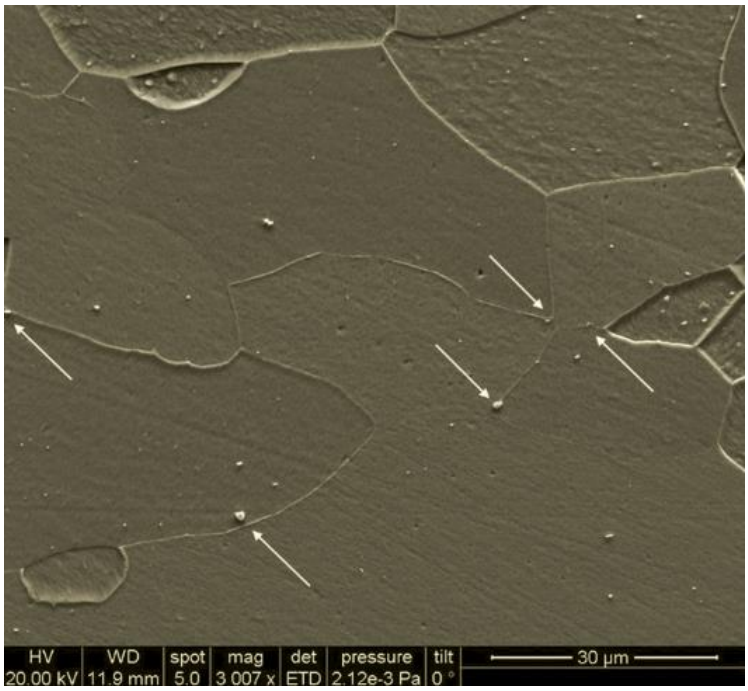

Figure 5-12 SEM image of precipitation at grain boundaries of (Nb + V)-stabilised steel.

It is well understood that Nb, V and Ti are all strong forming elements of carbide and nitride, and as mentioned in **Chapter 4** that the precipitation behaviour of second phase is complicated and mainly dependent on the liquid/solid condition, the solid solubility, the influences of other elements [106]. Besides TiN (FCC_A1#1 for NVT#) forms above the liquidus, the precipitation order based on the composition of NVT# is NbN, VN, TiC, NbC, VC [26], but for different producing process, the precipitation situation will be changed. SEM and TEM are frequently used for confirmation of type, size and distribution of precipitation, however, the method of extraction and X-ray diffraction (XRD) can be supplied to judge the precipitation accurately.

Since Nb-V-Ti system is testified not to be suitable for composition design of 18Cr-2Mo FSS thick plate, this study focuses on investigating the exact precipitation of NV#, and XRD was used to precisely distinguish the precipitates. In **Figure 5-13**, XRD result of NV# is given, which confirms the results of SEM and TEM. It is clear that the precipitates extracted mainly consist of NbC and $VN_{.81}$. NbN, NbCrN and Fe-Cr formed in a small amount during the whole process according to peak strength. NbCrN is one type of Z phase [158]. The lack of VC is possibly related with its unstability and low precipitation temperature, above which C is always occupied by Nb totally. The dynamic producing process modified the Thermo-Calc prediction of precipitation to some degree.

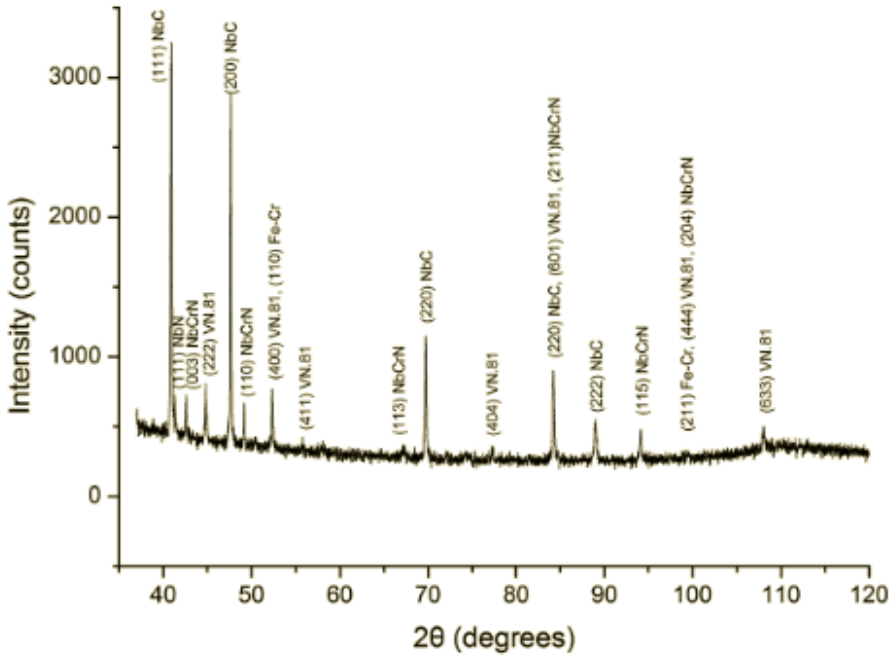

Figure 5-13 XRD result of extracted precipitates of (Nb + V)-stabilised steel.

5.4.2. Tensile strength and impact toughness

Usually, it is accepted that refinement of grain size can be an advantage to strength and toughness. For strength, the fine grain generates the pinning effect, which will increase the tensile strength undoubtedly. Besides fine grain size, other strengthening mechanisms, such as dispersion strengthening of precipitation, solution strengthening of the element of V may be helpful to the strength increase of NV#. And for toughness, Petch explained the reason why fine grain size is beneficial to the increasing of toughness [48], and pointed that DBTT occurs when **Equation 2-4** is satisfied. Meanwhile, the **Equation 2-6** [39] relating grain size to transition temperature has been verified for several metals.

At present, it is understandable that the coarse precipitates, such as TiN, result in a loss of toughness, since they should be associated with the initiation of brittle fracture [51, 89, 90], and meanwhile, the precipitation of TiN also influences the quantity of fine Nb and V carbonitrides, which is related with the modification of grain size. **Figure 5-14**(a) reveals that the found precipitate (Ti,Nb)N locating at the initiation of cleavage fracture, which testifies the negative effect of large particle and can be regarded as inclusions in some steels. The EDS result of the selected particle is given in **Figure 5-14**(b). Three critical steps are involved in a (Ti,Nb)N particle initiated cleavage fracture process, i.e. microcrack nucleates at a (Ti,Nb)N particle; the microcrack penetrates the matrix across the particle-matrix interface and grows into a grain-sized crack; the grain-sized crack continues to propagate across the grain boundaries and becomes unstable, resulting in cleavage

fracture [91]. This point together with grain size can be taken into account regarding the toughness comparison of two studied steels.

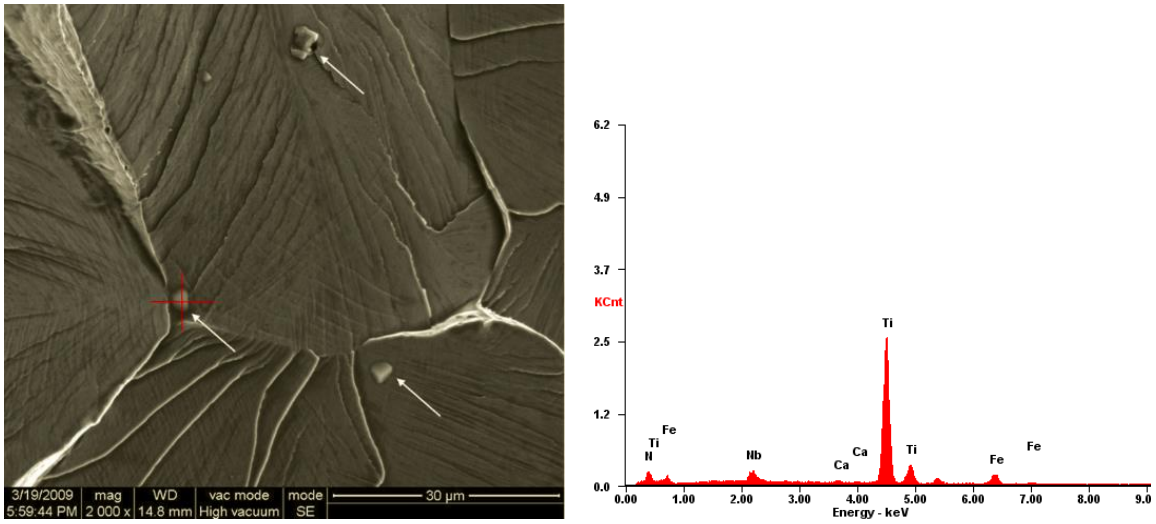

Figure 5-14 (Ti,Nb)N particles appearing at initiation of cleavage fracture.

5.5. CONCLUSIONS

The effects of microalloying on the grain size and precipitation of 18Cr-2Mo FSSs stabilised by (Nb + V) and (Nb + V + Ti) were investigated. The relationship between Ti addition and the properties was discussed. The following conclusions can be drawn:

(1) For (Nb + V) stabilised 18Cr-2Mo FSS, fine grain size, which is related with enough hot rolling reduction and fine precipitation of the particles at the grain boundaries, is beneficial to the tensile strength and impact toughness of 18Cr-2Mo FSS thick plate.

(2) For (Nb + V) steel, Nb(C,N), VN and NbC are main precipitates. By means of the extraction process and XRD analysis, NbC and $VN_{.81}$ are confirmed to be main precipitates, and NbN, NbCrN and Fe-Cr formed in a small amount. However for (Nb + V + Ti) steel, primary precipitates are (Ti,Nb)N, (Nb,Ti)C and NbC. The element of Ti can greatly modify the precipitation behaviour of (Nb + V) composition system.

(3) Ti addition degrades the toughness property of the studied steel due to the large (Ti,Nb)N particles, which usually initiate the cleavage fracture process. Hence, Ti is not a suitable element for stabilising 18Cr-2Mo FSS thick plate, to which high impact toughness is necessary.

(4) The effects of (C + N) on strength and toughness is exhibited for (Nb + V) and (Nb + V + Ti) steels. Besides the decrease of strength to some degree, the reduction of (C + N) will be beneficial to the increase of toughness. In the meantime, V was added to maintain the strength of low (C + N) FSS grade due to its dispersion and solution strengthening.

Based on above results, the collocation of (Nb + V) for stabilisation of FSS appears to be the combination of the mechanical properties, i.e. strength and toughness. Meanwhile, the effects of manufacturing parameters, such as hot rolling reduction and heat treatment, will not be overlooked.

6. PROCESSING OPTIMISATION

6.1. INTRODUCTION

In this study, the traditional hot rolling process of (Nb + V + Ti) stabilised 17Cr FSS thick plates was optimised to investigate the role of intermediate warm rolling procedure on microstructure, texture, grain boundary and then mechanical properties of the studied steels. Different total reductions for warm rolling processes were selected for comparing with the traditional one, and enhancing effect of properties was assessed.

The microstructure, texture and grain boundary, which are influenced during processing modification, have a close correlation with properties, especially mechanical properties of steels [177, 178].

The influences of microstructure, such as grain refinement, on mechanical properties of materials have been studied by a quantity of researchers. Then, crystalline texture can strongly affect grain boundary misorientation, leading to the change of coincidence site lattice (CSL), which is used by classifying grain boundaries [120]. It has been mentioned that grain boundary engineering (GBE) plays an important role in controlling mechanical properties of materials [119]. In GBE, grain boundary character distribution (GBCD) and grain boundary (GB) connectivity have shown to be related closely to these properties [120,

121]. As introduced, GBE aims to convert a fraction of high-energy grain boundaries to low-energy boundaries, or from high-Σ CSL boundaries (CSLBs, $\Sigma > 29$, i.e. random boundaries) to low-Σ CSLBs ($\Sigma \leq 29$) [123].

Thermomechanical processing (TMP), using single or multiple steps of deformation and subsequent annealing treatment, has been one of the most popular approaches applied for the modification of microstructure, texture, GBE [123], and finally mechanical properties. During TMP, warm working is frequently applied for the adjustment of grain, texture and grain boundary [179].

6.2. EXPERIMENTS

6.2.1. Materials

The manufacturing procedures of the materials used in this study were displayed in **Chapter 3.2.2**. The casting ingots were hot forged into the thickness of 26 mm (traditional and first optimised hot rolling process) and 35 mm (second optimised hot rolling process), hot rolled into 5.5 mm plate, and annealed at high temperatures for appropriate duration, aiming at sufficient recrystallisation and fine annealing microstructure, followed by cooling in water. The chemical composition of the 17Cr steel is shown in **Table 6-1**. The stabilisation ratio the studied steel is calculated to be 23.6 by **Equation 2-7**. The result means the designed steel can satisfy the requirements of intergranular corrosion resistance.

Table 6-1 Chemical composition (in wt.%) of studied 17Cr steel.

C	Si	Mn	Cr	Nb	V	Ti	N	Fe
0.005	0.19	0.28	17.0	0.04	0.12	0.10	0.006	Bal.

Two different warm rolling processes were selected to be in comparison with the traditional one, and the detailed processing parameters and reduction of each pass are displayed in **Table 6-2**. The total reductions of three rolling processes are 78.8%, 78.8% and 84.3%, respectively, and the reductions of different stages are exhibited in **Table 6-3**.

Table 6-2 Comparisons of three studied hot rolling processes.

Steel no.	Process	Hot rolling procedure		Warm rolling procedure		Final annealing procedure
		Temperature range (℃)	Intermediate thickness (mm)	Warm rolling temperature (℃)	Final thick-ness (mm)	Temperature/ time (℃/min)
17Cr T#	Traditional hot rolling	850 ~ 1100	-	-	5.5	900/7
17Cr P1#	Warm rolling-1	850 ~ 1100	12	260	5.5	850/5.5
17Cr P2#	Warm rolling-2	850 ~ 1100	16.4	260	5.5	850/5

Table 6-3 Pass distributions of three studied hot rolling processes.

Steel no.	Process	Hot rolling reduction (%)	Warm rolling reduction (%)
17CrT#	Traditional hot rolling	78.8	-
17CrP1#	Warm rolling-1	53.8	54.2
17CrP2#	Warm rolling-2	53.1	66.5

6.2.2. Phase calculation

The equilibrium phase diagrams were calculated using Thermo-Calc software, and the recommended temperature range is from 500 to 1600 ℃. The details of phases were illustrated by the scale of *Y* axis ranged from 0 to 1 mole and 5×10^{-3} mole.

6.2.3. Microstructure analyses

As-annealed specimens for microstructural analysis were cut, prepared according to the standard metallographic procedures, and then etched. The longitudinal section of specimen was observed using optical microscopy (OM) of Zeiss Axioplan 2. The grain sizes were measured by computer program using planimetric method.

6.2.4. Texture

The textures formed during different hot rolling processes were measured by using X-ray diffraction (XRD) on a Bruker D8 discover diffractometer with Co-K_α radiation, and orientation distribution functions (ODFs) $f(g)$ were calculated by the series expansion method according to Bunge from three incomplete pole figures {1 1 0}, {2 0 0} and {1 1 2}.

6.2.5. Grain boundary (GB)

To further characterise the microstructure, scanning electron microscopy (SEM) and electron backscatter diffraction (EBSD) were performed using a JEOL JSM 7001F field emission gun (FEG) SEM. Prior to EBSD mapping, the specimens were electropolished. The low-Σ CSLB and GB connectivity were interpreted by using the software Channel 5 based on the EBSD results.

6.2.6. Tensile strength and impact toughness testing

Tensile tests were performed at room temperature with strain rate of 5×10^{-3} s^{-1}. The transverse yield strength (YS), ultimate tensile strength (UTS) and elongation were measured. The Charpy testing was conducted in the temperature range from -40 to 60 ℃,

employing sub-size (5 mm × 10 mm × 55 mm) specimens. The testing standards are ASTM A370 [149], ASTM E8/E8M [150] and ASTM E23 [157].

6.3. RESULTS

6.3.1. Equilibrium diagram

Figure 6-1 shows the equilibrium phases of the studied 17Cr steels by Thermo-Calc prediction. It is well known that for medium Cr FSS with extremely low C and N contents, the main phase below the liquid, i.e. 1495 ℃, is ferrite, which means the pure 17%Cr FSS used in this paper is polycrystalline metal with single phase.

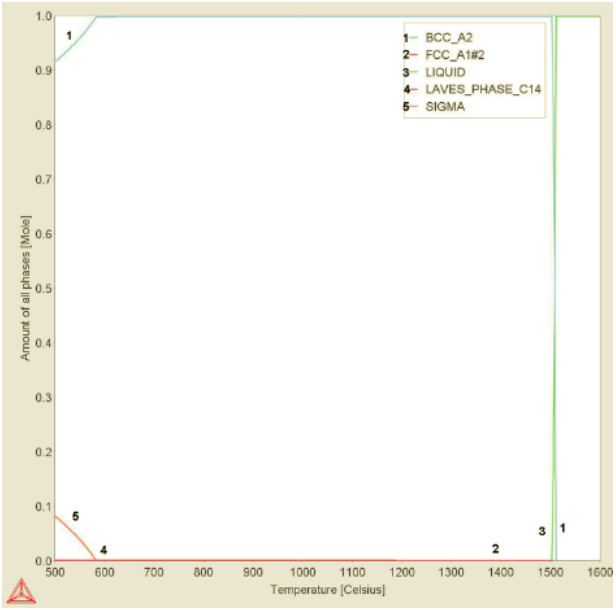

(a)

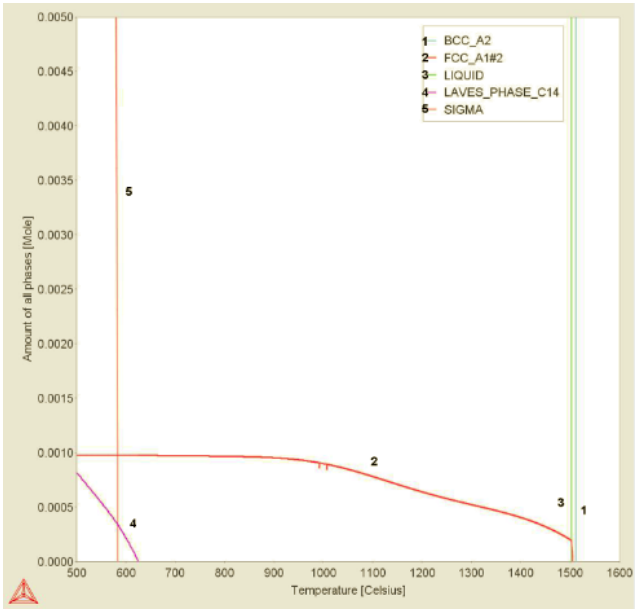

(b)

Figure 6-1 Calculated equilibrium phase molar fractions of studied steel: (a) *Y* axis ranged from 0 ~ 1 mole; (b) *Y* axis ranged from 0 ~ 5 $\times 10^{-3}$ mole.

1 Ferrite (BCC_A2); 2 Nb/Ti/V precipitate (FCC_A1#2); 3 Liquid (LIQUID); 4 Laves phase (LAVES_PHASE_C14); 5 Sigma phase (SIGMA).

6.3.2. Microstructure, texture and grain boundary analyses

6.3.2.1. Grain size

It can be seen from **Figure 6-2** that the microstructure of 17Cr FSS is single ferrite phase. The average grain sizes of 17CrT#, 17CrP1# and 17CrP2# are approximating to 52.3 μm, 29.9 μm and 21.0 μm, respectively. The grain size distributions are given in **Figure 6-3**.

The fractions of grains ranged from 10 to 40 μm for 17CrP1# and 17CrP2# are 77.8% and 85.8%, which are 40.8% and 48.8% higher than that of 17CrT#, 37.0%. And for the grain that from 40 to > 60 μm, 17CrT# owns 59.3% grains of this size. Even more than 29% grains are bigger than 60 μm in 17CrT#. By comparison, the steels 17CrP1# and 17CrP2# have finer grains than that of the steel 17CrT#, which means that warm rolling procedure and reduction are key factors that determine the refinement effectiveness of the ultra-purified FSS group. And with increase of reduction for similar processing, i.e. 17CrP1# and 17CrP2#, more refined grains appear.

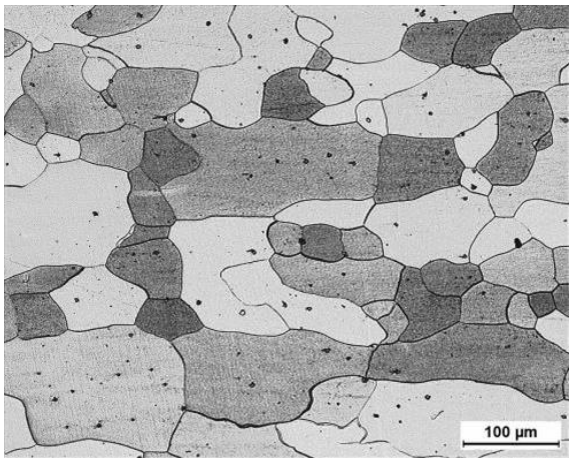

(a)

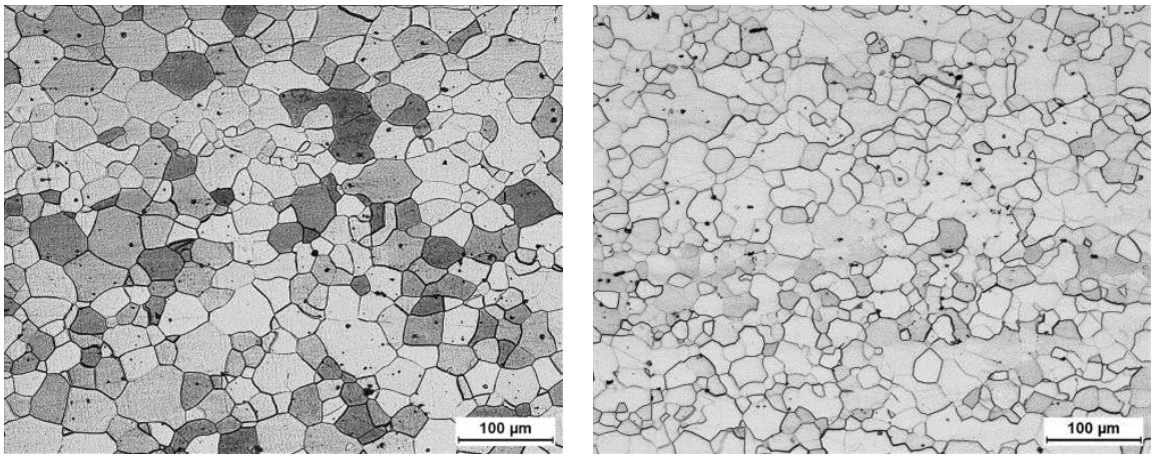

(b) (c)

Figure 6-2 OM images of studied steels: (a) 17CrT#; (b) 17CrP1#; (c) 17CrP2#.

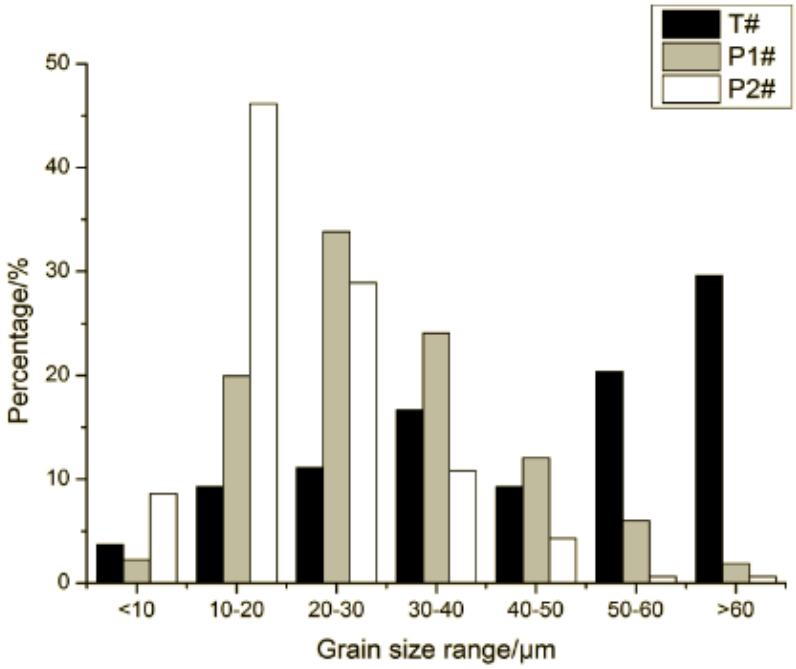

Figure 6-3 Grain size distributions of: (a) 17CrT#; (b) 17CrP1#; (c) 17CrP2#.

6.3.2.2. Orientation map

Figure 6-4 shows the orientation maps of the studied steels manufactured through three different hot rolling processes. These orientation maps illustrate the crystalline directions as indicated by the colours in the stereographic triangle. For 17CrT#, the fraction of the orientation {h k l}<0 0 1> is comparatively higher, while for 17CrP1# and 17CrP2#, the orientation {h k l}<1 1 1> is apparently dominant.

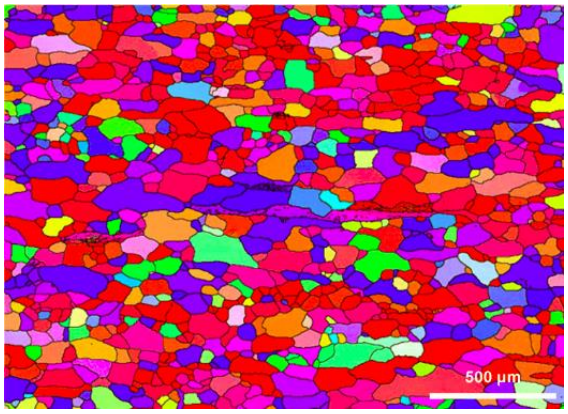

(a)

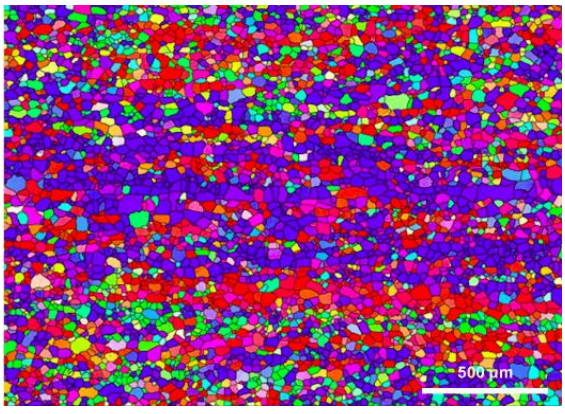

(b)

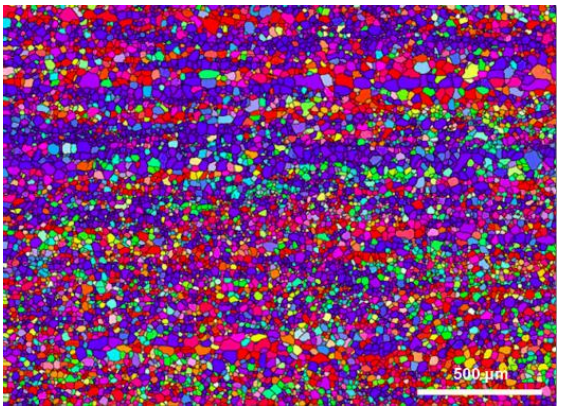

(c)

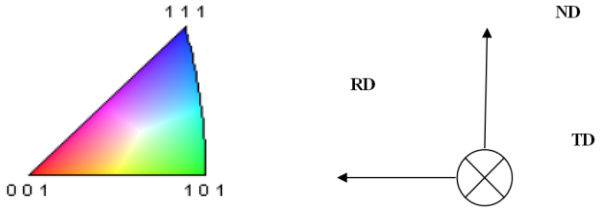

(d)

Figure 6-4 Orientation maps of three studied steels (RD: rolling direction; TD: transverse direction; ND: normal direction): (a) 17CrT#; (b) 17CrP1#; (c) 17CrP2#; (d) appendix.

6.3.2.3. Texture

The ODF maps (φ_2 = 45°) of the textures for three different hot rolling conditions are exhibited in **Figure 6-5**. For 17CrT#, the traditional hot rolling process, a pronounced texture is dominated by the θ-fibre with the maximum component at <0 0 1>//ND [$f(g)$ = 5.49], as shown in **Figure 6-5**(a). However, for 17CrP1# and 17CrP2#, γ-fibre is the main texture with the maximum intensity close to {1 1 1}<1 1 2>, whose $f(g)$s are 5.35 and 5.42, respectively, displayed in **Figure 6-5**(b) and (c).

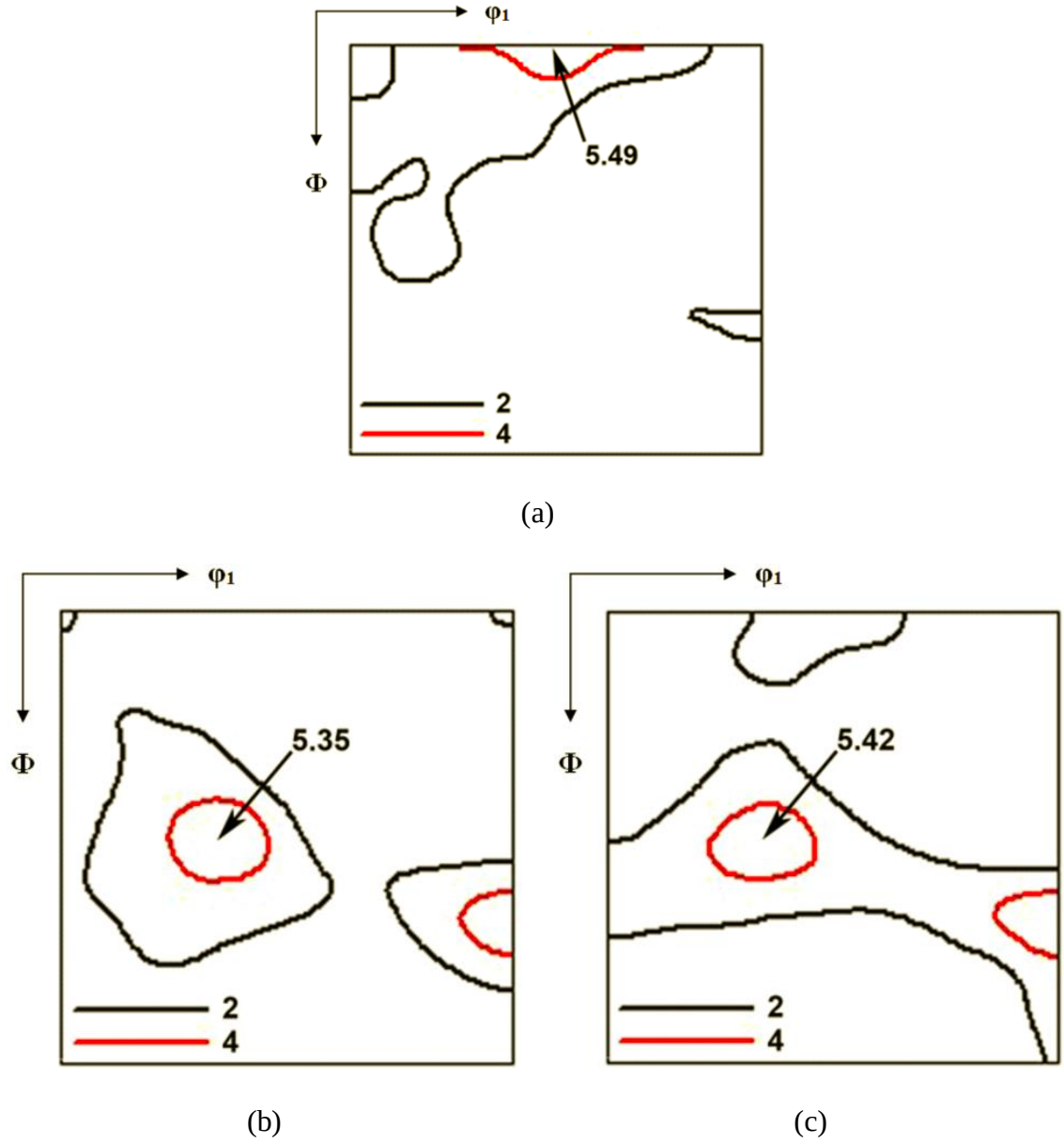

Figure 6-5 Texture analyses of three studied steels (φ_2 = 45 °): (a) 17CrT#; (b) 17CrP1#; (c) 17CrP2#.

6.3.2.4. Grain boundary engineering (GBE)

Grain boundary character distribution (GBCD)

The GBCD results of three studied steels are depicted in **Figure 6-6**. It is clear that the warm rolling processes cause higher fractions of low-Σ CSLBs ("special" boundaries [154]). The fractions of low angle boundaries (LABs) increase from 11.9% (17CrT#) to 18.1% (17CrP1#) and 18.3% (17CrP2#), and meanwhile, the fractions of Σ3 ~ Σ29 increase from 7.2% (17CrT#) to 8.6% (17CrP1#) and 9.8% (17CrP2#). For low-Σ CSLBs of 17CrT# (shown in **Figure 6-7**), the LABs (Σ1) and grain boundaries (Σ3 and Σ11) exhibit high frequencies. Compared the traditional rolling with the warming rolling processes, the frequency distributions of Σ1, Σ3 and Σ13 for 17CrP1# and 17CrP2# improve apparently, i.e. by 52.1%, 56.3%, 247.2% and by 53.8%, 196.9%, 177.8%, respectively. Furthermore, for 17CrP2#, Σ1, Σ3 and Σ11 appear a little more with increasing of pass reduction compared with 17CrP1#.

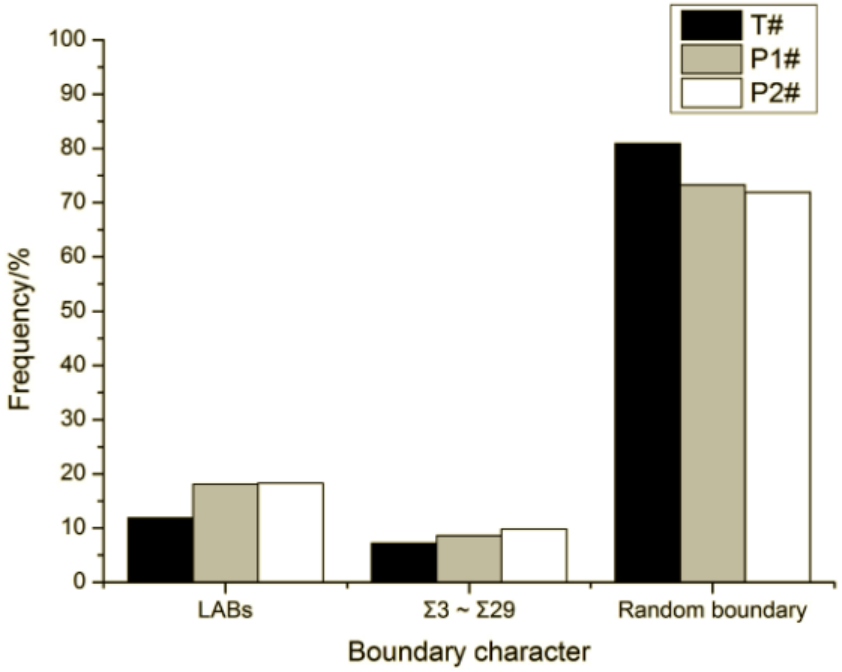

Figure 6-6 GBCD results of three studied steels.

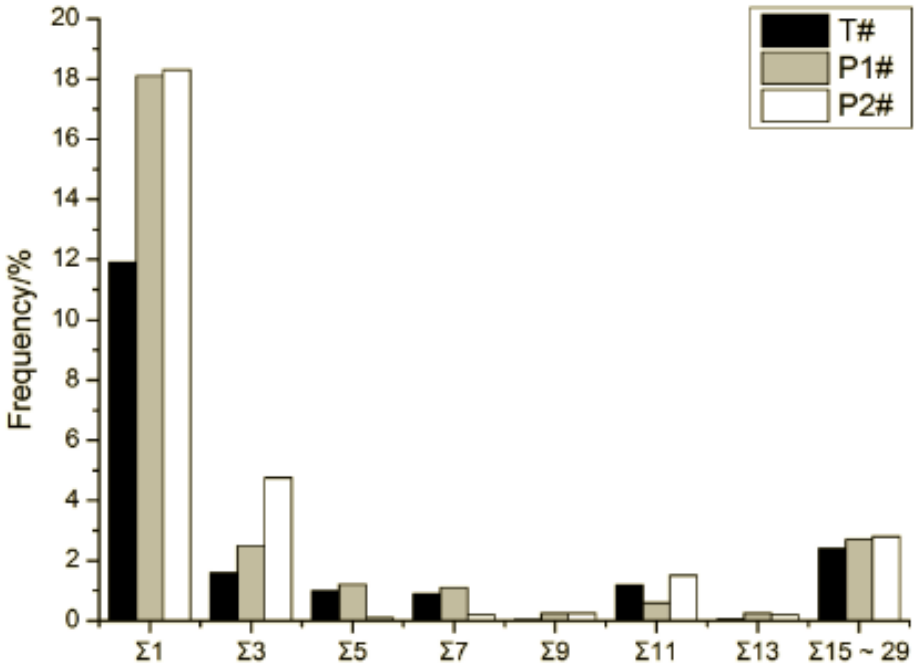

Figure 6-7 Low-Σ CSLBs distributions of three studied steels.

Grain boundary (GB) connectivity

Figure 6-8 shows two-dimensional grain boundary networks of three steels, and blue and red lines delegate special boundaries (low-Σ CSLBs, or Σ1 ~ Σ29 boundaries) and random boundaries, respectively. Besides the different frequencies of grain boundaries for three studied steels, the distributions of typical boundaries and the phenomena of reciprocal connectivity significantly vary. For 17CrT#, the fraction of low-Σ CSLBs is comparatively lower. With the application of warm rolling process, the considerable random boundaries are apparently segmented into fragments. And the increment of reduction improves the tendency of fragment division.

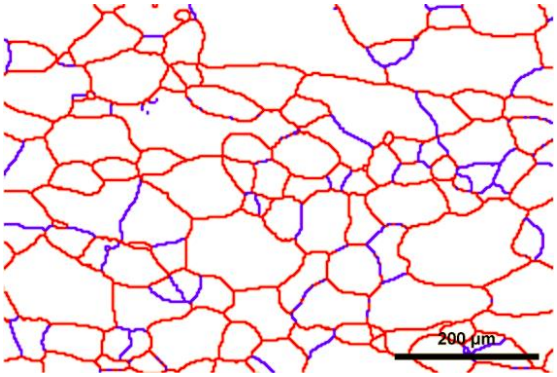

(a)

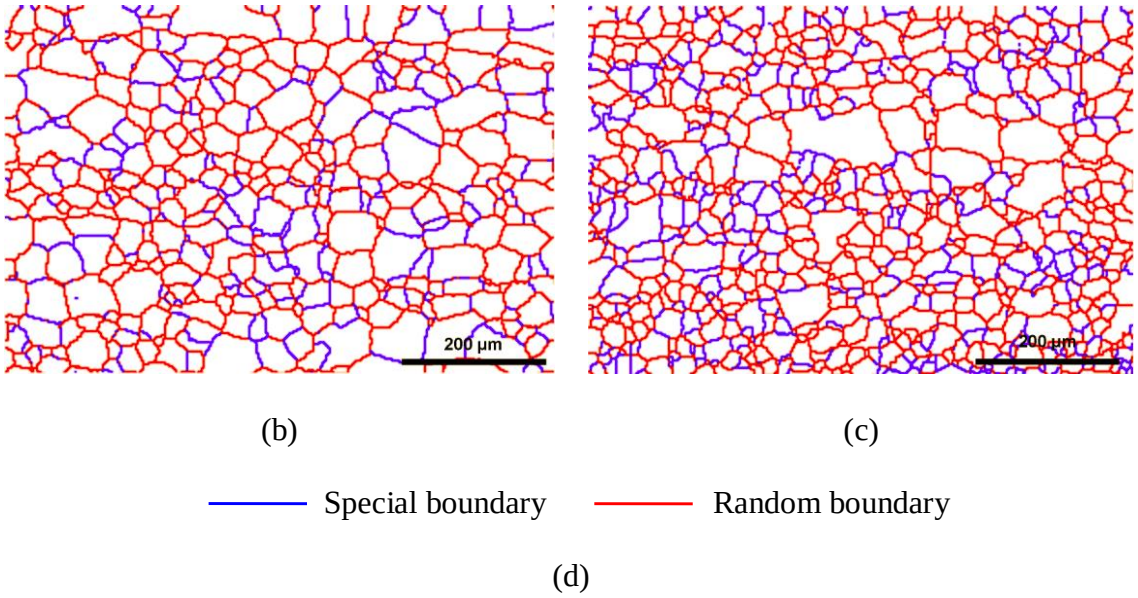

Figure 6-8 GB connectivity schematic of three studied steels: (a) 17CrT#; (b) 17CrP1#; (c) 17CrP2#; (d) appendix.

6.3.3. Mechanical properties

6.3.3.1. Tensile strength

The tensile strength properties of 17CrT#, 17CrP1# and 17CrP2# specimens at room temperature are listed in **Table 6-4**. It is understandable that the tensile properties are related to grain size. YS and UTS values of 17CrP1# and 17CrP2# are higher than those of 17CrT#, and the elongation value is decreased a little, i.e. 2.1% and 2.8%. The warm rolling procedure can improve the strength of the studied steels due to grain refinement. Meanwhile, the elongation is not influenced a lot.

Table 6-4 Tensile properties of studied 17Cr steels.

Steel no.	YS (MPa)	UTS (MPa)	Elongation (%)
17CrT#	191.0	365.0	26.2
17CrP1#	232.5	405.0	24.1
17CrP2#	239.0	418.0	23.4

6.3.3.2. Impact toughness

Figure 6-9 shows the impact toughness values of 17CrT#, 17CrP1# and 17CrP2# tested at temperatures from -60 to 40 ℃. Different testing temperature ranges are selected for three studied steels due to the considerably large variation of the values of ductile-brittle transition temperature (DBTT). For these three studied steels, the significant scatter for impact toughness occurs at approximately 0 ℃, -30 ℃ and -40 ℃, respectively, which can be assumed as the DBTT values. It is evident that the impact toughness properties of 17CrP1# and 17CrP2# are better than that of 17CrT#.

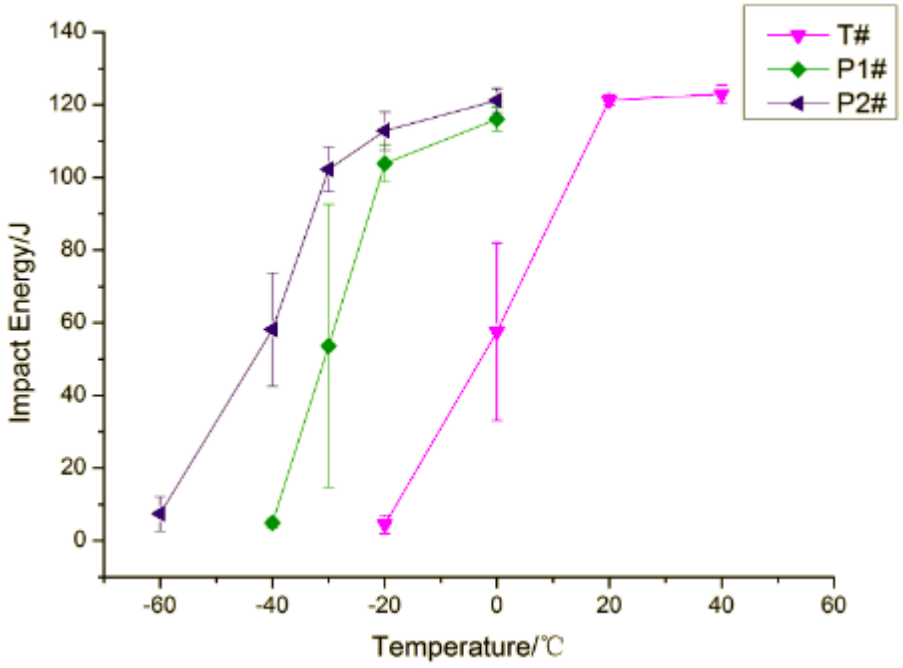

Figure 6-9 Charpy impact values of 17CrT#, 17CrP1# and 17CrP2# from -60 to 40 ℃.

6.4. DISCUSSION

The comparisons of the properties of three studied steels confirm that the warm rolling procedure is beneficial to the grain refinement, the modification of texture, and then the optimisation of grain boundary.

6.4.1. Grain size

It is well understood that due to the limitation of rolling reductions (from 26/35mm to 5.5mm, 78.8%/84.3%), fine grains are difficult to be achieved through the traditional

producing process because neither phase transformation nor recrystallisation behaviour occurs during this process. It is clearly seen from **Figure 6-1** that for ultra-purified 17%Cr FSS, no phase transformation of the matrix happens during hot rolling [180], which restricts the chances for the formation of fine grains during the traditional producing process. However, it has been described that the thermomechanical processing, viz. controlled rolling, heat treatment, etc., can influence the grain size [173]. Comparatively, the warm rolling process promotes the formation of fine deformed microstructure with high dislocation density, which is beneficial to sufficient static recrystallisation during the relatively long interval prior to finish rolling and its lower dynamic recovery rate associated with the lower processing temperature [181]. Therefore, the refined microstructure and the increased dislocation density after warm rolling can provide more nucleation sites along grain boundaries and higher driving force for recrystallisation during annealing.

It is explained in the previous chapters that uniform and refined grains are effective to simultaneously improve strength and toughness. For strength, the fine grains generate the strengthening effect of grain boundaries, and increase the strength as a result.

Based on **Equation 2-6** and the similar medium Cr (no Mo) FSS example that Paton provided [39], it is calculated that when the grain size ranges from 52.3 μm to 29.9 μm or 21.0 μm, T_c (the value of DBTT) can be varied from 29.7 ℃ to 13.5 ℃ or 0.6 ℃, respectively. This affirmed the relationship between grain size and DBTT in spite of little difference between predicted values and measured values.

6.4.2. Texture

From the results of the ODF maps (φ_2 = 45°) of three steels through different hot rolling processes, it is well known that the as-cast FSS is mainly comprised of columnar microstructure with {0 0 1}<u v w> orientation [182], which causes the strong θ-fibre with the maximum component at <0 0 1>//ND for the steel after the traditional rolling process. Since purified FSS undergoes rapid dynamic recovery before recrystallisation and no phase transformation occurs during the whole manufacturing process, the opportunities for texture randomisation and recrystallisation are restricted. The applying of warm rolling procedure is associated with small dynamic recovery rate and large accumulated deformation stored energy, which can modify the rotation of crystal from θ-fibre to stable γ-fibre, such as {1 1 1}<1 1 2>.

It is well accepted that both formation and subsequent growth of recrystalllisation nuclei depend on the crystallographic orientation of the deformed grains. The stored energy in the deformed regions of various grains represents the nucleation rate and driving force for the growth of the recrystallised nuclei during annealing and the scales with Taylor factor M of the respective grain [183]. The orientations at or near θ-fibre have low Taylor factors, which indicates that they are not likely to form nuclei and difficult to nucleate during annealing. Meanwhile, the γ-fibre orientations between {1 1 1}<1 1 0> and {1 1 1}<1 1 2> have higher Taylor factors, and higher stored energy than θ-fibre, resulting in the preferred nucleation in grains with γ-fibre. **Table 6-5** shows the ratios of the texture components for

three studied steels. It clearly illustrates the situations of each orientation, that is, the orientation of {1 1 1}<1 1 2> in 17CrP1# and 17CrP2# is much higher, and {1 1 1}<1 1 0> in three steels is at the same level.

Table 6-5 Texture component statistics of studied 17Cr steels.

Steel no.	Texture component (%)				
	{0 0 1}<1 1 0>	{1 1 2}<1 1 0>	{1 1 1}<1 1 0>	{1 1 1}<1 1 2>	Others
17CrT#	2.0	11.0	16.0	2.0	69.0
17CrP1#	4.0	12.0	15.0	26.5	42.5
17CrP2#	6.0	15.0	17.5	30.0	31.5

6.4.3. Grain boundary (GB)

As the interactive results of the polycrystal grains, the structures of GBs are determined firstly by the grain size and orientation. Also, the types and distributions of the boundaries are influenced by the misorientation of the adjacent grains. In this study, the two aspects of grain size and texture are combined to analyse the change of GBCD and GB connectivity.

It has been well established that GB plays an important role as preferential site for metallurgical phenomena, and grain refinement and texture evolution can influence the final situation of GB [121, 126]. From **Figure 6-6**, it is demonstrated that the frequencies of low-energy boundaries increase apparently after the addition of warm rolling procedure,

39.8% and 47.1% higher than that of traditional rolling process, approaching 30%, which suggest that the fractions of low-energy boundaries are closely related to the grain size.

The grains with similar orientations are easy to form the GBs of Σ1 or Σ3. For 17CrP1# and 17CrP2#, the grains with <0 0 1>//ND (ND: normal direction) and <1 1 1>//ND can promote the formation of Σ1 or Σ3 CSLBs. The grains with the orientations of {1 1 1}<1 1 0> and {1 1 1}<1 1 2> have an orientation relationship of 30 °<1 1 1>, which constitute Σ13. These are the reasons why more Σ1 and Σ3 appear after the addition of warm rolling process.

As the "special" boundaries, low-Σ CSLB involves lower boundary energies, less impurity or solute segregation, smaller diffusivity, higher resistance to GB sliding and crack nucleation and propagation compared to general boundaries (random boundaries). Among the low-Σ CSLBs, the contribution of Σ1 and Σ3 boundaries to property improvement was found to be the most prominent [164]. A higher frequency of random boundaries can bring about a dominant intergranular fracture. In other words, intergranular brittleness may happen when the frequency of random boundaries exceeds the limitation [165].

As a result of crystallographic constraints, GB connectivity is nonrandom, and used to describe the configurations of triple junctions, where three GBs come together. There are four types of triple junctions that can occur in a material, i.e., 0-CSL (R-R-R), 1-CSL (S-R-R), 2-CSL (S-S-R), and 3-CSL (S-S-S) [184, 185], shown in **Figure 6-10**. GB

connectivity, being often simulated with percolation theory, quantitatively evaluates the frequency of resistant triple junctions that have more low-Σ CSLBs coming together. It is well accepted that GB connectivity, which is regarded as the geometrical configuration of different types of GBs, is able to control a dominant fracture mode and probability of continued intergranular crack propagation in a polycrystal.

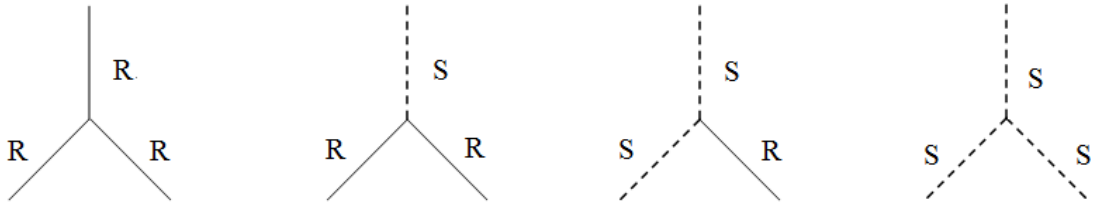

Figure 6-10 Four types of triple junctions (R: random boundary; S: special boundary): (a) 0-CSL; (b) 1-CSL; (c) 2-CSL; (d) 3-CSL.

The role of triple junctions should be considered for crack propagation in a polycrystal since the triple junction can act as either a crack arrester or an assister, depending on the geometrical configuration and the number of random boundaries meeting at a triple junction. When the fraction of special low-Σ is more than 30% that of existing boundaries, the role of triple junctions as crack arresters can be expected in crack propagation [121]. For 17CrT#, 17CrP1# and 17CrP2#, **Figure 6-11** displays the distributions of four types of triple junctions based on the statistical data of **Figure 6-8**. In order to assess the resistance of the microstructure, it is necessary to consider the distributions of those triple junctions, which comprise of at least one boundary that is susceptible to cracking. Hence, the 3-CSL

triple junctions (composed of three special boundaries) can be regarded as inactive entities in the process of arresting advancing cracks. Usually, the fractions of 2-CSL and 3-CSL triple junctions (composed of two or three special boundaries) are critical components in predicting the breaking up of the connectivity of the random boundary networks (or the continuous percolative paths in the microstructure) [186]. The value that the ratio of $f_{2\text{-CSL}}/f_{(1\text{-}3\text{-CSL})}$ ($f_{2\text{-CSL}}$: the fraction of triple junctions that have two special boundaries and are thus able to arrest intergranular cracks; $f_{(1\text{-}3\text{-CSL})}$: the fraction of triple junctions that are active unit entities in the microstructure) is calculated to evaluate whether or not the percolative paths in the microstructure can be broken [184-186]. For 17CrT#, 17CrP1# and 17CrP2#, the values calculated through $f_{2\text{-CSL}}/f_{(1\text{-}3\text{-CSL})}$ are 9.3%, 14.0% and 16.8%, respectively. And the applying of the warm rolling procedure obviously improve the resistance effect of the boundaries to the intergranular cracks.

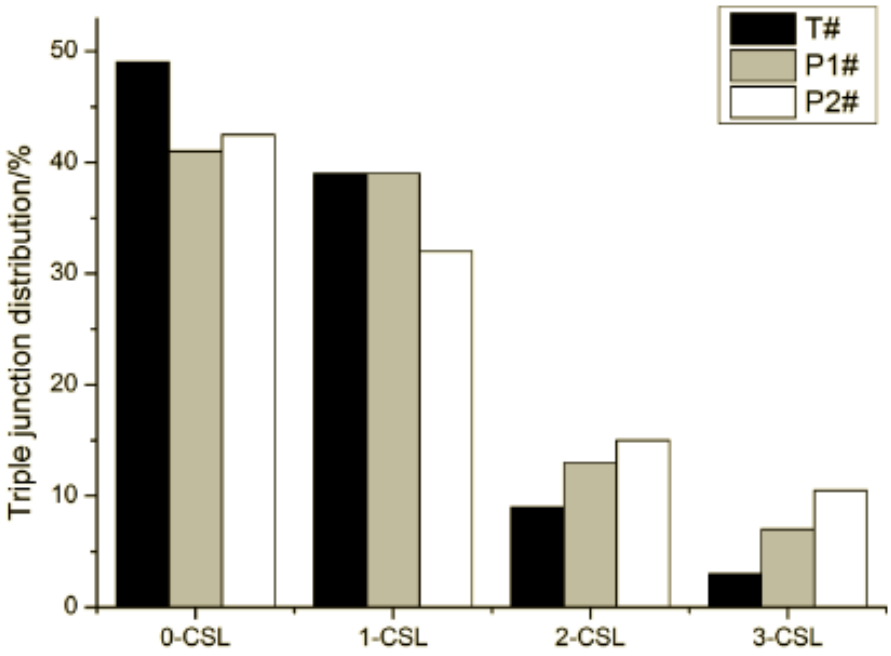

Figure 6-11 Triple junction distributions of 17CrT#, 17CrP1# and 17CrP2#.

In summary, the purpose of studying GBE is to improve materials' mechanical properties via increasing the fraction of low-Σ CSLBs, primarily Σ1 and Σ3 boundaries, and disrupting the connectivity of general boundaries (namely increasing the frequency of resistant triple junctions), which mitigate intergranular fracture in polycrystalline materials. The change of the fracture mode from intergranular to transgranular increases the strength and toughness properties of the materials [121], and meanwhile the elongation is not impaired significantly [120].

6.5. CONCLUSIONS

The effects of processing optimisation on the properties of 17Cr FSSs stabilised by (Nb + V + Ti) were investigated. The relationship between the modification of hot rolling processes and the microstructure, texture, grain boundary and mechanical properties was discussed. Based on the results, the following conclusions can be drawn:

(1) The grain refinement occurs with the additional warm rolling process. This is related to the sufficient static recrystallisation during the long interval before finish rolling and the lower dynamic recovery rate that determined by the lower processing temperature. The result of grain refinement is beneficial to the improvement of impact toughness and strength of the studied steels.

(2) Compared the warm rolling process with the traditional one, the transformation of the texture from the <0 0 1>//ND θ-fibre to γ-fibre orientations between {1 1 1}<1 1 0> and {1 1 1}<1 1 2>, which have higher Taylor factors and higher stored energy, leads to the preferred nucleation in grains.

(3) The modification of grain boundaries including type, structure and character distribution, which are induced by the adjustment of grain size and texture evolution, influences the mechanical properties through the modification of grain boundaries, including the increment of low energy boundaries, especially Σ1, Σ3, and 2-CSL and 3-CSL triple junctions, which are critical to break up the connectivity of the random boundary networks.

Based on above results, the warm rolling process is selectable to improve the mechanical properties, including strength and toughness, through the modification of grain size, texture and grain boundary.

7. FRICTION STIR WELDING

7.1. INTRODUCTION

For pure ferritic stainless steel (FSS) [34], which have been noted for their excellent properties, the fabricating process is of crucial importance if it has to be applied in a number of fields, such as construction. And welding is the most popular method that is selected to joint different parts. As mentioned previously, grain coarsening for thick plates inevitably occurs during manufacturing process if rolling reduction is limited [169], since this steel group does not experience any intermediate phase transformation at high temperature when solidifying from liquid to ferrite phase [187]. Hence, for 18Cr-2Mo steel, the heat generated during conventional liquid-solid welding process, e.g. arc welding, can lead to significant grain coarsening in the welded region, which is known to be harmful to the properties, such as toughness, ductility and corrosion resistance of welds [188]. Therefore, as a typical solid state joining process, friction stir welding (FSW) is frequently tried to put into practise in the field of FSS, especially ultra purified FSS. Apart from the characteristic of solid state joining, it is well known that FSW reduces manufacturing costs on account of the elimination of defects, shielding gas, and costly weld preparation. Also, the process produces high-quality joints with a finer homogeneous microstructure and better mechanical properties that conventional welding processes [131].

In this chapter, friction stir welding was applied for (Nb + V) stabilised 18Cr-2Mo FSS thick plates to investigate the influences of microstructure modification on mechanical properties. As mentioned in **Chapter 2**, FSW is a solid state joining process, which holds promise as an effective method of suppressing development of sensitisation in welds due to a low heat input welding process [129] and eliminates the melting and solidification associated problems, such as liquation and solidification cracking [130].

In this chapter, the welding procedure parameters, i.e. rotational speed and welding speed, were optimised during the FSW process of 5.4 mm 18Cr-2Mo FSS plate in order to obtain a high-quality joint, which is important to the manufacturing process of FSS thick plate.

7.2. EXPERIMENTS

7.2.1. Materials

The manufacturing procedures of the materials used in this study were displayed in **Chapter 3.2.3**, the designed size of the hot rolled plates is 30 mm × 250 mm × 200 mm (thickness × width × length). After being heated at 1150 ℃ for 240 min, the 30 mm forged plate was hot rolled into 5.4 mm plate (the rolling reduction is 82.0%) during the temperature range of 900 ~ 1120 ℃. Finally, this plate was annealed at 1050 ℃ for 6 min, followed by cooling in water.

The chemical composition of the 18Cr-2Mo steel, that welded and coded 18CrFSW#, is listed in **Table 7-1**. The stabilisation ratio of 18CrFSW# is 30.3 through **Equation 2-7**, which is recognised to be a little higher due to accurate control of C content and may influence the corrosion resistance to some degree.

Table 7-1 Chemical composition (in wt.%) of studied steel.

Steel no.	C	Si	Mn	Cr	Mo	Nb	V	N	Fe
18CrFSW#	0.0034	0.29	0.17	18.33	1.81	0.20	0.070	0.0105	Bal.

It is acceptable that the low C content will be beneficial to the properties of steel and its welds. However, the effects of high stabilisation ratio on corrosion resistance were not considered in this chapter.

7.2.2. Friction stir welding process

FSW was conducted using an argon shield around the tool made of cubic boron nitride (cBN) in a W-Re matrix to prevent oxidation of the joint surface and the tool. After extreme levels of plastic deformation and thermal exposure, the welded zone normally exhibits significant microstructural refinement and homogeneity [189]. The tool in this study is designed to friction stir weld FSS efficiently. The detailed design thought of the tool is supplemented in **Appendix**.

The rotational speed, 200 rpm, and the welding speed range between 100 and 160 mm/min (100, 130 and 160 mm/min) was selected to produce FSW joints, aiming at flaw-free joints. The schematic illustration of FSW process is attached in **Appendix** for reference.

7.2.3. Phase calculation

The equilibrium phase diagrams were calculated using Thermo-Calc software, and the recommended temperature range is from 500 to 1600 ℃. The details of precipitation were demonstrated by modifying the scale of *Y* axis from the range of 0 ~ 1 mole to 0 ~ 3 $\times 10^{-3}$ mole.

7.2.4. Microstructure analyses

The as-welded specimens were sectioned, prepared according to the standard metallographic procedures, and then electrolytic etched. The microstructure of the FSW joint was examined using a Leica DMR OM and a FEI Quanta 600 FEG SEM. Qualitative microanalysis of precipitates was determined by energy dispersive spectroscopy (EDS). To further characterise the microstructure, electron backscatter diffraction (EBSD) maps were constructed using a JEOL JSM 7001F FEG-SEM. The step size was 0.7 μm and 0.15 μm on the basis of grain size, and the map covered an area of 1.2 mm × 0.9 mm and 0.25 mm × 0.18 mm with the magnifications of 100× and 500×. The collected data was post-processed by HKL Channel 5 software.

7.2.5. Hardness and impact toughness testing

The Vickers hardness testing was performed at the centreline and mid-thickness of the joint using a load of 0.1 kg and a dwell time of 15 s according to ASTM E384 [190]. The Charpy V-notch impact testing was conducted for several special regions at room temperature, using sub-size (3.3 mm × 10 mm × 55 mm) specimens with T-L orientation according to ASTM A370 [149] and ASTM E23 [157]. The Vickers hardness and Charpy V-notch impact testing instruments are DuraScan 70 automatic hardness tester and Instron-9250 impact tester, respectively.

7.3. RESULTS

7.3.1. Friction stir welding experiment

Figure 7-1 shows the cross-sections of runs made at 100, 130 and 160 mm/min. It is evident that a flaw-free joint was obtained at 100 mm/min. At 130 mm/min and 160 mm/min, the presence of a small root flaw and a gross root flaw happened, which can be regarded as porosity. This affirms that the propensity for cracks or voids increases with the welding speed although there is an alloy-dependence [191].

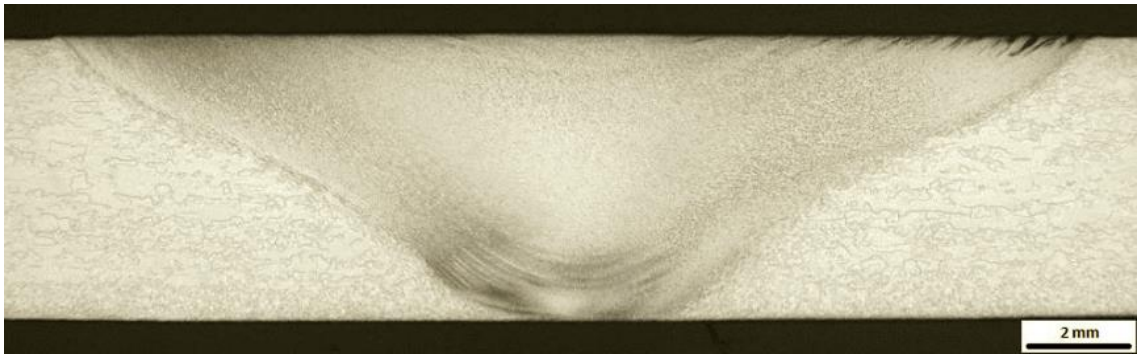

(a)

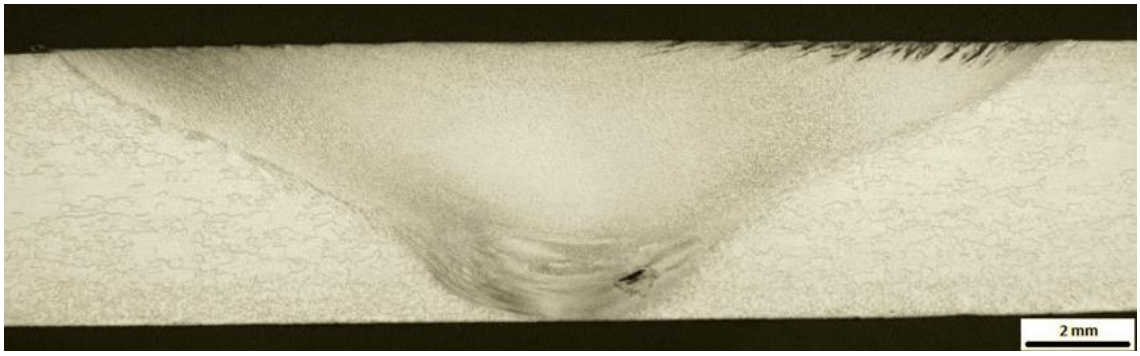

(b)

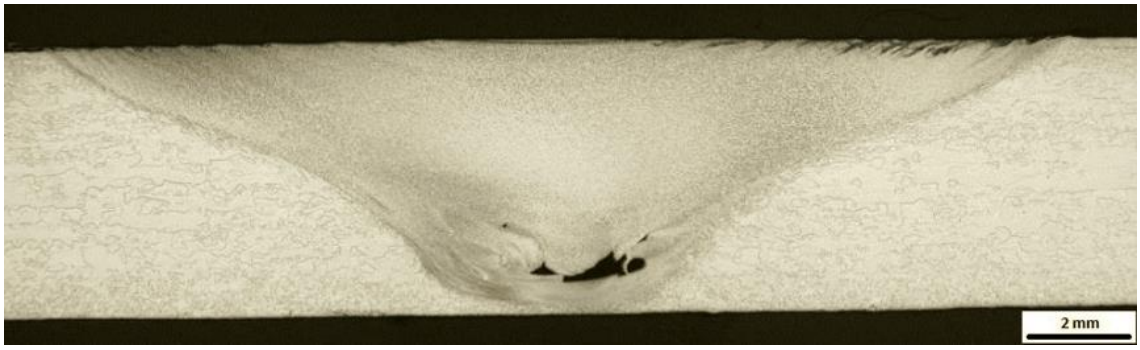

(c)

Figure 7-1 Cross-sections of FSW runs made in 5.4 mm at the designed speeds: (a) 100 mm/min; (b) 130 mm/min; (c) 160 mm/min.

Under the proper FSW parameters, a FSW joint of the studied 18Cr-2Mo FSS thick plate was successfully produced. The cross-sectional macrograph of the welded specimen with a plunge depth of 4.95 mm is displayed in **Figure 7-2**. The weld profile appears "basin-shape". And the macrostructure of the weld can be split into several distinct regions: the stir zone (SZ), the region either side of the SZ which can be termed the thermomechanically affected zone (TMAZ), the heat-affected zone (HAZ). The right- and left-hand sides of the weld centre correspond to advancing side (AS) and retreating side (RS) of the rotation tool, respectively. In addition, the "onion ring" found in the bottom of SZ region is an evidence of material transport phenomena occurring during the FSW process [11].

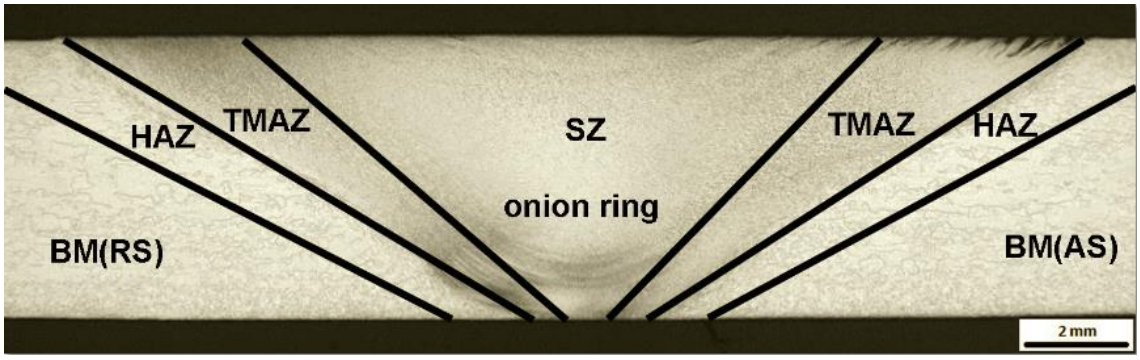

Figure 7-2 Cross-sectional macrograph of the FSW joint made at 100 mm/min.

7.3.2. Equilibrium diagram

The results of Thermo-Calc calculation are shown in **Figure 7-3**. For FSS with high Cr content, no ferrite/austenite phase transformation happens during the cooling process from

the liquidus. Precipitation forms during the temperature range of 600 ~ 1150 ℃ based on the prediction of equilibrium phase. Z phase, i.e. Cr(V,Nb)N, precipitates at 1110 ℃, and then the temperatures for the precipitates of Nb/V to appear are 1095 ℃ and 1008 ℃, respectively. It is known that the peak temperature is approximately 1010 ℃ at the rotational and transverse speeds of 400 rpm and 200 mm/min [192]. This temperature is close to the dissolving temperature of Z phases and Nb/V precipitates. Below 755 ℃, the phases of Chi, Laves and Sigma precipitate out in sequence. However, it has to take a long time for the formation of these three phases [141].

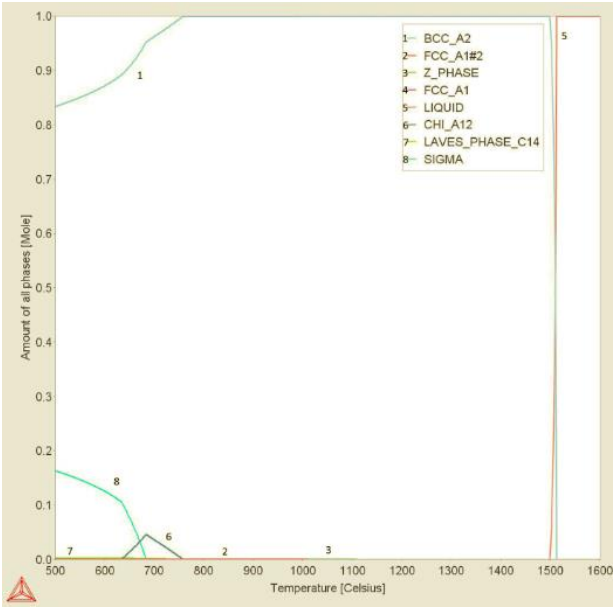

(a)

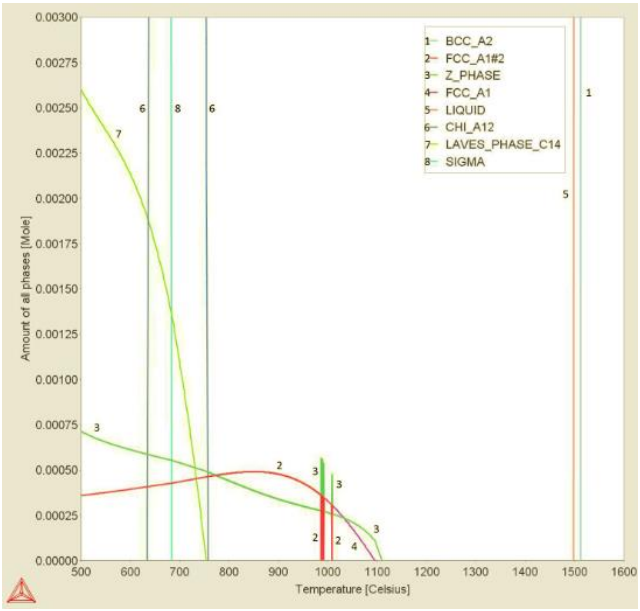

(b)

Figure 7-3 Calculated equilibrium molar fractions of phases in 18CrFSW#: (a) *Y* axis from 0 ~ 1 mole; (b) *Y* axis from 0 ~ 3 $\times 10^{-3}$ mole.

1 Ferrite (BCC_A2); 2 Nb/V precipitate (FCC_A1#2); 3 Z phase (Z_PHASE); 4 Nb/V precipitate (FCC_A1); 5 Liquid (LIGUID); 6 Chi phase (CHI_A12); 7 Laves phase (LAVES_PHASE_C14); 8 Sigma phase (SIGMA).

7.3.3. Microstructure

The schematic for distributed regions of the FSW joint is illustrated in **Figure 7-4**, and the relative OM images are displayed in **Figure 7-5**. For 5.4mm thick FSS plate, due to its limited reduction of hot rolling process and high temperature treatment, BM exhibits the microstructure of considerably coarse-grained ferrite. Fine equiaxed ferrite grains are

observed in the region of SZ. In the shoulder influenced SZ region (**Figure 7-5** (a)), fine ferrite grains form. And in the pin influenced SZ region (**Figure 7-5** (b)), fine and banded ferrite grains are found. A distorted structure with grains re-oriented forms in the regions of TMAZ by the effect of driving force of the tool (**Figure 7-5** (c) and (d)). The grains in the regions of HAZ, whose width is around 200 μm, are similar to that of BM due to the limitation of the temperature generating during the welding process since high temperature above 1000 ℃ definitely promotes grain growth. The HAZ grains turn distorted when suffered by the influences of TMAZ. From **Figure 7-5**(c) and (d), the grain sizes in the SZ of RS are slightly smaller than that in the SZ of AS.

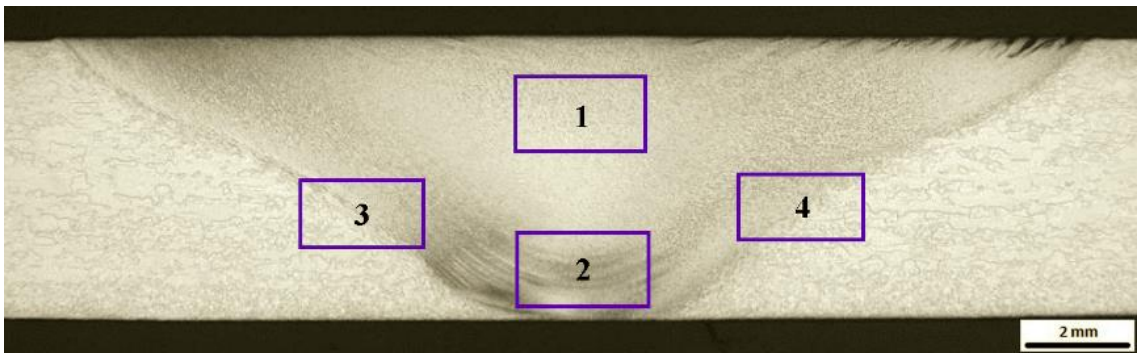

Figure 7-4 Schematic for distributed regions of friction stir welded specimen.

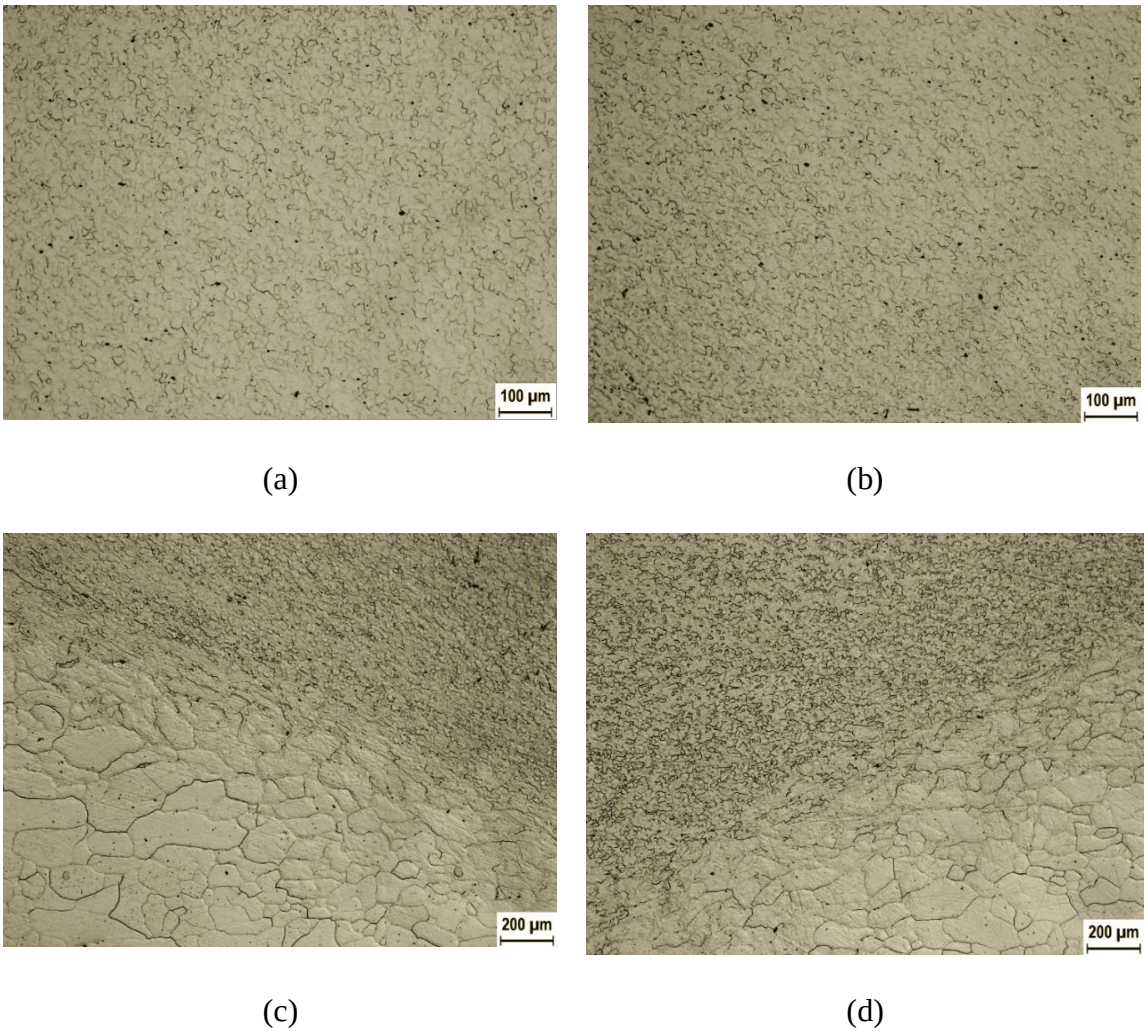

Figure 7-5 OM images of friction stir welded specimen: (a) SZ-shoulder influenced region (Region 1 in **Figure 7-4**); (b) SZ-pin influenced region (Region 2 in **Figure 7-4**); (c) RS (Region 3 in **Figure 7-4**); (d) AS (Region 4 in **Figure 7-4**).

7.3.4. Orientation maps and misorientation distribution

Figure 7-6 exhibits the orientation maps and misorientation-angle distribution of the BM, shoulder influenced and pin influenced regions in the SZ. The considerably fine and uniform grains generated in the SZ, whose average grain sizes are 10.5 μm and 11.9 μm for different influenced regions compared with the size of 88.5 μm for the BM.

In the orientation maps (**Figure 7-6** (a), (c) and (e)), for the BM, the volume fractions of the grains with three orientations are random. For the shoulder influenced SZ, the orientation {h k l}<1 1 1> is apparently dominant. However, for the pin influenced SZ, which is also the region of "onion ring", the orientation is changed to {h k l}<1 0 1>. This undoubtedly validates that severe deformation happens in the pin influenced SZ.

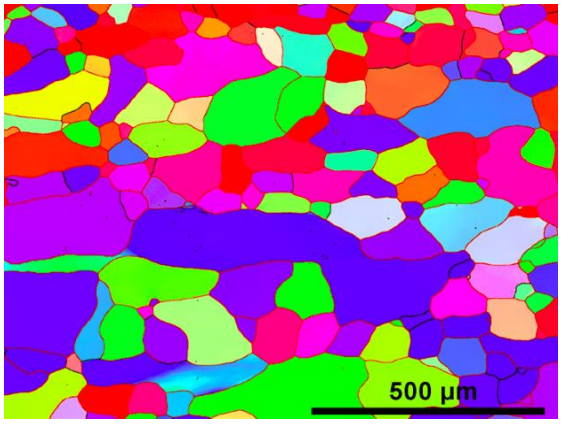

(a)

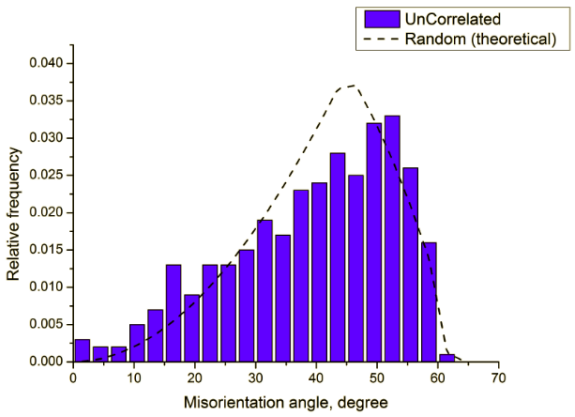

(b)

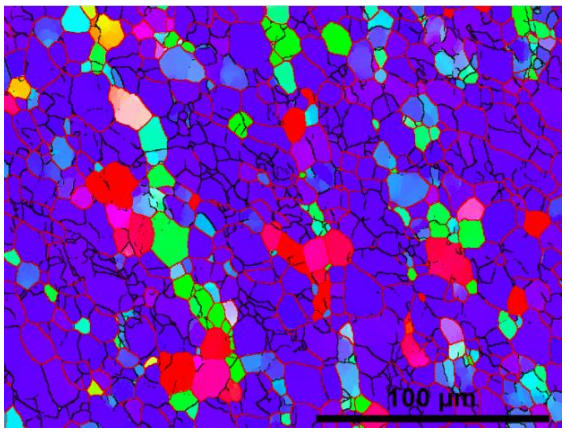

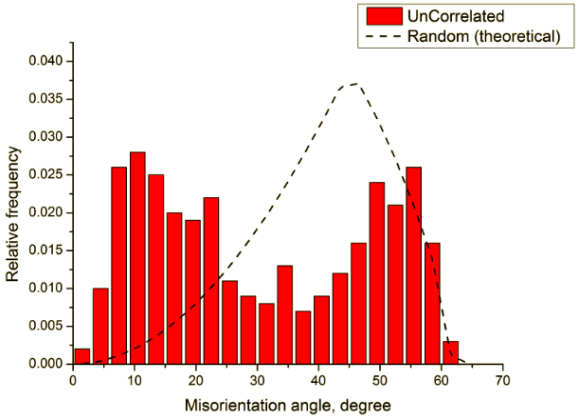

(c) (d)

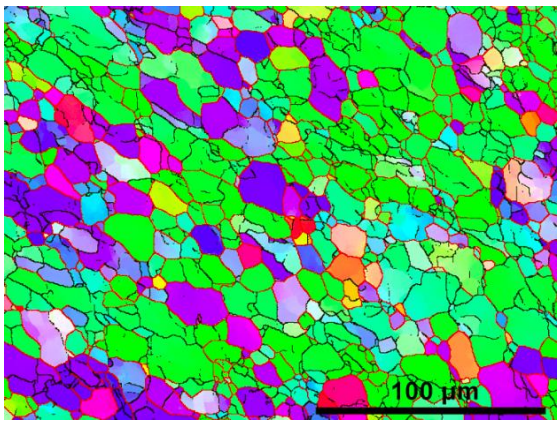

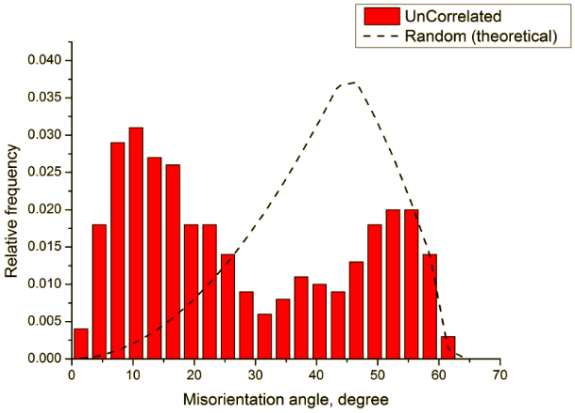

(e) (f)

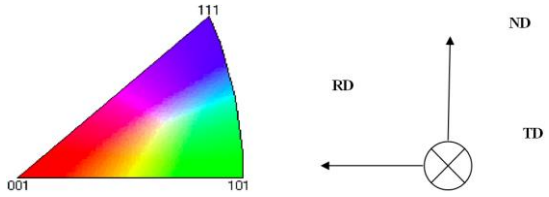

(g)

Figure 7-6 Orientation maps and misorientation-angle distribution (RD: rolling direction; TD: Transverse direction; ND: normal direction): (a)(b) BM; (c)(d) SZ-shoulder influenced region; (e)(f) SZ-pin influenced region; (g) appendix.

The inverse {1 1 0} pole figures of grain orientation are displayed in **Figure 7-7**. Different from the greatly random texture of the BM (**Figure 7-7** (a)), the texture of the SZ regions is consistent with a strong shear texture (**Figure 7-7** (b) and (c)).

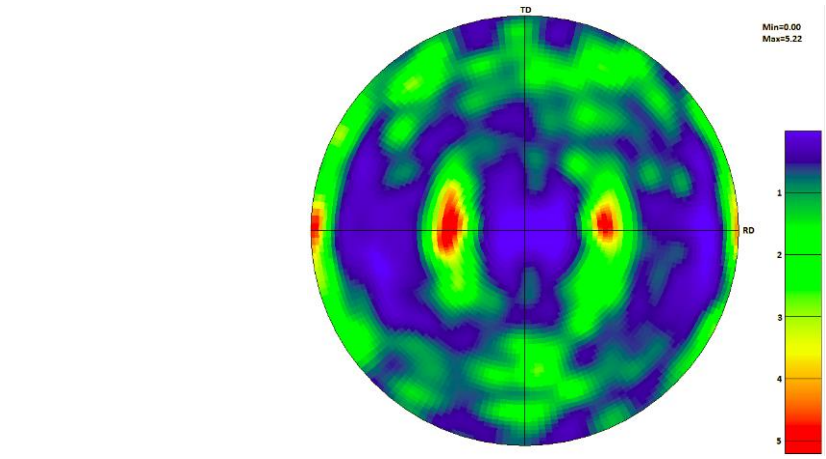

(a)

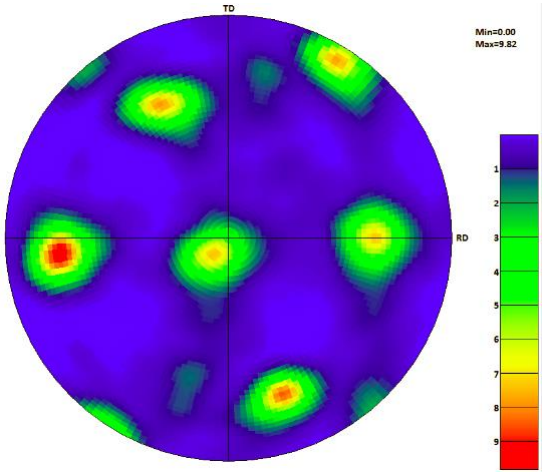

(b)

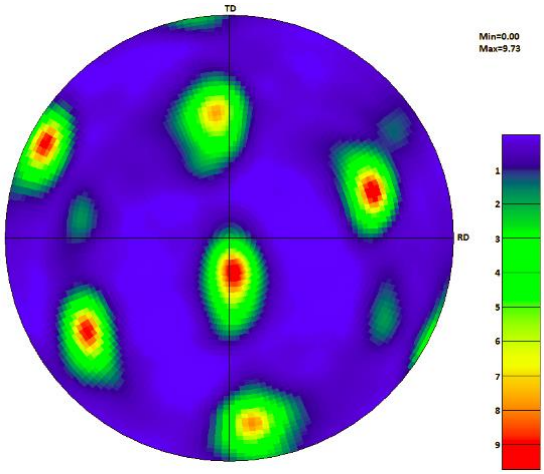

(c)

Figure 7-7 Inverse {1 1 0} pole figures of grain orientation: (a) BM; (b) SZ-shoulder influenced region; (c) SZ-pin influenced region.

7.3.5. Microhardness

The microhardness distributions in the centreline and across the mid-thickness of the FSW joint are shown in **Figure 7-8**. The hardness of the as-received BM is approximately 147 $HV_{0.1}$. The hardness of the SZ varies from 186 to 222 $HV_{0.1}$ in the weld centreline, and from 176 to 194 $HV_{0.1}$ across the mid-thickness. There is not an obvious fluctuation of hardness in the SZ, possibly due to the uniform distribution of ferrite grain sizes in this region. Even for the shoulder influenced and pin influenced regions, the hardness is still kept unchanged, which illustrates the good properties that the SZ microstructure brings to the FSW joint of FSS thick plate. The hardness of the TMAZ varies from 183 to 227 $HV_{0.1}$, and the values of HAZ change from 168 to 209 $HV_{0.1}$.

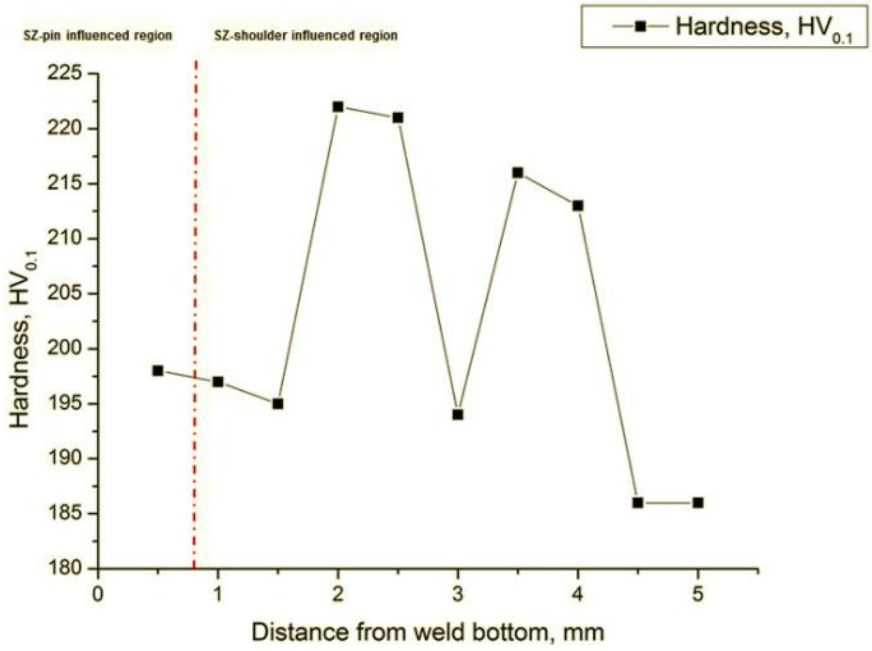

(a)

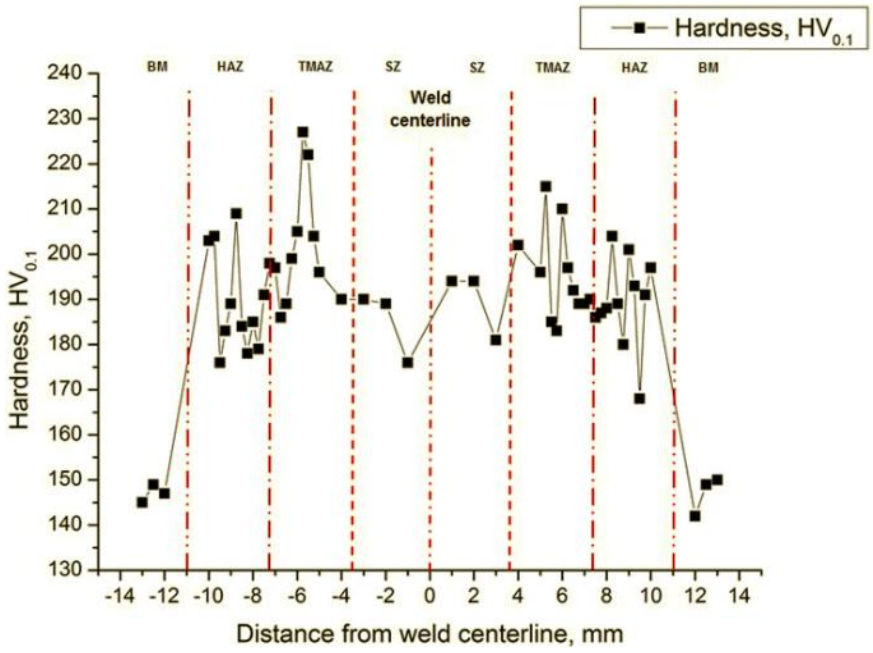

(b)

Figure 7-8 Microhardness distributions of the FSW joint: (a) in the centreline; (b) across the mid-thickness.

7.3.6. Impact toughness

The Charpy impact energy of the FSW joint was measured and displayed in **Figure 7-9**. Compared with the average toughness of BM (78 J), the impact values of the FSW joint exhibit only a slight drop and at the level of 61 ~ 71 J. It is accepted that the grain size significantly influences the mechanical properties of materials. For fine-grained materials, the usual weak boundaries of TMAZ/SZ, HAZ/TMAZ and even BM/HAZ keep the high impact toughness. Furthermore, the deformation of grains in the regions of TMAZ and HAZ does not influence the toughness of the joint either.

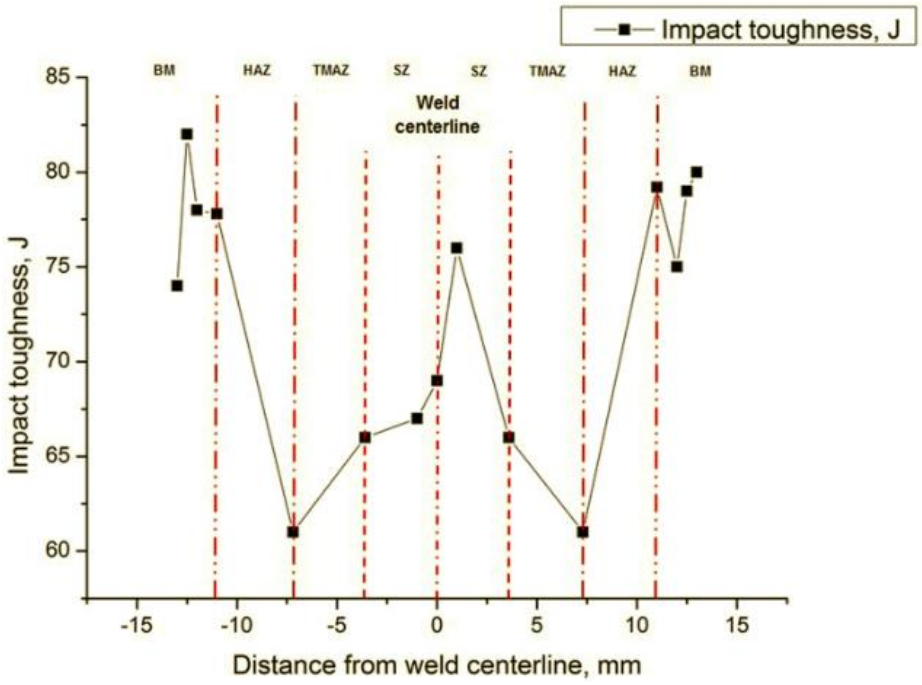

Figure 7-9 Impact toughness distribution of the FSW joint.

7.4. DISCUSSION

7.4.1. Welding quality

From **Figure 7-10**, no apparent precipitation is found in the SZ except some remnant oxides. **Figure 7-11** gives the results of SEM and EDS analyses in some part of the run welded, which display that the remnant oxides are originally from the tool and/or BM, mainly involving the oxides of Al, Si, Mg and Ca. For the FSW joints, the formation of tiny amounts of remnant oxides is unavoidable. The possibility of these oxides is related to oxygen from air during welding and/or the oxides inherited from the tool and/or BM.

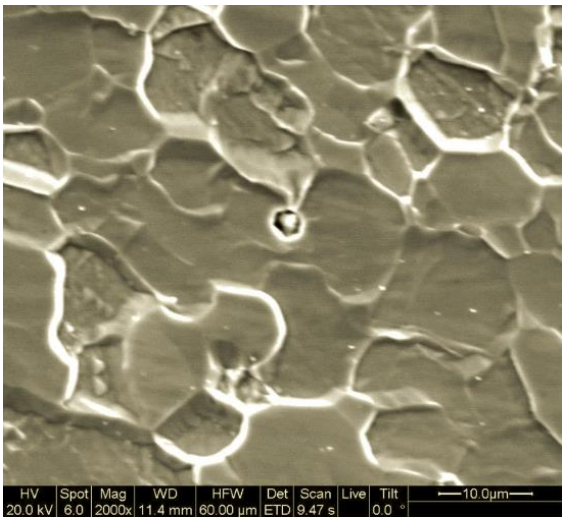

(a)

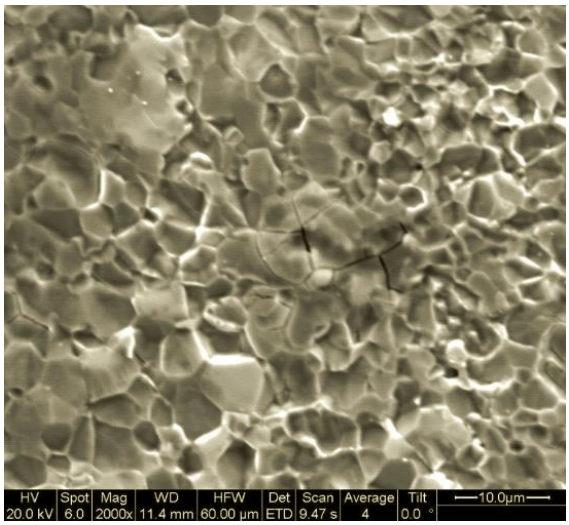

(b)

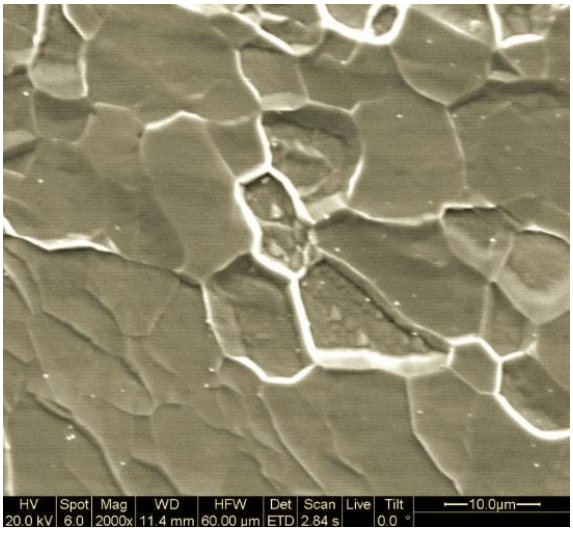

(c)

Figure 7-10 SEM micrographs of different regions of the FSW joint: (a) upper SZ; (b) lower SZ; (c) interface of SZ/HAZ.

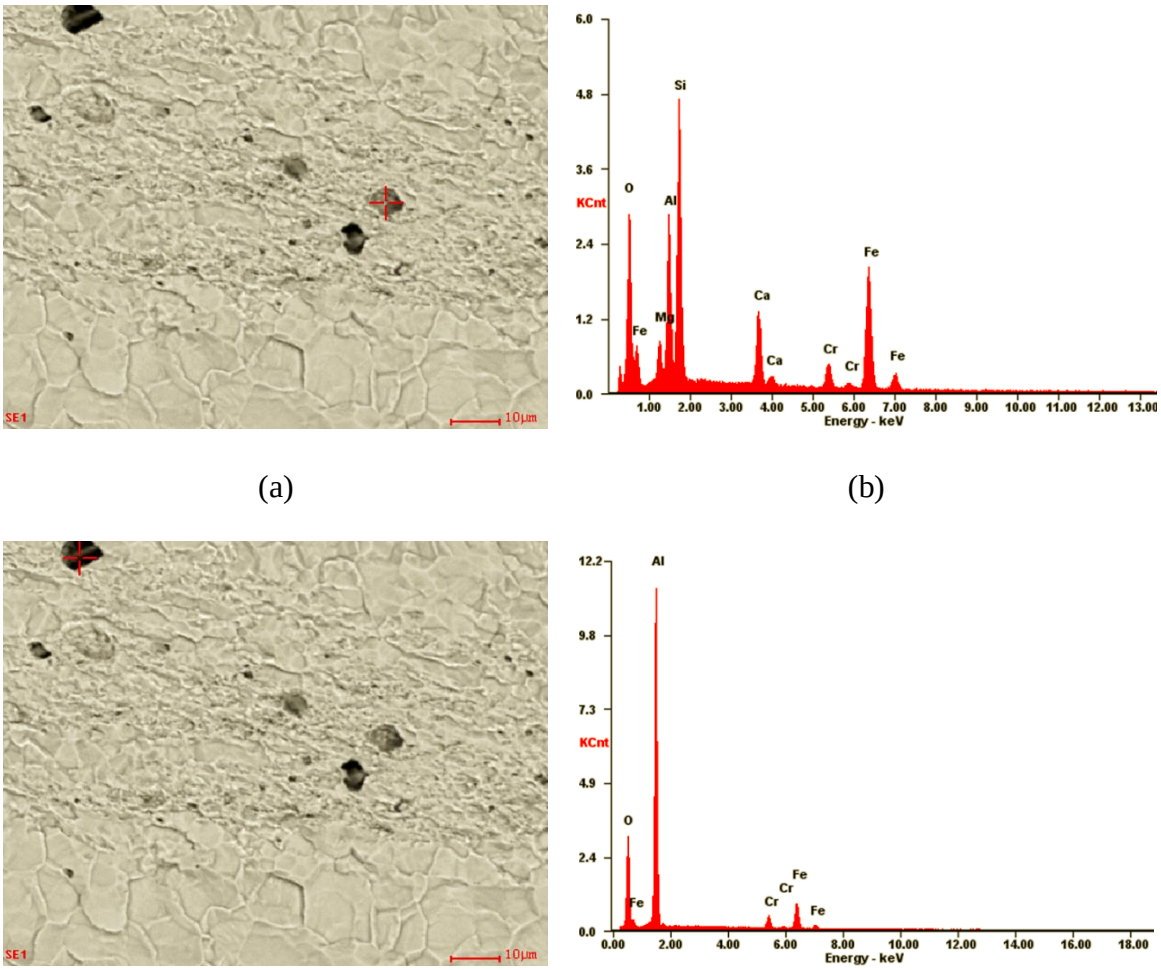

Figure 7-11 SEM results of remnant oxides and the corresponding EDS analysis in the weld root: (a)(c) SEM micrographs of the remnant oxides; (b)(d) EDS analyses of the remnant oxides.

7.4.2. Microstructure analyses

For SZ regions, besides the low peak temperature, which is positive to resist the growth of grains in the weld, the fine grain size in the weld is possibly related to the plastic flow caused by the rotated tool and the existence of stacking fault energy (SFE). With high SFE, the dislocation cells of FSS are more evenly distributed in the whole weld, which can be attributed to high frequency occurrence of dislocation cross-slip [193]. Dislocation cells usually act as nucleation sites during FSW process for recrystallisation. As a result, the higher SFE of FSS may strongly affect the continuous dynamic recrystallisation, resulting in fine grains [188]. In other words, the fine-grained microstructure in the SZ is associated with the dynamic recrystallisation caused by severe shear deformation and the heat generated during the FSW process. In addition, for the pin influenced region, the deformation is more severe, which will lead to the flow of the grains, shown in **Figure 7-5** and **Figure 7-6**. It is acceptable that both shoulder and pin influenced regions obtain much finer grains than that of BM, which is beneficial for the mechanical properties.

The reason why the grain size in the SZ of AS is slightly larger than that in the SZ of RS is related to the different temperature levels that two sides reach. It is known that the recrystallised grains form in the SZ of FSW weld, and then undergo grain growth during the cooling cycle. Since grain growth occurs more rapidly at a higher temperature, it may be suspected that the temperature was slightly higher in the AS than the RS during FSW. Cho et al. [194, 195] found that the temperature on the AS was about 100 ℃ higher than that on the RS.

7.4.3. Orientation and misorientation analyses

The low-angle boundaries (LABs) [164] and the high-angle boundaries (HABs) are depicted as black and red lines respectively in **Figure 7-5**(a), (c) and (e). It is well acceptable that the grain boundaries of the BM are composed of most HABs and a few LABs. Misorientation-angle distribution in the BM is close to a random distribution, which is shown as the dash line in **Figure 7-5**(b). But for the SZ regions, the ratios of LABs increase greatly, shown in **Figure 7-5**(d), (f) and listed in **Table 7-2**. Furthermore, the ratio of LABs in the pin influenced SZ is 5.6% more than that in the shoulder influenced SZ.

Table 7-2 Grain boundary ratios of LABs and HABs in different regions.

Region	Grain boundary ratios	
	LABs (%)	HABs (%)
BM	5.8%	94.2%
SZ-shoulder influenced	27.8%	72.2%
SZ-pin influenced	33.4%	67.6%

From the inverse {1 1 0} pole figures of grain orientation (**Figure 7-7**), the shear plane is presumably parallel to the border between the TMAZ and SZ [196]. Thus shear direction (SD) is identical to welding direction (WD, paralleling to TD) at the AS and the RS. In the SZ, the SD is parallel to RD. This point is applicable to the pole figures in **Figure 7-7**. The

texture caused by the FSW process is very similar to a shear texture associated with simple shear deformation of BCC materials.

7.4.4. Hardness and impact toughness

The hardness of HAZ regions is slightly lower than that of the TMAZ regions because of comparatively larger grain size. However, compared with BM, the hardness in HAZ is maintained in a high level due to the deformation of the grains. Furthermore, it is extensively accepted that refinement of grain size will be an advantage to toughness.

7.5. CONCLUSIONS

In this chapter, the suitable procedure parameters are selected to obtain the FSW joints for 5.4 mm 18Cr-2Mo FSS thick plate. The microstructure, orientation map, misorientaion-angle distribution and mechanical properties of welds were investigated. The following conclusions can be drawn:

(1) The high-quality welds were successfully produced using a composite tool with high volume percentage of cBN in a W-Re matrix, and selected the proper rotational and welding speed.

(2) The significant fine grain sizes were obtained in the regions of SZ and TMAZ due to the mechanical effect and dynamic recrystallisation that obtained by the severe shear deformation and heat generation during the FSW process. At the same time, the fraction of LABs and the degree of texture in the SZ regions increase apparently.

(3) The benefit of the grain refinement to the mechanical properties is confirmed, and the fine-grained microstructure maintains the high level of hardness and impact toughness. For the region of HAZ, the slight deformation of the grains influenced by friction stirring is not harmful to the toughness, and meanwhile, improves hardness apparently.

Based on above results, the FSW is a suitable method to fabricate high-quality 18Cr-2Mo FSS thick plate. The mechanical properties of the joints are maintained at a high level, which is related to the remarkably fine-grained microstructure of equiaxed ferrite in the friction stir welded joint. This modified microstructure after FSW affects the grain boundary and texture apparently.

PART C

CONCLUSIONS

&

REFERENCES

8. CONCLUSIONS AND FUTURE WORK

8.1. CONCLUSIONS

Detailed conclusions regrading 18Cr-2Mo and 17Cr ferritic stainless steel (FSS) thick plates have been described in the key chapters, i.e. chapter 4, 5, 6 and 7. The general conclusions are presented separately for each field as follows.

Microalloying

In this study, the effects of microalloying on the microstructure (grain size, precipitation, grain boundary, etc.) and mechanical properties of 18Cr-2Mo FSS thick grades stabilised by single Nb or combination of Nb, Ti and V have been discussed, and the following conclusions can be drawn.

- For Nb and (Nb + Ti) stabilised grades, the grain sizes of Nb stabilised steel are comparatively smaller, which is related to the fine precipitation at the grain boundaries and beneficial to the impact toughness. And the increase of its strength is not apparent due to the inhomogeneous grain sizes.

- For Nb and (Nb + Ti) stabilised grades, the grain boundary characters are similar, which are not the main factor related to their mechanical properties.

- Compared with (Nb + V + Ti) stabilised grade, (Nb + V) stabilised steel has fine grain size related to fine particles at the grain boundaries. This is beneficial to the improvement of tensile strength and impact toughness of the thick plates. The addition of V is positive to increase the strength of the steel due to its effects of dispersion and solution strengthening.

- For four grades, the main precipitation situations by SEM and TEM after annealing are listed below.

Steel no.	Main precipitates
N#	NbC, Nb(C,N)
NT#	(Ti,Nb)N/TiN, NbC
NV#	Nb(C,N), NbC, VN
NVT#	(Ti,Nb)N, (Nb,Ti)C, NbC

It is evident from the results that Ti can greatly modify the precipitation behaviours of Nb and (Nb + V) composition systems.

- Ti is not a suitable element for stabilising FSS thick plate, since the large TiN particles that form during the manufacturing process are detrimental to impact toughness in initiating the cleavage fracture process.

In sum, the addition of Nb in stabilising 18Cr-2Mo FSS thick plate appears to be applicable to the improvement of mechanical properties. The addition of V is effective in increasing strength and toughness. This suggests that the stabilisation of Nb or (Nb + V) for FSS is a suitable choice.

Processing optimisation

In this study, the effects of processing optimisation, i.e. warm rolling, on microstructure (grain size, texture, grain boundary, etc.) and mechanical properties of 17Cr FSS thick grades stabilised by the elements of Nb, Ti and V have been discussed, and the following conclusions can be drawn.

- The warm rolling procedure at comparatively low temperature leads to the sufficient static recrystallisation and a low dynamic recovery rate. And the grain refinement from warm rolling give rise to the improvement of mechanical properties for 17Cr FSS thick plate.

- The preferred nucleation sites in grains, which are related to the texture of <0 0 1>//ND θ-fiber, promote the grain refinement during the addition of warm rolling procedure.

- Grain boundaries, including type, structure and character distribution, are modified due to the adjustment of grain size and texture evolution during warm rolling process. Consequently, the mechanical properties are optimised through the increase of low energy boundaries and the reduction of random boundary networks.

Based on the above conclusions, processing optimisation, i.e. warm rolling, is beneficial to the mechanical properties of 17Cr FSS thick plate. Due to low C and N contents, no phase transformation was experienced during manufacturing process.

Friction stir welding (FSW)

In this study, the optimised welding parameters have been determined to produce the FSW joints of 18Cr-2Mo FSS thick plate. The effects of the welding procedures on microstructure (grain size, orientation, misorientaion-angle distribution, etc.) and mechanical properties of the FSW welds were investigated. The following conclusions can be drawn.

- A W-Re/cBN composite tool and the optimised rotational and travelling speeds are suitable for producing the FSW joints with high-quality.

- The fine grains in the regions of stir zone (SZ) and thermomechanically affected zone (TMAZ) form due to the severe shear deformation and heat generation during the FSW process. And high fraction of low-angle boundaries (LABs) and texture in the SZ evidently increase during FSW.

- High hardness and excellent impact toughness is considered to be related to the grain refinement that occurs in the regions of SZ and TMAZ. And in the heat-affected zone (HAZ), the slight deformation of the grains generated through friction stirring, has no negative influences on the toughness. Meanwhile, it is apparent that the deformation increases hardness.

- It is obvious that the grain refinement benefits the mechanical properties, and the fine-grained microstructure maintains the high level of hardness and impact toughness. In the HAZ, the slight deformation of the grains caused by friction stirring is not detrimental to the toughness, and meanwhile, evidently improves hardness.

Based on the above conclusions, FSW is suitable for joining 18Cr-2Mo FSS thick plates, which are prone to grain coarsening during conventional liquid-solid welding process. The grain refinement and deformation that the FSW process causes are important to maintain the mechanical properties compared to the base material (BM).

8.2. FUTURE WORK

In this study, some research work will be continued to find more valuable conclusions.

- The microalloying for 18Cr-2Mo FSS thick grades has been investigated. The element of Nb is beneficial to the mechanical properties. In the future, the different stabilisation ratios can be investigated the most optimised additions of Nb element.

- The processing optimisation for 18Cr-2Mo FSS thick grade can be performed to study the effects of warm rolling on the final properties.

- The feasibility of novel welding methods, such as hybrid laser welding and A-TiG, in the properties of 18Cr-2Mo FSS thick grades can also be part of the future work.

REFERENCES

1. Cunat PJ, *Alloying elements in stainless steel and other chromium-containing alloys.* The International Chromium Development Association (ICDA), Paris, 2004.

2. Cunat PJ, *The welding of stainless steels*. In *Materials and Applications Series.* Second ed. The European Stainless Steel Development Association (Euro Inox), Brussels, 2007.

3. Davison RM, Laurin TR, Redmond JD, Watanabe H and Semchyshen M, *A review of worldwide developments in stainless steels.* Materials & design, 1986. 7(3): p. 111-119.

4. Xiao JM, *Metallography issue of stainless steel*. 1st ed. Beijing: Metallorgical Industry Press, 2006.

5. *The Avesta welding manual practice and products for stainless steel welding*. Avesta Welding AB, 2004.

6. *What is stainless steel.* The European Stainless Steel Development Association (Euro Inox), Brussels.

7. *Australian stainless reference manual*. Australian Stainless Steel Development Association, Brisbane, 2005.

8. Lo K, Shek C and Lai J, *Recent developments in stainless steels.* Materials Science and Engineering: R: Reports, 2009. 65(4): p. 39-104.

9. *This is Outokumpu: stainless steel & high performance alloys.* Outokumpu: Espoo.

10. *Book of new application (stainless steel)*. International Stainless Steel Forum, Brussels, 2011.

11. Lippold JC and Kotecki DJ, *Welding metallurgy and weldability of stainless steels.* Wiley-VCH, 2005.

12. Kovach CW, *High-performance stainless steels*, Technical Marketing Resources Inc: Pittsburgh.

13. Schaeffler AL, *Selection of austenitic electrodes for welding dissimilar metals.* Welding Journal, 1947. 26(10): p. 601-620.

14. *Steel grades, properties and global standards.* Outokumpu: Espoo.

15. *BS EN 10088-2*: 2014, *Stainless steels: technical delivery conditions for sheet/plate and strip of corrosion resisting steels for general purposes*. 2014.

16. *www.thermocalc.com*.

17. Zheng HB, *Study of weldability of 12CrNi ferritic stainless steel*. PhD Thesis, Shenyang: Northeast University, 2010.

18. Zheng HB, Ye NX, Li JD, Jiang LZ, Liu ZY, Wang GD and Wang BS, *Effect of carbon content on microstructure and mechanical properties of hot-rolled low carbon 12Cr–Ni stainless steel.* Materials Science and Engineering: A, 2010. 527(27): p. 7407-7412.

19. Van Zwieten A and Bulloch J, *The influence of interstitial solute level on the Charpy toughness properties of a 40% Cr-Fe stainless steel.* International Journal of Pressure Vessels and Piping, 1993. 56(1): p. 69-91.

20. Van Zwieten A and Bulloch J, *The dynamic fracture toughness properties of a Fe-40 Cr alloy: The effect of interstitial solutes.* International Journal of Pressure Vessels and Piping, 1994. 57(1): p. 31-44.

21. Kaneko M and Isaacs H, *Effects of molybdenum on the pitting of ferritic-and austenitic-stainless steels in bromide and chloride solutions.* Corrosion Science, 2002. 44(8): p. 1825-1834.

22. Pardo A, Merino MC, Coy AE, Viejo F, Arrabal R and Matykina E, *Effect of Mo and Mn additions on the corrosion behaviour of AISI 304 and 316 stainless steels in H_2SO_4.* Corrosion Science, 2008. 50(3): p. 780-794.

23. Kuzucu V, Aksoy M, Korkut MH and Yildirim MM, *The effect of niobium on the microstructure of ferritic stainless steel.* Materials Science and Engineering: A, 1997. 230(1): p. 75-80.

24. Fujita N, Ohmura K, Kikuchi M, Suzuki T, Funaki S and Hiroshige I, *Effect of Nb on high-temperature properties for ferritic stainless steel.* Scripta Materialia, 1996. 35(6): p. 705-710.

25. Fujita N, Ohmura K and Yamamoto A, *Changes of microstructures and high temperature properties during high temperature service of Niobium added ferritic stainless steels.* Materials Science and Engineering: A, 2003. 351(1): p. 272-281.

26. Gordon W and Van Bennekom A, *Review of stabilisation of ferritic stainless steels.* Materials Science and Technology, 1996. 12(2): p. 126-131.

27. *www.worldstainless.org*.

28. *The ferritic solution (properties, advantages and applications)*. 2007, International Stainless Steel Forum: Brussels.

29. *JFE stainless steels.* JFE Steel Corporation.

30. *www.kitco.com*.

31. *JIS G 4304: 2012, Hot-rolled stainless steel plate, sheet and strip*. 2012.

32. *JIS G4305: 2012, Cold-rolled stainless steel plate, sheet and strip*. 2012.

33. Shan YS, Luo XH, Hu XQ and Liu S, *Mechanisms of solidification structure improvement of ultra pure 17 wt% Cr ferritic stainless steel by Ti, Nb addition.* Journal of Materials Science & Technology, 2011. 27(4): p. 352-358.

34. Yan HT, Bi HY, Li X and Xu Z, *Microstructure and texture of Nb+ Ti stabilized ferritic stainless steel.* Materials Characterization, 2008. 59(12): p. 1741-1746.

35. Du W, Jiang LZ, Sun QS, Liu ZY and Zhang X, *Microstructure, texture, and formability of Nb+ Ti stabilized high purity ferritic stainless steel.* Journal of Iron and Steel Research, International, 2010. 17(6): p. 47-52.

36. Shu J, Bi HY, Li X and Xu Z, *Effect of Ti addition on forming limit diagrams of Nb-bearing ferritic stainless steel.* Journal of Materials Processing Technology, 2012. 212(1): p. 59-65.

37. Almagro JF, Llovet X, Heredia A, Luna C and Sánchez, *Soluble fraction of stabilising elements in ferritic stainless steel.* Microchimica Acta, 2008. 161(3-4): p. 323-327.

38. Kim JK, Lee BJ, Lee BH, Kim YH and Kim KY, *Intergranular segregation of Cr in Ti-stabilized low-Cr ferritic stainless steel.* Scripta Materialia, 2009. **61**(12): p. 1133-1136.

39. Paton R, *Notch and fracture toughness studies on stainless steels containing vanadium.* ISIJ international, 1998. 38(9): p. 1007-1014.

40. Gao F, Liu ZY, Liu HT and Wang GD, *Toughness under different rolling processes in ultra purified Fe-17 wt% Cr alloy steels.* Journal of Alloys and Compounds, 2013. 567: p. 141-147.

41. *www.ndt-ed.org*.

42. *http://practicalmaintenance.net*.

43. Odette G, *On the ductile to brittle transition in martensitic stainless steels—mechanisms, models and structural implications.* Journal of Nuclear Materials, 1994. 212: p. 45-51.

44. Rosenfield A and Majumdar B, *Micromechanisms and toughness for cleavage fracture of steel.* Nuclear Engineering and Design, 1987. 105(1): p. 51-57.

45. Zhu XK and Joyce JA, *Review of fracture toughness (G, K, J, CTOD, CTOA) testing and standardization.* Engineering Fracture Mechanics, 2012. 85: p. 1-46.

46. Anderson TL, *Fracture Mechanics: Fundamentals and applications.* 3rd ed. USA: Taylor & Francis Group CRC Press. 2005.

47. Leffler B, *Stainless Steels and their Properties.* 2nd ed. ISBN 91-9720-216-9.

48. Van Zwieten A and Bulloch J, *Some considerations on the toughness properties of ferritic stainless steels—A brief review.* International Journal of Pressure Vessels and Piping, 1993. 56(1): p. 1-31.

49. Wright R and Rula R, *Toughness of ferritic stainless steels*. In *Toughness of Ferritic Stainless Steels.* ASTM International, 1980.

50. Mueller E, *Influence of carbon and nitrogen on the toughness of ferritic chromium steels.* Neue Heute, 1977. 22(5): p. 273-6.

51. Wolff I and Ball A, *Ductility in high-chromium super-ferritic alloys—I. Microstructural influences on the ductile-brittle transition.* Acta Metallurgica et Materialia, 1991. 39(11): p. 2759-2770.

52. Wolff I, Premachandra K and Cortie M, *Second-phase particles in ferritic stainless steels containing 40% chromium.* Materials Characterization, 1992. 28(2): p. 139-148.

53. Sello MP and Stumpf W, *Laves phase embrittlement of the ferritic stainless steel type AISI 441.* Materials Science and Engineering: A, 2010. 527(20): p. 5194-5202.

54. Guimarães A and Mei P, *Precipitation of carbides and sigma phase in AISI type 446 stainless steel under working conditions.* Journal of Materials Processing Technology, 2004. 155: p. 1681-1689.

55. Park JH, *Effect of inclusions on the solidification structures of ferritic stainless steel: Computational and experimental study of inclusion evolution.* Calphad, 2011. 35(4): p. 455-462.

56. Mintz B and Kolahi-Aval J, *Influence of grain boundary carbide density on impact behaviour of C-Mn-Nb-Al steels.* Materials Science and Technology, 1986. 2(10): p. 1046-1050.

57. Yoo O, Oh YJ, Lee BS and Nam SW, *The effect of the carbon and nitrogen contents on the fracture toughness of Type 347 austenitic stainless steels.* Materials Science and Engineering: A, 2005. 405(1): p. 147-157.

58. Binder W and Spendelow Jr HR, *The influence of chromium on the mechanical properties of plain chromium steels.* Transactions ASM, 1951. 43: p. 759-772.

59. Petty ER, *Physical metallurgy of engineering materials.* Allen & Unwin, 1968.

60. Semchyshen M, Bond PA and Dundas HJ, *Effects of composition on ductility and toughness of ferritic stainless steels.* Proceedings of Symposium on Toward Improved Ductility and Toughness, Kyoto, Japan, 1971, p. 239-253.

61. Rinebolt J and Harris Jr W, *Effect of alloying elements on notch toughness of pearlitic steels.* Transactions ASM, 1951. 43: p. 1175-1214.

62. Johnson AA and Storey RJ, *The effect of carbon on the Charpy V-notch ductile-brittle transition curve.* Technique Report.

63. Honda R and Taga H, *Effect of carbon and oxygen on the fracture of iron.* Metal Science, 1968. 2(1): p. 172-176.

64. Grubb JF and Wright RN, *The role of C and N in the brittle fracture of Fe-26 Cr.* Metallurgical Transactions A, 1979. 10(9): p. 1247-1255.

65. Petch N, *The ductile-brittle transition in the fracture of α-iron: I.* Philosophical Magazine, 1958. 3(34): p. 1089-1097.

66. Plumtree A and Gullberg R, *Influence of interstitial and some substitutional alloying elements.* In *Toughness of Ferritic Stainless Steels.* ASTM International, 1980.

67. Ohashi N, Ono Y, Kinoshita N and Yoshioka K, *Effects of metallurgical and mechanical factors in Charpy impact toughness of extra low interstitial ferritic stainless steels*. In *Toughness of Ferritic Stainless Steels.* ASTM International, 1980.

68. Wasen J, Hamberg K and Karlsson B, *The influence of grain size and fracture surface geometry on the near-threshold fatigue crack growth in ferritic steels.* Materials Science and Engineering: A, 1988. 102(2): p. 217-226.

69. Petch N, *The influence of grain boundary carbide and grain size on the cleavage strength and impact transition temperature of steel.* Acta Metallurgica, 1986. 34(7): p. 1387-1393.

70. Deverell H, *Toughness properties of vacuum induction melted high chromium ferritic stainless steels.* In *Toughness of Ferritic Stainless Steels.* ASTM International, 1980.

71. Mintz B, Morrison W and Jones A, *Influence of carbide thickness on impact transition temperature of ferritic steels.* Metals Technology, 1979. 6(1): p. 252-260.

72. Cavazos J, *Characterization of precipitates formed in a ferritic stainless steel stabilized with Zr and Ti additions.* Materials Characterization, 2006. 56(2): p. 96-101.

73. Ogwu A and Davies T, *Improving the sensitisation resistance of ferritic stainless steels.* Scripta Materialia, 1997. 37(3): p. 259-263.

74. Demo J, *Weldable and corrosion-resistant ferritic stainless steels.* Metallurgical Transactions, 1974. 5(11): p. 2253-2256.

75. *Baosteel manufacturing report-ferritic stainless steel B444M1*. Baosteel Iron & Steel Co. Ltd. 2010.

76. Lagneborg R, Siwecki T, Zajac S and Hutchinson B, *The role of vanadium in microalloyed steels.* Scandinavian Journal of Metallurgy, 1999. 28(5).

77. Gates J and Jago R, *Effect of nitrogen contamination on intergranular corrosion of stabilized ferritic stainless steels.* Materials Science and Technology, 1987. 3(6): p. 450-454.

78. Aksoy M, Kuzucu V, Korkut MH and Yildirim MM, *The effect of niobium and homogenization on the wear resistance and some mechanical properties of ferritic*

stainless steel containing 17-18 wt.% chromium. Journal of Materials Processing Technology, 1999. 91(1): p. 172-177.

79. Abo H, *Role of carbon and nitrogen on the toughness and intergranular corrosion of ferritic stainless steel*. In *Stainless Steels.* 1977.

80. Steigerwald R, *The physical metallurgy of Fe-Cr-Mo ferritic stainless steels: a review.* Metallurgical and Materials Technology, 1978. 10(4): p. 181-189.

81. Anttila S, Karjalainen LP and Porter DA. *The effect of stabilizers on the grain growth and impact toughness of 21% Cr ferritic stainless steels high-temperature heat-affected zones*. Materials Science Forum, 2013. 762: p. 562-569.

82. Terazawa T, Higashiyama H and Sekino S. *Towards improved ductility and toughness*. Kyoto International Conference, B1SI Translation, 1971.

83. Sousa C and Kuri S, *Relationship between niobium content and pitting corrosion resistance in ferritic stainless steels.* Materials Letters, 1995. 25(1): p. 57-60.

84. Malfliet A, Mompiou F, Chassagne F, Mithieux JD, Blanpain B and Wollants P, *Precipitation in Nb-stabilized ferritic stainless steel investigated with in-situ and ex-situ transmission electron microscopy.* Metallurgical and Materials Transactions A, 2011. 42(11): p. 3333-3343.

85. Sim GM, Ahn JC, Hong SC, Lee KJ and Lee KS, *Effect of Nb precipitate coarsening on the high temperature strength in Nb containing ferritic stainless steels.* Materials Science and Engineering: A, 2005. 396(1): p. 159-165.

86. Grubb J, *Stabilization of high-Chromium, ferritic stainless steels*. Proceedings of International Conference on Stainless Steels, Nippon Convention Center, Chiba, Japan, June 1991.

87. Redmond JD, *Toughness of 18Cr-2Mo stainless steel.* In *Toughness of Ferritic Stainless Steels.* ASTM International, 1980.

88. Min D, Liu SS, Hong H, Tao P and Zhang PL, *Strength and infrared assessment of spot-welded sheets on ferrite steel.* Materials & Design, 2013. 52: p. 353-358.

89. Du J, Strangwood M and Davis C, *Effect of TiN particles and grain size on the Charpy impact transition temperature in steels.* Journal of Materials Science & Technology, 2012. 28(10): p. 878-888.

90. Dirras GF, Donnadieu P and Douin J, *Dislocation/precipitate interaction mechanisms in 6xxx aluminum alloys.* Problems of Materials Science, 2003. 1: p. 33-40.

91. Yan W, Shan Y and Yang K, *Influence of TiN inclusions on the cleavage fracture behavior of low-carbon microalloyed steels.* Metallurgical and Materials Transactions A, 2007. 38(6): p. 1211-1222.

92. Wood JR, *Effect of residual elements and molybdenum additions on annealed and welded mechanical properties of 18Cr ferritic stainless steels.* In *Toughness of Ferritic Stainless Steels.* ASTM International, 1980.

93. Grubb JF, Wright RN and Farrar Jr P, *Micromechanisms of brittle fracture in titanium-stabilized and α'-embrittled ferritic stainless steels.* In *Toughness of Ferritic Stainless Steels.* ASTM International, 1980.

94. Folkhard E, *Welding metallurgy of stainless steels.* New York: Springer-Verlag Wien, 1987.

95. Devine T, Ritter A and Drummond B, *Influence of heat treatment on the sensitization of 18Cr-2Mo-Ti stabilized ferritic stainless steel.* Metallurgical Transactions A, 1981. 12(12): p. 2063-2069.

96. Villafuerte J, Kerr H and David S, *Mechanisms of equiaxed grain formation in ferritic stainless steel gas tungsten arc welds.* Materials Science and Engineering: A, 1995. 194(2): p. 187-191.

97. Kuzucu V, Aksoy M and Korkut M, *The effect of strong carbide-forming elements such as Mo, Ti, V and Nb on the microstructure of ferritic stainless steel.* Journal of Materials Processing Technology, 1998. 82(1): p. 165-171.

98. Premachandra K, *Innovation stainless steel*. Florence, Italy, 1993.

99. ASTM A240/A240M-05, *Standard specification for chromium and chromium-nickel stainless steel plate, sheet, and strip for pressure vessels and for general applications.* 2005.

100. Wang LX, Song CJ, Sun FM, Li LJ and Zhai QJ, *Microstructure and mechanical properties of 12wt.% Cr ferritic stainless steel with Ti and Nb dual stabilization.* Materials & Design, 2009. 30(1): p. 49-56.

101. Craven AJ, He K, Garvie LAJ and Baker TN, *Complex heterogeneous precipitation in titanium–niobium microalloyed Al-killed HSLA steels—I.(Ti, Nb)(C, N) particles.* Acta Materialia, 2000. 48(15): p. 3857-3868.

102. Tokuno K, Hamada K, Uemori R, Takeda T and Itoh K, *A complex carbonitride of niobium and vanadium in 9% Cr ferritic steels.* Scripta Metallurgica et Materialia, 1991. 25(4): p. 871-876.

103. Onizawa T, Wakai T, Ando M and Aoto K, *Effect of V and Nb on precipitation behavior and mechanical properties of high Cr steel.* Nuclear Engineering and Design, 2008. 238(2): p. 408-416.

104. Najafi H, Rassizadehghani J and Asgari S, *As-cast mechanical properties of vanadium/niobium microalloyed steels.* Materials Science and Engineering: A, 2008. 486(1): p. 1-7.

105. Show BK, Veerababu R, Balamuralikrishnan R and Malakondaiah, *Effect of vanadium and titanium modification on the microstructure and mechanical properties of a microalloyed HSLA steel.* Materials Science and Engineering: A, 2010. 527(6): p. 1595-1604.

106. Yong QL, *Second phase in steel materials*. Beijing: Metallurgical Industry Press, 2006.

107. Šmida T and Bošanský J, *Deformation twinning and its possible influence on the ductile brittle transition temperature of ferritic steels.* Materials Science and Engineering: A, 2000. 287(1): p. 107-115.

108. Šmida T and Bošanský J, *Fracture mode transition phenomena in steels as a consequence of the change of operating deformation mode.* Materials Science and Engineering: A, 2002. 323(1): p. 21-26.

109. ASTM E112-13, *Standard test methods for determining average grain size.* 2013.

110. Tanaka T, *Controlled rolling of steel plate and strip.* International Metals Reviews, 1981. 26(1): p. 185-212.

111. Taguchi M, Sumitomo H, Ishibashi R and Aono Y, *Effect of Zirconium oxide addition on mechanical properties in ultrafine grained ferritic stainless steels.* Materials Transactions, 2008. 49(6): p. 1303-1310.

112. Nichol TJ, *Mechanical properties of a 29 Pct Cr-4 Pct Mo-2 Pct Ni ferritic stainless steel.* Metallurgical Transactions A, 1977. 8(2): p. 229-237.

113. Franson I, *Mechanical properties of high purity Fe-26 Cr-1 Mo ferritic stainless steel.* Metallurgical Transactions, 1974. 5(11): p. 2257-2264.

114. Van Zwieten A, *The effect of hot work on the impact energy of Fe-40Cr.* Final year project report, University of the Witwatersrand, 1985.

115. Plumtree A and Gullberg R, *Influence of interstitial content on the ductile-brittle transition temperature of Fe-25 Cr ferritic stainless steels.* ASTM Journal of Testing and Evaluation, 1974. 2(5): p. 331-336.

116. Gutiérrez I, *Effect of microstructure on the impact toughness of Nb-microalloyed steel. Generalisation of existing relations from ferrite-pearlite to high strength microstructures.* Materials Science and Engineering: A, 2013. 571: p. 57-67.

117. Linaza MA, Romero JL, Rodríguez-Ibabe JM and Urcola JJ, *Improvement of fracture toughness of forging steels microalloyed with titanium by accelerated cooling after hot working.* Scripta Metallurgica et Materialia, 1993. 29(9): p. 1217-1222.

118. Tikhonova M, Kaibyshev R, Fang X, Wang W and Belyakov A, *Grain boundary assembles developed in an austenitic stainless steel during large strain warm working.* Materials Characterization, 2012. 70: p. 14-20.

119. Patala S, Mason JK and Schuh CA, *Improved representations of misorientation information for grain boundary science and engineering.* Progress in Materials Science, 2012. 57(8): p. 1383-1425.

120. Tan L, Allen TR and Busby JT, *Grain boundary engineering for structure materials of nuclear reactors.* Journal of nuclear materials, 2013. 441(1): p. 661-666.

121. Watanabe T and Tsurekawa S, *The control of brittleness and development of desirable mechanical properties in polycrystalline systems by grain boundary engineering.* Acta Materialia, 1999. 47(15): p. 4171-4185.

122. Diaz-Fuentes M, Iza-Mendia A and Gutiérrez I, *Analysis of different acicular ferrite microstructures in low-carbon steels by electron backscattered diffraction. Study of their toughness behavior.* Metallurgical and Materials Transactions A, 2003. **34**(11): p. 2505-2516.

123. Cao SQ, Zhang JX, Wu JS and Chen JG, *Study of texture and grain boundary character distributions of IF steels.* Acta Metallurgica Sinica-Chinese Edition-(Acta Metall Sin), 2004. 40: p. 1045-1050.

124. Gertsman VY and Bruemmer SM, *Study of grain boundary character along intergranular stress corrosion crack paths in austenitic alloys.* Acta Materialia, 2001. 49(9): p. 1589-1598.

125. Allen T, Was G and Gan J, *Grain boundary engineering and radiation resistance of GFR candidate metallic materials. Project: High temperature metallic materials for GFR.* Technical Report, July 2006.

126. Watanabe T, *Grain boundary design for advanced materials on the basis of the relationship between texture and grain boundary character distribution (GBCD).* Textures and Microstructures, 1993. 20: p. 195-216.

127. Bhattacharjee D and Davis CL, *Influence of processing history on mesotexture and microstructure-toughness relationship in control-rolled and normalised steels.* Scripta Materialia, 2002. 47(12): p. 825-831.

128. Mishra RS and Mahoney MW, *Friction stir welding and processing*. USA: ASM International, 2007.

129. Park SHC, Sato YS, Kokawa H, Okamoto K and Hirano S, *Corrosion resistance of friction stir welded 304 stainless steel.* Scripta Materialia, 2004. 51(2): p. 101-105.

130. Santos TFA, Hermenegildo TFC, Afonso CRM, Marinho RR, Paes MTP and Ramirez AJ, *Fracture toughness of ISO 3183 X80M (API 5L X80) steel friction stir welds.* Engineering Fracture Mechanics, 2010. **77**(15): p. 2937-2945.

131. Sato YS, Kurihara Y, Park SHC, Kokawa H and Tsuji N, *Friction stir welding of ultrafine grained Al alloy 1100 produced by accumulative roll-bonding.* Scripta Materialia, 2004. 50(1): p. 57-60.

132. Nandan R, DebRoy T and Bhadeshia HKDH, *Recent advances in friction-stir welding–process, weldment structure and properties.* Progress in Materials Science, 2008. 53(6): p. 980-1023.

133. Sato YS, Nelson TW and Sterling CJ, *Recrystallization in type 304L stainless steel during friction stirring.* Acta Materialia, 2005. 53(3): p. 637-645.

134. Yano Y, Sato YS, Sekio Y, Ohtsuka S, Kaito T, Ogawa R and Kokawa H, *Mechanical properties of friction stir welded 11Cr-ferritic/martensitic steel.* Journal of nuclear materials, 2013. 442(1): p. S524-S528.

135. Lakshminarayanan AK and Balasubramanian V, *An assessment of microstructure, hardness, tensile and impact strength of friction stir welded ferritic stainless steel joints.* Materials & Design, 2010. 31(10): p. 4592-4600.

136. Lakshminarayanan AK and Balasubramanian V, *Assessment of fatigue life and crack growth resistance of friction stir welded AISI 409M ferritic stainless steel joints.* Materials Science and Engineering: A, 2012. 539: p. 143-153.

137. Thomas WM, Wiesner CS, Marks DJ and Staines DG, *Conventional and bobbin friction stir welding of 12% chromium alloy steel using composite refractory tool materials.* Science and Technology of Welding & Joining, 2009. 14(3): p. 247-253.

138. Ahn BW, Choi DH, Kim DJ and Jung SB, *Microstructures and properties of friction stir welded 409L stainless steel using a Si3N4 tool.* Materials Science and Engineering: A, 2012. 532: p. 476-479.

139. Park SHC, *Microstructure and mechanical properties of friction stir welded 430 stainless steel*. Proceedings of the Fifteenth International Offshore and Polar Engineering Conference, 2005.

140. Bilgin MB and Meran C, *The effect of tool rotational and traverse speed on friction stir weldability of AISI 430 ferritic stainless steels.* Materials & Design, 2012. 33: p. 376-383.

141. Tavares SSM, De Souza JA, Herculano LFG, De Abreu HFG and De Souza Jr CM, *Microstructural, magnetic and mechanical property changes in an AISI 444 stainless steel aged in the 560 ℃ to 800 ℃ range.* Materials Characterization, 2008. 59(2): p. 112-116.

142. De Abreu HFG, Bruno ADS, Tavares SSM, Santos RP and Carvalho, *Effect of high temperature annealing on texture and microstructure on an AISI-444 ferritic stainless steel.* Materials Characterization, 2006. 57(4): p. 342-347.

143. *Stainless steel heavy plates*, J.S. Corporation, Editor. 2004: Tokyo.

144. *Stainless steel heavy plate*. 2009, Nippon Steel & Sumikin Stainless Steel Corporation: Tokyo.

145. *NSSC stainless steels*. 2003, Nippon Steel & Sumikin Stainless Steel Corporation: Tokyo.

146. ASTM A240/A240M-15, *Standard specification for chromium and chromium-nickel stainless steel plate, sheet, and strip for pressure vessels and for general applications.* 2015.

147. *GB/T 3280-2007, Cold-rolled stainless steel plate, sheet and strip*. 2007.

148. *GB/T 4237-2007, Hot-rolled stainless steel plate, sheet and strip*. 2007.

149. ASTM A370-14, *Standard test methods and definitions for mechanical testing of steel products*. 2014.

150. ASTM E8/E8M-13a, *Standard test methods for tensile testing of metallic materials*. 2013.

151. *http://enterprise.astm.org/filtrexx40.cgi?+REDLINE_PAGES/E23.htm*.

152. ASTM E384-11e1, *Standard test method for microindentation hardness of materials*. 2011.

153. ASTM E3-11, *Standard guide for preparation of metallographic specimens*. 2001.

154. Randle V, *The effects of thermomechanical processing on interfacial crystallography in metals*. Materials Science Forum, 1998. 294-296: p. 51-58.

155. Tullmin MAA, Witcomb MJ, Cortie MB and Robinson FPA, *Intergranular corrosion in low interstitial 40% Cr ferritic stainless steels.* British Corrosion Journal, 1990. 25(3): p. 191-196.

156. Ma L, Han J, Shen JQ and Hu SS, *Effects of microalloying and heat-treatment temperature on the toughness of 26Cr–3.5 Mo super ferritic stainless steels.* Acta Metallurgica Sinica (English Letters), 2014. 27(3): p. 407-415.

157. ASTM E23-12c, *Standard test methods for notched bar impact testing of metallic materials*. 2012.

158. Danielsen HK, *Z-phase in 9-12% Cr steels*. PhD Thesis, Lyngby: Technical University of Denmark, 2007.

159. Kashiwar A, Phani Vennela N, Kamath SL and Khatirkar RK, *Effect of solution annealing temperature on precipitation in 2205 duplex stainless steel.* Materials Characterization, 2012. 74: p. 55-63.

160. Escriba DM, Materna-Morris E, Plaut RL and Padilha, *Chi-phase precipitation in a duplex stainless steel.* Materials Characterization, 2009. 60(11): p. 1214-1219.

161. Yan HT, Bi HY, Li X and Xu Z, *Precipitation and mechanical properties of Nb-modified ferritic stainless steel during isothermal aging.* Materials Characterization, 2009. 60(3): p. 204-209.

162. Sello MP and Stumpf WE, *Laves phase precipitation and its transformation kinetics in the ferritic stainless steel type AISI 441.* Materials Science and Engineering: A, 2011. 528(3): p. 1840-1847.

163. Gladman T, *The physical metallurgy of microalloyed steels*. London: Institute of Materials, Minerals and Mining, 2002.

164. Yang P, *EBSD technology and application*. Beijing: Metallurgical Industry Press, 2013.

165. Watanabe T, Hirano T, Ochiai T and Oikawa. *Texture and grain boundary character distribution (GBCD) in B-free ductile polycrystalline Ni3Al*. *Materials Science Forum*, 1994. 157-162: p. 1103-1108.

166. Fairchild D, *Local brittle zones in structural welds.* The Metallurgical Society/AIME, 1987: p. 303-318.

167. Moon J, Lee CH, Uhm SH and Lee JB, *Coarsening kinetics of TiN particle in a low alloyed steel in weld HAZ: Considering critical particle size.* Acta Materialia, 2006. 54(4): p. 1053-1061.

168. Ghosh P, Ray RK, Ghosh C and Bhattacharjee D, *Comparative study of precipitation behavior and texture formation in continuously annealed Ti and Ti+ Nb added interstitial-free high-strength steels.* Scripta Materialia, 2008. 58(11): p. 939-942.

169. Han J, Li HJ and Xu HG, *Microalloying effects on microstructure and mechanical properties of 18Cr–2Mo ferritic stainless steel heavy plates.* Materials & Design, 2014. 58: p. 518-526.

170. Xu WC and Sun FY, *The fine structure of Nb and V precipitates in Nb-V steel.* Acta Metallrugica Sinica, 1983. 6.

171. Zhao JW, Jiang ZY and Lee CS, *Enhancing impact fracture toughness and tensile properties of a microalloyed cast steel by hot forging and post-forging heat treatment processes.* Materials & Design, 2013. 47: p. 227-233.

172. Wang ST, Yang K, Shan YY and Li LF, *Plastic deformation and fracture behaviors of nitrogen-alloyed austenitic stainless steels.* Materials Science and Engineering: A, 2008. 490(1): p. 95-104.

173. Meng FM and Fu JY, *Modern Nb-containing stainless steel*. 1st ed. Beijing: Metallurgical Industry Press, 2004.

174. Shi CX, Cheng GG, Li ZJ and Zhao P, *Solidification structure refining of 430 ferrite stainless steel with TiN nucleation.* Journal of Iron and Steel Research, International, 2008. 15(3): p. 57-60.

175. Andersen I and Grong Ø, *Analytical modelling of grain growth in metals and alloys in the presence of growing and dissolving precipitates—I. Normal grain growth.* Acta metallurgica et materialia, 1995. 43(7): p. 2673-2688.

176. Andersen I, Grong Ø and Ryum N, *Analytical modelling of grain growth in metals and alloys in the presence of growing and dissolving precipitates—II. Abnormal grain growth.* Acta metallurgica et Materialia, 1995. 43(7): p. 2689-2700.

177. Yan HT, Bi HY, Li X and Xu Z, *Microstructure, texture and grain boundaries character distribution evolution of ferritic stainless steel during rolling process.* Journal of Materials Processing Technology, 2009. 209(5): p. 2627-2631.

178. Yan HT, Bi HY, Li X and Zhang X, *Effect of two-step cold rolling and annealing on texture, grain boundary character distribution and r-value of Nb+ Ti stabilized ferritic stainless steel.* Materials Characterization, 2009. 60(1): p. 65-68.

179. Huh MY and Engler O, *Effect of intermediate annealing on texture, formability and ridging of 17% Cr ferritic stainless steel sheet.* Materials Science and Engineering: A, 2001. 308(1): p. 74-87.

180. Liu HT, Liu ZY and Wang GD, *Texture development and formability of strip cast 17% Cr ferritic stainless steel.* ISIJ International, 2009. 49(6): p. 890-896.

181. Zhang C, Liu ZY and Wang GD, *Effects of hot rolled shear bands on formability and surface ridging of an ultra purified 21% Cr ferritic stainless steel.* Journal of Materials Processing Technology, 2011. 211(6): p. 1051-1059.

182. GAO F, Liu ZY, Liu HT and Wang GD, *Evolution of Through-Thickness Texture in Ultra Purified 17% Cr Ferritic Stainless Steels.* Journal of Iron and Steel Research, International, 2013. 20(4): p. 31-38.

183. Huh MY, Cho YS, Kim JS and Engler O, *Effect of lubrication on the evolution of through-thickness texture gradients in cold rolled and recrystallized low carbon steel.* Zeitschrift für Metallkunde, 1999. 90(2): p. 124-131.

184. Fortier P, Aust K and Miller W, *Effects of symmetry, texture and topology on triple junction character distribution in polycrystalline materials.* Acta Metallurgica et Materialia, 1995. 43(1): p. 339-349.

185. Fortier P, Miller W and Aust K, *Triple junction and grain boundary character distributions in metallic materials.* Acta Materialia, 1997. 45(8): p. 3459-3467.

186. Kumar M, King WE and Schwartz AJ, *Modifications to the microstructural topology in fcc materials through thermomechanical processing.* Acta Materialia, 2000. 48(9): p. 2081-2091.

187. Folkhard E, *Welding Metallurgy of Stainless Steels.* New York: Springer-Verlag Wien, 1988.

188. Cho HH, Han HN, Hong ST, Park JH, Kwon YJ, Kim SH and Steel RJ, *Microstructural analysis of friction stir welded ferritic stainless steel.* Materials Science and Engineering: A, 2011. 528(6): p. 2889-2894.

189. Chen Y and Nakata K, *Evaluation of microstructure and mechanical properties in friction stir processed SKD61 tool steel.* Materials Characterization, 2009. 60(12): p. 1471-1475.

190. ASTM E384-11e1, *Standard test method for Knoop and Vickers hardness of materials*. 2011.

191. Leal R and Loureiro A, *Defects formation in friction stir welding of aluminium alloys*. *Materials Science Forum*. 2004: 455-456: p. 299-302.

192. Miyano Y, Fujii H, Sun YF, Katada Y, Kuroda S and Kamiya O, *Mechanical properties of friction stir butt welds of high nitrogen-containing austenitic stainless steel.* Materials Science and Engineering: A, 2011. 528(6): p. 2917-2921.

193. Vecchio KS and Hertzberg RW, *The influence of stacking fault energy on ductile fracture micromorphology.* Journal of Materials Science, 1988. 23(6): p. 2220-2224.

194. Cho JH, Boyce DE and Dawson PR, *Modeling strain hardening and texture evolution in friction stir welding of stainless steel.* Materials Science and Engineering: A, 2005. 398(1): p. 146-163.

195. Cho JH and Dawson PR, *Investigation on texture evolution during friction stir welding of stainless steel.* Metallurgical and Materials Transactions A, 2006. 37(4): p. 1147-1164.

196. Mironov S, Sato Y and Kokawa H, *Microstructural evolution during friction stir-processing of pure iron.* Acta Materialia, 2008. 56(11): p. 2602-2614.

PART D

APPENDIX

&

PUBLICATIONS

APPENDIX

A composite tool with the addition of high fraction (60 ~ 70 vol.%) cBN in a W-Re matrix serves two primary functions, heating and deforming the material. The tool in this study possesses a nominal 5.0 mm length conical probe with a stepped spiral design, aiming at promoting material flow to the root of the weld. The tool shoulder features the scroll geometry, to facilitate material flow from the periphery of the tool to the centre. Additionally, the shoulder is slightly convex, allowing the plunge depth to be varied according to the requirements of the BM. The shoulder diameter varies from 15 mm at its narrowest point to 23 mm at the shoulder periphery.

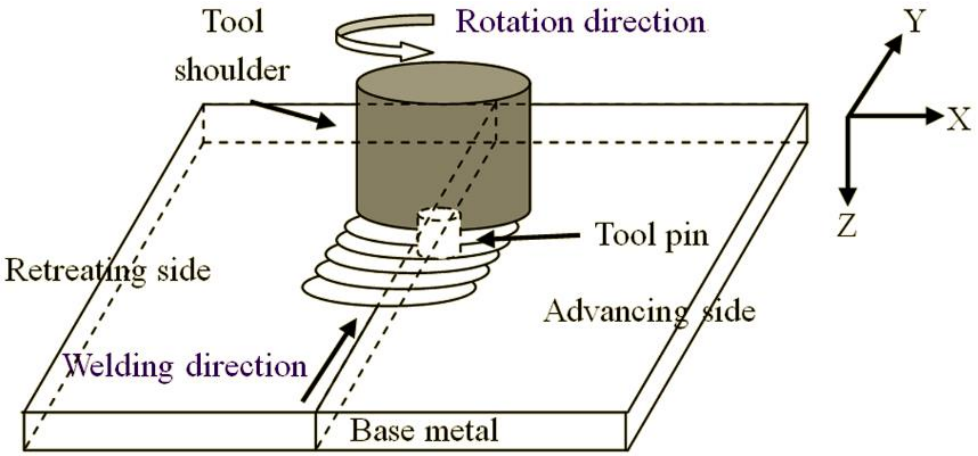

Figure Schematic illustration of FSW process.

Due to the high cBN volume fraction in the tool, a high rotation speed of 800 rpm was used during the tool plunge stage of the welding cycle, to soften the workpiece material to a large extent, and therefore avoid premature tool damage. Once the tool approached

to the target depth in the workpiece material, the rotational speed was reduced to 200 rpm for the remainder of the welding cycle.

PUBLICATIONS

1. **J. Han**, H. J. Li, Z. X. Zhu, L. Z. Jiang, H. G. Xu and L. Ma. "Effects of processing optimisation on microstructure, texture, grain boundary and mechanical properties of Fe-17Cr ferritic stainless steel thick plates", Materials Science & Engineering A, 2014, 616, 20-28.

2. **J. Han**, H. J. Li, F. Barbaro, L. Z. Jiang, Z. X. Zhu, H. G. Xu and L. Ma. "Precipitation and impact toughness of Nb-V stablised 18Cr-2Mo ferritic stainless steel during isothermal aging", Materials Science & Engineering A, 2014, 612, 63-70.

3. **J. Han**, H. J. Li, Z. X. Zhu, F. Barbaro, L. Z. Jiang, H. G. Xu and L. Ma. "Microstructure and mechanical properties of friction stir welded 18Cr-2Mo ferritic stainless steel thick plate", Materials & Design, 2014, 63, 238-246.

4. L. Ma, **J. Han**, J. Q. Shen and S. S. Hu. "Effects of microalloying and heat-treatment temperature on the toughness of 26Cr-3.5Mo super ferritic stainless steels", Acta Metallurgica Sinica (English Letters), 2014, 27 (3), 407-415.

5. H. J. Li, **J. Han** and F. Barbaro. "Microstructure and mechanical properties of friction stir welded 18Cr-2Mo ferritic stainless steel heavy plate", 10th Friction Stir Welding Symposium (10FSWS), May 2014, Beijing, China.

6. **J. Han**, H. J. Li and H. G. Xu. "Microalloying effects on microstructure and mechanical properties of 18Cr-2Mo ferritic stainless steel heavy plates", Materials & Design, 2014, 58, 518-526.

7. S. S. Hu, R. F. Han, J. Q. Shen, **J. Han** and H. G. Xu. "Effect of pulse frequency on microstructure of 21% Cr ferritic stainless steel in pulsed gas tungsten arc welding", Transactions of Tianjin University, 2013, 19 (2): 127-129.

8. R. F. Han, S. S. Hu, J. Q. Shen, **J. Han** and H. G. Xu. "Effect of different welding parameters on the microstructure of 21% Cr ferritic stainless steel", Advanced Materials Research, 2012, 452-453, 1446-1449.

9. H. G. Xu, Z. Y. Wang, **J. Han** and H. F. Yu. "Welding technologies of medium chromium pure ferritic stainless steels SUS444 and B445J1M", 8th Chinese Iron and Steel Annual Conference, October 2011, Beijing, China.

10. K. P. Geng, S. S. Hu, J. Q. Shen, **J. Han** and H. G. Xu. "Effect of Nb: YAG laser welding parameters on the microstructure of 21% Cr ferritic stainless steel", Advanced Materials Research, 2011, 291-294, 999-1002.

11. Z. Y. Wang, **J. Han**, H. M. Song, L. Z. Jiang, W. W. Wu and W. Zhang. "Comparative analysis for joint performance of duplex stainless steel by different

arc welding methods", Hanjie Xuebao/Transactions of the China Welding Institution, 2011, 32 (4), 37-40.